A coupled environmental-mechanical damage model for structural analysis of RC constructions.

Dissertation

submitted to and approved by the

Department of Architecture, Civil Engineering and Environmental Sciences
University of Braunschweig – Institute of Technology

and the

Department of Civil and Environmental Engineering
University of Florence

in candidacy for the degree of a
Doktor-Ingenieur (Dr.-Ing.) /
Dottore di Ricerca in Mitigation of Risk due to Natural Hazards on Structures and Infrastructures[*)]

by
Diego Alejandro Talledo
Born 19 October 1984
From Cogollo del Cengio, Italy

Submitted on	13 September 2013
Oral examination on	08 November 2013
Professorial advisors	Prof. Anna Saetta Prof. Harald Budelmann

2014

*) Either the German or the Italian form of the title may be used.

Examination committee:

Prof. Klaus Thiele

Prof. Harald Budelmann

Prof. Hocine Oumeraci

Prof. Anna Saetta

Prof. Gianni Bartoli

Prof. Claudio Borri

A coupled environmental-mechanical damage model for structural analysis of RC constructions.

Dissertation

submitted to and approved by the

Department of Architecture, Civil Engineering and Environmental Sciences
University of Braunschweig – Institute of Technology

and the

Department of Civil and Environmental Engineering
University of Florence

in candidacy for the degree of a
Doktor-Ingenieur (Dr.-Ing.) /
Dottore di Ricerca in Mitigation of Risk due to Natural Hazards on Structures and Infrastructures[*)]

by
Diego Alejandro Talledo
Born 19 October 1984
From Cogollo del Cengio, Italy

Submitted on	13 September 2013
Oral examination on	08 November 2013
Professorial advisors	Prof. Anna Saetta Prof. Harald Budelmann

2014

*) Either the German or the Italian form of the title may be used.

To my parents
and my brother

ABSTRACT

The aim of this work is to assess the collapse safety of both new and existing reinforced concrete structures. The latter can also be subjected to environmental degradation processes. To this aim the behavior of concrete and reinforced concrete structures eventually degraded by physical-chemical attacks need to be accurately described with theoretical and numerical models that can take into account the main characteristics of this kind of structures.

In this work a coupled environmental-mechanical scalar plastic-damage model originally developed by other authors (Faria et al.[1], Scotta [2], Saetta et al. [3], [4]) was modified, enhancing both the mechanical and the environmental aspects. In particular an innovative formulation able to accounting for the physical deterioration mechanism due to freeze-thaw cycles was developed within the framework of the environmental damage approach, while a more comprehensive representation of the mixed tension-compression domain and an enhancement of the plastic evolution law were proposed within the framework of the mechanical damage approach. The model was enriched with a Shear Retention Factor (Scotta et al. [5]) that was extended to the two-parameters scalar damage model here presented.

To validate and calibrate the mechanical damage model, it was applied to reproduce some tests taken from literature. Particular attention was dedicated in reproducing the tests on biaxial loaded concrete specimens and to simulate the response of a Single-Edge-Notched beam, typical example of mixed-mode failure. In both cases experimental and numerical results compare well, demonstrating the ability of the model to predict structural response and crack patterns of such examples.

The constitutive model proposed aims to be general and, thus, suitable for several types of reinforced concrete structural elements, while at the same time balancing accuracy with computational efficiency so as to be suitable for structural analysis of large structural models. A first application of the constitutive model can be on fiber-beam elements for slender reinforced concrete members constraining the general 3D

constitutive law to 1D. The models obtained with these elements are suitable for the simulation of large scale structures but they are limited to cases of moderate shear demand, since they do not address the material response under significant biaxial stress conditions. To simulate the inelastic behavior of reinforced concrete panels, an efficient membrane was proposed assuming superposition of different membranes (i.e. concrete and an appropriate number of steel bars). On the other hand, to assess the nonlinear behavior of reinforced concrete plates, an efficient plate model was proposed following a layered approach.

Concerning the environmental aspect, the coupled environmental-mechanical damage model was calibrated by using a limited number of tests carried out on concrete specimens under mono-axial and bi-axial compressive stresses, subjected to freeze-thaw cycles with different levels of deterioration. Finally the proposed coupled model was used as a predictive tool both for simulating a different series of biaxial concrete specimens subjected to freeze-thaw cycles and to evaluate the load carrying capacity of a frost damaged beam.

REFERENCES:

[1] Faria, R., Oliver, J., Cervera, M. (1998). A strain-based viscous-plastic-damage model for massive concrete structures, *Int. J. Solids and Structures*, 35, 1533-1558

[2] Scotta, R. (1997). Analisi meccanica di strutture in calcestruzzo mediante modelli di danno, *PhD Thesis*, Università degli studi di Padova, Dipartimento di Costruzioni e Trasporti

[3] Saetta, A., Scotta, R., Vitaliani, R. (1998). Mechanical behavior of concrete under physical-chemical attacks, *J. Eng. Mech.*, 124, 1100-1109

[4] Saetta, A., Scotta, R., Vitaliani, R. (1999). Coupled environmental-mechanical damage model of reinforced concrete structures, *J. Eng. Mech.*, 125, 930-940

[5] Scotta, R., Vitaliani, R., Saetta, A., Oñate, E., Hanganu, A. (2001). A scalar damage model with a shear retention factor for the analysis of reinforced concrete structures: theory and validation, *Comput. Struct.*, 79, 737-755

ACKOWLEDGMENTS

This doctoral thesis was carried out with the help and the support of the very kind people around me. This is why I would like to express my gratitude to each of them.

Foremost, I would like to express my deep appreciation and gratitude to my Italian advisor Prof. Anna Saetta for her continuous support and motivation during my Ph.D study; her guidance, together with her enthusiasm and patience helped me during all the time of my research and during the writing of this thesis.

Moreover I would like to express my gratitude to my German advisor Prof. Harald Budelmann for supervising my work with constructive suggestions and fruitful discussions throughout the course of my studies.

I am also grateful to the coordinators of the Graduate College during the years of my studies, Prof. Antonio Borri and Prof. Udo Peil for making it possible for me to live this experience.

I would like to express my deepest gratitude to Dr. Luisa Berto. I had the opportunity to work with her since my bachelor's thesis appreciating her patience, her enthusiasm and her guidance throughout my studies. Moreover her support and care helped me many times overcoming setbacks. I am sincerely grateful for her friendship.

I also wish to express my deep appreciation and gratitude to Dr. Leopoldo Tesser for his friendship, his encouragement and advice during my Ph.D work. Our talks were constructive and enriching both scientifically and privately. I had the chance to share with him different experiences and to profitably combine fun and work!

Additionally I would like to thank Prof. Renato Vitaliani and Dr. Roberto Scotta for the stimulating talks, helpful discussions, suggestions and comments on the wide range of topics covered in this work.

Last but not least, my deepest and most sincere thanks to my family, who always supported me. I am deeply indebt to my father Miguel and my mother Fabiana for

being able to reach this important step. Words can not express how thankful I am to them for all the sacrifices they made on my behalf. Moreover I am grateful to Leandro: I had the opportunity to grow up sharing the room and life with a great brother! We shared a lot of serious as well as funny moments over the years.

Finally I wish to express my greatest gratitude to Daiana for her love and constant support; she believed in me and she encouraged me throughout the difficult time making it easier to overcome setbacks. I am deeply grateful for the wonderful life that we share together.

CONTENTS:

ABSTRACT ..... **III**

ACKOWLEDGMENTS ..... **V**

CONTENTS: ..... **VII**

LIST OF FIGURES ..... **XI**

LIST OF TABLES ..... **XVII**

CHAPTER 1: INTRODUCTION **19**

1.1 MOTIVATION AND SCOPE OF THE RESEARCH 19
1.2 OVERVIEW OF THE THESIS 21
1.3 REFERENCES 22

CHAPTER 2: MODELING OF CONCRETE **23**

2.1 INTRODUCTION 24
2.2 CONCRETE BEHAVIOR 24
2.2.1 Behavior in compression *25*
2.2.2 Behavior in tension *28*
2.2.3 Multiaxial behavior *31*
2.2.4 Cyclic behavior *31*
2.3 MODELING OF CONCRETE 33
2.3.1 Basic concepts of plasticity theory *34*
2.3.2 Basic concepts of smeared crack models *35*
2.3.3 Basic concepts of continuum damage mechanics *39*
2.3.3.1 Definition of damage variables 40
2.3.3.2 Hypotheses of mechanical equivalence 44
2.3.3.2.1 Hypothesis of strain equivalence 44
2.3.3.2.2 Hypothesis of stress equivalence 45
2.3.3.2.3 Hypothesis of energy equivalence 45

2.4 STRAIN LOCALIZATION AND MESH OBJECTIVITY 46
2.4.1 Mesh-adjusted softening modulus 50
2.4.2 Non-local continuum 52
2.5 REFERENCES 53

CHAPTER 3: MECHANICAL DAMAGE MODEL FOR CONCRETE 59

3.1 THERMODYNAMIC ASPECTS 60
3.2 DAMAGE CRITERIA 64
3.3 EVOLUTION OF PLASTIC STRAIN TENSOR 68
3.4 EVOLUTION OF DAMAGE VARIABLES 70
3.5 ADOPTED DAMAGE AND CRITERIA EVOLUTION LAWS 71
3.5.1 Parameters of damage evolution laws 74
3.6 SHEAR RETENTION FACTOR 77
3.7 STRAIN LOCALIZATION AND MESH OBJECTIVITY 79
3.7.1 Tension 79
3.7.1.1 Adjusted softened modulus method 79
3.7.1.2 Numerical application: panel subjected to uniaxial tension 80
3.7.2 Compression 81
3.7.2.1 Adjusted softened modulus method 81
3.7.2.2 Numerical application: specimen subjected to uniaxial compression 83
3.8 BASIC CONCEPTS ON THE INTEGRATION ALGORITHM 90
3.9 VALIDATION TESTS 92
3.9.1 Cyclic uniaxial compression test 92
3.9.2 Cyclic uniaxial tension test 93
3.9.3 Tests under biaxial load conditions 93
3.9.3.1 Four Biaxial tensile-compressive tests 93
3.9.3.2 Simulation of failure domain 94
3.9.4 Single Edge Notched Test 96
3.10 REFERENCES 99

CHAPTER 4: F.E. MODELLING OF REINFORCED CONCRETE ELEMENTS 103

4.1 OPENSEES 104
4.1.1 Objected oriented programming 104
4.1.2 OpenSEES Framework 105
4.2 REINFORCEMENT CONSTITUTIVE LAWS 106
4.3 FIBER BEAM-COLUMN ELEMENTS 108
4.4 MEMBRANE MODEL FOR R/C PANELS 109
4.5 VALIDATION STUDIES OF R/C MEMBRANE MODEL 110
4.5.1 Uniaxial tension test by Bhide and Collins (Panel PB2) 110
4.5.2 Cyclic shear tests by Mansour and Hsu 111
4.5.3 Shear test by Vecchio and Collins (specimen PV20) 126

4.5.4 Simply supported beams without shear reinforcement testes by Leonhardt *127*
4.5.5 Shear walls tested by Maier – Thürlimann *133*
4.5.5.1 Rectangular cross section under monotonic loading (Specimen S4) 133
4.5.5.2 I cross section under monotonic loading (Specimen S2) 135
4.5.5.3 I cross section under cyclic loading (Specimen S5) 136
4.6 PLATE MODEL FOR R/C PANELS 138
4.7 VALIDATION STUDIES FOR R/C PLATE MODEL 139
4.7.1 Reinforced concrete slab *140*
4.7.2 Box-shaped shear wall *142*
4.7.3 U-shaped shear wall *144*
4.8 REFERENCES 148

CHAPTER 5: COUPLED ENVIRONMENTAL-MECHANICAL DAMAGE MODEL 151

5.1 DEGRADATION PROCESSES ON RC STRUCTURES 153
5.1.1 Corrosion of reinforcement *153*
5.1.2 Degradation of concrete *154*
5.2 COUPLED ENVIRONMENTAL MECHANICAL DAMAGE MODEL 157
5.3 MODELING OF SOME COMMON DEGRADATION PROCESSES 159
5.4 ENHANCEMENT FOR FREEZE-AND-THAW CYCLES 164
5.4.1 Uniaxial compressive load *166*
5.4.2 Biaxial compressive load *169*
5.5 VALIDATION EXAMPLE 172
5.5.1 Frost-Damaged Beam *172*
5.6 REFERENCES 175

CHAPTER 6: CONCLUSIONS AND FUTURE DEVELOPMENTS 179

APPENDIX A: MESH REGULARIZATION IN COMPRESSION 183

LIST OF FIGURES

FIGURE 2.1 - FORCE-DISPLACEMENT CURVES FOR DIFFERENT MATERIALS: (A) DUCTILE; (B) PERFECTLY BRITTLE; (C) QUASI-BRITTLE [1] 24
FIGURE 2.2 - SCALE LEVELS FOR CONCRETE AS PROPOSED BY WITTMANN [5] 25
FIGURE 2.3 - SCHEMATIC LOAD-DISPLACEMENT CURVE FOR CONCRETE SPECIMEN SUBJECTED TO UNIAXIAL COMPRESSION 27
FIGURE 2.4 - MECHANISM OF DAMAGING FOR COMPRESSIVE LOADS IN MESO-LEVEL 27
FIGURE 2.5 - STRESS-STRAIN CURVES FOR SPECIMENS OF DIFFERENT SIZES [8] 27
FIGURE 2.6 - POST-PEAK STRESS-DISPLACEMENT CURVES FOR SPECIMENS OF DIFFERENT SIZES [8] 28
FIGURE 2.7 - TYPICAL STRESS-DEFORMATION CURVE FOR CONCRETE UNDER UNIAXIAL TENSION [10] 29
FIGURE 2.8 - LOAD-DEFORMATION CURVE FOR CONCRETE UNDER UNIAXIAL TENSION [11] 29
FIGURE 2.9 - SCHEMATIC REPRESENTATION OF RELATIVE SIZE OF FPZ, NON-LINEAR ZONE(NLZ) AND LINEAR ELASTIC ZONE (LEZ) FOR: (A) CONCRETE; (B) METALS; (C) LEFM 30
FIGURE 2.10 - SCHEMATIC REPRESENTATION OF: (A) DISCRETE CRACK MODEL; (B) CRACK BAND MODEL [14] 30
FIGURE 2.11 - BIAXIAL STRENGTH ENVELOPE (KUPFER ET AL. [17]) 32
FIGURE 2.12 - STRENGTH OF CONCRETE UNDER TRI-AXIAL STRESS STATE (CHEN [18]) 32
FIGURE 2.13 - STIFFNESS RECOVERY (YANKELEVSKY AND REINHARDT [19]) 32
FIGURE 2.14 - YIELD SURFACE IN STRESS SPACE WITH LOADING/UNLOADING CRITERIA 35
FIGURE 2.15 - (A) MODE-I FRACTURE; (B) MODE-II FRACTURE 37
FIGURE 2.16 - SCHEMATIC REPRESENTATION OF SMEARED CRACK MODELS [36]: (A) FIXED CRACK MODEL (FCM); (B) ROTATING CRACK MODEL (RCM); (C) MULTIPLE FIXED CRACKS MODEL (MFCM) 39
FIGURE 2.17 - EFFECTIVE AREA CONCEPT 40
FIGURE 2.18 - (A) UNDAMAGED CONFIGURATION; (B) DAMAGED CONFIGURATION; (C) FICTITIOUS UNDAMAGED CONFIGURATION 41
FIGURE 2.19 - SCHEMATIC REPRESENTATION OF STRAIN EQUIVALENCE HYPOTHESIS 45
FIGURE 2.20 - SCHEMATIC REPRESENTATION OF STRESS EQUIVALENCE HYPOTHESIS 45

FIGURE 2.21 - HYPOTHESIS OF COMPLEMENTARY STRAIN ENERGY EQUIVALENCE FOR UNIAXIAL STRESS CONDITION 46
FIGURE 2.22 - STRAIGHT BAR UNDER UNIAXIAL TENSION 48
FIGURE 2.23 - (A) STRESS-STRAIN LAW WITH LINEAR SOFTENING; (B) POSSIBLE LOAD DISPLACEMENT DIAGRAMS (FAN SHADED IN GREY) 48
FIGURE 2.24 - (A) STRAIN SOFTENING VS. ELASTIC UNLOADING; (B) POSSIBLE STRAIN PROFILE ALONG BAR 48
FIGURE 2.25 - MESH-SENSITIVITY OF RESULT FOR A UNIAXIAL TENSION TEST. (A) LOAD-DISPLACEMENT CURVES; (B) STRAIN DISTRIBUTION ALONG THE BAR AT GIVEN DISPLACEMENT; (C) STRAIN DISTRIBUTION ALONG THE BAR AT GIVEN FORCE 49
FIGURE 2.26 - CHARACTERISTIC LENGTH OF FINITE ELEMENT WITH GENERIC CRACK ORIENTATION .. 52
FIGURE 3.1 - DAMAGE CRITERIA IN EQUIVALENT STRESSES SPACE 66
FIGURE 3.2 - INITIAL DAMAGE SURFACE FOR ORIGINAL MODEL (FARIA ET AL. [1]) 67
FIGURE 3.3 - INITIAL DAMAGE SURFACE FOR PROPOSAL A 67
FIGURE 3.4 - INITIAL DAMAGE SURFACE FOR PLANE STRESS CONDITIONS FOR DIFFERENT PROPOSALS 68
FIGURE 3.5 - STRESS-STRAIN CURVE FOR DIFFERENT VALUES OF β 69
FIGURE 3.6 - POLAR COORDINATES 72
FIGURE 3.7 - GEOMETRIC REPRESENTATION OF DAMAGE SURFACE IN EQUIVALENT STRESSES SPACE 74
FIGURE 3.8 - PURE SHEAR LOAD CONDITION; (A) EVOLUTION OF DAMAGE THRESHOLD IN THE EQUIVALENT STRESSES SPACE; (B) STRESS-STRAIN PATH ALONG THE PRINCIPAL COMPRESSION DIRECTION; (C) STRESS-STRAIN PATH ALONG THE PRINCIPAL TENSION DIRECTION 74
FIGURE 3.9 - LOAD–DISPLACEMENT CURVES IN TENSION FOR DIFFERENT LEVEL OF MESH REFINEMENT 80
FIGURE 3.10 - POSITIVE DAMAGE CONTOUR FOR SPECIMEN SUBJECTED TO TENSION. (A) 1 ELEMENT MESH; (B) 4X4 ELEMENTS MESH 81
FIGURE 3.11 - COMPRESSION SOFTENING MODEL ADOPTED BY FEENSTRA [17] 82
FIGURE 3.12 - CONCRETE SPECIMENS WITH DIFFERENT HEIGHTS 84
FIGURE 3.13 - (A) STRESS-STRAIN RELATION ACCORDING TO MODEL CODE 1990 [21]; CRUSHING ENERGY UNDER: (B) HYPOTHESIS 0; (C) HYPOTHESIS ;, (D) HYPOTHESIS 2 86
FIGURE 3.14 - STRESS-STRAIN CURVES FOR DIFFERENT SPECIMENS 86
FIGURE 3.15 – (A) STRESS-STRAIN CURVE AND (B) CORRESPONDING STRESS-δ_p CURVE 87
FIGURE 3.16 - FORCE-DISPLACEMENT FOR DIFFERENT SPECIMENS 87
FIGURE 3.17 - NEGATIVE DAMAGE CONTOUR AND DEFORMED SHAPE FOR DIFFERENT DISCRETIZATION 89
FIGURE 3.18 - STRESS-STRAIN CURVES FOR ELEMENTS OF 8-ELEMENT DISCRETIZATION 89
FIGURE 3.19 - MEAN-STRESS-MEAN-STRAIN CURVES FOR EACH DISCRETIZATION 90
FIGURE 3.20 - MEAN-STRESS-MEAN-STRAIN CURVES FOR EACH DISCRETIZATION WITH KENT-PARK MODEL 90
FIGURE 3.21 - MEAN-STRESS-MEAN-STRAIN CURVES FOR EACH DISCRETIZATION WITHOUT ANY REGULARIZATION 90

FIGURE 3.22 - COMPARISON OF NUMERICAL AND EXPERIMENTAL RESULTS FOR CYCLIC UNIAXIAL TEST 92
FIGURE 3.23 - COMPARISON BETWEEN NUMERICAL AND EXPERIMENTAL RESPONSE OF A CONCRETE SPECIMEN SUBJECTED TO UNIAXIAL CYCLIC TENSILE LOAD 94
FIGURE 3.24 - COMPARISON BETWEEN NUMERICAL AND EXPERIMENTAL RESPONSE OF A CONCRETE SPECIMEN SUBJECTED TO BIAXIAL COMPRESSIVE LOADS 95
FIGURE 3.25 – FAILURE SURFACE AND COMPARISON WITH KUPFER'S DOMAIN FOR PROPOSALS A AND B 95
FIGURE 3.26 – REPRESENTATION OF KUPFER'S DOMAIN, NUMERICAL INITIAL DAMAGE SURFACE AND NUMERICALLY OBTAINED FAILURE POINTS 96
FIGURE 3.27 - GEOMETRIC AND LOAD CHARACTERISTICS OF SEN BEAM 97
FIGURE 3.28 - SEN-BEAM: (A) EXPERIMENTAL ENVELOPES AND NUMERICAL PREDICTIONS OF THE CRACK PATTERN: (B) NUMERICAL PREDICTIONS OF THE CRACK PATTERN WITH SMEARED CRACK MODEL, [28] 98
FIGURE 3.29 - LOAD-CMSD CURVE AND COMPARISON WITH EXPERIMENTAL ENVELOPE 98
FIGURE 4.1 - (A) PROCEDURAL PROGRAM (B) OBJECT-ORIENTED PROGRAM 105
FIGURE 4.2 - MAIN ABSTRACTIONS OF FRAMEWORK OPENSEES [1] 106
FIGURE 4.3 - MAIN ABSTRACTIONS OF DOMAIN 106
FIGURE 4.4 - STRUCTURE OF MATERIAL ENTITY 106
FIGURE 4.5 - ELASTIC-PLASTIC LAW WITH KINEMATIC HARDENING: (A) MODEL PARAMETERS (B) HYSTERETIC BEHAVIOR 107
FIGURE 4.6 - GIUFFRÉ-MENEGOTTO-PINTO LAW HYSTERETIC BEHAVIOR [3] 108
FIGURE 4.7 - FINITE ELEMENT MESH ADOPTED FOR SIMULATION OF SPECIMEN PB2 110
FIGURE 4.8 - STRESS-STRAIN RESPONSE FOR SPECIMEN PB2 111
FIGURE 4.9 - REINFORCEMENT ORIENTATION IN TESTED PANELS: (A) CE SERIES (A2=90°); (B) CF SERIES (AS=79.8°); (C) CD SERIES (A2=68.2°); (D) CA AND CB SERIES (A2=45°) [9] 113
FIGURE 4.10 - LOADING HISTORY FOR SPECIMEN CA3 [9] 114
FIGURE 4.11 - ELEMENTS UNDER PURE SHEAR 114
FIGURE 4.12 - HORIZONTAL STRESS VS. VERTICAL STRESS FOR PANEL CA2 116
FIGURE 4.13 - COMPARISON NUMERICAL-EXPERIMENTAL OF SHEAR STRESS-SHEAR STRAIN RESPONSES OF PANEL CA2 116
FIGURE 4.14 - CRACKED R/C ELEMENT WITH α_2 = 45° (CA SERIES) 117
FIGURE 4.15 - VERTICAL STRAIN VS. HORIZONTAL STRAIN. COMPARISON NUMERICAL-EXPERIMENTAL FOR PANEL CA2 117
FIGURE 4.16 - COMPARISON NUMERICAL-EXPERIMENTAL OF SHEAR STRESS-SHEAR STRAIN RESPONSES OF PANEL CA3 118
FIGURE 4.17 - COMPARISON NUMERICAL-EXPERIMENTAL OF SHEAR STRESS-SHEAR STRAIN RESPONSES OF PANEL CA4 119
FIGURE 4.18 - COMPARISON NUMERICAL-EXPERIMENTAL OF SHEAR STRESS-SHEAR STRAIN RESPONSES OF PANEL CB3 120

FIGURE 4.19 - COMPARISON NUMERICAL-EXPERIMENTAL OF SHEAR STRESS-SHEAR STRAIN RESPONSES OF PANEL CB4 120
FIGURE 4.20 - COMPARISON NUMERICAL-EXPERIMENTAL OF SHEAR STRESS-SHEAR STRAIN RESPONSES OF PANEL CD2 121
FIGURE 4.21 - COMPARISON NUMERICAL-EXPERIMENTAL OF SHEAR STRESS-SHEAR STRAIN RESPONSES OF PANEL CD3 122
FIGURE 4.22 - COMPARISON NUMERICAL-EXPERIMENTAL OF SHEAR STRESS-SHEAR STRAIN RESPONSES OF PANEL CD4 122
FIGURE 4.23 - COMPARISON NUMERICAL-EXPERIMENTAL OF SHEAR STRESS-SHEAR STRAIN RESPONSES OF PANEL CE2 123
FIGURE 4.24 - COMPARISON NUMERICAL-EXPERIMENTAL OF SHEAR STRESS-SHEAR STRAIN RESPONSES OF PANEL CE3 123
FIGURE 4.25 - COMPARISON NUMERICAL-EXPERIMENTAL OF SHEAR STRESS-SHEAR STRAIN RESPONSES OF PANEL CE4 123
FIGURE 4.26 - CRACKED R/C ELEMENT WITH $\alpha_2 = 90°$ (CE SERIES) 124
FIGURE 4.27 - VERTICAL STRAIN VS. HORIZONTAL STRAIN. COMPARISON NUMERICAL-EXPERIMENTAL FOR PANEL CE3 124
FIGURE 4.28 - VERTICAL STRESS VS. VERTICAL STRAIN. COMPARISON NUMERICAL-EXPERIMENTAL FOR PANEL CE3 125
FIGURE 4.29 - COMPARISON NUMERICAL-EXPERIMENTAL OF SHEAR STRESS-SHEAR STRAIN RESPONSES OF PANEL CF2 126
FIGURE 4.30 - SHEAR STRESS-SHEAR STRAIN CURVE FOR SPECIMEN PV20 127
FIGURE 4.31 – GEOMETRY OF THE SIMPLY SUPPORTED BEAMS WITHOUT SHEAR REINFORCEMENT TESTED BY LEONHARDT [11] 127
FIGURE 4.32 – PICTURES OF CRACK PATTERN AT FAILURE CONDITION AS REPORTED BY LEONHARDT [11] 128
FIGURE 4.33 - COMPARISON OF NUMERICAL AND EXPERIMENTAL RESULTS IN TERMS OF FAILURE LOAD VS. SHEAR SPAN TO DEPTH RATIO 129
FIGURE 4.34 - LOAD-DISPLACEMENT CURVES FOR ALL BEAMS 129
FIGURE 4.35 - TENSILE DAMAGE CONTOUR FOR BEAM T4 AT: (A) 1 MM DISPLACEMENT; (B) 2.2 MM DISPLACEMENT 130
FIGURE 4.36 - RESULTS FOR BEAM T4 AT FAILURE LOAD (A) MAXIMUM PRINCIPAL STRESS; (B) MINIMUM PRINCIPAL STRESS 131
FIGURE 4.37 - RESULTS FOR BEAM T9 AT INCIPIENT FAILURE (DISPLACEMENT NEAR 100 MM). (A) POSITIVE DAMAGE CONTOUR; (B) NEGATIVE DAMAGE CONTOUR 131
FIGURE 4.38 - RESULTS FOR BEAM T10 AT INCIPIENT FAILURE (DISPLACEMENT NEAR 100 MM). (A) POSITIVE DAMAGE CONTOUR; (B) NEGATIVE DAMAGE CONTOUR 132
FIGURE 4.39 - EXPERIMENTAL SETUP OF SHEAR WALLS TESTES BY MAIER AND THÜRLIMANN [12] 133
FIGURE 4.40 - LOAD-DISPLACEMENT CURVE FOR SPECIMEN S4 AND COMPARISON WITH EXPERIMENTAL DATA 134

FIGURE 4.41 - COMPRESSIVE DAMAGE CONTOUR AT THE HORIZONTAL DISPLACEMENT OF 11 MM FOR PANEL S4 134
FIGURE 4.42 - PICTURE OF SPECIMEN S4 AT FAILURE [12] 135
FIGURE 4.43 - LOAD-DISPLACEMENT CURVE FOR SPECIMEN S2 AND COMPARISON WITH EXPERIMENTAL DATA 135
FIGURE 4.44 - POSITIVE DAMAGE PARAMETER AT DISPLACEMENT OF 0.7 MM FOR SPECIMEN S2 136
FIGURE 4.45 - NEGATIVE DAMAGE PARAMETER AT INCIPIENT FAILURE FOR SPECIMEN S2 136
FIGURE 4.46 - LOAD-DISPLACEMENT CURVE FOR SPECIMEN S5 AND COMPARISON WITH EXPERIMENTAL DATA 137
FIGURE 4.47 - NEGATIVE DAMAGE PARAMETER AT DISPLACEMENT OF 20 MM FOR SPECIMEN S2 137
FIGURE 4.48 - PICTURE OF SPECIMEN S5 AT FAILURE [12] 138
FIGURE 4.49 - SCHEMATIC REPRESENTATION OF THE R/C PLATE MODEL 139
FIGURE 4.50 – LOAD-CENTER DEFLECTION CURVES FOR NUMERICAL AND EXPERIMENTAL RESULTS 140
FIGURE 4.51 - STRAINS ALONG BOTTOM TRANSVERSE BAR AT CENTER OF SPECIMEN AND COMPARISON WITH EXPERIMENTAL DATA 141
FIGURE 4.52 - STRAINS AT CENTER OF SPECIMEN IN BOTTOM BARS RUNNING IN THE DIRECTION OF IN-PLANE LOAD AND COMPARISON WITH EXPERIMENTAL DATA 141
FIGURE 4.53 - DISTRIBUTION OF POSITIVE DAMAGE IN THE BOTTOM LAYER OF THE SPECIMEN AND COMPARISON WITH THE PICTURE OF A SIMILAR PANEL 142
FIGURE 4.54 - LOAD-DISPLACEMENT CURVE FOR BOX-SHAPED SHEAR WALL AND COMPARISON WITH EXPERIMENTAL DATA 143
FIGURE 4.55 - POSITIVE DAMAGE DISTRIBUTION AFTER THE FIRST CYCLE IS COMPLETE 144
FIGURE 4.56 - NEGATIVE DAMAGE DISTRIBUTION DURING AT INCIPIENT FAILURE DURING THE LAST LOADING CYCLE 144
FIGURE 4.57 - SECTION SCHEME WITH REINFORCEMENT DETAIL [20] 145
FIGURE 4.58 - LOAD HISTORY APPLIED TO THE U-SHAPED WALL 145
FIGURE 4.59 - LOAD-DISPLACEMENT CURVE OF U-SHAPED WALL AND COMPARISON WITH EXPERIMENTAL DATA ALONG X DIRECTION (PARALLEL TO WEB) 146
FIGURE 4.60 - LOAD-DISPLACEMENT CURVE OF U-SHAPED WALL AND COMPARISON WITH EXPERIMENTAL DATA ALONG Y DIRECTION (PARALLEL TO FLANGES) 146
FIGURE 4.61 - EXPERIMENTAL AND NUMERICAL DEFORMATIONS AT THE BASE EDGE OF THE FLANGES FOR U-SHAPED WALL 147
FIGURE 4.62 - NEGATIVE DAMAGE DISTRIBUTION AT DISPLACEMENT OF -40 MM IN BOTH DIRECTIONS 147
FIGURE 5.1 - SCHEMATIC CLASSIFICATION OF DEGRADATION PROCESSES ON REINFORCED CONCRETE STRUCTURES 153
FIGURE 5.2 - SCHEMATIC REPRESENTATION OF TWO MAIN TYPES OF FROST DAMAGE (FROM [21]) 156
FIGURE 5.3 - RESISTING SURFACE OF (A) UNDAMAGED SPECIMEN (B) MECHANICALLY DAMAGED SPECIMEN (C) SPECIMEN SUBJECTED TO COUPLE CHEMICAL-MECHANICAL DAMAGE 157

FIGURE 5.4 - EVOLUTION OF DAMAGE VARIABLE D_{CHEM} WITH DIFFERENT VALUES OF φ 158
FIGURE 5.5 - EFFECT OF D_{ENV} ON STRESS-STRAIN CONSTITUTIVE LAW 158
FIGURE 5.6 - DAMAGE-TYPE BOND LAW [31] 164
FIGURE 5.7 - EFFECT OF D_{BOND} AND β ON THE BOND LAW [31] 164
FIGURE 5.8 – EFFECT OF FTC ON COMPRESSIVE BEHAVIOR OF CONCRETE [28] 165
FIGURE 5.9 – EFFECT OF FTC ON TENSILE BEHAVIOR OF CONCRETE [28] 165
FIGURE 5.10 – EFFECT OF DIFFERENT CONCRETE CHARACTERISTICS ON FROST DAMAGE MODEL 166
FIGURE 5.11 - STRESS-STRAIN CURVES OBTAINED FROM OPTIMIZATION OF 1D COMPRESSION TESTS COMPARED WITH EXPERIMENTAL RESULTS FOR: (A) N = 0 FTC; (B) N = 25 FTC; (C) N = 75 FTC 167
FIGURE 5.12 - PROPOSED RELATIONS BETWEEN: (A) $D_{ENV} - N_{EQ}$; (B) β - N_{EQ} 168
FIGURE 5.13 - SIMULATION OF UNIAXIAL COMPRESSION TEST FOR N = 50 AND COMPARISON WITH EXPERIMENTAL RESULTS 168
FIGURE 5.14 - PROPOSED RELATION BETWEEN: R - N_{EQ} 169
FIGURE 5.15 - COMPARISON BETWEEN EXPERIMENTAL AND NUMERICALLY PREDICTED RESULTS FOR 2D COMPRESSION TEST REPRESENTED IN: (A) STRESS - α PLANE (B) PRINCIPAL STRESS PLANE 171
FIGURE 5.16 - GEOMETRY AND REINFORCEMENT OF BEAMS R1 (SOUND) AND D1 (DEGRADED) . 172
FIGURE 5.17 - LOAD DISPLACEMENT CURVES FOR BEAMS R1 AND D1 COMPARED WITH EXPERIMENTAL CURVES 174
FIGURE 5.18 – DAMAGE PARAMETERS DISTRIBUTION AT INCIPIENT FAILURE FOR BEAM R1 174
FIGURE 5.19 - DAMAGE PARAMETERS DISTRIBUTION AT INCIPIENT FAILURE FOR BEAM D1 174

LIST OF TABLES

TABLE 3.1 - VALUES FOR THE EXPONENTS OF THE DAMAGE EVOLUTION LAWS 72
TABLE 3.2 - MATERIAL CHARACTERISTICS ASSUMED 81
TABLE 3.3 - MATERIAL CHARACTERISTICS ASSUMED 84
TABLE 3.4 - GEOMETRICAL CHARACTERISTICS OF DIFFERENT SPECIMENS 84
TABLE 3.5- PARAMETERS OF CONSTITUTIVE LAW OBTAINED FOR DIFFERENT SPECIMENS 85
TABLE 3.6 - MATERIAL CHARACTERISTICS ASSUMED 92
TABLE 3.7 - MATERIAL CHARACTERISTICS ASSUMED 94
TABLE 3.8 - MATERIAL CHARACTERISTICS ASSUMED 98
TABLE 4.1- MATERIAL CHARACTERISTICS FOR SPECIMEN PB2 110
TABLE 4.2- CHARACTERISTICS OF TEST SPECIMENS: THICKNESS, MATERIAL PROPERTIES, ORIENTATION OF STEEL BARS, PERCENTAGE OF STEEL BARS 114
TABLE 4.3 - CONCRETE MODEL PARAMETERS ADOPTED IN SIMULATION 115
TABLE 4.4 - GEOMETRIC CHARACTERISTICS OF ANALYZED BEAMS 128
TABLE 4.5 - MATERIAL CHARACTERISTICS ADOPTED FOR SIMULATION OF LEONHARDT BEAMS 129
TABLE 4.6 - RESULTS OF SIMULATION OF LEONHARDT BEAMS 130
TABLE 5.1 - MATERIAL PARAMETERS FOR UNIAXIAL COMPRESSION TESTS ON FROST-DAMAGED CONCRETE 167
TABLE 5.2 - UNIAXIAL COMPRESSION TEST ON FROST DAMAGE CONCRETE: EXPERIMENTAL (EXP) AND NUMERICALLY PREDICTED (PRED) SOLUTION 168
TABLE 5.3 - BIAXIAL COMPRESSION TEST ON FROST DAMAGE CONCRETE: ERRORS BETWEEN NUMERICAL AND EXPERIMENTAL RESULTS 170
TABLE 5.4 - MATERIAL PARAMETERS FOR BEAMS R1 AND D1 173

CHAPTER 1:
INTRODUCTION

1.1 Motivation and scope of the research

Reinforced concrete represents one of the most common materials for constructions. Indeed since the beginning of the last century it was widely used to construct buildings and infrastructures. Since its introduction a lot of progress has been reached. The research focused initially on the mechanical characteristics of the material introducing particular constructive technologies to increase the strength of a structure (e.g. fiber reinforced concrete, high strength concrete, prestressed concrete, …). In the last decades the attention was focused among others to the crucial problem of durability: indeed it was observed that reinforced concrete structures are not durable under all environmental conditions. In particular when reinforced concrete is exposed to an aggressive environment, degradation processes may occur leading to several consequences that can even be extremely dangerous, also in regard to life safety requirement. Among the degradation processes that affect reinforced concrete structures, experience shows that the most severe effects on reinforced concrete elements are those that lead to reinforcement corrosion (e.g. carbonation, chloride attack) and those that produce expansive products, like sulphate attack and freeze-thaw cycles, the latter especially in cold climate regions.

Moreover, in the last decades, the concept that the total cost of a building is not composed only by immediate construction costs, gained attention. In fact, the total costs of a building comprise also costs of maintenance, repair and rehabilitation.

Modern civil engineering deals with the topics cited and in particular with the evaluation of the safety of a structure during its whole service life. Within such a design approach, requested by modern building codes, the engineer has to guarantee an adequate safety factor for the structure for its entire service life, despite degradation and aging of materials. Moreover for existing structures, and in particular for cultural heritage, there is the need to evaluate the expected service life. These evaluations need to consider both the mechanical and environmental damaging processes on reinforced concrete structures to proper represent the variation of the safety level with time.

The considerations above mentioned are even more relevant if the structure is struck by a seismic event. Indeed, the degradation processes may lead to a drastic reduction of both load-carrying capacity and ductility and the seismic performance of the structure may be greatly compromised. The safety of the structure may even become lower than the accepted value.

In view of these observations, it is important to have at disposal some theoretical and numerical tools that can be effectively adopted for both the design of new structures and the safety assessment of the existing ones. To this aim a model that can profitably describe the main characteristics of concrete's behavior coupled with a model that is able to simulate the environmental degradation processes is developed.

Within the available constitutive theories, in previous works the continuum damage mechanics was chosen as the reference framework and a mechanical scalar plastic-damage model for concrete structures was proposed (Faria et al. [1], Scotta [2]). Moreover, such a model was coupled with the environmental aspect, e.g. Saetta et al. [3], [4]. The coupled environmental-mechanical damage model has been effectively adopted to investigate the effects of different degradation processes like carbonation, chloride attack, corrosion and sulfate attack (e.g. [3], [4], [6], [7], [8]).

In the present work, the mechanical model was enhanced with a more comprehensive representation of the mixed tension-compression domain. The ability of representing the behavior of concrete under biaxial stress states (both compression-compression and tension-compression fields), is a fundamental task, especially when brittle shear failure is expected. This is the case, for instance, of reinforced concrete shear walls, which are widely used as lateral force resisting system of structures in seismic risk zones.

Concerning the durability aspect, an innovative formulation able to account for the physical deterioration mechanism due to freezing-thawing cycles has been developed within the cited framework of coupled damage approach. In particular, considering a limited number of experimental tests carried out on concrete specimens under mono-axial and bi-axial compressive states, the parameters of the

coupled-environmental damage model have been correlated with the number of freeze-and-thaw cycles.

Finally the proposed model was adopted to simulate some real structures, both concerning the mechanical and the environmental aspects, so demonstrating its reliability and numerical efficiency and highlighting the suitability of the proposed procedure for large scale simulations.

1.2 Overview of the thesis

Since the research has started with the mechanical constitutive modeling of concrete material, the second chapter briefly describes the behavior of concrete and the most common constitutive modeling frameworks based on literature review.

In the third chapter the mechanical damage model for concrete proposed in this work is introduced. The model takes inspiration on previous works ([1], [2]) and is able to take into account the main features that characterize the cyclic behavior of concrete: strain hardening, strain softening, stiffness degradation and stiffness recovery for cyclic loads due to crack closing. Moreover the new model is able to consider the interaction between tension and compression load conditions and is therefore suitable for analysis of reinforced concrete elements subjected to mixed tension states (e.g. shear walls, panels, etc.). The model is enriched with a Shear Retention Factor (Scotta et al. [5]) that was extended to the two-parameters scalar damage model here presented. Some tests are reported as validation of the procedure. Finally some considerations about mesh-objectivity, with the description of the adopted technique, are reported.

The fourth chapter deals with efficient models for analyzing reinforced concrete structures. The description of 1D elements with fiber discretization is reported. Then 2D elements are presented, considering two classes of elements: reinforced concrete membranes (subjected only to in-plane load conditions) and reinforced concrete plates (subjected to out-of-plane load conditions). In the first case a membrane model based on perfect bond assumption with superposition of different membranes (i.e. concrete and appropriate number of steel bars) is presented. In the latter case a reinforced concrete plate model with a layered approach is reported. In both cases some validation tests are presented.

Chapter five is dedicated to degradation processes on reinforced concrete structures. A coupled mechanical-environmental damage model based on previous works (e.g. Saetta et al. [3], [4]) that was profitably used to model carbonation and chloride attack on concrete, is enhanced to consider also freezing and thawing attack. To this aim an innovative formulation for freezing and thawing degradation is proposed.

The formulation was obtained with calibration using a limited number of tests carried out on concrete specimens under mono-axial and bi-axial compressive stresses, subjected to freeze-thaw cycles with different levels of deterioration. Finally the proposed coupled environmental-mechanical damage model was used as a predictive tool both for simulating a different series of biaxial concrete specimens subjected to freeze-thaw cycles and to evaluate the load carrying capacity of a frost damaged beam.

The last chapter summarizes the achievements of the research and presents recommendations for further developments in this field.

1.3 References

[1] Faria, R., Oliver, J., Cervera, M. (1998). A strain-based viscous-plastic-damage model for massive concrete structures, *Int. J. Solids and Structures*, 35, 1533-1558

[2] Scotta, R. (1997). Analisi meccanica di strutture in calcestruzzo mediante modelli di danno, *PhD Thesis*, Università degli studi di Padova, Dipartimento di Costruzioni e Trasporti

[3] Saetta, A., Scotta, R., Vitaliani, R. (1998). Mechanical behavior of concrete under physical-chemical attacks, *J. Eng. Mech.*, 124, 1100-1109

[4] Saetta, A., Scotta, R., Vitaliani, R. (1999). Coupled environmental-mechanical damage model of reinforced concrete structures, *J. Eng. Mech.*, 125, 930-940

[5] Scotta, R., Vitaliani, R., Saetta, A., Oñate, E., Hanganu, A. (2001). A scalar damage model with a shear retention factor for the analysis of reinforced concrete structures: theory and validation, *Comput. Struct.*, 79, 737-755

[6] Saetta, A. (2005). Deterioration of Reinforced Concrete Structures due to chemical-physical phenomena: Model-based simulation, *J. Mat. Civil Eng., ASCE*, 17, 313-319

[7] Berto, L, Simioni, P, Saetta, A. (2008). Numerical modeling of bond behavior in RC structures affected by reinforcement corrosion, *Eng. Struct.*, 30, 1375-1385

[8] Berto, L., Simioni, P., Saetta, A., Vitaliani, R. (2009). Seismic assessment of existing RC structures affected by degradation phenomena, *Struct. Safety*, 31, 284-297

CHAPTER 2:
MODELING OF CONCRETE

In this chapter a brief discussion on the experimental behavior of concrete is reported. In particular the behavior under uniaxial compression and tension, biaxial and cyclic loading is briefly reported in order to highlight the main characteristics that the constitutive model developed in this work should have to represent in a sufficiently accurate way the mechanical behavior of concrete.

Moreover some of the most used techniques to model non-linear behavior of concrete are briefly presented. In particular the constitutive laws based on plasticity theory, continuum damage mechanics and smeared crack models are cited in order to show the main characteristics of these frameworks. Since the framework chosen for the proposed model in this work is continuum damage mechanics, more attention will be dedicated to this framework.

The main aim of this chapter is to underline some concepts that may be useful for the exposition included in this work.

2.1 Introduction

The microstructure of a typical engineering material contains a large number of micro-defects such as micro-cracks, dislocations, pores and decohesions. Some of these defects are induced during the process of manufacturing, and are present in the material before subjecting it to loads and thermal fields. In general, these defects are small and distributed throughout most of the volume.

Phenomenologically, plastic (ductile) deformation is distinguished by the fact that the unloading segment of the stress-strain curve is parallel with the initial (elastic) segment of the loading curve (Figure 2.1a).

Brittle deformation can be defined in a complementary sense as a deformation during which the lattice itself changes as a result of the net loss (rupture or dissociation) of atomic bonds. Consequently, the stiffness of the material in the direction of the ruptured bonds is reduced. In a perfectly brittle deformation, the specimen fails abruptly as soon as the fracturing becomes unstable (Figure 2.1b).

A deformation will be referred to as quasi-brittle if the failure is preceded by some accumulation of distributed damage reflected in the curvature of the force-displacement curve (Figure 2.1c).

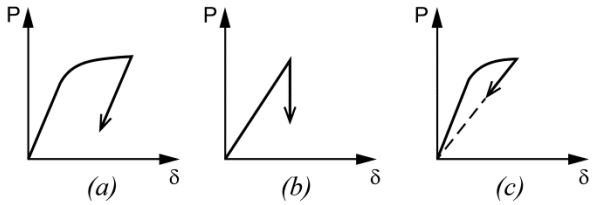

Figure 2.1 - Force-displacement curves for different materials: (a) ductile; (b) perfectly brittle; (c) quasi-brittle [1]

2.2 Concrete behavior

Concrete is a heterogeneous material, mainly composed by aggregates, air voids, water and cement matrix, which is itself a composite of particles of smaller size. Some researchers considered the concrete composed by three constituents: the cement matrix, the aggregates and the interface between matrix and aggregates. It is widely accepted that the interface (also called halo [2]) represents the weakest zone. Indeed it was observed with different techniques that damage was located mainly in the interface zone and cement matrix.

This characteristic of concrete is far from negligible when softening is investigated (e.g. [3], [4]).

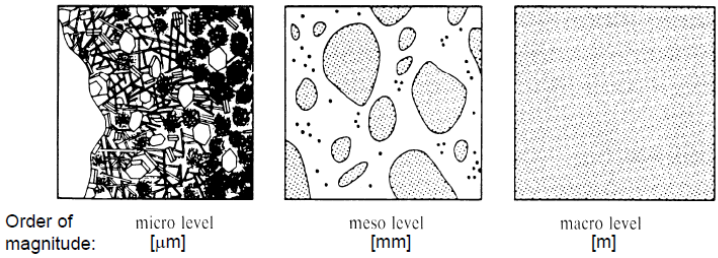

Figure 2.2 - Scale levels for concrete as proposed by Wittmann [5]

It has been shown that analysis of a phenomenon on a small scale serve to gain insight into the phenomenon itself and model it on a larger scale. For concrete research, Wittmann [5] has proposed a practical subdivision into three scale levels (Figure 2.2):

- Micro-level: considers the physical and chemical processes at a molecular level in cement paste, which is itself heterogeneous
- Meso-level: considers the complex structure of concrete which is a composite of aggregates, pores, cracks
- Macro-level: considers a homogenous material whose behavior is described by simplified phenomenological laws

In this thesis the attention will be focused on macro-level since a law developed at this level can profitably be used for applications in structural engineering.

2.2.1 Behavior in compression

A schematic load-displacement curve for a concrete specimen subjected to uniaxial compression is reported in Figure 2.3This curve can be divided in a pre-peak domain in which the load increases, and a post-peak domain where a decrease of load and an increase of deformation characterize the response of the specimen.

In the first part of the pre-peak domain, pre-existing cracks (due for instance to thermal expansion, hydration heat and shrinkage) doesn't propagate significantly, thus the curve shows an elastic response. With load increasing stress concentrations lead to crack initiation and growing. This was explained by some researches (e.g. [3], [4]) with considerations on the meso-level previously introduced. For normal weight concrete of normal strength, the stiffness of the aggregates is some order of magnitude greater than the stiffness of the surrounding matrix. Thus, under uniaxial compression, lateral deformations of the softer matrix are greater than those of the aggregates. This leads to the rupture of bond between aggregate and matrix and to

activation of shear stresses at top and bottom of the aggregate (Figure 2.4a). With load increasing these microcracks propagate inside matrix along the triaxial compression regions activated after the initiation of the shear stresses above and below the aggregate (Figure 2.4b).

Around the peak, cracks grow further and interact with each other. Lateral displacements increase faster than axial displacement due to crack opening, thus the volume of the specimen starts to increase again. The volume reaches its minimum value near the peak.

This explanation of compression failure of concrete is reported also by other researchers who identified the halo zone to be subjected to high stress concentrations and thus to failure.

After this point the propagation becomes unstable and the post-peak domain starts exhibiting in load-displacement curve a softening branch. During softening, the unstable cracks open and propagate further, and the load decreases while deformations continue increasing. Lateral deformations increase drastically, thus the volume of the specimen increases. The behavior of the specimen during softening was observed to be strongly dependent on specimen geometry, boundary conditions and composition of concrete (e.g. [4], [6], [7]); a significant dependence of strain softening on specimen's slenderness was reported, furthermore an influence of lateral restraint (e.g. steel platen, brush platen, …) was observed. The latter seems to influence the softening behavior because it affects the stress field inside the specimen leading to formation of triaxial compression regions or in general to complex multiaxial stress states. This effect has to be taken into account because its influence may overcome the effect on softening of specimen size. Van Mier [6] carried out tests using brush loading platens that are known to influence the compressive failure significantly less than rigid loading platens. The founds of his experimental tests indicate a strong dependence between slenderness of specimen and softening branch of stress-strain curve (Figure 2.5). This seems to indicate that the post-peak behavior of concrete specimens under uniaxial compressive loads is governed by local fracturing process as found in uniaxial tension (see 2.2.2). Furthermore an almost constant fracture energy was measured, irrespective of the specimen's size as it can be seen in Figure 2.6, where w-w_peak represents the post-peak displacement, being w the displacement and w_peak the displacement corresponding to the peak strength of the specimen. From these works it was concluded that strain-softening is the response of the structure formed by the specimen and the complete loading system and thus it was pointed out that it shouldn't be treated as a material property but it should be considered a structural response [4], [6], [8], [9].

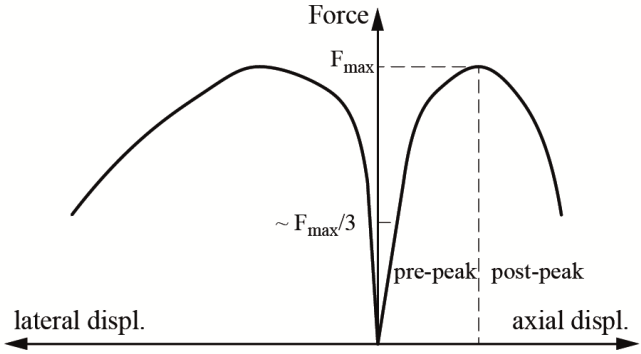

Figure 2.3 - Schematic load-displacement curve for concrete specimen subjected to uniaxial compression

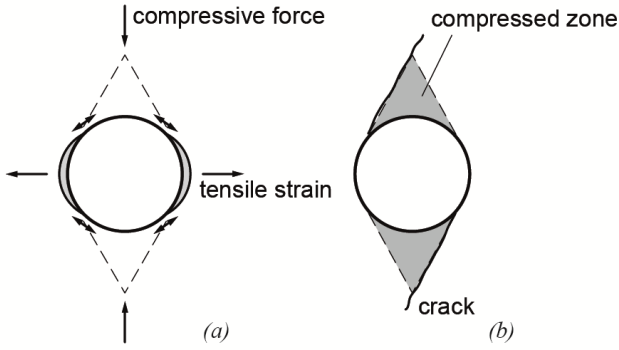

Figure 2.4 - Mechanism of damaging for compressive loads in meso-level

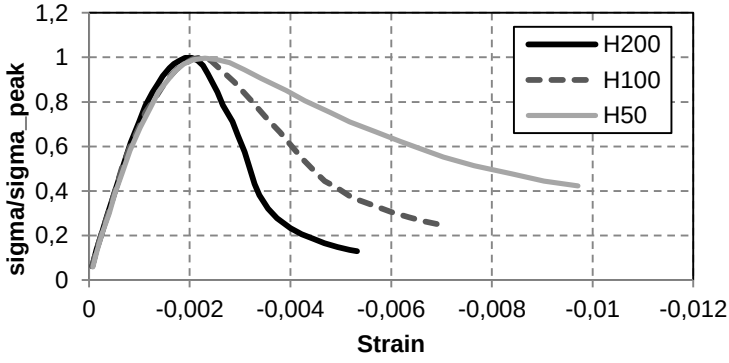

Figure 2.5 - Stress-strain curves for specimens of different sizes [8]

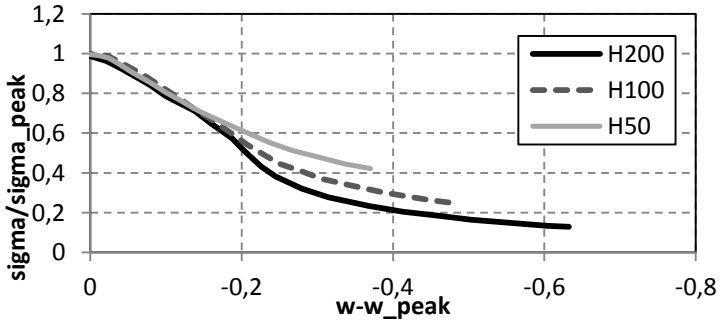

Figure 2.6 - Post-peak stress-displacement curves for specimens of different sizes [8]

2.2.2 Behavior in tension

In tension, concrete is weak and a failure of interface between aggregate and cement matrix can be observed. Previous researches have shown that the tensile strength is a fraction of compressive strength, in particular values that range from 8 to 15 per cent were found. For instance in [10] the authors proposed the following law that relates the two properties:

$$f_t = 0.54\sqrt{f_c} \tag{2.1}$$

with f_t the tensile strength in MPa and f_c the compressive strength also in MPa. Other relations have been proposed during last decades and some of them have been widely accepted. CEB-FIP Model Code 2010 suggests the following relation valid for normal weight concrete with class lower than C50:

$$f_t = 0.3 f_{ck}^{2/3} \tag{2.2}$$

where f_{ck} is the characteristic compressive strength of the material.

The softening behavior of concrete under tension and the localization process of the fracture of concrete were studied by many researchers. In Figure 2.7 is reported a typical stress-deformation curve for concrete subjected to a uniaxial tension test [10]. In this curve the average stress is defined as the load measured by experimental equipment and the net area of the specimen. It is worth noting that in some specimens a notch was provided and the authors seem to indicate that no significant influence of notch on average curves is reported comparing notched and un-notched specimens' responses. The material behaves almost linearly with no damage almost up to the peak strength. Near the peak strength micro-cracking starts and a lightly non-linear pre-peak and tension softening post peak branch can be observed (from point A to C in Figure 2.8). Moreover after a certain deformation (indicated with

point C in Figure 2.8), the tension softening part may be explained with frictional effects [11].

The area under the stress-displacement curve is a material property called fracture energy Gf and represents the work needed to open a crack of unit area. Gf can be measured in Nm/m^2 or N/m. CEB-FIP Model Code 2010 suggests the following relation valid for normal weight concrete:

$$G_f = 73 f_{cm}^{0.18} \tag{2.3}$$

where f_{cm} is the mean compressive strength of the material. CEB-FIP Model Code 1990 suggests the following relation for normal weight concrete:

$$G_f = G_{f0}\left(f_{cm}/10\right)^{0.7} \tag{2.4}$$

where G_{f0} is the base fracture energy which depends on the maximum aggregate size.

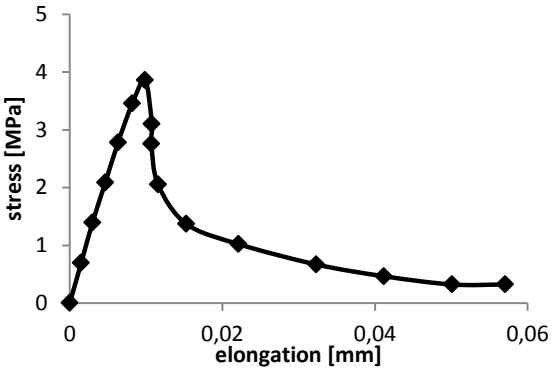

Figure 2.7 - Typical stress-deformation curve for concrete under uniaxial tension [10]

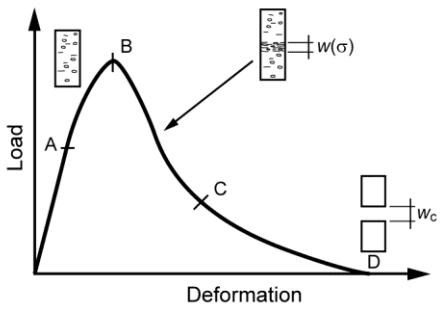

Figure 2.8 - Load-deformation curve for concrete under uniaxial tension [11]

Fracture was originally studied with linear elastic fracture mechanics (LEFM) since the works of Griffith [12] and later of Irwin [13] who introduced the concept of

stress intensity factor. These theories predict well the crack propagation of some kind of materials (e.g. glass) but the application of them in crack analysis of concrete and other quasi-brittle materials showed a deviation from experimental evidence [14]. The reason for this deviation was explained by the fact that concrete exhibits a non-linear softening behavior characterized by micro-cracking in a relatively large zone adjacent to the fracture tip called fracture process zone (FPZ), while this zone is requested to be small by LEFM (e.g. [11], [14], [15]). This is illustrated in Figure 2.9 in which is represented the size of FPZ for elastic materials, metals and concrete. Also metals exhibit a relatively large non-linear zone, but the main difference is that for these materials the FPZ is small, thus the theories developed for metals were not directly applicable to concrete structures.

For these reasons non-linear fracture mechanics (NLFM) have been used and applied to analysis of concrete structures considering the crack as discrete like the fictitious crack model proposed by Hillerborg [16] or as smeared like in the crack band model proposed by Bazant and Oh [14]. The concept of discrete crack and smeared crack are represented in Figure 2.10a and Figure 2.10b respectively. Considering the computational cost aspect, discrete crack models are generally computationally expensive. Furthermore it is often complicated to program and integrate in an existing F.E. framework models within such a formulation [14].

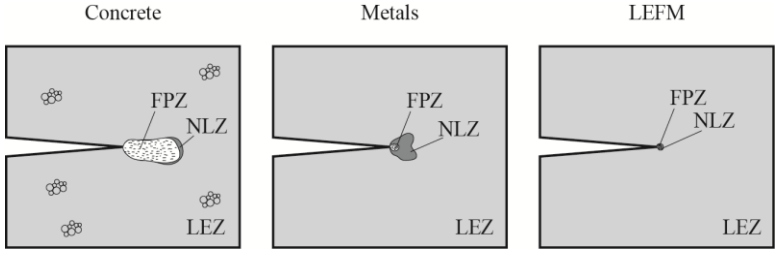

Figure 2.9 - Schematic representation of relative size of FPZ, non-linear zone(NLZ) and linear elastic zone (LEZ) for: (a) concrete; (b) metals; (c) LEFM

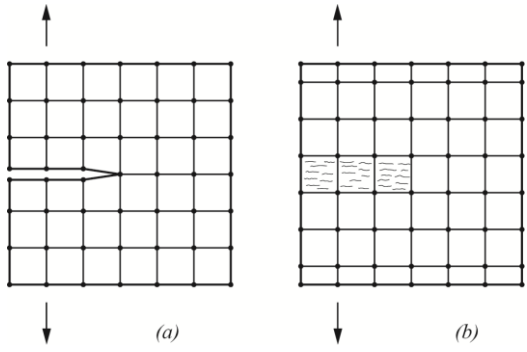

Figure 2.10 - Schematic representation of: (a) Discrete Crack Model; (b) Crack Band Model [14]

2.2.3 Multiaxial behavior

Experimental tests conducted in the second half of the last century aimed to understand the behavior of concrete subjected to bi-axial or tri-axial stress states. Similar conclusions as the one depicted for uniaxial tension and compression can be drawn in case of multiaxial stress state. Researches aimed to individuate the strength envelope of concrete. It is worth noting that another surface can be introduced that may be particularly useful for the development of constitutive laws: the elastic-limit envelope. Often the equations of these surfaces are proposed in terms of stress invariants I_1, J_2 and J_3.

The strength of concrete under biaxial compressive stresses was observed to be greater than the uniaxial compressive strength. For instance Kupfer et al. [17] found that strength under biaxial stresses with ratio $\sigma 1/\sigma 2$ near 0.5 is 1.25 times uniaxial strength and with a ratio $\sigma 1/\sigma 2$ of 1, the biaxial strength is 1.16 times uniaxial strength (Figure 2.11).

Under tri-axial stress states the compressive strength may be even 10 to 20 times higher than the uniaxial compressive strength [18] (Figure 2.12).

On the other hand, in case of bi-axial tensile stress state, the strength is almost unaffected and is nearly equal to the uniaxial tensile strength (Figure 2.11).

2.2.4 Cyclic behavior

Experimental results have shown the effect of stiffness recovery under cyclic load conditions. For instance Yankelevsky and Reinhardt [19] observed that, for cyclic test between tensile envelope and a comparable compressive stress, the low unloading stiffness increases after the specimen has reached a certain compressive stress. In fact, the unloading curve in tension becomes a loading curve in compression [19] and thus the stiffness is higher. From a physical point of view this effect can be interpreted considering that under tension the specimen may form microcracks if the tensile strength is reached and consequently the stiffness is degraded (e.g. in a damage-like approach); subsequent inversion of load leads to the progressive closure of microcracks and the material reacts with an higher stiffness. This phenomenon, called “unilateral effect” was described among others by Mazars and Pijaudier-Cabot [20].

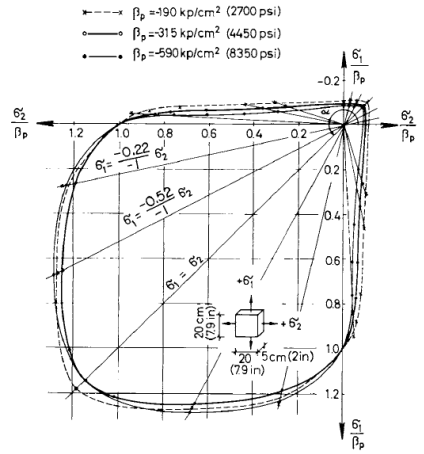

Figure 2.11 - Biaxial strength envelope (Kupfer et al. [17])

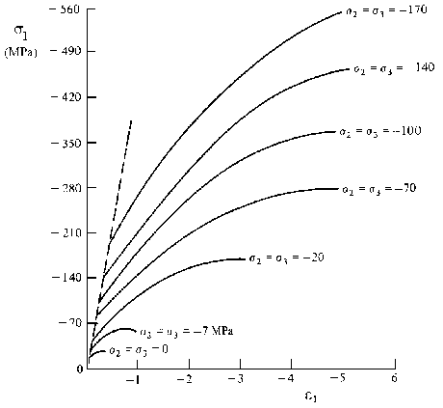

Figure 2.12 - Strength of concrete under tri-axial stress state (Chen [18])

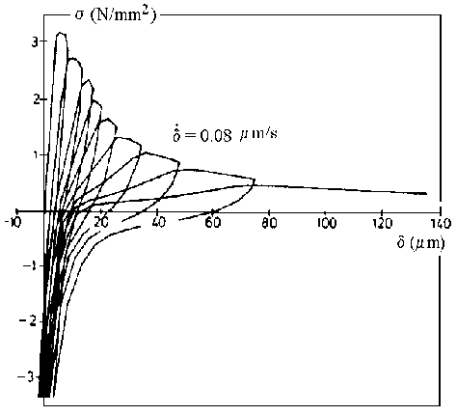

Figure 2.13 - Stiffness recovery (Yankelevsky and Reinhardt [19])

2.3 Modeling of concrete

In this section some of the most common approaches to model concrete elements are presented. In particular attention will be focused on continuum constitutive laws for concrete. Indeed different strategies of modeling of concrete material have been proposed during the last decades. They include fracture mechanics (linear and non-linear), as discussed previously, and constitutive laws based among others on plasticity theory, smeared crack models, continuum damage mechanics and microplane models.

The idea behind discrete crack models is to enhance the continuum description introducing displacement discontinuities that represent cracks. The part of the body that remains continuous is described by a constitutive law that provides a stress-strain relation which can be elastic as well as inelastic. Such an approach can be found in the pioneering work of Ngo and Scordelis [21] and in the already cited work of Hillerborg [16] who introduced the fictitious crack model. The main drawback of this kind of models is that it requires the adoption of re-meshing techniques, unless the crack trajectory is known a-priori. Thus, these models are generally computationally demanding.

The use of a constitutive law that provides a suitable relation between average stresses and average strains represents the discontinuity (i.e. cracks) of the material by a cracking strain over a representative volume. This is of particular interest in a F.E. approach in which the cracking strain is distributed on the finite element. From this point of view one can define smeared approach the opposite of discrete approach including for instance the models based on plasticity or damage mechanics. However in literature the term smeared crack model is generally used to indicate a specific class of constitutive models [23]. The pioneering work of Rashid [22] introduced the concept of smeared crack concept as the opposite of discrete crack concept [21].

The theory of plasticity has been widely used in development of constitutive laws for concrete. One of the most used forms is the flow theory of plasticity formulated in stress space. According to this theory, generally the strain tensor is decomposed into an elastic and a plastic part and the stiffness is assumed to remain constant to the initial elastic one.

Theories based on continuum damage mechanics have been developed since the pioneering work of Kachanov [24] who introduced an internal variable to describe the damage due to creep on metals. Since then a lot of progresses have been achieved and models were developed in different versions, from isotropic scalar damage models, to more complex anisotropic damage models, in which anisotropy

was taken into account by means of damage vectors [26], second-order tensor [27], fourth-order tensor [28], and even of eight-order tensor [29].

Models based on the concept of smeared crack share some characteristics with plasticity models and with damage models. Similarly to plasticity, they decompose the total strain into two parts: one elastic and one inelastic. The inelastic part is due to a crack opening and is related directly with the force transmitted across a crack. The first models of this category assumed a fixed crack direction [22], while latter have been proposed the use of rotating cracks [30] or the extension of the fixed crack direction to multiple non-orthogonal cracking [31].

Microplane models provide the tensorial stress-strain law by averaging the strain and stress vectors obtained projecting stress and strain tensors on a set of microplanes with given orientation [32]. For concrete modeling the kinematic constrain is often used to develop the model: according to this the strains on microplanes (also called microstrains) are evaluated by projection of strain tensor (also called macrostrain), then the macrostresses are evaluated from the contributions of microstresses.

It is worth noting that quite often the models developed for concrete combine two or more theories. As an example the combination of plasticity with damage theories is used in some cases.

2.3.1 Basic concepts of plasticity theory

The flow theory of plasticity is characterized by the decomposition of strain into elastic and plastic parts:

$$\boldsymbol{\varepsilon} = \boldsymbol{\varepsilon}^e + \boldsymbol{\varepsilon}^p \tag{2.5}$$

The stress-strain law for the elastic part is:

$$\boldsymbol{\sigma} = \mathbf{C}^e : \boldsymbol{\varepsilon}^e \tag{2.6}$$

where $\mathbf{C}^e$ is the elastic stiffness tensor. For a proper definition of a model according to this theory, the other ingredients needed are: the yield criterion, the flow rule and the hardening law. They can be generally described by following equations:

$$f(\boldsymbol{\sigma}, \mathbf{q}) \le 0 \tag{2.7}$$

$$\dot{\boldsymbol{\varepsilon}}^p = \dot{\lambda} g(\boldsymbol{\sigma}, \mathbf{q}) \tag{2.8}$$

$$\dot{\boldsymbol{\kappa}} = \dot{\lambda} k(\boldsymbol{\sigma}, \boldsymbol{\kappa}) \tag{2.9}$$

$$\mathbf{q} = h(\boldsymbol{\kappa}) \tag{2.10}$$

Equation (2.7) represents the yield criterion where *f* is the yield function, the flow rule is expressed in (2.8) where $\dot{\lambda}$ is the plastic multiplier and *g* specifies the

direction of plastic flow, while the hardening law is written in the two equations (2.9) and (2.10). The former defines the evolution of hardening variables collected in vector $\boldsymbol{\kappa}$, while the latter defines the relation between $\boldsymbol{\kappa}$ and **q**, used in (2.7) and (2.8).

The loading/unloading conditions are expressed in Kuhn-Tucker form:

$$f \le 0 \qquad \dot{\lambda} \ge 0 \qquad \dot{\lambda} f = 0 \tag{2.11}$$

Finally the consistency condition is expressed by:

$$\dot{\lambda} \dot{f} \le 0 \tag{2.12}$$

According to these equations, if the material is in an elastic state ($f < 0$), there is neither plastic strain evolution nor hardening evolution ($\dot{\lambda} = 0$). On the other hand, if the current state is plastic ($f = 0$) then the plastic flow can continue ($\dot{\lambda} > 0$ and $\dot{f} = 0$) or the material can unload elastically ($\dot{f} < 0$ and subsequently $\dot{\lambda} = 0$); the neutral loading condition is characterized by $\dot{f} = 0$ and $\dot{\lambda} = 0$. This is shown in Figure 2.14.

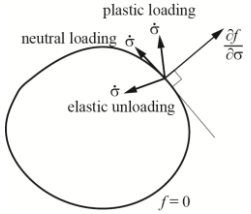

Figure 2.14 - Yield surface in stress space with loading/unloading criteria

When function *g* in (2.8) is assumed equal to $\partial f / \partial \sigma$ the flow rule is said to be associated and the plastic strain increment is normal to the yield surface. The general case when *g* in (2.8) is different than $\partial f / \partial \sigma$ the flow rule is called non-associated. To effectively describe the peculiar characteristics of concrete's behavior, and in particular the dilatancy, generally a non-associated plastic flow rule is adopted.

In this general framework, different theories were developed for concrete with different complexity level and accuracy in representing the observed experimental behavior. Different yield surfaces were defined and different plastic potentials were proposed and the resulting models exhibited different numbers of material parameters, e.g. [18], [33], [34].

2.3.2 Basic concepts of smeared crack models

The pioneering work of Rashid [22] introduced the concept of smeared crack concept. In particular his model fits into smeared crack models which are a particular class of constitutive laws that have some common characteristics with

plasticity and damage. Indeed de Borst [35] showed that smeared crack models can be considered as a special case of anisotropic damage models. Thus it is instructive to briefly recall the features and the evolution of this class of models. For a detailed description of the models and of the long evolution of them, the reader is referred to the works of de Borst [35], Weihe and Kröplin [36] and to the state-of-the-art report [37].

The first versions of smeared crack models were characterized by a total strain formulation, a fixed crack plane whose direction did not change during load history, and an elastic-perfect brittle for Mode-I and for Mode-II fracture. Considering for sake of simplicity a plane stress condition, the constitutive law of the material up to cracking can be written with the well-known relation for linear elastic and isotropic materials:

$$\begin{bmatrix} \sigma_x \\ \sigma_y \\ \tau_{xy} \end{bmatrix} = \frac{E}{1-\nu^2} \begin{bmatrix} 1 & \nu & 0 \\ \nu & 1 & 0 \\ 0 & 0 & \dfrac{1-\nu}{2} \end{bmatrix} \begin{bmatrix} \varepsilon_x \\ \varepsilon_y \\ \gamma_{xy} \end{bmatrix} \tag{2.13}$$

where E and ν are Young's modulus and Poisson's modulus respectively. It is necessary to define a tension cut-off criterion that indicates the initiation of microcracking in the material. A widely used crack initiation criterion is the Rankine criterion of maximum principal stress. According to this, when the maximum principal stress reaches the tensile strength of the material, a new computational crack perpendicular to the corresponding principal direction is formed.

When the tension cut-off is violated, the isotropic elastic stiffness matrix of (2.13) is substituted by the following orthotropic stiffness matrix in the reference system of the crack plane *n*, *s*. In this coordinates system *n* is the direction normal to the crack plane (a line in plane stress conditions) that corresponds to mode-I fracture (Figure 2.15a), while *s* represents the direction tangent to the crack which is correspondent to mode-II fracture (Figure 2.15b). The constitutive law proposed in [22] is:

$$\begin{bmatrix} \sigma_{nn} \\ \sigma_{ss} \\ \tau_{ns} \end{bmatrix} = \begin{bmatrix} 0 & 0 & 0 \\ 0 & E & 0 \\ 0 & 0 & 0 \end{bmatrix} \begin{bmatrix} \varepsilon_{nn} \\ \varepsilon_{ss} \\ \gamma_{ns} \end{bmatrix} \tag{2.14}$$

which can be written in compact form:

$$\boldsymbol{\sigma}_{ns} = \mathbf{D}^{s}_{ns} \boldsymbol{\varepsilon}_{ns} \tag{2.15}$$

According to (2.14), the stresses normal to cracks and the shear stresses transferred across the crack are assumed to abruptly drop to zero suddenly when the crack condition is reached. This condition is an approximation of the real behavior of concrete which, as previously mentioned, is characterized by the presence of the

FPZ with a tension-softening behavior due to the ability of transferring tractions across the crack.

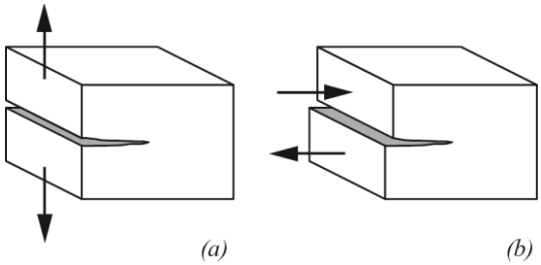

Figure 2.15 - (a) Mode-I fracture; (b) Mode-II fracture

The relations (2.14)-(2.15) can be written in the global reference system *x*, *y* defining the transformation matrixes $T_\varepsilon(\Phi)$ and $T_\sigma(\Phi)$ for strains and stresses respectively being Φ the angle between *x* axis and *n* axis. Indicating with *c* the quantity cos(Φ) and with *s* the quantity sin(Φ) the matrixes can be written as:

$$\mathbf{T}_\sigma(\Phi)=\begin{bmatrix} c^2 & s^2 & 2cs \\ s^2 & c^2 & -2cs \\ -cs & cs & c^2-s^2 \end{bmatrix}$$
$$\mathbf{T}_\varepsilon(\Phi)=\begin{bmatrix} c^2 & s^2 & cs \\ s^2 & c^2 & -cs \\ -2cs & 2cs & c^2-s^2 \end{bmatrix} \tag{2.16}$$

The constitutive law in the global reference system can be written:

$$\boldsymbol{\sigma}_{xy}=\mathbf{T}_\sigma^{-1}(\Phi)\mathbf{D}_{ns}^{s}\mathbf{T}_\varepsilon(\Phi)\boldsymbol{\varepsilon}_{xy} \tag{2.17}$$

As already mentioned, the first versions of smeared cracked model assumed that the crack plane orientation remains fixed upon the crack formation. Thus Φ, $T_\varepsilon(\Phi)$ and $T_\sigma(\Phi)$ are constant for all the load history. This class of models is referred as fixed crack models (FCM).

Driven from the considerations stated in the previous paragraph, some researchers proposed some enhancements of the model. In particular both the laws assumed for normal and shear tractions across the crack are unrealistic as mentioned because they represent a sudden stress drop; further the secant stiffness matrix assumed is ill-conditioned and can lead to numerical difficulties. The introduction of a shear retention factor β and of a softening reduction factor μ represented an enhancement of the model both from the physical and from the computational point of view. Indeed the stiffness matrix assumed reduces the numerical problems and better represents the real behavior of concrete considering both the tension softening

concept and a shear transfer across the crack simulating the aggregate interlock [38]. The resulting stiffness matrix in the crack reference system is:

$$\mathbf{D}_{ns}^{s} = \begin{bmatrix} \mu E & 0 & 0 \\ 0 & E & 0 \\ 0 & 0 & \beta G \end{bmatrix} \begin{bmatrix} \varepsilon_{nn} \\ \varepsilon_{ss} \\ \gamma_{ns} \end{bmatrix} \tag{2.18}$$

where G is the usual shear modulus of elasticity. The shear retention factor β was often assumed constant which represents a rough approximation of concrete behavior because it permits an unphysical shear transfer across a wide open crack. In other words, the introduction of a constant shear retention factor may lead to a rotation of the principal stresses due to the presence of shear stresses across the crack plane and to an uncontrolled growth of maximum principal stresses that can overcome the tensile strength of the material. For this reason some works proposed to use a variable factor which depends on strain [39].

Considering also the Poisson effect after cracking the following stiffness matrix is adopted [41] which is, except for the shear term, equal to the stiffness matrix obtained by the inversion of the compliance matrix proposed by Bazant and Oh [14]:

$$\mathbf{D}_{ns}^{s} = \begin{bmatrix} \dfrac{\mu E}{1-\nu^2\mu} & \dfrac{\nu\mu E}{1-\nu^2\mu} & 0 \\ \dfrac{\nu\mu E}{1-\nu^2\mu} & \dfrac{\mu E}{1-\nu^2\mu} & 0 \\ 0 & 0 & \beta G \end{bmatrix} \tag{2.19}$$

The main drawbacks of these models include, among others, the fact that the crack patterns (being the plane fixed) may be mispredicted especially in case of mixed-mode fracture which is characterized by both opening (mode-I) and sliding (mode-II), and the fact that the formulation is based on total strain: in particular with this approach it is difficult to combine cracking with other non-linear phenomena like plasticity, creep, etc. To overcome these problems, de Borst proposed a strain decomposition into a concrete part and a crack part [31], [40]:

$$\boldsymbol{\varepsilon} = \boldsymbol{\varepsilon}^{co} + \boldsymbol{\varepsilon}^{cr} \tag{2.20}$$

where $\boldsymbol{\varepsilon}^{co}$ is the part of strain associated to concrete and $\boldsymbol{\varepsilon}^{cr}$ is the part of strain associated to the microcracking process. This separation resembles the strain decomposition of plasticity theory expressed by (2.5), although in smeared crack model the strain related to concrete may be non-linear itself. For instance in [31] a plasticity-based model is adopted for that part.

Furthermore the strain decomposition (2.20) permits to sub-decompose the cracking part considering different non-orthogonal cracks contributions defining the multiple fixed crack model (MFCM) [31]:

$$\boldsymbol{\varepsilon}^{cr} = \boldsymbol{\varepsilon}_1^{cr} + \boldsymbol{\varepsilon}_2^{cr} + \ldots \tag{2.21}$$

where $\boldsymbol{\varepsilon}^{cr}_i$ represents the strain contribution of *i*-th crack. In this way when the principal strain depicted from shear and normal stress transfer across the crack overcomes the tensile strength in another direction a secondary crack can be initiated. Furthermore the subsequent cracks are assumed to be activated only if the direction of principal stresses has rotated more than a threshold angle $\Delta\alpha^{Th}$ from the direction of the previously activated cracks. The threshold angle is assumed as a material parameter and the choice of it (judiciously selected by the analyst) may lead to different results [36].

An alternative approach for mixed-mode fracture was proposed firstly by Cope et al. [30] which assumed that the crack plane can rotate during load history. This class of models is called Rotating crack models (RCM). According to this approach the crack plane is always normal to the principal stress direction. Thus Φ, $T_\varepsilon(\Phi)$ and $T_\sigma(\Phi)$ are not constant during all the analysis and the crack reference system *n*, *s* rotates continuously. Consequently the shear stiffness term in (2.18) is always null. It was shown that RCM can be considered somehow a special case of MFCM [42].

In Figure 2.16 the basic concepts expressed for FCM, MFCM and RCM are represented.

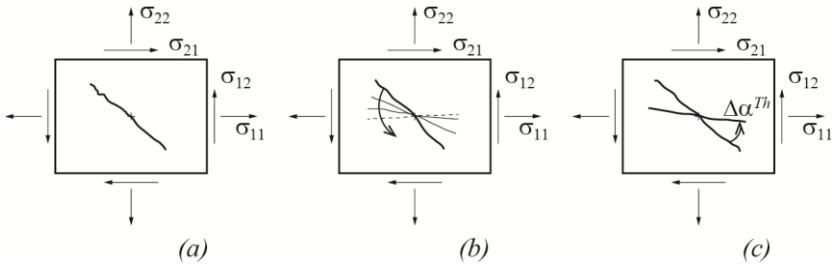

Figure 2.16 - Schematic representation of smeared crack models [36]: (a) fixed crack model (FCM); (b) rotating crack model (RCM); (c) multiple fixed cracks model (MFCM)

2.3.3 Basic concepts of continuum damage mechanics

In his pioneering work, Kachanov [24] started the field of continuum damage mechanics which is a constitutive theory that aims to describe at macro- and meso-level the process of nucleation, propagation and coalescence of microcracks, microvoids, microcavities and other microdefects which lead to a degradation of the material stiffness observed in the macroscale and to the initiation of macrocracks. Thus, the damage development effect in meso- and macro-scales is actually a process that can be observed also in microscopic and atomic scales ([43], [44]). The concept of representative volume element (RVE) is adopted in continuum damage

mechanics in order to represent the mechanical effects of the microstructure as a macroscopic homogeneous effect of the material. This RVE should be large enough to contain a sufficient number of discontinuities and at the same time should be small enough to approximate the stress and strain field as homogeneous. The size of RVE should depend on the material properties and its microstructure; for concrete a typical value of 100 mm3 was suggested. For a more detailed discussion on the RVE concept the reader is referred to [43], [44].

2.3.3.1 Definition of damage variables

A key point of continuum damage mechanics is the definition of the damage variables which represent an internal variable for the state definition of the RVE. The first definition, proposed by Kachanov [24] was a scalar damage variable ψ ($0 \leq \psi \leq 1$) where the condition $\psi = 1$ represents the undamaged state and $\psi = 0$ represents the completely damaged state. Rabotnov [45] modified that definition introducing the damage variable defined as $D = 1- \psi$. With such an approach the damage variable D assumes the value zero when the material is in its initial undamaged state, while reaches the value 1 when it is completely damaged. Independently from this different definition, the scalar damage parameter can be interpreted as reduction factor of area or as the effective area parameter [24]. To illustrate this concept, considering a generic damaged body, taking a RVE around a certain point $P(\mathbf{x})$ and considering a surface element dA with its normal vector $\boldsymbol{n}$, the damage state of the surface dA can be characterized by the microvoids whose total area is equal to dA_D. The effective area that carries the internal forces can be called effective area and can be written as follows:

$$d\bar{A} = dA - dA_D \tag{2.22}$$

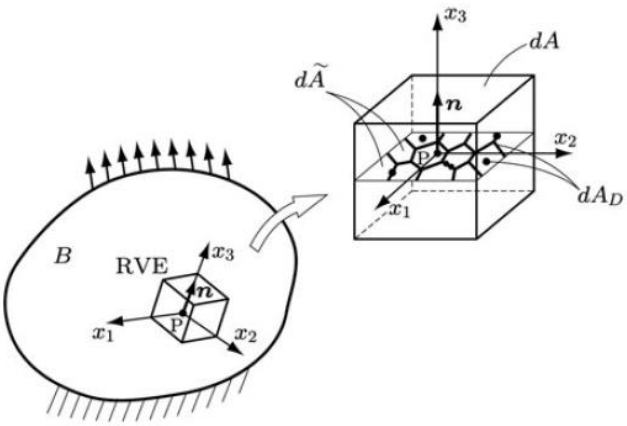

Figure 2.17 - Effective area concept

With this definition of effective area, the damage variable can be expressed by:

$$D(\boldsymbol{x},\boldsymbol{n}) = 1-\psi = \frac{dA-d\bar{A}}{dA} = \frac{dA_D}{dA} \tag{2.23}$$

The damage variable defined by previous equation can be interpreted as the ratio between area of voids and defects and total area. Furthermore, according to this definition of damage, it is evident that D is a monotonically increasing quantity. Indeed, when the damage is initiated the effective load carrying area is reduced permanently due to the accumulation of microdefects. This denotes the irreversibility of the damage process.

A body in damaged state subjected to a load with cross area dA is mechanically equivalent to a fictitious undamaged body subjected to the same force, but with a cross section of $d\bar{A}$. The latter state is often referred as fictitious undamaged configuration [46] or pseudo-undamaged configuration [43]. This concept is illustrated in Figure 2.18 for a bar subjected to a uniaxial load condition. From this figure is also possible to introduce the concept of effective stress. The mechanical equivalence of the two damaged and pseudo-undamaged states permits to write the following equilibrium equation:

$$dF = \sigma dA = \bar{\sigma} d\bar{A} \tag{2.24}$$

which, considering (2.23), leads to the definition of effective stress [24]:

$$\bar{\sigma} = \sigma \frac{dA}{d\bar{A}} = \sigma \frac{dA}{dA-dA_D} = \frac{\sigma}{1-D} \tag{2.25}$$

As already mentioned the process of damage from the atomic or micro- scale point of view is smeared in the RVE and their effects on the macro-scale may be interpreted as a reduction of internal properties of the material, like the reduction of stiffness. Thus, an alternative representation of damage and of effective stress is depicted considering the variation of elastic modulus of the bar in Figure 2.18.

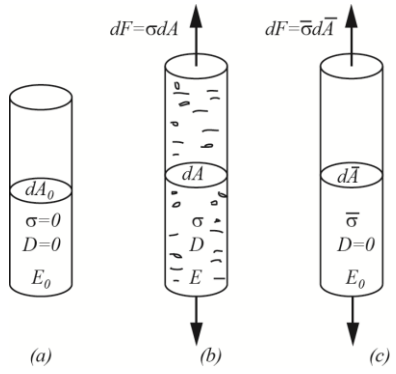

Figure 2.18 - (a) undamaged configuration; (b) damaged configuration; (c) fictitious undamaged configuration

The mechanical equivalence of the damaged and pseudo-undamaged states leads to consider the strain in the two systems of Figure 2.18b and Figure 2.18c equal:

$$\varepsilon = \frac{\sigma}{E(D)} = \frac{\bar{\sigma}}{E_0} \tag{2.26}$$

where E_0 and $E(D)$ are the Young's modulus in initial and damaged state respectively. The effective stress can then be defined alternatively as:

$$\bar{\sigma} = \frac{E_0}{E(D)}\sigma \tag{2.27}$$

Combination (2.25) and (2.27) leads to:

$$D = 1 - \frac{E(D)}{E_0} \tag{2.28}$$

which relates damage variable with the variation of Young's modulus.

It is worth noting that (2.27) represent the basis of the hypothesis of strain equivalence for 1D case which will be further discussed in 2.3.3.2.1 to be generalized and extended to the 3D case.

According to equation (2.23) the damage is dependent on the direction represented by normal ***n***, thus damage process is in general an anisotropic phenomena and the damage variable should be of tensorial nature. Different theories have been proposed to model the damage process in three-dimensions considering different internal variables that characterize damage going from scalar damage variables to fourth- or higher- order tensors.

When random distribution of microdefects characterizes the damaged state of the material, it can be assumed as isotropic; thus the internal damage variable can be represented by a scalar damage variable *D*. This condition is usually valid for metals and a scalar damage variable has been often applied to problems of creep damage [24], elastic-plastic damage [47], ductile and fatigue damage [48]. When microdefects have oriented geometry the damaged state should be considered anisotropic. For the study of concrete, isotropic damage models have been successfully adopted (e.g. [49], [50], [51], [52], [53]). Some researchers have observed that a single scalar damage variable is insufficient to describe the damage process in materials like concrete, due to the very different behavior in compression and in tension (see section 2.2). Thus the single scalar damage models have been extended to plural scalar damage theory. For instance two independent scalar damage variables have been proposed in the work of Ju [54] and Faria et al. [55]. The main advantage of this class of models is that they are easier in the mathematical formulation and computationally efficient.

Considering the anisotropic nature of damage some researchers proposed the adoption of different damage variables to consider the orientation of damage process. Kachanov ([56], [26]) extended his definition of damage expressed by (2.22), (2.23) proposing the adoption of a vector damage variable:

$$\boldsymbol{\psi} = \psi_n \mathbf{n} \tag{2.29}$$

A second-order damage tensor can be adopted and the previous (2.25) can be extended according to [44]:

$$\bar{\boldsymbol{\sigma}} = (\mathbf{I} - \mathbf{D})^{-1} \boldsymbol{\sigma} \tag{2.30}$$

where $\bar{\boldsymbol{\sigma}}$ is the effective stress tensor, **I** is the second-order identity tensor and **D** is the second order damage tensor, while $\boldsymbol{\sigma}$ is the usual Cauchy stress tensor.

Second-order damage tensors have been used to formulate constitutive theories for instance in [27], [57], [58].

A fourth- or eighth-order damage tensor can be adopted. The extension of the previous (2.27)-(2.28) is written according to:

$$\bar{\boldsymbol{\sigma}} = \left[\mathbf{C}_0 : \mathbf{C}(\mathbf{D})^{-1}\right] : \boldsymbol{\sigma} \tag{2.31}$$

where $\mathbf{C}_0$ is the fourth-order elastic stiffness tensor, $\mathbf{C}(\mathbf{D})$ is the fourth-order damaged stiffness tensor and **D** is an eighth-order tensor that maps $\mathbf{C}_0$ into $\mathbf{C}(\mathbf{D})$. The use of an eighth-order damage tensor can be found in the work of Chaboche [29]. However due the mathematical complication by using an eighth-order tensor, some researchers proposed the use of a fourth-order damage tensor **D** and defined the following relation for the transformation of stiffness tensor:

$$\mathbf{C}(\mathbf{D}) = (\mathbf{I} - \mathbf{D}) : \mathbf{C}_0 \tag{2.32}$$

where **I** represents the fourth-order unit tensor and **D** is the following fourth-order damage tensor:

$$\mathbf{D} = \mathbf{I} - \mathbf{C}(\mathbf{D}) : \mathbf{C}_0^{-1} \tag{2.33}$$

and (2.27) is extended according to:

$$\bar{\boldsymbol{\sigma}} = (\mathbf{I} - \mathbf{D})^{-1} : \boldsymbol{\sigma} \tag{2.34}$$

The main drawback of this class of models is the mathematical difficulty in developing the theory and the computational cost in evaluating the anisotropic damage variable.

For a detailed review of anisotropic damage models the reader is referred to [43], [44].

Due to the computational efficiency and simplicity of the plural scalar damage models, and considering that promising results have been obtained with these

models, the constitutive model for concrete proposed in this work is based on these considerations and adopts two independent scalar damage variables to describe the damaging process of concrete.

2.3.3.2 Hypotheses of mechanical equivalence

The constitutive equations according to continuum damage mechanics can be derived considering the mechanical equivalence of the damaged state characterized by the variables ($\boldsymbol{\varepsilon}$, $\boldsymbol{\sigma}$) and the pseudo-undamaged state characterized by the effective variables ($\bar{\boldsymbol{\varepsilon}}$, $\bar{\boldsymbol{\sigma}}$). Different mechanical equivalence concepts have been used in continuum damage mechanics and some of them are briefly reported herein.

2.3.3.2.1 Hypothesis of strain equivalence

Lemaitre and Chaboche [59] proposed the principle of strain equivalence:

"*The strain associated with a damaged state under the applied stress* $\boldsymbol{\sigma}$ *is equivalent to the strain associated with the undamaged state under the effective stress* $\bar{\boldsymbol{\sigma}}$ "

The concept expressed by this principle is depicted in Figure 2.19. This hypothesis was assumed in section 2.3.3.1 for a 1D state as previously mentioned.

Since the model for concrete proposed in this work stands among isotropic scalar damage models, the following equations are written for the isotropic case to define the effective variables:

$$\bar{\boldsymbol{\varepsilon}}(\bar{\boldsymbol{\sigma}},0)=\boldsymbol{\varepsilon}(\boldsymbol{\sigma},D) \tag{2.35}$$

$$\bar{\boldsymbol{\sigma}}=\frac{\boldsymbol{\sigma}}{1-D} \tag{2.36}$$

Equation (2.36) is the three-dimensional generalization of (2.27) for isotropic damage and represents the effective stress tensor. For anisotropic case refer to [43] and [44].

From a physical point of view, this concept can be interpreted considering the effective stress $\bar{\boldsymbol{\sigma}}$ being the stress that should be applied to a fictitious body (pseudo-undamaged state in Figure 2.19) to cause the same strain tensor that is observed on the real body (damaged-state in Figure 2.19) subjected to the real stress $\boldsymbol{\sigma}$ [49].

It is worth noting that the assumption of the hypothesis of strain equivalence leads to the fact that Poisson's modulus is not affected by damage, i.e. $\bar{\nu}=\nu$.

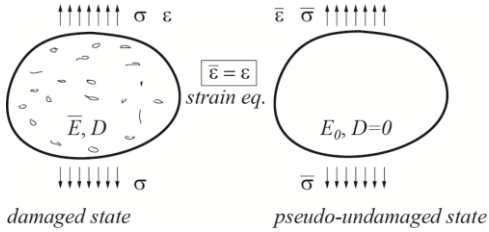

Figure 2.19 - Schematic representation of strain equivalence hypothesis

2.3.3.2.2 Hypothesis of stress equivalence

Simo and Ju [49] proposed the principle of stress equivalence:

"*The stress associated with a damaged state under the applied strain* $\boldsymbol{\varepsilon}$ *is equivalent to the stress associated with the undamaged state under the effective strain* $\bar{\boldsymbol{\varepsilon}}$ "

The concept expressed by this principle is depicted in. This principle is dual to the concept of strain equivalence and the dual effective strain variable can be defined. For the isotropic case, which is of interest in this work, the effective variables are defined as:

$$\bar{\boldsymbol{\sigma}}(\bar{\boldsymbol{\varepsilon}},0) = \boldsymbol{\sigma}(\boldsymbol{\varepsilon}, D) \tag{2.37}$$

$$\bar{\boldsymbol{\varepsilon}} = (1-D)\boldsymbol{\varepsilon} \tag{2.38}$$

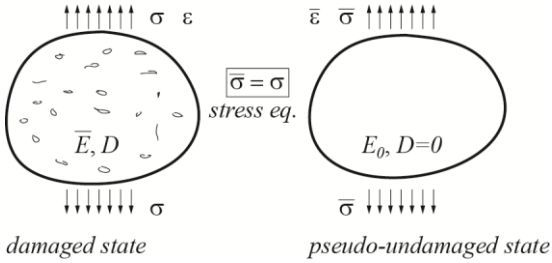

Figure 2.20 - Schematic representation of stress equivalence hypothesis

2.3.3.2.3 Hypothesis of energy equivalence

The models developed according to one of the previous hypothesis in case of anisotropic damage variables exhibit an a-symmetric stiffness tensor. Moreover both principles lead to simplifications since the reduction due to microvoids and microdefects affect the effective stress or the effective strain while strain or stress remain unchanged for strain equivalence and stress equivalence principles respectively. To overcome these problems Cordebois and Sidoroff [60] proposed the complementary elastic energy equivalence, according to which the complementary elastic energy defined by:

$$\Phi^e = \frac{1}{2}\boldsymbol{\sigma} : \boldsymbol{\varepsilon}^e \tag{2.39}$$

and

$$\overline{\Phi}^e = \frac{1}{2}\overline{\boldsymbol{\sigma}} : \overline{\boldsymbol{\varepsilon}}^e \tag{2.40}$$

for damaged and pseudo-undamaged states respectively, is equivalent.

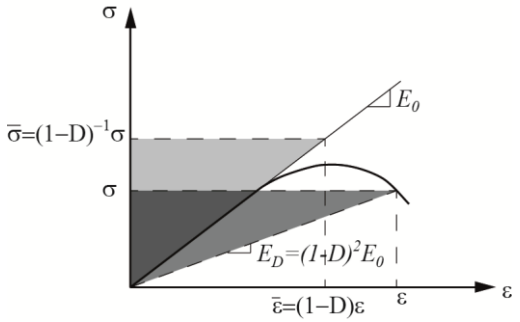

Figure 2.21 - Hypothesis of complementary strain energy equivalence for uniaxial stress condition

In Figure 2.21, the concept of complementary strain energy equivalence is graphically represented for the uniaxial stress condition. For more details on the hypotheses of energy equivalence refer to [44].

2.4 Strain localization and mesh objectivity

As illustrated in section 2.2, concrete exhibits both in tension and in compression a strain-softening behavior and strain localization was documented for experimental tests of concrete specimens subjected to uniaxial tension or uniaxial compression.

On the other hand, adopting strain-softening constitutive laws makes possible strain localization also for numerical analyses [61]. Moreover the solution of problems that involves strain-softening laws presents both numerical and mathematical problems. This is related to ill-posedness of the boundary value problem; the localization issues were related to the loss of ellipticity of the governing differential equations [62], [63]. From the numerical point of view, this ill-posedness may be manifested by a significant mesh-sensitivity with the result that can be severely dependent on the size of the finite elements.

Constitutive laws developed according to the classes previously defined, are not suitable to take into account these phenomena. Indeed the constitutive relations between stress and strain tensors are generally proposed on the base of experimental force-displacement results. Average stress is obtained dividing the force by the

initial cross-area, while average strains are obtained dividing the displacements by the initial length of the specimen: in this way one obtains a uniform stress and strain field which may be sensibly different from the real experimental evidence (see also 2.2).

To overcome these problems, different theories have been proposed to enrich the standard continuum to take somehow into account the micro-structure of the material and can effectively force a mesh-independent strain localization zone (in fact these theories are often referred as localization limiters); some of the most common techniques include non-local approach (e.g. [64]) in which the concept of non-local averaging is used, gradient approach (e.g. [65], [66]), Cosserat-continuum approach (e.g. [67]), viscous approach (e.g. [68]) in which the localization is limited by the adding of rate-dependent terms.

These theories, although very effective in the solution of the problem here considered, are generally difficult to use for simulation of large real structures. Indeed in concrete the FPZ is nearly $3d_a$ where d_a is the dimension of the aggregate [14]. To proper describe in finite element framework the kinematics of FPZ are generally needed two-three elements. Thus the number of elements necessary to model an entire structure is extremely high even if mesh-adapting techniques are adopted [69].

A widely used method which partially overcomes the problem of mesh-dependency is often referred as *mesh-adjusted softening modulus*, ore *crack band approach* since the concept was reported by Bazant and Oh [14].

To better illustrate the nature of the problem under discussion, a bar with constant cross-section A and length L subjected to uniaxial tension can be considered. (see Figure 2.22).

The constitutive law assumed is elastic up to tensile strength and characterized by linear tension-softening after (Figure 2.23a):

$$\sigma = \begin{cases} E\varepsilon & \text{for } \varepsilon \le \varepsilon_0 \\ f_t + H(\varepsilon - \varepsilon_0) & \text{for } \varepsilon_0 \le \varepsilon \le \varepsilon_f \end{cases} \tag{2.41}$$

where E is Young's modulus, f_t is tensile strength and ε_0 is the corresponding strain, ε_f is the ultimate stress-free strain and H is the softening modulus defined as:

$$H = -\frac{f_t}{\varepsilon_f - \varepsilon_0} \tag{2.42}$$

Assuming that the bar is loaded in tension with a displacement control procedure, the complete force-displacement curve with the softening branch may be described. The response will remain linear up to the displacement $u_0 = L\varepsilon_0$ (ascending branch of Figure 2.23b). At this point the force observed in a load-displacement relation

assumes its peak value $F_t=Af_t$. After that point the strength of bar starts to decrease. If the material is considered uniform and without any imperfection, each cross section of the bar can exhibit a stress reduction with increasing strain (i.e. strain-softening behavior) or with decreasing strain (i.e. elastic unloading) as it is illustrated in Figure 2.24a. Each cross section may indifferently have one of the two strains and the profile of strain along the bar may assume different distributions like for instance the one depicted in Figure 2.24b. Defining the variables L_s and $L_u=L-L_s$ the length of softening region and unloading region respectively and considering the end of the load procedure in which stress is zero and strain is zero in unloading region and ε_f in softening region, it is possible to express the elongation of the bar as:

$$u_f = L_u\varepsilon_u + L_s\varepsilon_s = L_s\varepsilon_f \tag{2.43}$$

In case of homogeneous and perfect material, L_s can be any value and infinite solutions are possible. In Figure 2.23b the area of the fan of the possible solutions is shaded. This area comprehends the limits $u_f=L\varepsilon_f$ when $L_s=L$, and $u_f=0$ when $L_s=0$.

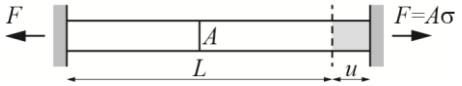

Figure 2.22 - Straight bar under uniaxial tension

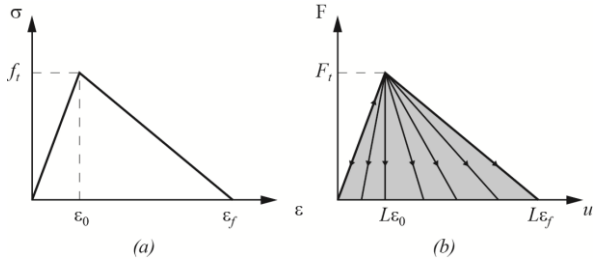

Figure 2.23 - (a) Stress-strain law with linear softening; (b) possible load displacement diagrams (fan shaded in grey)

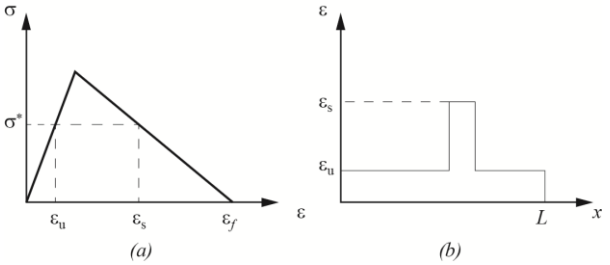

Figure 2.24 - (a) strain softening vs. elastic unloading; (b) possible strain profile along bar

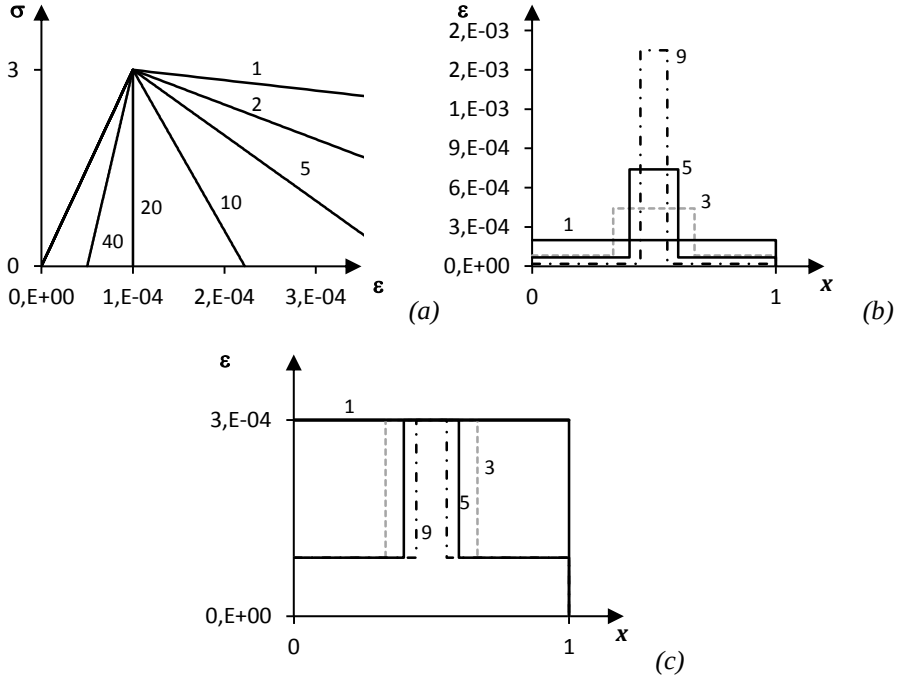

Figure 2.25 - Mesh-sensitivity of result for a uniaxial tension test. (a) load-displacement curves; (b) strain distribution along the bar at given displacement; (c) strain distribution along the bar at given force

Considering an imperfection of the material with a small region characterized by a slightly reduced strength, the ambiguity stated before disappears and the material outside the weak region exhibits elastic unload, while the weak region exhibits softening with strain increasing. If the weak zone is sufficiently small, the load-displacement curve can exhibit a snap-back behavior which complicates the numerical procedure since a suitable strategy should be adopted (e.g. arc-length). Moreover if the weak region is very small, the softening branch can be extremely close to the elastic branch of the load-displacement curve with a total amount of energy dissipated by the failure process equal to zero, which is a physically meaningless statement.

On the other hand considering the problem from the numerical point of view, it can be shown that the response is dependent on the mesh size (e.g. [70]). Considering the problem of the bar just exposed, suppose to discretize it with *n* elements with linear displacement interpolation. On one element an imperfection is imposed with a reduction of the tensile strength. The response in terms of load-displacement curve with different discretization and the strain distribution along element for some of

discretization adopted at a given displacement and at a given force are depicted in Figure 2.25.

In the following, the mesh-adjusted softening modulus technique is briefly recalled since it was selected for its simplicity and computational efficiency in this work. Then the non-local continuum approach is briefly presented since a non-local formulation of the scalar damage model used as the basis for the developed work was implemented (Scotta [78]).

2.4.1 Mesh-adjusted softening modulus

The fictitious crack model (FCM) proposed initially by Hillerborg [16] and cited in section 2.2.2 stands among the discrete approach. The cohesive zone proposed in the FCM is a zero-length zone where a law stress-crack opening displacement is adopted. Thus the fracture energy is constant and independent on the discretization of the problem. The fracture energy is represented by the area under the load-displacement curve (see 2.2.2), and is defined by the following:

$$G_f = \int \sigma du \tag{2.44}$$

where σ and u are the stress and the displacement of the cohesive zone (i.e. the FPZ).

On the other hand the smeared approach introduced in the work of Bazant and Oh [14] who proposed crack band model considers the FPZ with the dimension of one element. Indeed in their work, the authors underlined that the minimum element dimension should be equal to the FPZ size. Moreover they stated that FPZ in concrete has a roughly constant dimension equal to three times the dimension of the aggregate. The crack opening is considered smeared in the length of crack band w_c (i.e. the FPZ), thus a specific fracture energy can be introduced:

$$g_f = \int \boldsymbol{\sigma} d\boldsymbol{\varepsilon} \tag{2.45}$$

The specific fracture energy in a uniaxial case (e.g. Mode-I opening) is represented by the area under the stress-strain law (Figure 2.23a) and is related to fracture energy through the crack band width w_c:

$$G_f = g_f w_c \tag{2.46}$$

With this technique, the softening branch of the constitutive law depends on mesh characteristics. The first application of the technique can be found in [71] for softening plasticity, but the concept applied to crack process is reported in the work of [14].

Applying this concept to the bar described previously, the crack opening ω is smeared over the distance w_c and the crack strain is:

$$\varepsilon^c = \frac{\omega}{w_c} \tag{2.47}$$

The integral of (2.45) is solved for the stress-strain law depicted in (2.41); considering (2.46) the following equation for strain ε_f can be written:

$$\varepsilon_f = \frac{2G_f}{f_t w_c} \tag{2.48}$$

In this way, the softening modulus is related to the crack band w_c. Indeed, considering the numerical solution of the straight bar discretized in m elements, it results that $w_c = L/m$ and the softening modulus reads:

$$H = -\frac{Lf_t^2}{2G_f m - \frac{f_t^2 L}{E}} \tag{2.49}$$

The softening modulus expressed by (2.49) is then inversely proportional to number of elements m. Applying (2.43), which is written for the final stress-free state, for a generic stress state and observing that $L_s = w_c = L/m$ leads to the following expression for displacement u:

$$u = \frac{L\sigma}{E} + \frac{2G_f\left(f_t - \sigma\right)}{f_t^2} \tag{2.50}$$

or alternatively expressed as average strain [70]:

$$\bar{\varepsilon} = \frac{\sigma}{E} + \frac{2G_f\left(f_t - \sigma\right)}{Lf_t^2} \tag{2.51}$$

Equations (2.50) and (2.51) state that the post-peak response is independent to the element size (L/m) and thus different discretizations lead to the same result and to the same dissipated energy.

It is worth noting that a key aspect of this approach is the proper evaluation of w_c. Bazant and Oh [14] observed that when finite elements with a characteristic length l_{ch}, related to its dimension, bigger than w_c, in (2.46) w_c should be replaced by l_{ch}. This was done for the bar example presented above although the symbol w_c was maintained in the equations to avoid complications due to the introduction of the characteristic length concept. Furthermore, the determination of the characteristic length is difficult in practice because often the crack progresses not aligned with sides of mesh. For instance the projection of the size of the element along crack direction could be employed [72] (see Figure 2.26).

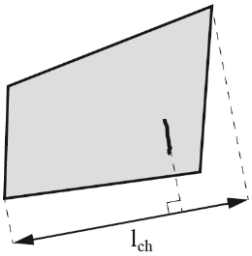

Figure 2.26 - Characteristic length of finite element with generic crack orientation

Other researchers (e.g. [75]) proposed simplified relations that often represent a good approximation:

$$l_{ch} = \sqrt[3]{V^{(e)}} \tag{2.52}$$

for solid finite elements and:

$$l_{ch} = \sqrt{A^{(e)}} \tag{2.53}$$

for bi-dimensional finite elements, where $V^{(e)}$ and $A^{(e)}$ are the volume and the area of the finite element respectively.

Moreover the crack band width depends also on the type of finite element; in particular it depends on the order of finite elements used. For instance if the element has quadratic interpolation of displacements, strain may localize only on 2 gauss points. Thus some researchers (e.g. [73], [74]) proposed the following relation for the evaluation of the characteristic length l_{ch}:

$$l_{ch} = \beta\sqrt{A^{(e)}} = \beta\sqrt{\sum_{\xi=1}^{ni}\sum_{\eta=1}^{ni} w_\xi w_\eta \det(\mathbf{J})} \tag{2.54}$$

where w_ξ and w_η are the weight factors of the integration rule, *ni* is the number of integration points, **J** is the jacobian of the transformation between the global coordinates system and the local isoparametric one at the integration point and β is a corrective factor which is equal to 1 for quadratic elements and to $\sqrt{2}$ for linear elements.

2.4.2 Non-local continuum

A widely used localization limiter is based on the concept of non-local averaging. The idea of a non-local continuum was introduced in the sixties in elasticity (e.g. Kröner [76], Eringen and Edelen [77]) and consists in considering the stress at a point as function of the average strain on a representative volume of material around that point. The theory was then applied to strain softening materials and improved by the non-local damage theory proposed by Pijaudier-Cabot and Bazant [64], where

the key aspect was the introduction of the non-local concept only for the variables that control damage and softening behavior and not for stresses and strain in the constitutive relation. With such an approach the strain localization is limited to a zone which size is assumed as a material property.

If $f(\mathbf{x})$ represents a certain local variable on a domain V, the corresponding non-local variable $\bar{f}(\mathbf{x})$ can be defined as a weighted mean on a certain surrounding reference volume V_r:

$$\bar{f}(\mathbf{x}) = \frac{1}{V_r}\int_V \alpha(\mathbf{x}-\mathbf{s}) f(\mathbf{x}) dV \tag{2.55}$$

where:

$$V_r = \int_V \alpha(\mathbf{x}-\mathbf{s}) dV \tag{2.56}$$

and $\alpha(\mathbf{x}\text{-}\mathbf{s})$ is a certain weight always decreasing function from source point $\mathbf{x}$. Finally $\mathbf{x}\text{-}\mathbf{s}$ represents the distance from the point $\mathbf{x}$, being $\mathbf{s}$ the position vector of a generic point on the volume. The weight function often assumed is the Gauss distribution (e.g. [64], [72], [78], [79]):

$$\alpha(\mathbf{x}-\mathbf{s}) = \exp\left(-\frac{|\mathbf{x}-\mathbf{s}|}{2l^2}\right) \tag{2.57}$$

where l is an internal parameter that is assumed as a material property which controls the size of localization zone. Bazant and Oh [14] and Bazant and Pijaudier-Cabot [80] proposed a value of this parameter related with the maximum aggregate size d_a by:

$$l = (2.7 \div 3) d_a \tag{2.58}$$

The relations abovementioned actually are modified to handle the cases of points located near the boundary of the domain. In such condition a part of the representative volume is located outside the domain and some techniques need to be employed like the rescale of the weight function [72].

2.5 References

[1] Krajicinovic, (1995). Some fundamental issues of damage mechanics, *Mechanics of Materials* , 217-230

[2] Mazars, J., Pijaudier-Cabot, G. (1989). Continuum damage theory – Application to concrete, *J. Eng. Mech.*, 115, 345-365

[3] Grassl, P. (2002). Constitutive Modelling of Concrete in Compression, *Thesis for the degree of Licentiate of Engineering*, Department of Structural Engineering, Chalmers University of Technology, Goeteborg, Sweden

[4] Vonk, R.A. (1992). Softening of Concrete Loaded in Compression, *PhD Thesis*, University of Technology Eindhoven, the Nederlands

[5] Wittmann, F.H. (1987). Structure of Concrete and Crack formation, *Fracture of Non-Metallic Materials*, 309-340

[6] Van Mier, J.G.M. (1984). Strain-softening of concrete under multiaxial loading conditions, *PhD Thesis*, University of Technology Eindhoven, The Netherlands

[7] Kotsovos, M.D. (1983). Effect of testing techniques on the post-ultimate behavior of concrete in compression, *Materials and Structures*, RILEM, 16, 3-12

[8] Van Mier, J.G.M. (1986a). Multiaxial strain-softening of concrete, part I: fracture, part II: load-histories, *Materials and Structures*, RILEM, 19, 179-200

[9] Van Mier, J.G.M. (1986b). Fracture of Concrete under Complex Stress, *Heron*, 31

[10] Gopalaratnam, V.S., Shah, S.P. (1985). Softening response of Plain Concrete in Direct Tension, *ACI J. Procedings*, 82, 310-323

[11] Karihaloo, B.L. (1995). Fracture Mechanics & Structural Concrete, *Concrete design & Construction Series*

[12] Griffith, A.A. (1921). The phenomena of rupture and flow in solids, *Phil. Trans. Roy. Soc. Of London*, 221, 163-197

[13] Irwin, G.R. (1957). Analysis of stresses and strains near the end of a crack traversing a plate, *J. Appl. Mech.*, 24, 361-364

[14] Bazant, Z.P., Oh, B.H. (1983). Crack band theory for fracture of concrete, *Mat. And Struct.*, 16, 155-177

[15] Shi, Z. (2009). Crack Analysis in Structural Concrete. Theory and applications, *Elsevier*

[16] Hilerborg, A., Modeer, M., Petersson, P.E. (1976). Analysis of crack formation and crack growth in concrete by means of fracture mechanics and finite elements, *Cem. and Concr. Res.*, 6, 773-782

[17] Kupfer, H., Hilsdorf, H.K., Rusch, H. (1969). Behavior of concrete under biaxial stresses, *ACI J.*, 66, 656-666

[18] Chen, W.F. (1982). Plasticity in reinforced concrete, *McGraw-Hill*, New York

[19] Yankelevsky, D.Z., Reinhardt, H.W. (1989). Uniaxial behavior of concrete in cyclic tension, *J. Struct. Eng.*, 115, 166-182

[20] Mazars, J., Pijaudier-Cabot, G. (1989). Continuum damage theory – Application to concrete, *J. Eng. Mech.*, 115, 345-365

[21] Ngo, D., Scordelis, A.C. (1967). Finite element analysis of reinforced concrete beams, *ACI Journal*, 64, 152-163

[22] Rashid, Y.R. (1968). Analysis of prestressed concrete pressure vessels, *Nucl. Eng. Design*, 7, 334-344

[23] Jirasek, M., Zimmermann, T. (1998). Analysis of rotating crack model, *J. Eng. Mech.*, 124, 842-851

[24] Kachanov, L.M. (1958). Time of the rupture process under creep conditions, *Izv. AN SSR*, Otd. Tekhn. Nauk, 8, 26-31 (in Russian)

[25] Kachanov, L.M. (1999). Rupture time under creep conditions, *Int. J. Fract.*, 97, 11-18 (translated from [24])

[26] Kachanov, L.M. (1986). Introduction to continuum damage mechanics, *The Netherlands: Martinus Nijhoff*

[27] Murakami, S., Ohno, N. (1981). A continuum theory of creep and creep damage, *Creep in Structures*, ed. Ponter, 442-444d

[28] Caboche, J.L. (1982). Mechanical behavior of anisotropic solids, *ed. Boehler*, J.P., Martinus Nijhof

[29] Caboche, J.L. (1981). Continous damage mechanics – a tool to describe phenomena before crack initiation, *Nucl. Eng. Des.*, 64, 233-247

[30] Cope, R.J., Rao, P.V., Clark, L.A., Norris, P. (1980). Modelling of reinforced concrete behavior for finite element analysis of bridge slabs, *Num. Meth. Non-Linear Probl.*, Pineridge Press, Swansea, 1, 457-470

[31] De Borst, R., Nauta, P. (1985). Non-orthogonal cracks in a smeared finite element model, *Eng. Comp.*, 2, 35-46

[32] Bazant, Z.P., Gambarova, P.G. (1984). Crack shear in concrete: crack band micro plane model, *J. Struct. Eng., ASCE*, 110, 2015-2036

[33] Simo, J.C., Hughes, T.J.R. (1998). Computational inelasticity, *Springer*

[34] Owen, D.R.J., Hinton, E. (1980). Finite elements in plasticity: theory and practice, *Pineridge Press*

[35] De Borst, R. (2002). Fracture in quasi-brittle materials: a review of continuum damage-based approaches, *Eng. Fract. Mech.*, 69, 95-112

[36] Weihe, S., Kröplin, B. (1998). Classification of smeared crack models based on material and structural properties, *Int. J. Solids Struct.*, 35, 1289-1308

[37] ACI Committee 446 (1997). Finite Element analysis of fracture in concrete structures, *ACI Rep. 446.3R-97*

[38] Suidan, M., Schnobrich, W.C. (1973). Finite element analysis of reinforced concrete, *J. Struct. Div.*, 99, 2109-2121

[39] Kolmar, W., Mehlhorn, G. (1984). Comparison of shear stiffness formulations for cracked reinforced concrete elements, *Proc. Of Int. Conf. on Computer Aided Analysis and Design of Concrete Struc.*, Swansea: Pineridge Press, 133-147

[40] De Borst, R., (1987). Smeared cracking, plasticity, creep and thermal loading-a unified approach, *Comp. Meth. Appl. Mech. Eng.*, 62, 89-110

[41] Rots, J.G., Nauta, P., Kusters, G.M.A., Blaauwendraad, J. (1984). Smeared crack approach and fracture localization in concrete, *HERON*, 30, 1-48

[42] Rots, J.G., Blaauwendraad, J. (1989) Crack models for concrete: discrete or smeared? Fixed, multi-directional or rotating?, *HERON*, 34, 1-59

[43] Skrzypek, J., Ganczarski, A. (1999). Modeling of material damage and failure of structures – Theory and applications, *Springer*

[44] Murakami, S. (2012). Continuum Damage Mechanics – A continuum mechanics approach to the analysis of damage and fracture, *Springer*

[45] Rabotnov, Y.N. (1968). Creep rupture, *Proc. Appl. Mech. Conf.*, Standford University, Springer, 342-349

[46] Murakami, S., Ohno, N. (1988) Continuum theory of material damage at high temperature, *in: High Temperaturare creep-fatigue*, Elsevier, 43-64

[47] Gurson, A.L. (1977). Continuum theory of ductile rupture by void nucleation and growth: Part I – Yield criteria and flow rules for porous ductile media, *J. Eng. Mat. Tech.*, 99, 2-13

[48] Chaboche, J.L. (1988). Continuum damage mechanics: part I: General concepts, part II: Damage growth, crack initiation, and crack growth, *J. Appl. Mech.*, 55, 59-71

[49] Simo, J.C., Ju, J.W. (1987). Strain- and Stress- based Continuum Damage Models – I. Formulation, *Int. J. Solids Structures.*, 23, 821-840

[50] Oliver, J., Cervera, M., Oller, S., Lubliner, J. (1990). Isotropic damage models and smeared cracked analysis of concrete, *Proc. 2nd Int. Conf. on Comp. Aided Design of Conc. Struct.*, Pineridge press, 2, 945-958

[51] Mazars, J. (1991). Damage models for concrete and their usefulness for seismic loadings, *Exp. And Num. Meth. In Earth. Eng.*, 95-105

[52] Cervera, M., Oliver, J., Oller, S., Galindo M. (1990). Pathological behavior of large concrete dams analyzed via isotropic damage models, *Proc. 2nd Int. Conf. on Comp. Aided Design of Conc. Struct.*, 633-643

[53] Cervera, M., Oliver, J., Galindo, M. (1991). Simulacion numerica de patologias en presas de hormigon, *Monografia CIMNE*, 4, 633-643

[54] Ju, J.W. (1989). On energy-based coupled elastoplastic damage theories: constitutive modeling and computational aspects, *Int. J. Solids Struct.*, 25, 803-833

[55] Faria, R., Oliver, J., Cervera, M. (1998). A strain-based viscous-plastic-damage model for massive concrete structures, *Int. J. Solids and Structures*, 35, 1533-1558

[56] Kachanov, L.M. (1974). Foundations of fracture mechanics, Moscow, Nauka

[57] Murakami, S., Kamiya, K. (1997). Constitutive and damage evolution equations of elastic-brittle materials based on irreversible thermodynamics, *Int. J. Mech. Sci.*, 39, 473-486

[58] Skrzypek, J., Ganczarski, A. (1998a). Application of the orthotropic damage growth rule to variable principal directions, *Int. J. Damage Mech.*, 7, 180-206

[59] Lemaitre, J., Chaboche, J.L. (1978). Aspect phenomenologique de la rapture per endommagement, *J. De Méchanique applique*, 2, 317-635

[60] Cordebois, J.P., Sidoroff, F. (1979). Anisotropie elastique induite par endommagement, *Colloque Euromesh 115, Grenoble, Ed. Du CNRS*, 295

[61] Oliver, J. (1989). A consistent characteristic length for smeared cracking models, *Int. J. Numer. Meth. Eng.*, 28, 461-474

[62] Rice, J.R. (1977). The localization of plastic deformation, *Proc. 14th Int. Congr. Theor. Appl. Mech.*, ed. W.T. Koiter, North-Holland, Amsterdam, 207-220

[63] Belytshko, T., Fish, J., Engelmann, B.E. (1988). A finite element with embedded localization zones, *Comp. Meth. Appl. Mech. Eng.*, 70, 59-89

[64] Pijaudier-Cabot, G., Bazant, Z.P. (1987). Nonlocal damage theory, *J. Eng. Mech., ASCE*, 113, 1152-1533

[65] Aifantis, E.C. (1984). On the microstructural origin of certain inelastic models, *J. Eng. Mater. Tech.*, 106, 326-330

[66] De Borst, R., Mülhaus, H.B. (1992). Gradient-dependent plasticity: Formulation and algorithmic aspects, *Int. J. Num. Meth. Eng.*, 35, 521-539

[67] de Borst, R. (1993). A generalization of J2-flow theory for polar continue, *Comp. Meth. Appl. Mech. Eng.*, 103, 347-362

[68] Needleman, A. (1988). Material rate dependence and mesh sensitivity in localization problems, *Comp. Meth. Appl. Mech. Eng.*, 67, 69-86

[69] Askes, H., Bodé, L., Sluys, L.J. (1998). ALE analysis of localization in wave propagation problems, *Mech. Coh.-frict. Mat.*, 3, 105-126

[70] De Borst, R. (2001). Some recent issues in computational failure mechanics, *Int. J. Numer. Meth. Eng.*, 52, 63-95

[71] Pietruszczak, S., Mròz, Z. (1981). Finite element analysis of deformation of strain softening materials, *Int. J. Numer. Meth. Eng.*, 17, 327-334

[72] Jiràsek, M. (2011). Damage and smeared crack modes, *Numerical modeling of concrete cracking, Ed. Günter Hofstetter, Günther Meschke, Springer*, 532, 1-49

[73] Feenstra, P.H. (1993). Computational aspects of biaxial stress in plain and reinforced concrete, *PhD Thesis*, Delft University of Technology, The Netherlands

[74] Rots, J.G. (1988). Computation modeling of concrete fracture, *PhD Thesis*, Delft University of Technology, The Netherlands

[75] Scotta, R., Vitaliani, R., Saetta, A., Oñate, E., Hanganu, A. (2001). A scalar damage model with a shear retention factor for the analysis of reinforced concrete structures: theory and validation, *Comput. Struct.*, 79, 737-755

[76] Kröner, E. (1967). Elasticity theory of materials with long range cohesive forces, *Int. J. Solids Struct.*, 3, 731-742

[77] Eringen, A.C., Edelen, D.G.B. (1972). On nonlocal elasticity, *Int. J. Eng. Science*, 10, 233-248

[78] Scotta, R. (1997). Analisi meccanica di strutture in calcestruzzo mediante modelli di danno, *PhD Thesis*, Università degli studi di Padova, Dipartimento di Costruzioni e Trasporti

[79] Jirasek, M., Zimmermann, T. (1998). Rotating crack model with transition to scalar damage, *J. Eng. Mech.*, 124, 277-284

[80] Bazant, Z.P., Pijaudier-Cabot, G. (1989). Measurement of the characteristic length of nonlocal continuum, *J. Eng. Mech.*, 115, 755-767

CHAPTER 3:
MECHANICAL DAMAGE MODEL FOR CONCRETE

In this chapter a phenomenological isotropic plastic-damage model is presented. It is based on the model originally proposed for concrete by Faria et al. [1], Scotta [2], Saetta et al. (1999). The formulation stands among the framework of strain space models as depicted by Simo and Ju [9] since it is based on strain equivalence hypothesis and the concept of effective stress tensor.

The model is able to describe the overall nonlinear stress-strain behavior of concrete by means of two scalar damage variables d^+ and d^- for tensile and compressive load conditions respectively. Within such an approach, the split of effective stress tensor into a positive $\overline{\boldsymbol{\sigma}}^+$ and negative $\overline{\boldsymbol{\sigma}}^-$ component, related to tensile and compressive load conditions respectively, is performed. Differently to other isotropic damage models (e.g. Mazars and Pijaudier-Cabot [4]) which define an equivalent strain, in the present model two equivalent stresses τ^+ and τ^- are assumed for positive and negative part respectively as scalar measures of the corresponding parts of effective stress tensor.

The capability of the constitutive law of describing the strain softening response, the stiffness degradation mechanism, the crack closure-opening under cyclic external loads, the behavior under biaxial and triaxial stress states is shown.

3.1 Thermodynamic aspects

As shown in previous chapter, Continuum Damage Mechanics is based on the thermodynamics framework of the irreversible processes. According to this, the first and second principles of thermodynamics are always satisfied. In the present work the Helmholtz free energy is considered as a possible form for the free energy potential, which characterizes the local thermodynamic state and is necessary to obtain the constitutive load consistent with the Continuum Damage Mechanics framework.

The damage and plastic unloading/reloading processes are assumed to be elastic. The decomposition of the total strain tensor into elastic-damage ε^e and plastic-damage $\boldsymbol{\varepsilon}^p$ contributions gives:

$$\boldsymbol{\varepsilon} = \boldsymbol{\varepsilon}^e + \boldsymbol{\varepsilon}^p \tag{3.1}$$

The effective stress tensor $\overline{\boldsymbol{\sigma}}$ is defined by Faria et al. [1]:

$$\overline{\boldsymbol{\sigma}} = \mathbf{C}_0 : \boldsymbol{\varepsilon}^e = \mathbf{C}_0 : \left(\boldsymbol{\varepsilon} - \boldsymbol{\varepsilon}^p\right) \tag{3.2}$$

with $\mathbf{C}_0$ the fourth-order elastic stiffness tensor.

According to the work of Faria et al. [1], two independent damage parameters d^+ and d^- are introduced. Furthermore, the total strain tensor $\boldsymbol{\varepsilon}$ is assumed as free variable, while the plastic strain tensor $\boldsymbol{\varepsilon}^p$ and the damage variables d^+ and d^- are considered as internal variables. The introduction of the two damage parameters permits to take into account both tensile and compressive failure modes of concrete and each damage parameter affects one of the two independent parts of the effective stress tensor. The stress split is performed with the following relations:

$$\overline{\boldsymbol{\sigma}}^+ = \sum_{i=1}^{3} \left\langle \overline{\sigma}_i \right\rangle \mathbf{p}_i \otimes \mathbf{p}_i \tag{3.3}$$

$$\overline{\boldsymbol{\sigma}}^- = \overline{\boldsymbol{\sigma}} - \overline{\boldsymbol{\sigma}}^+ \tag{3.4}$$

where $\overline{\sigma}_i$ is the *i*-th principal stress from tensor $\overline{\boldsymbol{\sigma}}$, $\mathbf{p}_i$ is the unit vector associated to the *i*-th principal direction and the symbol $\langle \cdot \rangle$ indicate the MacAuley brackets defined by:

$$\langle x \rangle = \begin{matrix} x \text{ if } x > 0 \\ 0 \text{ if } x \leq 0 \end{matrix} \tag{3.5}$$

Considering these relations, the following definition for Helmholtz free energy inspired to works of La Borderie et al. [3] and Mazars and Pijaudier-Cabot [4] can be written [1]:

$$\begin{aligned}\Psi(\boldsymbol{\varepsilon},\boldsymbol{\varepsilon}^p,d^+,d^-) &= (1-d^+)\Psi_0^+(\boldsymbol{\varepsilon},\boldsymbol{\varepsilon}^p)+(1-d^-)\Psi_0^-(\boldsymbol{\varepsilon},\boldsymbol{\varepsilon}^p)= \\ \Psi(\boldsymbol{\varepsilon},\boldsymbol{\varepsilon}^p,d^+,d^-) &= (1-d^+)\frac{1}{2}\overline{\boldsymbol{\sigma}}^+:\mathbf{C}_0^{-1}:\overline{\boldsymbol{\sigma}}+(1-d^-)\frac{1}{2}\overline{\boldsymbol{\sigma}}^-:\mathbf{C}_0^{-1}:\overline{\boldsymbol{\sigma}}= \\ &= (1-d^+)\frac{1}{2}\overline{\boldsymbol{\sigma}}^+:\boldsymbol{\varepsilon}^e+(1-d^-)\frac{1}{2}\overline{\boldsymbol{\sigma}}^-:\boldsymbol{\varepsilon}^e\end{aligned} \tag{3.6}$$

where d^+ and d^- represent the positive (tensile) and negative (compressive) damage parameters, Ψ_0^+ and Ψ_0^- are elastic free energies associated to positive and negative part of effective stress tensor and $\mathbf{C}_0^{-1}$ is the fourth-order elastic compliance tensor.

Equation (3.6) can be also written in following form:

$$\Psi(\boldsymbol{\varepsilon},\boldsymbol{\varepsilon}^p,d^+,d^-) = \frac{1}{2}\overline{\boldsymbol{\sigma}}:(\mathbf{I}-\mathbf{D}):\boldsymbol{\varepsilon}^e \tag{3.7}$$

where $\mathbf{D}$ is the fourth-order damage tensor with the following expression (Wu et al. [5]):

$$\mathbf{D} = d^+\mathbf{P}^+ + d^-\mathbf{P}^- \tag{3.8}$$

with $\mathbf{P}^+$ and $\mathbf{P}^-$ the fourth-order positive and negative projection tensors, respectively. These have the following definition:

$$\mathbf{P}^+ = \sum_{i=1}^{3} H(\overline{\sigma}_i)\cdot\mathbf{p}_{ii}\otimes\mathbf{p}_{ii} \tag{3.9}$$

$$\mathbf{P}^- = \mathbf{I}-\mathbf{P}^+ \tag{3.10}$$

where H is the Heaviside step function, $\overline{\sigma}_i$ is the *i*-th principal stress of the effective stress tensor $\overline{\boldsymbol{\sigma}}$, and $\mathbf{p}_{ii}$ is the second order tensor associated to the *i*-th (Wu et al. [5]):

$$\mathbf{p}_{ii} = \mathbf{p}_i\otimes\mathbf{p}_i \tag{3.11}$$

With some calculations reported in the work of Faria and Oliver [6] it is possible to demonstrate that the positive and negative elastic free energies are always positive:

$$\Psi_0^+ \geq 0 \quad ; \quad \Psi_0^- \geq 0 \tag{3.12}$$

Considering equation (3.6) it can be demonstrated that the total free energy when no damage and plasticity have yet occurred is equal to the elastic free energy satisfying a fundamental thermodynamical demand:

$$\Psi(\boldsymbol{\varepsilon},\boldsymbol{\varepsilon}^p=0,d^+=0,d^-=0) = \Psi_0 = \Psi_0^+ + \Psi_0^- = \frac{1}{2}\boldsymbol{\varepsilon}:\mathbf{C}_0:\boldsymbol{\varepsilon} \tag{3.13}$$

Furthermore, observing that damage variables need to satisfy

$$0 \leq d^+ \leq 1 \quad \text{and} \quad 0 \leq d^- \leq 1 \tag{3.14}$$

it can be concluded that:

$$\Psi(\boldsymbol{\varepsilon}, \boldsymbol{\varepsilon}^p, d^+, d^-) = \left(1-d^+\right)\Psi_0^+ + \left(1-d^-\right)\Psi_0^- \geq 0 \tag{3.15}$$

The thermodynamic forces conjugate to the damage variables, also called damage energy release rates, are expressed as:

$$Y^+ = -\frac{\partial \Psi}{\partial d^+} = \Psi_0^+ \text{ and } Y^- = -\frac{\partial \Psi}{\partial d^-} = \Psi_0^- \tag{3.16}$$

and represent the energy release rate associated to a unit damage variation. These thermodynamic forces have a physical meaning analogous to fracture energy G_f in fracture mechanics (Lemaitre [7], Chaboche [8]) since they represent the energy release rate associated to a unit damage growth.

During a physical process the energy dissipation has to be non-negative in agreement with the first thermodynamic principle. An admissible load-deformation process respects the following Clausius-Duhem inequality:

$$-\dot{\Psi} + \boldsymbol{\sigma} : \dot{\boldsymbol{\varepsilon}} \geq 0 \tag{3.17}$$

From equation (3.6) it is possible to write the following relation:

$$\dot{\Psi} = \frac{\partial \Psi}{\partial \boldsymbol{\varepsilon}} : \dot{\boldsymbol{\varepsilon}} + \frac{\partial \Psi}{\partial \boldsymbol{\varepsilon}^p} : \dot{\boldsymbol{\varepsilon}}^p + \frac{\partial \Psi}{\partial d^+}\dot{d}^+ + \frac{\partial \Psi}{\partial d^-}\dot{d}^- \tag{3.18}$$

Substituting equation (3.18) in (3.17) it is possible to obtain the alternative expression for dissipation:

$$\left[\boldsymbol{\sigma} - \frac{\partial \Psi}{\partial \boldsymbol{\varepsilon}}\right] : \dot{\boldsymbol{\varepsilon}} - \left[\frac{\partial \Psi}{\partial d^+}\dot{d}^+ + \frac{\partial \Psi}{\partial d^-}\dot{d}^-\right] - \frac{\partial \Psi}{\partial \boldsymbol{\varepsilon}^p} : \dot{\boldsymbol{\varepsilon}}^p \geq 0 \tag{3.19}$$

Being the total strain $\boldsymbol{\varepsilon}$ a free variable, $\dot{\boldsymbol{\varepsilon}}$ can assume any arbitrary value. Since equation (3.19) needs to maintain its generality for any admissible process, the term in the first bracket should be always zero. This gives one of the Coleman's relations (Simo and Ju [9]), essential for the definition of the constitutive law:

$$\boldsymbol{\sigma} = \frac{\partial \Psi}{\partial \boldsymbol{\varepsilon}} \tag{3.20}$$

Considering equations (3.1) and (3.2), the constitutive law can be written as follows:

$$\boldsymbol{\sigma} = \frac{\partial \Psi}{\partial \boldsymbol{\varepsilon}^e}\frac{\partial \boldsymbol{\varepsilon}^e}{\partial \boldsymbol{\varepsilon}} = \frac{\partial \Psi}{\partial \boldsymbol{\varepsilon}^e}\mathbf{I} \tag{3.21}$$

where $\mathbf{I}$ is the fourth-order identity tensor. So, equation (3.20) can be expresses as:

$$\boldsymbol{\sigma} = (1-d^+)\frac{\partial \Psi_0^+}{\partial \boldsymbol{\varepsilon}^e} + (1-d^-)\frac{\partial \Psi_0^-}{\partial \boldsymbol{\varepsilon}^e} \tag{3.22}$$

Since $\bar{\boldsymbol{\sigma}}\left(\boldsymbol{\varepsilon}^e\right)$ is linearly dependent on $\boldsymbol{\varepsilon}^e$ and being the stress splitting performed according to equations (3.3)-(3.4), the following relations are valid for any arbitrary scalar α :

$$\bar{\boldsymbol{\sigma}}^+\left(\alpha\boldsymbol{\varepsilon}^e\right)=\alpha\bar{\boldsymbol{\sigma}}^+\left(\boldsymbol{\varepsilon}^e\right) \tag{3.23}$$

$$\bar{\boldsymbol{\sigma}}^-\left(\alpha\boldsymbol{\varepsilon}^e\right)=\alpha\bar{\boldsymbol{\sigma}}^-\left(\boldsymbol{\varepsilon}^e\right) \tag{3.24}$$

showing that both $\bar{\boldsymbol{\sigma}}^+$ and $\bar{\boldsymbol{\sigma}}^-$ are homogeneous functions of first degree on $\boldsymbol{\varepsilon}^e$.

Euler's theorem state that if $\Phi(x)$ is an homogeneous function of *m*-th degree on *x*, i.e. for every scalar λ is:

$$\Phi(\lambda x)=\lambda^m\Phi(x) \tag{3.25}$$

then the following is valid:

$$\Phi(x)=\frac{1}{m}x\frac{\partial\Phi}{\partial x} \tag{3.26}$$

Therefore, according to Euler's theorem one can write:

$$\bar{\boldsymbol{\sigma}}^+\left(\boldsymbol{\varepsilon}^e\right)=\boldsymbol{\varepsilon}^e:\frac{\partial\bar{\boldsymbol{\sigma}}^+}{\partial\boldsymbol{\varepsilon}^e} \tag{3.27}$$

$$\bar{\boldsymbol{\sigma}}^-\left(\boldsymbol{\varepsilon}^e\right)=\boldsymbol{\varepsilon}^e:\frac{\partial\bar{\boldsymbol{\sigma}}^-}{\partial\boldsymbol{\varepsilon}^e} \tag{3.28}$$

The derivatives of equation (3.22) are evaluated considering equations (3.27) and (3.28) obtaining:

$$\frac{\partial\Psi_0^+}{\partial\boldsymbol{\varepsilon}^e}=\frac{1}{2}\frac{\partial\bar{\boldsymbol{\sigma}}^+}{\partial\boldsymbol{\varepsilon}^e}:\boldsymbol{\varepsilon}^e+\frac{1}{2}\bar{\boldsymbol{\sigma}}^+=\bar{\boldsymbol{\sigma}}^+ \tag{3.29}$$

$$\frac{\partial\Psi_0^-}{\partial\boldsymbol{\varepsilon}^e}=\frac{1}{2}\frac{\partial\bar{\boldsymbol{\sigma}}^-}{\partial\boldsymbol{\varepsilon}^e}:\boldsymbol{\varepsilon}^e+\frac{1}{2}\bar{\boldsymbol{\sigma}}^-=\bar{\boldsymbol{\sigma}}^- \tag{3.30}$$

With these relations, equation (3.22) can be finally explicited, giving the relation between effective stress and Cauchy stress tensors:

$$\boldsymbol{\sigma}=(1-d^+)\bar{\boldsymbol{\sigma}}^+ +(1-d^-)\bar{\boldsymbol{\sigma}}^-=(\mathbf{I}-\mathbf{D}):\bar{\boldsymbol{\sigma}} \tag{3.31}$$

The second and third term of equation (3.19) provide the damage and the plastic dissipation inequalities respectively. These are:

$$-\frac{\partial\Psi}{\partial d^+}\dot{d}^+-\frac{\partial\Psi}{\partial d^-}\dot{d}^-=\Psi_0^+\dot{d}^+ +\Psi_0^-\dot{d}^-\geq 0 \tag{3.32}$$

$$-\frac{\partial\Psi}{\partial\boldsymbol{\varepsilon}^p}:\dot{\boldsymbol{\varepsilon}}^p\geq 0 \tag{3.33}$$

The contribution indicated in equation (3.32) is a non-negative quantity because Ψ_0^+ and Ψ_0^- are positive quantities (see equation (3.12)) and $\dot{d}^+$ and $\dot{d}^-$ are non-negative due to kinematics of damage as it will be shown later in this chapter.

Due to chain rule, the derivative expressed in equation (3.33) can be written as:

$$\frac{\partial \Psi}{\partial \boldsymbol{\varepsilon}^p} = \frac{\partial \Psi}{\partial \boldsymbol{\varepsilon}^e} : \frac{\partial \boldsymbol{\varepsilon}^e}{\partial \boldsymbol{\varepsilon}^p} \tag{3.34}$$

The assumed plastic evolution flow, which is described in 3.3, is given by the following compact relation:

$$\dot{\boldsymbol{\varepsilon}}^p = a\boldsymbol{\varepsilon} = a\mathbf{C}_0^{-1} : \bar{\boldsymbol{\sigma}} \tag{3.35}$$

where scalar value a is a positive scalar value defined in 3.3; according to this formulation the plastic strain rate is assumed to have the direction of the elastic strain tensor.

According to equation (3.1), the following derivative can be evaluated:

$$\frac{\partial \boldsymbol{\varepsilon}^e}{\partial \boldsymbol{\varepsilon}^p} = -\mathbf{I} \tag{3.36}$$

consequently equation (3.33) can be written as:

$$-\frac{\partial \Psi}{\partial \boldsymbol{\varepsilon}^p} : \dot{\boldsymbol{\varepsilon}}^p = a\frac{\partial \Psi}{\partial \boldsymbol{\varepsilon}^e} : \mathbf{C}_0^{-1} : \bar{\boldsymbol{\sigma}} \tag{3.37}$$

which can be expressed, according to equations (3.21)-(3.22) and (3.31), as:

$$-\frac{\partial \Psi}{\partial \boldsymbol{\varepsilon}^p} : \dot{\boldsymbol{\varepsilon}}^p = a\left[\left(1-d^+\right)\bar{\boldsymbol{\sigma}}^+ : \mathbf{C}_0^{-1} : \bar{\boldsymbol{\sigma}} + \left(1-d^-\right)\bar{\boldsymbol{\sigma}}^- : \mathbf{C}_0^{-1} : \bar{\boldsymbol{\sigma}}\right] \tag{3.38}$$

The term in square brackets is 2Ψ (see equation (3.6)), thus equation (3.38) can be written as:

$$-\frac{\partial \Psi}{\partial \boldsymbol{\varepsilon}^p} : \dot{\boldsymbol{\varepsilon}}^p = 2a\Psi \geq 0 \tag{3.39}$$

which is non-negative since Ψ is non-negative according to equation (3.15) and $a \geq 0$ (see 3.3).

Finally it is possible to conclude that the Clausius-Duhem inequality expressed in equations (3.17) and (3.19) is satisfied.

3.2 Damage criteria

In order to define the damage criteria, it is useful to define a scalar positive quantity, named equivalent stress. In Simo and Ju [9] it was defined the comparable concept

of equivalent strain which enables to compare different tridimensional stress states evaluating a suitable norm of their respective stress tensors. In previous works is possible to find some definitions for the tensile and compressive equivalent stresses which are suitable norms of positive and negative stress tensor respectively (Faria et al.[1], Scotta [2]).

For instance, the following definition can be adopted from [1]:

$$\tau^{+} = \sqrt{\overline{\boldsymbol{\sigma}}^{+} : \mathbf{C}_0^{-1} : \overline{\boldsymbol{\sigma}}^{+}} \tag{3.40}$$

$$\tau^{-} = \sqrt{\sqrt{3}\left(K\overline{\sigma}_{oct}^{-} + \overline{\tau}_{oct}^{-}\right)} = \sqrt{\sqrt{3}\left(K\frac{\bar{I}_1^{-}}{3} + \sqrt{\frac{2}{3}\bar{J}_2^{-}}\right)} \tag{3.41}$$

In present work two alternative proposals for equivalent stress definitions are considered: proposal A in which both equivalent stresses are in terms of a tension and proposal B in which both equivalent stresses are in terms of a square root of a tension, similarly to original formulation (Faria et al. [1]).

In detail, the proposal A is:

$$\tau^{+} = \sqrt{E\overline{\boldsymbol{\sigma}}^{+} : \mathbf{C}_0^{-1} : \overline{\boldsymbol{\sigma}}^{+}} \tag{3.42}$$

$$\tau^{-} = \sqrt{3}\left(K\overline{\sigma}_{oct}^{-} + \overline{\tau}_{oct}^{-}\right) = \sqrt{3}\left(K\frac{\bar{I}_1^{-}}{3} + \sqrt{\frac{2}{3}\bar{J}_2^{-}}\right) \tag{3.43}$$

while the proposal B is:

$$\tau^{+} = \sqrt[4]{E\overline{\boldsymbol{\sigma}}^{+} : \mathbf{C}_0^{-1} : \overline{\boldsymbol{\sigma}}^{+}} \tag{3.44}$$

$$\tau^{-} = \sqrt{\sqrt{3}\left(K\overline{\sigma}_{oct}^{-} + \overline{\tau}_{oct}^{-}\right)} = \sqrt{\sqrt{3}\left(K\frac{\bar{I}_1^{-}}{3} + \sqrt{\frac{2}{3}\bar{J}_2^{-}}\right)} \tag{3.45}$$

where $\bar{I}_1^{-}$ is the first invariant of $\overline{\boldsymbol{\sigma}}^{-}$ and $\bar{J}_2^{-}$ is the second invariant of the deviatoric part of $\overline{\boldsymbol{\sigma}}^{-}$, $\overline{\sigma}_{oct}^{-}$ and $\overline{\tau}_{oct}^{-}$ are the octahedral normal stress and the octahedral shear stress of $\overline{\boldsymbol{\sigma}}^{-}$ respectively. E is Young modulus of concrete and K is a material property that accounts for the uniaxial compressive strength increase due to biaxial compression.

In the proposed model a unique damage criterion is defined in order to consider the interaction between tensile and compressive damage evolutions with the following quadratic functional form:

$$g\left(\tau^{+}, \tau^{-}, r^{+}, r^{-}\right) = \left(\frac{\tau^{+}}{r^{+}}\right)^2 + \left(\frac{\tau^{-}}{r^{-}}\right)^2 - 1 \le 0 \tag{3.46}$$

where r^+ and r^- are the scalar damage thresholds monitoring the size of the damage surface in tension and compression respectively. The inequality of equation (3.46) defines the elastic unloading/reloading domain and its closure is the damage surface of incipient damage condition and represents an ellipse in the equivalent stresses space with major and minor axis equal to r^- and r^+ respectively as shown in Figure 3.1.

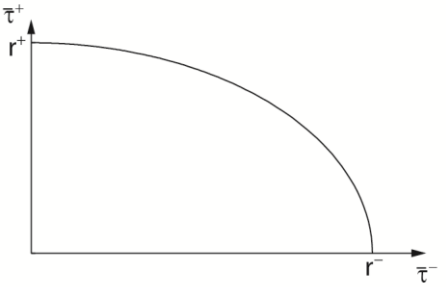

Figure 3.1 - Damage criteria in equivalent stresses space

The initial elastic domain for the virgin material is determined by the damage thresholds under uniaxial tension and compression, r_0^+ and r_0^-, respectively.

The damage surface defined by equation (3.46) represents in the positive octant domain of the effective stress space ($\bar{\sigma}_1, \bar{\sigma}_2, \bar{\sigma}_3 \geq 0$) an ellipsoid centered on the origin (Figure 3.2-Figure 3.3). If $\nu = 0$ the ellipsoid reduces to a sphere. In the negative octant domain, the limit surface represents a Drucker-Pragger cone in which parameter K controls the slope of the cone. This parameter is equal to (see Faria and Oliver [6] for more details):

$$K = \sqrt{2}\frac{1-R_0}{1-2R_0} \tag{3.47}$$

where R_0 is the ratio between 2D and 1D maximum elastic compressive stresses:

$$R_0 = \frac{f_{02d}^-}{f_{01d}^-} \tag{3.48}$$

The remaining octant domains represent mixed tension-compression stress states. The shape of the surface for the original Faria et al. [1] model and for proposal A of present model is shown in Figure 3.2 and Figure 3.3 respectively.

In Figure 3.4 the initial damage threshold obtained with the two different proposals (A and B) are represented in $\sigma_1 - \sigma_2$ plane and compared with the original criterion of Faria et al. [1]. As expected, all the initial damage surfaces, i.e. the elastic limit surfaces, are identical in the compression-compression and in the tension-tension field, whereas they are significantly different in the tension-compression domain,

where the original criterion of Faria et al. [1] neglects the influence of orthogonal tensile stress/strain on the compressive strength, which is widely experimentally confirmed. As above mentioned, the criterion of Faria et al. [1], the proposal A and the proposal B are respectively represented by a constant, ellipse, and linear function.

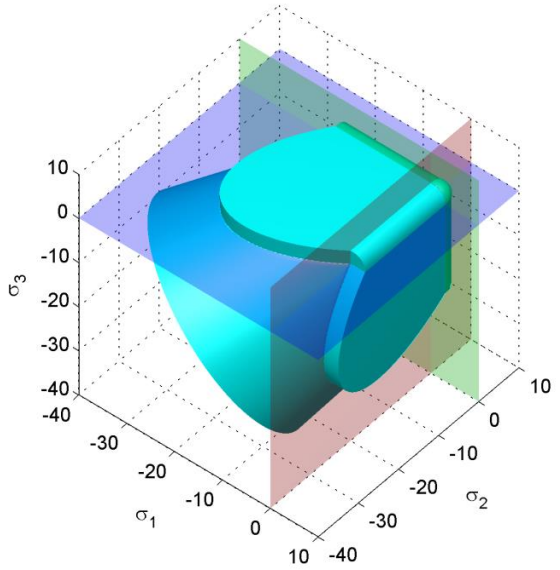

Figure 3.2 - Initial damage surface for original model (Faria et al. [1])

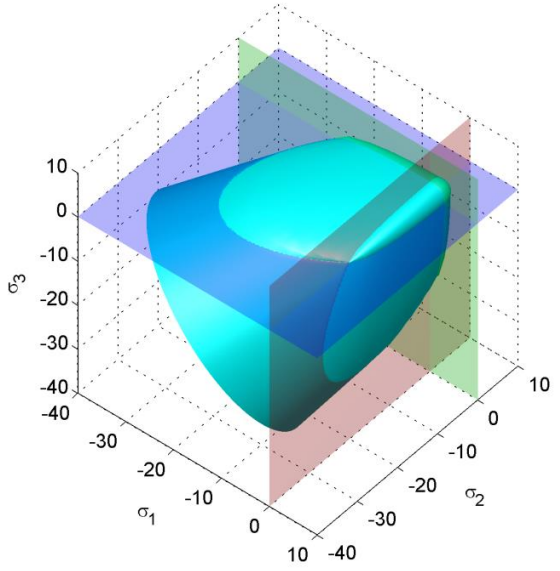

Figure 3.3 - Initial damage surface for proposal A

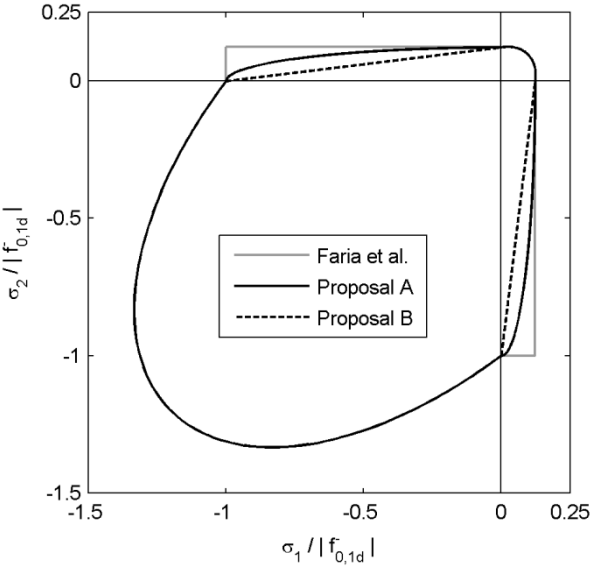

Figure 3.4 - Initial damage surface for plane stress conditions for different proposals

3.3 Evolution of plastic strain tensor

The proposed constitutive model assumes that the damage criterion also describes the plastic surface so that the development of material damage is simultaneous with the accumulation of irreversible strains for all stress states.

With reference to the work by Faria et al. [1] the following plastic evolution law is defined:

$$\dot{\boldsymbol{\varepsilon}}^{p} = \beta EH\left(\dot{d}\right)\frac{\left\langle \overline{\boldsymbol{\sigma}} : \dot{\boldsymbol{\varepsilon}} \right\rangle}{\overline{\boldsymbol{\sigma}} : \overline{\boldsymbol{\sigma}}}\mathbf{C}_0^{-1} : \overline{\boldsymbol{\sigma}} \tag{3.49}$$

where β is a plastic strain coefficient that is assumed as an input parameter of the model (i.e. it is assumed as a material characteristic). The range of this coefficient is $0 \le \beta \le 1$ where the value 0 has the meaning of neglecting plastic strain accumulation. Typical values of this coefficient for normal concrete ranges between 0.2 and 0.6. For more information about the determination of parameter β, the reader can refer to the work of Faria and Oliver[6]. Finally $\dot{d}$ is defined as:

$$\dot{d} = \dot{d}^{+} + \dot{d}^{-} \tag{3.50}$$

The effect of different values for β parameters in the concrete constitutive law is shown in Figure 3.5. Equation (3.49) is enhanced respect to previous works because

it considers that, according to experimental evidence, concrete exhibits an irreversible deformation also under tension stress states.

The idea behind this formulation is that the plastic strain rate is assumed to have the same direction of elastic strain tensor.

Defining:

$$a = \beta E H\left(\dot{d}\right)\frac{\left\langle \bar{\boldsymbol{\sigma}} : \dot{\boldsymbol{\varepsilon}} \right\rangle}{\bar{\boldsymbol{\sigma}} : \bar{\boldsymbol{\sigma}}} \tag{3.51}$$

relation (3.49) can be written as (3.35) which is repeated here for reader's convenience:

$$\dot{\boldsymbol{\varepsilon}}^{p} = a\boldsymbol{\varepsilon} = a\mathbf{C}_0^{-1} : \bar{\boldsymbol{\sigma}} \tag{3.35}$$

The MacAuley brackets enable to set a non-negative product $\bar{\boldsymbol{\sigma}} : \dot{\boldsymbol{\varepsilon}}$ ensuring that $a \geq 0$. The Heaviside function is introduced in order to cancel plastic strain accumulation during unloading or partial reloading. Indeed when at least one of the damage variables d^{+} or d^{-} is increasing, $H\left(\dot{d}\right) = 1$; on the other hand, when both damage variables are constant, it results $H\left(\dot{d}\right) = 0$ preventing the accumulation of plastic strain.

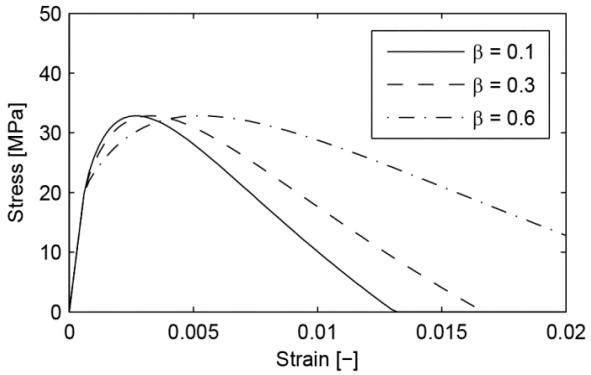

Figure 3.5 - Stress-strain curve for different values of β

It is clear that the proposed plastic strain evolution involves several simplifications relative to the "effective stress space plasticity" model [11] used to couple the damage evolution with the plastic flow. This simplification is in the spirit of obtaining an efficient model for large scale analyses without undue sacrifice of accuracy, as the validation tests will show. With this assumption the coupling between damage and plasticity is simplified, eliminating additional iterations during the material state determination process. A consequent limitation of the model is the inaccurate representation of concrete dilatancy which is observed in experimental tests where concrete subjected to compressive loads exhibits a volumetric expansion

after a certain level near the peak strength. Non-associated flow rules in plasticity models with suitable plastic potentials were proposed to proper represent the dilatancy of concrete. Thus, in cases in which dilatancy plays an important role in the response of the structural element a different plastic potential should be used with the proposed constitutive model.

3.4 Evolution of damage variables

The expansion of the damage surface is determined by the evolution of the damage thresholds by the following rate equations:

$$\dot{r}^{+} = \dot{\mu}\frac{\partial g}{\partial \bar{\tau}^{+}} \text{ and } \dot{r}^{-} = \dot{\mu}\frac{\partial g}{\partial \bar{\tau}^{-}} \tag{3.52}$$

where $\dot{\mu}$ is the damage consistency parameter. The relative Kuhn-Tucker conditions give [9]-[10]:

$$g \le 0 \qquad \dot{\mu} \ge 0 \qquad \dot{\mu} g = 0 \tag{3.53}$$

while the consistency condition is

$$\dot{\mu}\dot{g} = 0 \tag{3.54}$$

Similarly to previous works (e.g. [1], [2]) the following rate equations are considered to describe the evolution of damage variables:

$$\dot{d}^{+} = \dot{r}^{+}\frac{\partial G^{+}\left(\bar{\tau}^{+}\right)}{\partial \bar{\tau}^{+}} = \dot{\mu}\frac{\partial g}{\partial \bar{\tau}^{+}}\frac{\partial G^{+}\left(\bar{\tau}^{+}\right)}{\partial \bar{\tau}^{+}} \tag{3.55}$$

$$\dot{d}^{-} = \dot{r}^{-}\frac{\partial G^{-}\left(\bar{\tau}^{-}\right)}{\partial \bar{\tau}^{-}} = \dot{\mu}\frac{\partial g}{\partial \bar{\tau}^{-}}\frac{\partial G^{-}\left(\bar{\tau}^{-}\right)}{\partial \bar{\tau}^{-}} \tag{3.56}$$

where G^{+} and G^{-} are appropriate monotonically increasing functions that need to satisfy condition (3.14).

When $g < 0$, the last condition of equation (3.53) is satisfied only if $\dot{\mu} = 0$. This means, according to equations (3.52), that no damage surface evolution is possible and no damage increment can occur as it can be seen from equations (3.55)-(3.56).

When $\dot{\mu} > 0$ the damage surface evolves and from equations (3.55)-(3.56) at least one of the damage variables increases depending on the stress state. It is noteworthy that the quadratic form of the damage criterion assures independent evolution of the positive and negative damage thresholds for uniaxial tensile and compressive conditions, respectively. In fact, the partial derivatives of equations (3.52) are alternatively zero when either $\bar{\tau}^{+}$ or $\bar{\tau}^{-}$ is zero.

Under uniaxial tensile conditions the second of (3.52) is zero, the consistency condition is observed only if $\dot{g} = 0$, thus it is possible to write the following equation:

$$\frac{\partial g}{\partial \bar{\tau}^+} \dot{\bar{\tau}}^+ + \frac{\partial g}{\partial r^+} \dot{r}^+ = 0 \tag{3.57}$$

Substituting equation (3.46) in (3.57) one obtains:

$$\frac{2\bar{\tau}^+}{r^{+2}} \dot{\bar{\tau}}^+ - \frac{2\bar{\tau}^{+2}}{r^{+3}} \dot{r}^+ = 0 \tag{3.58}$$

$$\frac{2\bar{\tau}^{+2}}{r^{+3}} \dot{r}^+ = \frac{2\bar{\tau}^+}{r^{+2}} \dot{\bar{\tau}}^+ \tag{3.59}$$

$$\dot{r}^+ = \frac{2\bar{\tau}^+}{r^{+2}} \frac{r^{+3}}{2\bar{\tau}^+} \dot{\bar{\tau}}^+ \tag{3.60}$$

Which leads to the following:

$$\dot{d}^+ = \frac{r^+}{\bar{\tau}^+} \dot{\bar{\tau}}^+ \frac{\partial G^+\left(\bar{\tau}^+\right)}{\partial \bar{\tau}^+} = \frac{r^+}{\bar{\tau}^+} \dot{G}^+\left(\bar{\tau}^+\right) \geq 0 \tag{3.61}$$

In case of uniaxial compression, with the same procedure, it is possible to obtain:

$$\dot{d}^- = \frac{r^-}{\bar{\tau}^-} \dot{\bar{\tau}}^- \frac{\partial G^-\left(\bar{\tau}^-\right)}{\partial \bar{\tau}^-} = \frac{r^-}{\bar{\tau}^-} \dot{G}^-\left(\bar{\tau}^-\right) \geq 0 \tag{3.62}$$

Equations (3.61) and (3.62) demonstrate that the damage variables rate is non-negative ensuring that damage in the material can only increase.

3.5 Adopted damage and criteria evolution laws

For the present work, the following damage evolution laws are adopted:

$$d^+ = 1 - \left(\frac{r_0^+}{\bar{\tau}^+}\right)^{n^+} \cdot \exp\left(A^+ \cdot \left[1 - \left(\frac{\bar{\tau}^+}{r_0^+}\right)^{n^+}\right]\right) \tag{3.63}$$

$$d^- = 1 - \left(\frac{r_0^-}{\bar{\tau}^-}\right)^{n^-} \cdot \left(1 - A^-\right) - A^- \cdot \exp\left[B^- \cdot \left(1 - \left(\frac{\bar{\tau}^-}{r_0^-}\right)^{n^-}\right)\right] \tag{3.64}$$

where r_0^+, r_0^- are the initial damage thresholds; A^+, A^-, B^- are material parameters that control the shape of the constitutive law, n^+ and n^- are evaluated according to Table 3.1. Such a reformulation allows to obtain the same damage evolution law, i.e. the same uniaxial stress strain constitutive law, regardless the adopted proposal.

	n^+	n^-
Original Definition – [1]	1	1
Proposal A – equations (3.42)-(3.43)	1	0.5
Proposal B – equations (3.44)-(3.45)	2	1

Table 3.1 - Values for the exponents of the damage evolution laws

The expansion of the damage surface is determined by the evolution of the damage thresholds. The evolution of the threshold proposed in this work is reported in the following. The surface increments $\dot{r}^+$ and $\dot{r}^-$ are written in incremental form:

$$\dot{r}^+ = r^+_{n+1} - r^+_n \tag{3.65}$$

$$\dot{r}^- = r^-_{n+1} - r^-_n \tag{3.66}$$

where r^+_n and r^-_n represent the actual threshold of damage criteria and r^+_{n+1} and r^-_{n+1} represent the new threshold of the expanded damage surface.

As already shown equation (3.46) represents an ellipse in equivalent stress space. It is convenient to re-write it in a polar coordinates system (ρ, ϑ) (see Figure 3.6):

$$\rho^2 = \frac{\left(r^+_n\right)^2 \left(r^-_n\right)^2}{\left(r^-_n\right)^2 \sin^2\vartheta + \left(r^+_n\right)^2 \cos^2\vartheta} \tag{3.67}$$

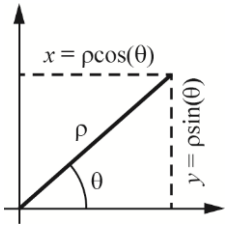

Figure 3.6 - Polar coordinates

The current stress point is represented by point *Q* in Figure 3.7, while point *P* indicates the intersection of $\overline{OQ}$ with the damage threshold. Denoting with $\alpha_s = \rho_Q / \rho_P > 1$ a scalar coefficient that measures how much the equivalent stress is outside of the current damage surface, the following updating rule for r^+_n and r^-_n is proposed in this work:

$$r^-_{n+1} = r^-_n \cdot \alpha^-_s \tag{3.68}$$

$$r^+_{n+1} = r^+_n \cdot \alpha^+_s \tag{3.69}$$

where α^+_s and α^-_s depend on the actual position of point Q. The following relations are proposed for α^+_s and α^-_s :

$$\begin{cases} \alpha_s^- = \dfrac{(\alpha_s - 1)}{(\rho_L - r_n^+)}(\rho_P - r_n^+) + 1 & \text{if} \quad \rho_P \le \rho_L \\ \alpha_s^+ = \dfrac{(\alpha_s - 1)}{(r_n^- - \rho_L)}(r_n^- - \rho_P) + 1 & \text{if} \quad \rho_P > \rho_L \end{cases} \tag{3.70}$$

where L represents the point where ellipse's normal has the same projection on $\bar{\tau}^+$ and $\bar{\tau}^-$. Coordinates of point L can be determined with the following relations:

$$\vartheta_L = \tan^{-1}\left(\frac{r_n^{+2}}{r_n^{-2}}\right) \tag{3.71}$$

$$\rho_L = \sqrt{\frac{(r_n^+)^2 (r_n^-)^2}{(r_n^-)^2 \sin^2 \vartheta_L + (r_n^+)^2 \cos^2 \vartheta_L}} \tag{3.72}$$

It can be easily seen that when $P \equiv L$ the surface expands in homothetic way. Indeed, according to equation (3.70), it results that $\alpha_s^+ = \alpha_s^- = \alpha_s$ and therefore, considering equations (3.68)-(3.69), the statement is demonstrated to be true.

The other equations needed to evaluate (3.68) and (3.69) are obtained forcing the new damage surface to honor point Q:

$$\begin{cases} \alpha_s^+ = \dfrac{1}{r_n^+}\sqrt{\dfrac{(r_n^- \alpha_s^-)^2 (\bar{\tau}_Q^+)^2}{(r_n^- \alpha_s^-)^2 - (\bar{\tau}_Q^-)^2}} & \text{if} \quad \rho_P \le \rho_L \\ \alpha_s^- = \dfrac{1}{r_n^-}\sqrt{\dfrac{(r_n^+ \alpha_s^+)^2 (\bar{\tau}_Q^+)^2}{(r_n^+ \alpha_s^+)^2 - (\bar{\tau}_Q^+)^2}} & \text{if} \quad \rho_P > \rho_L \end{cases} \tag{3.73}$$

A geometric representation is reported in Figure 3.7.

A pure shear test is simulated to test damage model behavior under tension-compression loads. In Figure 3.8 three different graphs are plotted. The evolution of damage surface in the equivalent stresses space is reported in Figure 3.8a, while Figure 3.8b and Figure 3.8c show the resulting stress-strain paths for compression and tension respectively. The bold blue line represents the damaged Cauchy stress, dashed green line the effective stress (elastic stresses) and finally the red and magenta curves represents the evolution of compressive damage and tensile damage respectively. It is evident that due to tension in one direction, compression strength along the other direction is reduced. In fact compression damage occurs as can be noted in Figure 3.8b and Figure 3.8c.

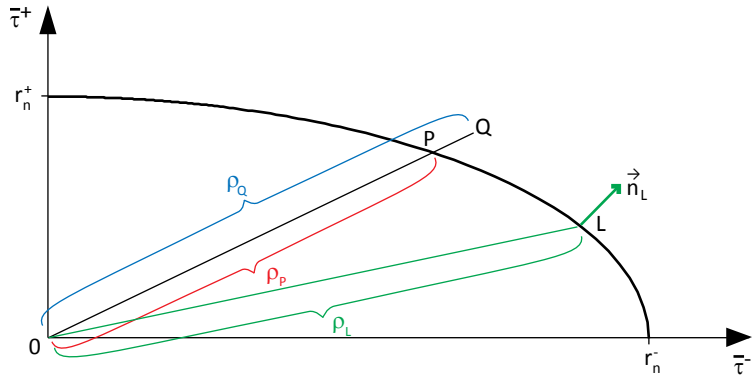

Figure 3.7 - Geometric representation of damage surface in equivalent stresses space

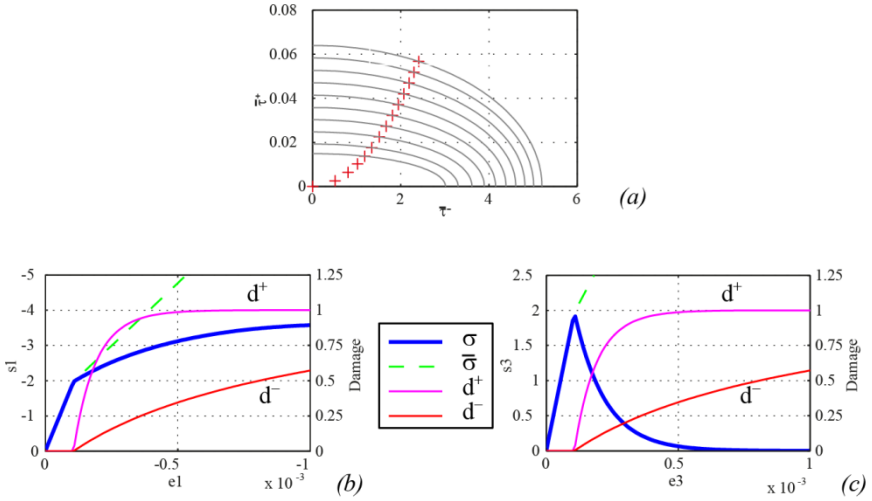

Figure 3.8 - Pure shear load condition; (a) Evolution of damage threshold in the equivalent stresses space; (b) stress-strain path along the principal compression direction; (c) stress-strain path along the principal tension direction

3.5.1 Parameters of damage evolution laws

The damage evolution laws (3.63) and (3.64) contain the material parameters r_0^+, r_0^-, A^+, A^- , B^-. The evaluation of these parameters is discussed in this section.

A uniaxial tensile test is sufficient to determine the parameters r_0^+ and A^+. In particular, being f_0^+ the uniaxial tensile strength of the specimen, for proposal A, equation (3.42) gives:

$$r_0^+ = f_0^+ \tag{3.74}$$

while for proposal B, the application of (3.44) leads to:

$$r_0^+ = \sqrt{f_0^+} \tag{3.75}$$

The parameter A^+ can be evaluated considering the specific dissipated energy on a uniaxial tensile test:

$$g_f^{(+)} = \int_0^\infty \sigma d\varepsilon \tag{3.76}$$

The evaluation is performed in the following for proposal A, but it can be easily demonstrated that is valid also for proposal B. Being the test a uniaxial process it follows that:

$$\varepsilon^e = \varepsilon(1-\beta) + \beta\varepsilon_0 \tag{3.77}$$

where ε_0 is the strain corresponding to the tensile limit f_0^+. Equation (3.42) gives:

$$\bar{\tau}^+ = \bar{\sigma} = E\varepsilon^e \tag{3.78}$$

The damage evolution law expressed in (3.63) is simplified according to following relation:

$$d^+ = 1 - \frac{\varepsilon_0}{\varepsilon_e}\exp\left(A^+\left(1-\frac{\varepsilon_e}{\varepsilon_0}\right)\right) \tag{3.79}$$

Thus, the integral in (3.76) can be solved:

$$\begin{aligned}
g_f^{(+)} &= \int_0^\infty \sigma d\varepsilon = \frac{1}{2} f_0^+ \varepsilon_0 + \int_{\varepsilon_0}^\infty \sigma d\varepsilon = \\
&= \frac{1}{2} f_0^+ \varepsilon_0 + \int_{\varepsilon_0}^\infty (1-d^+)\bar{\sigma} d\varepsilon = \frac{1}{2} f_0^+ \varepsilon_0 + \int_{\varepsilon_0}^\infty (1-d^+) E\varepsilon_e d\varepsilon = \\
&= \frac{1}{2} f_0^+ \varepsilon_0 + \int_{\varepsilon_0}^\infty \left(\frac{\varepsilon_0}{\varepsilon_e}\exp\left(A^+\left(1-\frac{\varepsilon_e}{\varepsilon_0}\right)\right)\right) E\varepsilon_e d\varepsilon = \\
&= \frac{1}{2} f_0^+ \varepsilon_0 + E\varepsilon_0 \int_{\varepsilon_0}^\infty \exp\left(A^+\left(1-\frac{\varepsilon_e}{\varepsilon_0}\right)\right) d\varepsilon = \\
&= \frac{1}{2} f_0^+ \varepsilon_0 + E\varepsilon_0 \int_{\varepsilon_0}^\infty \exp\left(A^+\left(1-\frac{\varepsilon_e}{\varepsilon_0}\right)\right) d\varepsilon = \\
&= \frac{1}{2} f_0^+ \varepsilon_0 + E\varepsilon_0 \int_{\varepsilon_0}^\infty \exp\left(A^+\left(1-\frac{\varepsilon(1-\beta)+\beta\varepsilon_0}{\varepsilon_0}\right)\right) d\varepsilon = \\
&= \frac{1}{2} f_0^+ \varepsilon_0 + E\varepsilon_0 \int_{\varepsilon_0}^\infty \exp\left(A^+\left(\frac{(\beta-1)(\varepsilon-\varepsilon_0)}{\varepsilon_0}\right)\right) d\varepsilon =
\end{aligned} \tag{3.80}$$

$$= \frac{1}{2} f_0^+ \varepsilon_0 + \frac{E\varepsilon_0{}^2}{A^+(\beta-1)} \left[\exp\left(A^+ \left(\frac{(\beta-1)(\varepsilon-\varepsilon_0)}{\varepsilon_0} \right) \right) \right]_{\varepsilon_0}^{\infty} =$$

$$= \frac{1}{2} f_0^+ \varepsilon_0 + \frac{E\varepsilon_0{}^2}{A^+(1-\beta)} = \frac{f_0^{+2}}{E} \left(\frac{1}{2} + \frac{1}{A^+(1-\beta)} \right)$$

which leads to:

$$A^+ = \left[(1-\beta) \left(\frac{g_f^{(+)} E}{f_0^{+2}} - \frac{1}{2} \right) \right]^{-1} \tag{3.81}$$

In this way the parameter A^+ is related to the specific dissipated energy on a uniaxial tensile test.

The definition of the parameters r_0^-, A^- and B^- that characterize the compressive damage evolution law requests a uniaxial compressive test.

The parameter r_0^- is easily determined applying equation (3.43) for proposal A and (3.45) for proposal B, obtaining respectively:

$$r_0^+ = \frac{\left(K-\sqrt{2}\right)}{\sqrt{3}} f_{0,1d}^- \tag{3.82}$$

$$r_0^+ = \sqrt{\frac{\left(K-\sqrt{2}\right)}{\sqrt{3}} f_{0,1d}^-} \tag{3.83}$$

The elastic limit in uniaxial compression $f_{0,1d}^-$ is evaluated in this work with the following:

$$f_{0,1d}^- = n \cdot f_c \tag{3.84}$$

where f_c is the compressive strength of concrete and n is generally assumed to vary between 0.5 and 0.7.

The determination of parameters A^- and B^- is not straightforward because they don't have a precise physical meaning. In [6] the authors proposed a numerical procedure in which they impose that the constitutive law satisfies two selected points of a uniaxial compressive test. In particular point 1 is characterized by Cauchy stress σ_1, strain ε_1, effective stress $\bar{\sigma}_1$ and equivalent stress $\bar{\tau}_1^-$. Similarly, point 2 is characterized by σ_2, ε_2, $\bar{\sigma}_2$ and $\bar{\tau}_2^-$. The satisfaction of the two selected points is represented by the following system of two non-linear equations:

$$\begin{cases} \sigma_1 = \left\{ \dfrac{r_0^-}{\bar{\tau}_1^-}\left(1-A^-\right) + A^- \cdot \exp\left[B^- \cdot \left(1 - \left(\dfrac{\bar{\tau}_1^-}{r_0^-} \right)^{n^-} \right) \right] \right\} \bar{\sigma}_1 \\ \sigma_2 = \left\{ \dfrac{r_0^-}{\bar{\tau}_2^-}\left(1-A^-\right) + A^- \cdot \exp\left[B^- \cdot \left(1 - \left(\dfrac{\bar{\tau}_2^-}{r_0^-} \right)^{n^-} \right) \right] \right\} \bar{\sigma}_2 \end{cases} \tag{3.85}$$

This system can be solved by numerical methods like a Newton-Raphson iterative method to obtain the values of the two parameters.

He main drawback of this method is that it is not related to fracture energy in compression (crushing energy) and thus the model may suffer of mesh in-objectivity. To prevent this problem, in this work is proposed a procedure that correlate the two parameters A^- and B^- with the crushing energy. This is reported in 3.7.2.

3.6 Shear retention factor

The presented damage model does not take into account some of the shear mechanisms that experimentally were observed in reinforced concrete beams. Indeed most design codes include the secondary shear transfer mechanisms. Among these mechanisms, the arch mechanism and the concrete cantilevers mechanism are considered implicitly by the damage model, while dowel action and aggregate interlock are not considered by the model [12].

Similarly to smeared crack models (see 2.3.2), a shear retention factor was proposed for the one-parameter scalar damage model (Scotta et al. [12]). This approach is simple and computational efficient and permits to take into account in a phenomenological way the shear resistant mechanisms not considered by the damage model. The stiffness matrix of the material is then modified and the constitutive law can be written according to:

$$\sigma_{ij} = \left[1 - d + \left(1 - \delta_{ij}\delta_{kl} \right) \beta_s d \right] C^0_{ijkl} \varepsilon_{kl} \tag{3.86}$$

In [12] the authors shown how a constant shear retention factor is a too crude approximation and the strength of the structure may be overestimated. Indeed, as stated in 2.3.2 for smeared crack models, a constant shear retention factor means that a shear stress can be transferred across a wide open crack which seems an unrealistic condition. For this reason the authors proposed a linear evolution law for the shear retention factor:

$$\beta_{s,ij} = 1 - \left| \frac{\varepsilon_{ij}}{\varepsilon_{ref}} \right| \geq 0 \qquad i \neq j \tag{3.87}$$

where ε_{ij} is the shear deformation and ε_{ref} is a reference shear deformation value that need to be provided as input parameter for the material. This parameter can be determined through calibration comparing numerical and experimental results.

In this work this concept was adopted and extended to the two-parameters scalar damage model proposed. The modified constitutive law reads:

$$\begin{aligned} \sigma_{ij} &= \left[1 - d^{+} + \left(1 - \delta_{ij}\delta_{kl}\right)\beta_{s,ij}^{+} d^{+}\right]\overline{\sigma}_{ij}^{+} + \left[1 - d^{-} + \left(1 - \delta_{ij}\delta_{kl}\right)\beta_{s,ij}^{-} d^{-}\right]\overline{\sigma}_{ij}^{-} \\ \sigma_{ij} &= \left[1 - d^{+} + \left(1 - \delta_{ij}\delta_{kl}\right)\beta_{s,ij}^{+} d^{+}\right]P_{ijmn}^{+} C_{mnkl}^{0} \varepsilon_{kl}^{e} + \\ &+ \left[1 - d^{-} + \left(1 - \delta_{ij}\delta_{kl}\right)\beta_{s,ij}^{-} d^{-}\right]P_{ijmn}^{-} C_{mnkl}^{0} \varepsilon_{kl}^{e} \end{aligned} \tag{3.88}$$

where two shear retention factors $\beta^{+}_{s,ij}$ and $\beta^{-}_{s,ij}$ are introduced respectively for the positive and the negative parts of the effective stress tensor. In some of the simulations presented in this work the negative shear retention factor $\beta^{-}_{s,ij}$ is assumed equal to zero relating the shear retention factor only to the positive part of the effective stress and thus affecting only the positive damage parameter for shear stresses.

According to this formulation, for normal stresses (i.e. when $i=j$ and $k=l$), the constitutive law is unaffected by shear retention factor:

$$\sigma_{ij} = \left(1 - d^{+}\right)\overline{\sigma}_{ij}^{+} + \left(1 - d^{-}\right)\overline{\sigma}_{ij}^{-} \tag{3.89}$$

On the other hand, for shear stresses (3.90) leads to a reduction of damage effect in order to consider a residual shear strength even for a completely damaged material. Indeed when $d^{+} = d^{-} = 1$, $i \neq j$ and $k \neq l$, the following is valid:

$$\sigma_{ij} = \beta_{s,ij}^{+}\overline{\sigma}_{ij}^{+} + \beta_{s,ij}^{-}\overline{\sigma}_{ij}^{-} \tag{3.90}$$

To date, the shear retention factor represent an artificial remedy to the deficiency of the model in capturing some of shear-resisting mechanisms. From the energetic point of view, the introduction of the shear retention factor implies a greater storage of free energy as pointed out in [12].

Further research is needed; in particular a deeper investigation on the effects of shear retention factor and on the possible correlation with the physical quantities that governs the shear-resistance mechanisms not considered implicitly by the mechanical damage model. In particular the dowel action should depended mainly on the diameter and distribution of the reinforcing steel bars, while the aggregate interlock mechanism should depend among others on the aggregate size and the crack opening.

3.7 Strain localization and mesh objectivity

As already shown in previous chapter, the assumption of a constitutive law characterized by a softening branch, leads to problems of mesh-dependency because strain localizes in a limited number of elements.

In the present work this mesh-dependency was partially overcome with a mesh-adjusted softening module called also “fracture energy regularization technique”. In particular, within this approach the fracture energy G_f is introduced as a material property and the constitutive law parameters depend on element size which is assumed representative of the effective length of the crack band (e.g. [13], [14], [15], [16]).

3.7.1 Tension

3.7.1.1 Adjusted softened modulus method

The parameter A^+ was correlated to the specific dissipated energy in 3.5.1. Within a finite element framework with a local formulation, the specific fracture energy is related to the fracture energy G_f of the material and to a characteristic length $l_c^{(e)}$ dependent on the geometrical dimension of each element used in the mesh:

$$g_f = \frac{G_f}{l_c^{(e)}} \tag{3.91}$$

substitution of (3.91) into (3.81) leads to the following expression:

$$A^+ = \left[(1-\beta)\left(\frac{G_f E}{l_c^{(e)} f_0^{+2}} - \frac{1}{2} \right) \right]^{-1} \tag{3.92}$$

In the present work the following expression for $l_c^{(e)}$ is adopted in case of three-dimensional elements:

$$l_c^{(e)} = \sqrt[3]{V^{(e)}} \tag{3.93}$$

and in case of two-dimensional elements:

$$l_c^{(e)} = \sqrt{A^{(2)}} \tag{3.94}$$

where $V^{(e)}$ and $A^{(e)}$ are the element volume and area respectively.

With such an approach, the positiveness condition for parameter A^+ leads to a limitation of finite element’s size according to the following expression:

$$l_c^{(e)} < \frac{2G_f E}{f_0^{+2}} \tag{3.95}$$

The adoption of such a technique of regularization makes the structural response less sensitive with regard to mesh refinement in terms of global response (e.g. load-displacement curve).

3.7.1.2 Numerical application: panel subjected to uniaxial tension

In the following a numerical application is reported to show the ability of the proposed procedure to obtain a mesh-independent global response in terms of dissipated energy.

A panel whose geometry is reported in Figure 3.9 is subjected to a uniaxial tensile condition. The specimen was simulated with two different discretizations: a mesh of 1 element and a mesh of 4x4 elements. Model parameters are reported in Table 3.2. Finally an imperfection was introduced in a finite element (represented with shaded area in Figure 3.9) by means of a 1% reduction of tensile strength.

As it can be seen from Figure 3.9, the global force-displacement curves are independent on the chosen discretization which ensures the same energy dissipation.

In Figure 3.10 (a) and (b) are reported the positive damage contours for the two different discretization. It is worth noting that the technique adopted doesn't solve entirely the problem of strain localization: indeed the strain localizes in a very narrow band. For the aims of the present work it is an acceptable simplification since it's a straightforward method with an high computational efficiency and thus it seems a reasonable compromise for the analysis of large structures.

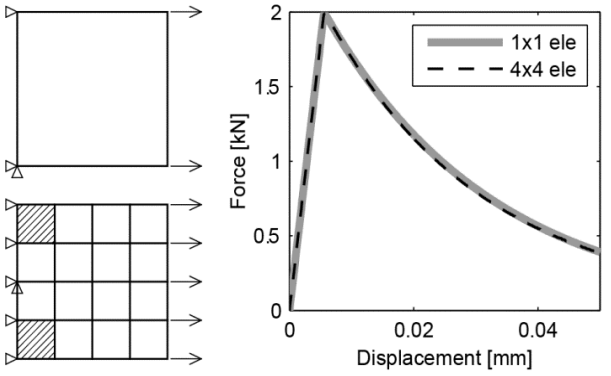

Figure 3.9 - Load–displacement curves in tension for different level of mesh refinement

Description	Symbol	Value
Young Modulus	E	36000 MPa
Poisson ration	ν	0.15
Tensile strength	f_t	2.0 MPa
Plasticity factor	β	0.3
Fracture energy	G_f	60 N/m

Table 3.2 - Material characteristics assumed

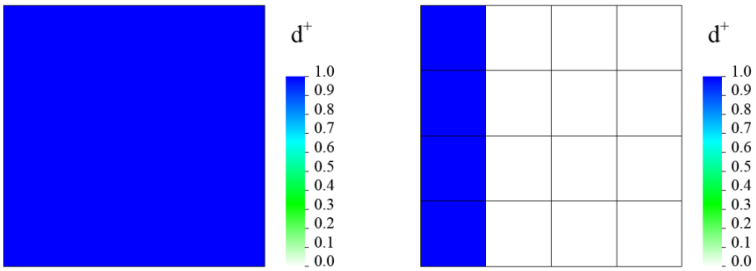

(a) (b)

Figure 3.10 - Positive damage contour for specimen subjected to tension. (a) 1 element mesh; (b) 4x4 elements mesh

3.7.2 Compression

3.7.2.1 Adjusted softened modulus method

It is widely accepted that strain localization mainly affects tensile behavior of quasi-brittle materials. For this reason a lot of researchers adopt regularization techniques only concerning behavior of materials under tensile load conditions.

As already shown in previous chapter, strain localization affects also behavior under compressive load. Some researchers introduced the concept of compressive fracture energy, also called by other researchers crushing energy, and proposed a similar approach to the one adopted in tension for the softening behavior of concrete loaded in compression, e.g. Comi and Perego [15], Feenstra and de Borst [16], Feenstra [17].

With such an approach, Feenstra [17], Feenstra and de Borst [16] adopted a parabolic constitutive law in compression expressed as function of the specific crushing energy in analogy with the softening modulus adjustment in tension:

$$g_c = \frac{G_c}{l_c^{(e)}} \tag{3.96}$$

which represents the area under the stress-strain curve after the peak strength (Figure 3.11).

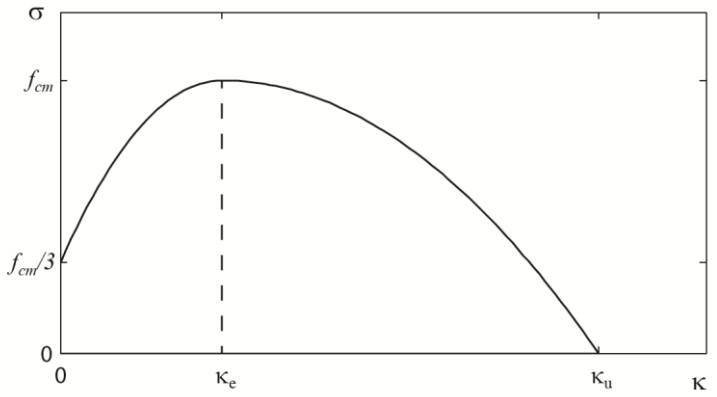

Figure 3.11 - Compression softening model adopted by Feenstra [17]

In the present work a similar procedure is adopted. The shape of the constitutive law is determined by the values of two parameters as already shown previously: A^- and B^- which need to be related to the specific crushing energy g_c to partially overcome the mesh-dependency problem also in compression load condition.

Due to the complicated expression of d^- it is not possible to find a closed-form relation that takes into account the dependency of specific crushing energy. The basic equations that are considered are reported in the following system:

$$\begin{cases} f_{c1d} = \sigma\left(\varepsilon_{c1d}\right) & \text{peak evaluation} \\ \left.\dfrac{\partial\sigma}{\partial\varepsilon}\right|_{\varepsilon=\varepsilon_{c1d}} = 0 & \text{peak evaluation} \\ \sigma\left(\varepsilon_u\right) = 0 & \text{evaluation of } \varepsilon_u \\ \displaystyle\int_{\varepsilon_{c1d}}^{\varepsilon_u} \sigma(\varepsilon)d\varepsilon + \frac{1}{2} f_{c1d}\varepsilon_{c1d}^e = g_c & \text{crusching energy} \end{cases} \tag{3.97}$$

where f_{c1d} is uniaxial compressive strength of concrete, ε_{c1d} is the corresponding strain, ε_u is the strain at which the stress vanishes and ε_{c1d}^e is the elastic strain corresponding to the strength f_{c1d}. The first equation relates peak stress with peak strength, the second equation represent the condition of null derivative for $\varepsilon = \varepsilon_{c1d}$. It is worth noting that the first equation alone is not sufficient to constrain the strength of the constitutive law. In fact the first equation simply assures that the function passes through the point $(\varepsilon_{c1d}, f_{c1d})$ while the combination with the third equation assures that the point is a global maximum point. It will be shown shortly that operating in this way the peak point may move exhibiting different peak strains

ε_{c1d}. The third equation of the system is needed to evaluate the strain ε_u and can be also written as:

$$d^-(\varepsilon_u) = 1 \tag{3.98}$$

Finally the fourth equation represent the specific fracture energy of the constitutive law that is imposed to be equal to g_c which is evaluated according to ([16]):

$$g_c = \frac{G_c}{l_c^{(e)}} \tag{3.99}$$

G_c can be evaluated from experimental results of a compressive uniaxial test with a stable softening branch (e.g. [18], [19], [20]). In [17] the author reported that a reasonable relation between fracture energy and crushing energy is expressed by the following range:

$$G_c \approx (50 \div 100) G_f \tag{3.100}$$

Considering the experimental evidences reported by Karsan and Jirsa [24], the crushing fracture energy is related to the compressive strength. Thus the following relation is proposed:

$$G_c = 495 \frac{f_{c1d}^{\ 2}}{E} \tag{3.101}$$

The system of non-linear equations is solved with a Newton-Raphson algorithm obtaining finally the constitutive law parameters. More details can be found in Appendix A.

3.7.2.2 Numerical application: specimen subjected to uniaxial compression

A simple numerical example is reported to clarify the concepts reported in the previous paragraph.

Similarly to the experimental tests reported in [18], three uniaxial compression tests on different height cylinders were simulated (Figure 3.12). Material characteristics assumed are reported in Table 3.3. The specimens were simulated with one plane stress 4-node quad thus leading to the characteristic element lengths $l_c^{(e)}$ reported in Table 3.4.

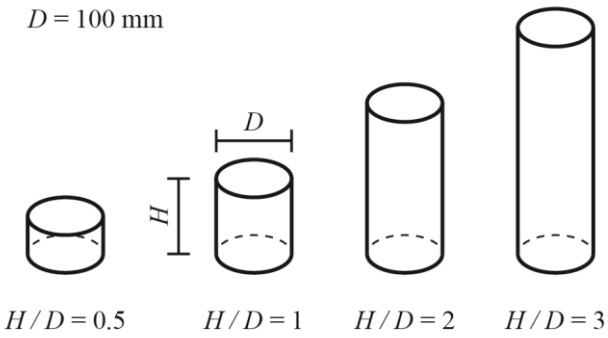

Figure 3.12 - Concrete specimens with different heights

Description	Symbol	Value
Young Modulus	E	33000 MPa
Poisson ration	ν	0.0
Compressive strength	f_c	-37.6 MPa
Elastic limit in compression	f_{01d}	0.65fc
Plasticity factor	β	0.3

Table 3.3 - Material characteristics assumed

Specimen n.	Height (H) [mm]	$l_c^{(e)}$ [mm]
1	50	50
2	100	100
3	200	200
4	300	300

Table 3.4 - Geometrical characteristics of different specimens

The constitutive law for concrete proposed in Model Code 1990 [21] is considered to calibrate the proposed model (Figure 3.13a):

$$\sigma = -\frac{\dfrac{E_{ci}}{E_{c1}}\dfrac{\varepsilon}{\varepsilon_{c1}} - \left(\dfrac{\varepsilon}{\varepsilon_{c1}}\right)^2}{1+\left(\dfrac{E_{ci}}{E_{c1}}-2\right)\dfrac{\varepsilon}{\varepsilon_{c1}}} f_{cm} \qquad |\varepsilon| < |\varepsilon_{c,\lim}| \qquad (3.102)$$

$$\sigma = -\left[\left(\frac{1}{\varepsilon_{c,\lim}/\varepsilon_{c1}}\xi - \frac{2}{\left(\varepsilon_{c,\lim}/\varepsilon_{c1}\right)^2}\right)\left(\frac{\varepsilon_c}{\varepsilon_{c1}}\right)^2 + \left(\frac{4}{\varepsilon_{c,\lim}/\varepsilon_{c1}} - \xi\right)\frac{\varepsilon_c}{\varepsilon_{c1}}\right]^{-1} f_{cm} \qquad |\varepsilon| > |\varepsilon_{c,\lim}| \qquad (3.103)$$

where f_{cm} is the mean strength of concrete, E_{ci} is the tangent elastic modulus, ε_{c1}= –0.0022 , E_{c1}= f_{cm}/ε_{c1} is the secant modulus from the origin to the peak, $\varepsilon_{c,\lim}$ is the strain corresponding to $\sigma_{c,\lim} = 0.5 f_{cm}$, and with:

$$\xi = \frac{4\left[\left(\frac{\varepsilon_{c,\lim}}{\varepsilon_{c1}}\right)^2\left(\frac{E_{ci}}{E_{c1}}-2\right)+2\frac{\varepsilon_{c,\lim}}{\varepsilon_{c1}}-\frac{E_{ci}}{E_{c1}}\right]}{\left[\frac{\varepsilon_{c,\lim}}{\varepsilon_{c1}}\left(\frac{E_{ci}}{E_{c1}}-2\right)+1\right]} \tag{3.104}$$

As well known this law is valid for 200 mm cylinders. It was used to calculate the crushing energy as the integral evaluated on the stress-strain curve according to different hypotheses times the height of the specimen. Firstly it was considered a non-linear elastic behavior in which the unloading path is identical to loading path. Under such an hypothesis, the crushing energy is represented by the shaded area in Figure 3.13b and is equal to $G_{c0} = 25273\text{N/m}$. In Figure 3.13c is reported in shaded area the crushing energy evaluated with the assumption of an unload path with secant elastic modulus for which the result is $G_{c1} = 22502\text{N/m}$. Finally it can be assumed an unload with initial elastic modulus; the corresponding crushing energy is $G_{c2} = 18459\text{N/m}$ and is shaded in Figure 3.13d.

Applying the equation (3.101) it was obtained a value of $G_c = 21206\text{N/m}$ which is in reasonable accordance to the previously obtained value.

For each test the parameters of the constitutive damage law were obtained solving the system of non-linear equations reported in (3.97). The values obtained are reported in Table 3.5.

The results obtained in term of stress-strain curves are reported in Figure 3.14. It can be seen that, in accordance with previous researches (e.g. [18], [20]), the descending branch of the stress-strain curves is strongly dependent on the size of the specimen. It is worth noting that, due to the chosen law for damage evolution, the calibration of parameters discussed previously leads to a slight modification of the pre-peak behavior of specimen. As it will be shown shortly, this problem makes less effective the proposed procedure to reduce mesh sensitivity in compression.

Specimen n.	A^-	B^-
1	1.2	0.904
2	2.2	0.821
3	6.0	0.803
4	12.3	0.826

Table 3.5- Parameters of constitutive law obtained for different specimens

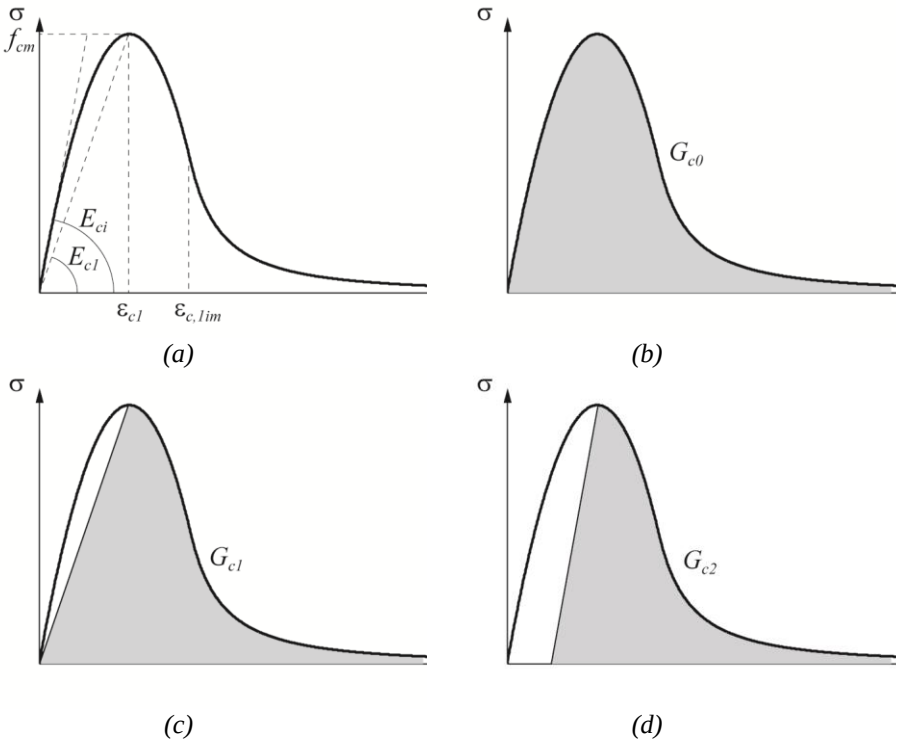

Figure 3.13 - (a) Stress-strain relation according to Model Code 1990 [21]; Crushing energy under: (b) hypothesis 0; (c) hypothesis ;, (d) hypothesis 2

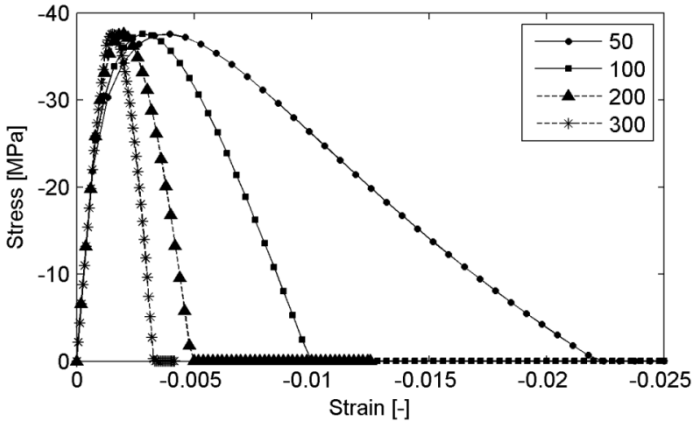

Figure 3.14 - Stress-strain curves for different specimens

Introducing the post-peak displacement δ_p defined as (Figure 3.15a):

$$\delta_{pp} = \varepsilon_{pp} \cdot H = \left(\varepsilon - \varepsilon_{c1d} + \frac{f_{c1d} - \sigma}{E_d} \right) \cdot H \tag{3.105}$$

where E_d is the damaged elastic modulus $E\left(1-d^{-}\right)$ and H is the height of the cylinder, the crushing energy is equal to the integral under stress-δ_{pp} curve (Figure 3.15b). In Figure 3.16 are reported the results in terms of stress-δ_{pp} curves for the analyzed tests. It can be seen, in accordance to previous researches that the differences in post-peak behavior for specimens with different sizes almost disappear completely, i.e. the crushing energy is the same independently from the element size, while the specific crushing energy is sensibly different for different sizes of elements.

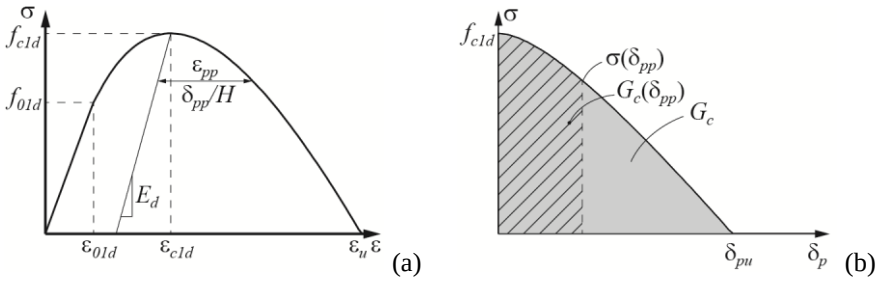

Figure 3.15 – (a) Stress-strain curve and (b) corresponding stress-δ_p curve

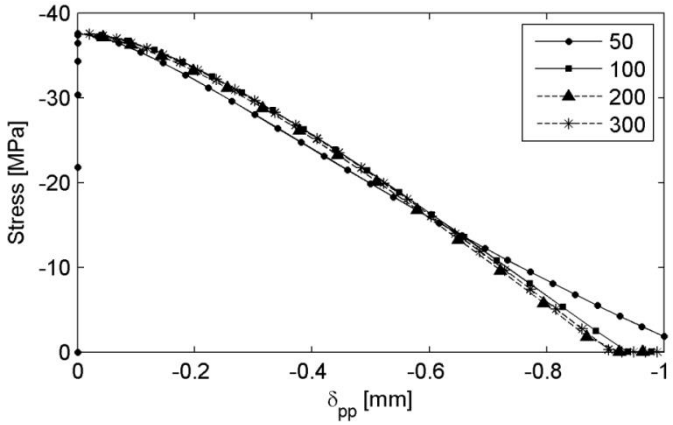

Figure 3.16 - Force-displacement for different specimens

A second application regarded the simulation of the uniaxial compression test on the 200 mm height specimen with different discretization. In particular the specimen was discretized with 1 element, 2 elements, 4 elements and 8 elements.

With such models strain localization on one element is expected thus an imperfection was applied to one element reducing by 1% the elastic modulus. In those elements localization will appear.

In Figure 3.17 are reported the negative damage contour for the different discretization and the deformed mesh in which it is possible to see the effect of strain localization. In particular, for the 8-elements specimen, the effect of discretization is evident also in Figure 3.18 in which the stress-strain curves corresponding to different elements is reported. As it can be seen, in element 2 there is a strain accumulation and the response of it follows the complete strain-softening branch, while the other elements unload elastically.

In Figure 3.19 the mean-stress mean-strain curves for different discretization are reported. The global response is less size-sensitive at least in terms of dissipated energy. As evidenced previously, the main reason for the slight difference of the curves is that the proposed procedure guarantees some key characteristics of the constitutive law like crushing energy and peak strength but doesn't guarantee the peak strain which can be sensibly different with different characteristic lengths (Figure 3.14). This is a limit of the present negative damage evolution function which could be overcome only defining a new damage evolution law. Indeed the same test performed with a Kent-Park law with linear softening for concrete permits to change the post-peak slope without affecting the pre-peak part of the curve. This leads to the results reported in Figure 3.20 in which is shown an almost complete independence between global response (thus dissipated energy) and mesh size.

Finally in Figure 3.21 the results of the same test without any regularization are reported. Comparing them with those reported in Figure 3.19 it is clear that the proposed procedure, although quite simple, is extremely important for the solution of strain localization problems in compression.

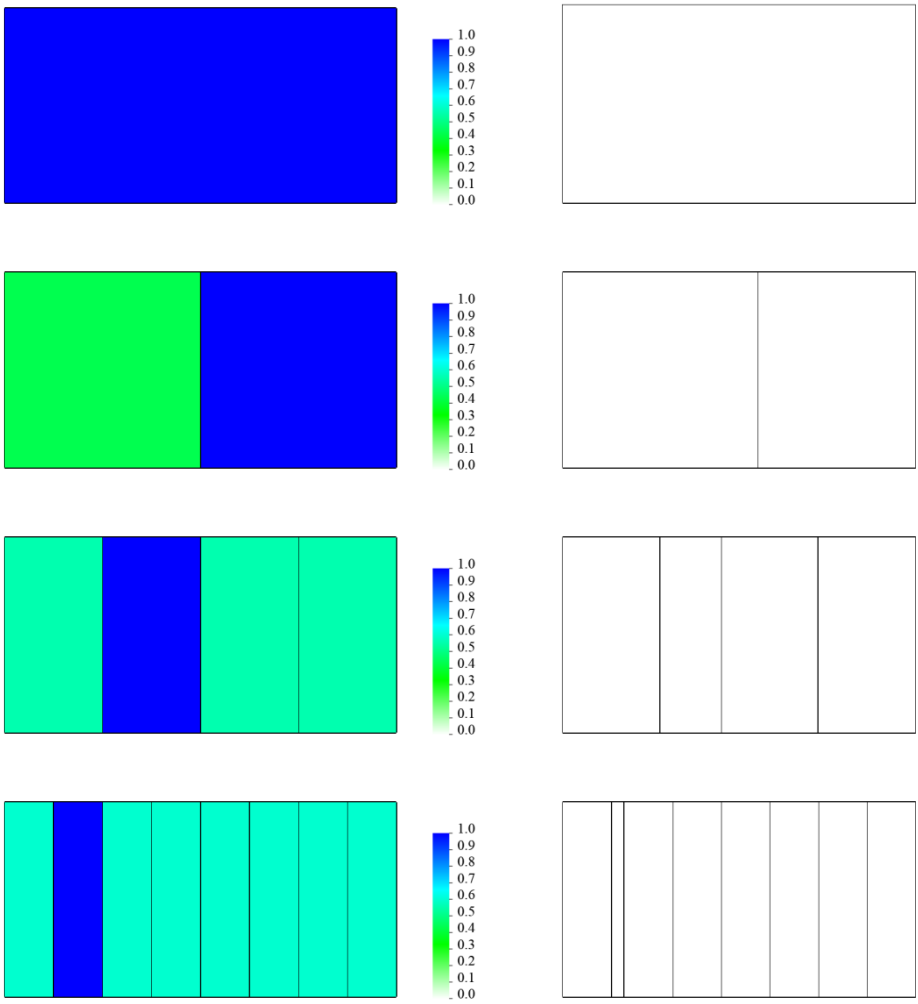

Figure 3.17 - Negative damage contour and deformed shape for different discretization

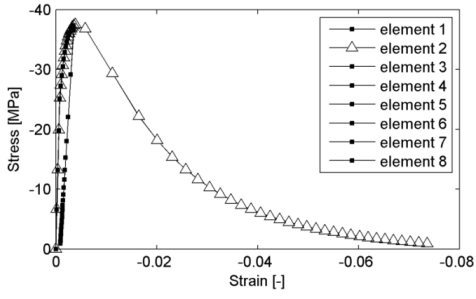

Figure 3.18 - Stress-strain curves for elements of 8-element discretization

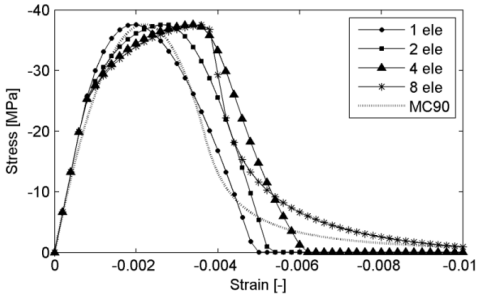

Figure 3.19 - Mean-stress-mean-strain curves for each discretization

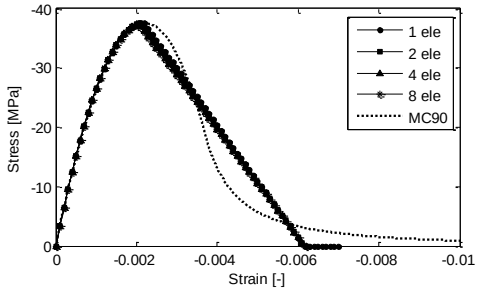

Figure 3.20 - Mean-stress-mean-strain curves for each discretization with Kent-Park model

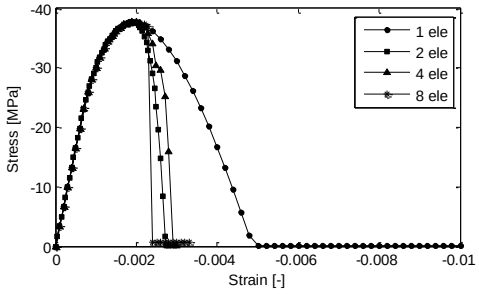

Figure 3.21 - Mean-stress-mean-strain curves for each discretization without any regularization

3.8 Basic concepts on the integration algorithm

The concrete material state determination makes use of the return-map algorithm for classical plasticity [22] and is, therefore, quite straightforward.

The total strain is updated for the given incremental displacement field:

$$\boldsymbol{\varepsilon}_{n+1} = \boldsymbol{\varepsilon}_n + \nabla^s(\Delta \mathbf{u}) \tag{3.106}$$

And the trial elastic state is computed as:

$$\bar{\boldsymbol{\sigma}}_{n+1}^{trial} = \mathbf{C}_0 : (\boldsymbol{\varepsilon}_{n+1} - \boldsymbol{\varepsilon}_n^p) \tag{3.107}$$

If the plastic-damage criterion expressed by equation (3.46) is satisfied, there is no evolution of plastic strain, damage thresholds or damage parameters, leading to the following:

$$\boldsymbol{\varepsilon}_{n+1}^p = \boldsymbol{\varepsilon}_n^p \tag{3.108}$$

$$\mathbf{r}_{n+1} = \mathbf{r}_n \tag{3.109}$$

$$\mathbf{d}_{n+1} = \mathbf{d}_n \tag{3.110}$$

where the vectors $\mathbf{r} = (r^+, r^-)^{\mathrm{T}}$ and $\mathbf{d} = (d^+, d^-)^{\mathrm{T}}$ are defined.

Consequently, the trial effective stress becomes the actual stress:

$$\bar{\boldsymbol{\sigma}}_{n+1} = \bar{\boldsymbol{\sigma}}_{n+1}^{trial} \tag{3.111}$$

If the plastic-damage criterion expressed by equation (3.46) is violated, the return-map algorithm is used to update the effective stress, the plastic strain and the plastic-damage thresholds according to the following relations:

$$\bar{\boldsymbol{\sigma}}_{n+1} = \alpha \bar{\boldsymbol{\sigma}}_{n+1}^{trial} \tag{3.112}$$

$$\alpha = 1 - \beta E \frac{\left\langle \mathbf{l}_{\bar{\boldsymbol{\sigma}}_{n+1}^{trial}} : \Delta\boldsymbol{\varepsilon} \right\rangle}{\left\| \bar{\boldsymbol{\sigma}}_{n+1}^{trial} \right\|} \tag{3.113}$$

$$\boldsymbol{\varepsilon}_{n+1}^p = \boldsymbol{\varepsilon}_n^p + \beta E \frac{\left\langle \mathbf{l}_{\bar{\boldsymbol{\sigma}}_{n+1}^{trial}} : \Delta\boldsymbol{\varepsilon} \right\rangle}{\left\| \bar{\boldsymbol{\sigma}}_{n+1}^{trial} \right\|} \mathbf{C}_0^{-1} : \bar{\boldsymbol{\sigma}}_{n+1} \tag{3.114}$$

$$g\left(\bar{\boldsymbol{\tau}}_{n+1}, \mathbf{r}_{n+1}\right) = 0 \tag{3.115}$$

where the vector $\bar{\boldsymbol{\tau}} = (\bar{\tau}^+, \bar{\tau}^-)^{\mathrm{T}}$ is defined.

The numerical algorithm is fast since it doesn't require iterations in the determination of the material state but it reduces to a two-step procedure: calculation of the predictor tensor and evaluation of the scale factor for returning to the damage-plasticity criteria.

Afterwards, the damage parameters can be calculated directly:

$$\mathbf{d}_{n+1} = \mathbf{d}_{n+1}(\mathbf{r}_{n+1}, \mathbf{r}_0) \tag{3.116}$$

Once the damage parameters are updated, the Cauchy stress is determined from:

$$\boldsymbol{\sigma}_{n+1} = (\mathbf{I} - \mathbf{D}_{n+1}) : \bar{\boldsymbol{\sigma}}_{n+1} \tag{3.117}$$

3.9 Validation tests

The ability of the proposed model to simulate the 1D and 2D behavior of concrete under tensile and compressive cyclic loading is studied comparing analytical response with experimental results. These tests are also useful for the calibration of the plastic strain coefficient, which is the only available parameter after the selection of material parameters.

3.9.1 Cyclic uniaxial compression test

Experiment AC2-09 by Karsan and Jirsa [24] is selected for the simulation of the cyclic uniaxial compression behavior. The cylindrical concrete compressive strength is f_c = 23.5 MPa. The model parameters are listed in Table 3.6 where the symbol ε_c stands for the total concrete strain corresponding to the compressive cylinder strength.

Description	Symbol	Value
Compressive strength	f_c	-23.5 MPa
Elastic limit in compression	f_{01d}	0.55fc
Plasticity factor	β	0.5
Normalized Young Modulus	$E\varepsilon_c/(2f_c)$	1.05

Table 3.6 - Material characteristics assumed

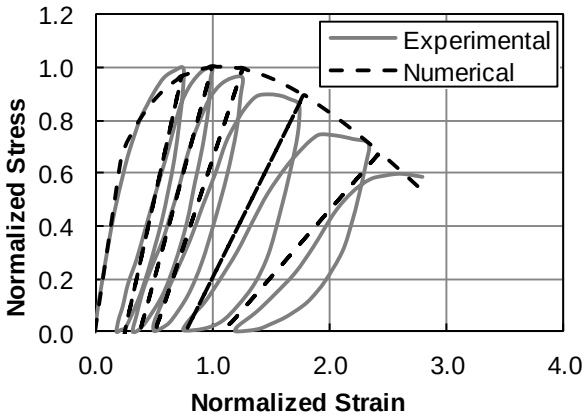

Figure 3.22 - Comparison of numerical and experimental results for cyclic uniaxial test

The numerical stress-strain response is compared with the experimental measurements in Figure 3.22. The overall nonlinear behavior of the specimen is represented well. The numerical envelope describes a linear elastic path followed by hardening and then softening response. The unloading and reloading branches are characterized by progressive damage and the evolution of plastic strain. In fact, the stiffness reduction is related to the value of compressive damage, while the residual strain depends on the plastic strain accumulation for each cycle.

The hysteresis of the reloading loop cannot be represented by the model because of the rate-independent elastic unloading/reloading assumption, but the progressive degradation of secant modulus fits the experimental curves on average well. This representation is sufficiently accurate for the simulation of large scale structures.

3.9.2 Cyclic uniaxial tension test

The second validation test regards a concrete specimen subjected to cyclic uniaxial load conditions. The comparison between experimental data by Gopalaratnam and Shah [25] and numerical results is illustrated in Figure 3.23. The tensile strength of concrete is f_t = 3.5 MPa, while the plastic factor β is assumed equal to 0.5. The stiffness degradation and the residual strains at each unloading/reloading cycle are represented well confirming the ability of damage parameter and plastic strain variable to capture the physical behavior.

It is worth noting that the residual strains in tension are very important for the simulation of the cyclic local and global response of reinforced concrete membranes under shear, because they influence the crack closure at loading reversals.

Another consideration that can be drawn is that a difference in the post-peak tension envelope between the model and the experimental data is quite evident, meaning that the fracture energy is overestimated. It should be pointed out that the descending branch experimentally obtained is not perfectly representable with the exponential damage evolution adopted in the present work. As it can be seen in Figure 3.23 the initial softening slope is almost vertical. Furthermore the selected response seems to be a good compromise between the envelope descending branch and the accumulation of residual strains.

3.9.3 Tests under biaxial load conditions

3.9.3.1 Four Biaxial tensile-compressive tests

Four concrete specimens were subjected to different load conditions up to failure by Kupfer et al. [26]. The third principal stress was kept in all cases equal to zero (σ_3 =

0), while the other two principal stresses were incremented to failure by maintaining the following ratios: (1) σ_1/σ_2 = - 1/0, (2) σ_1/σ_2 = - 1/0.052, (3) σ_1/σ_2 = - 1/0.103 and (4) σ_1/σ_2 = -1/0.204. The concrete cylinder compressive strength is f_c = 31.5 MPa. The material parameters of the model for the correlation study are listed in Table 3.7. The test results are shown in Figure 3.24 for all three specimens. The compressive strength reduction under different orthogonal tension is correctly represented by the numerical model confirming the accuracy of the proposed damage limit surface and its evolution law.

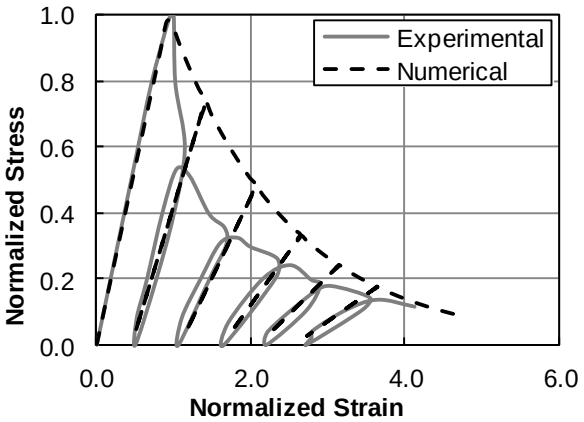

Figure 3.23 - Comparison between numerical and experimental response of a concrete specimen subjected to uniaxial cyclic tensile load

Description	Symbol	Value
Compressive strength	f_c	-31.5 MPa
Elastic limit in compression	f_{01d}	0.45fc
Plasticity factor	β	0.5
Normalized Young Modulus	$E\varepsilon_c/(2f_c)$	1.10

Table 3.7 - Material characteristics assumed

3.9.3.2 Simulation of failure domain

The simulation of the biaxial concrete-strength tests developed by Kupfer et al. [26]. Concrete specimens of 20x20x5 cm^3 were tested with different load conditions by maintaining constant the ratio of the principal stresses σ_2/σ_1 up to failure. The unconfined uniaxial prismatic compressive strength of concrete is f_c = 31.5 MPa.

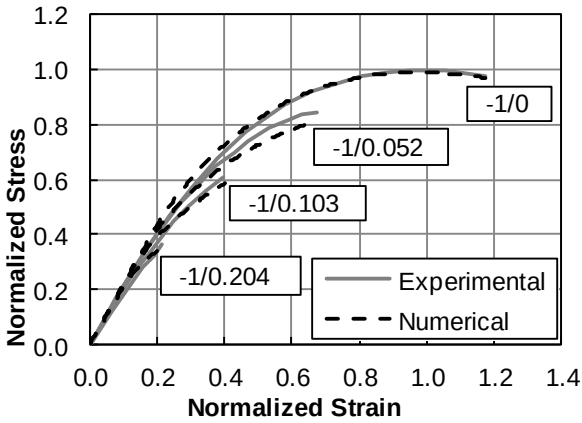

Figure 3.24 - Comparison between numerical and experimental response of a concrete specimen subjected to biaxial compressive loads

In Figure 3.25 is reported the comparison in the compression–tension field between the experimental results at failure and the numerical ones for the two proposals A and B. It can be observed that proposal A is able to effectively simulate the compressive strength reduction under different orthogonal tension: indeed the points at failure fit very well the experimental Kupfer domain. On the other hand, proposal B predicts a drastic reduction of compressive strength also for low values of transverse tensile stress in contrast with the experimental evidence. Therefore proposal A was selected in the present work and accordingly the definitions of the equivalent stress expressed by equations (3.42)-(3.43) were adopted in the mechanical damage model.

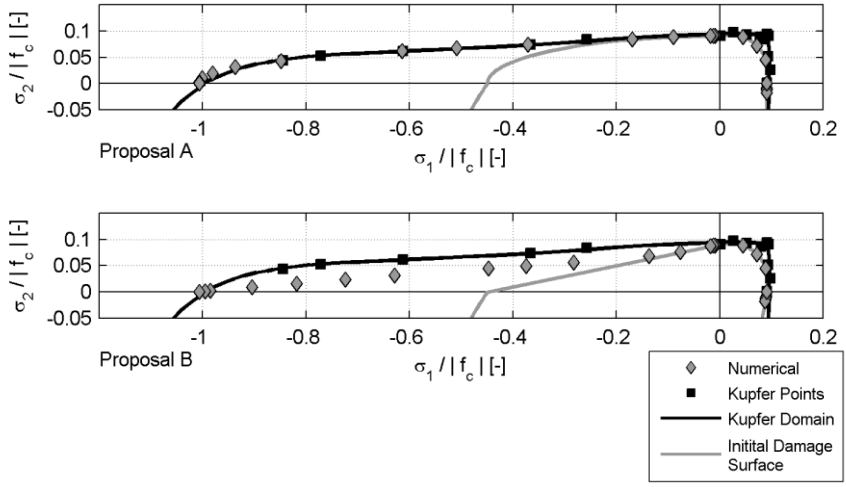

Figure 3.25 – Failure surface and comparison with Kupfer's domain for proposals A and B

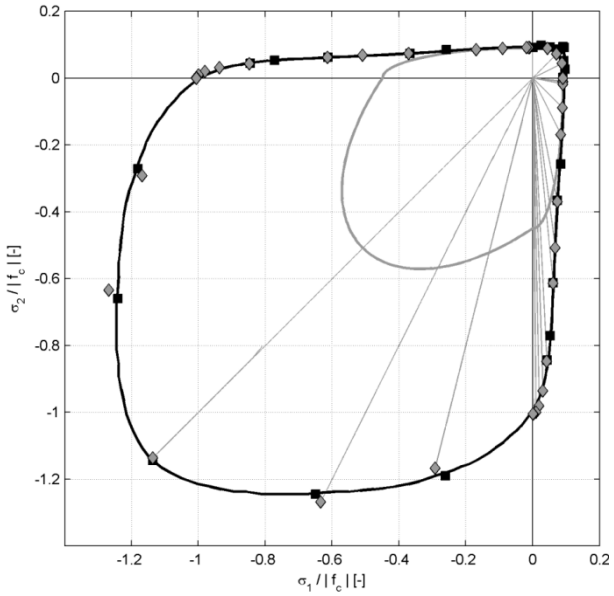

Figure 3.26 – Representation of Kupfer's domain, numerical initial damage surface and numerically obtained failure points

Finally in Figure 3.26 the complete experimental failure domain is compared with the one obtained with the proposal A, proving the capability of the proposed damage model to simulate the concrete-strength for all the biaxial stress values. In the same figure, as a reference, it is also depicted the initial damage surface (i.e. the limit of the elastic domain). It is evident that in the compression-compression field the numerical points at failure lie on a curve homothetic to the initial damage surface, whereas in tension-compression field it does not occur due to the contemporary evolution of tension and compression damage.

3.9.4 Single Edge Notched Test

The damage model has been applied to simulate an unreinforced Single-Edge-Notched (SEN) beam tested by Arrea and Ingraffea [27] and subjected to non-symmetric load conditions. This test is characterized by a mixed mode failure with fracture propagation from the notch, showing both opening and sliding.

This test represents a classical benchmark for concrete numerical models and has been reproduced by many researchers using different approaches (e.g. [28] ÷ [30]). In the experimental program three series of beams have been tested, one of which involved beams made with mortar; in the present work only the concrete beams of the series B are investigated. The beams are characterized by a thickness of 152 mm

and a notch depth of 82.4 mm. In Figure 3.27 the specimen's geometrical and load characteristics together with the finite element discretization adopted are reported.

The finite elements used for carrying out the analysis are four-node plane stress elements with a four-point Gaussian integration. The damage model parameters for concrete are summarized in Table 3.8. It is important to note that the only material properties measured in [27] are: the compressive strength f_{c1D}, the Young's modulus E and the Poisson's ratio ν. Concerning the tensile strength f_t and the fracture energy G_f, both necessary to define the tensile softening behavior, the values were obtained with the relations recommended in Model Code 1990, [21]. The other parameters were estimated considering a typical stress-strain curve for unconfined concrete, according to [21].

In the experimental setup, the load was applied at point C of the steel beam and was controlled by a feedback mechanism with the Crack Mouth Sliding Displacement (CMSD) as a control parameter. Numerically it was solved, similarly to the experimental procedure, with an indirect displacement control that involves a constrain equation based on a chosen degree of freedom.

Figure 3.28a shows the contour of positive damage d^+ near failure together with the experimental crack zone. As it is evident, the positive damage localizes in a very narrow zone, which therefore may be interpreted as zone where the crack develops. Comparing this zone with the experimental one it can be observed that the latter starts from the notch and reaches the top of the beam at the right side of the load whereas the predicted crack zone runs steeply and remains at the left side of the load. Similar steep crack paths were found by other researcher with smeared crack model, such as [28] which is reported in Figure 3.28b for comparison.

The numerical results in terms of load-CMSD curve are reported in Figure 3.29, where the experimental envelope is superimposed for comparison; a quite good agreement can be observed.

The obtained results show that the proposed model, even though it is developed in the framework of isotropic damage mechanics, is able to reproduce quite accurately the global behavior of the real specimen, even in test conditions characterized by a non-proportional loading with rotation of principal strains.

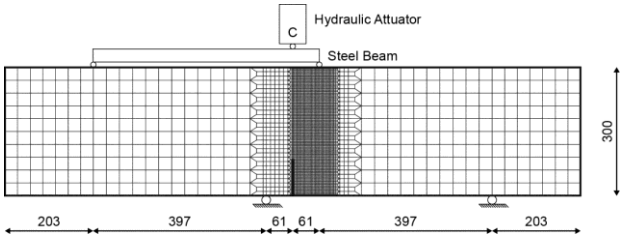

Figure 3.27 - Geometric and load characteristics of SEN beam

Description	Symbol	Value
Young Modulus	E	24800 MPa
Poisson's ratio	ν	0.15
Compressive strength	f_{c1d}	-45.5 MPa
Biaxial strength factor	R_0	1.2
Tensile strength	f_t	3.4 MPa
Plasticity factor	β	0.3
Negative damage parameter	A^-	3
Negative damage parameter	B^-	0.8
Fracture energy	Gf	110 N/m

Table 3.8 - Material characteristics assumed

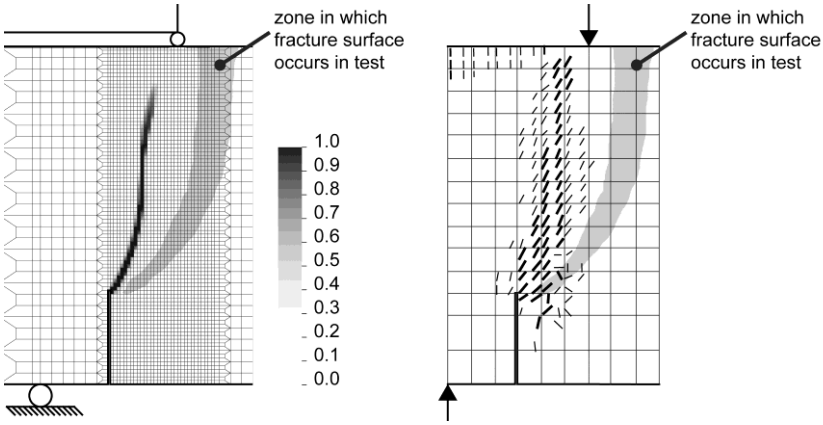

Figure 3.28 - SEN-beam: (a) Experimental envelopes and numerical predictions of the crack pattern: (b) numerical predictions of the crack pattern with smeared crack model, [28]

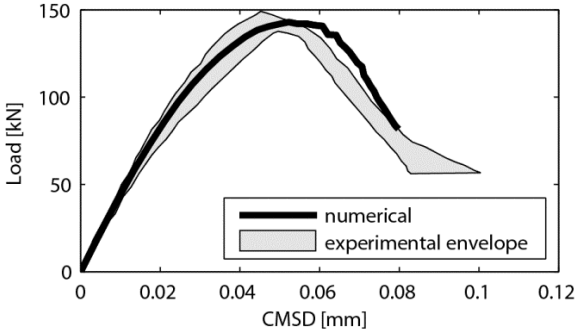

Figure 3.29 - Load-CMSD curve and comparison with experimental envelope

3.10 References

[1] Faria, R., Oliver, J., Cervera, M. (1998). A strain-based viscous-plastic-damage model for massive concrete structures, *Int. J. Solids and Structures*, 35, 1533-1558

[2] Scotta, R. (1997). Analisi meccanica di strutture in calcestruzzo mediante modelli di danno, *PhD Thesis*, Università degli studi di Padova, Dipartimento di Costruzioni e Trasporti

[3] La Borderie, C., Berthaud, Y., Pijaudier-Cabot, G. (1990). Crack closure effects in Continuum Damage Mechanics – Numerical Implementations, *Proc. 2nd Int. Conf. on Comp. Aided Analysis and Design of Concr. Struct.*, Zell am See, Austria

[4] Mazars, J., Pijaudier-Cabot, G. (1989). Continuum Damage Theory – Application to Concrete, *J. of Eng. Mech.*, ASCE, 115, 345-365

[5] Wu, J.Y., Li, J., Faria, R. (2006). An energy release rate-based plastic-damage model for concrete, *Int. J. Solids Structures*, 43, 583-612

[6] Faria, R., Oliver, J. (1993). A rate dependent platic-damage constitutive model for large scale computations in concrete structures, *Monografia Cimne*, 17, Barcelona, Spain

[7] Lemaitre, J. (1984). How to use damage mechanics, *Nuclear Eng. And Design*, 80, 233-245

[8] Chaboche, J.L. (1988). Continuum Damage Mechanics: Part I – General Concepts, *J. of Appl. Mech.*, 55, 59-64

[9] Simo, J.C., Ju, J.W. (1987). Strain- and Stress- based Continuum Damage Models – I. Formulation, *Int. J. Solids Structures.*, 23, 821-840

[10] Oliver, J., Cervera, M., Oller, S., Lubliner, J. (1990). Isotropic damage models and smeared crack analysis of Concrete, *Proc. 2nd Int. Conf. on Comp. Aided Analysis and Design of Concr. Struct.*, Zell am See, Austria

[11] Ju, J.W. (1990). On energy-based coupled elastoplastic damage theories: constitutive modeling and computational aspects, *Int. J. Solids Structures.*, 25, 803-833

[12] Scotta, R., Vitaliani, R., Saetta, A., Oñate, E., Hanganu, A. (2001). A scalar damage model with a shear retention factor for the analysis of reinforced concrete structures: theory and validation, *Comput. Struct.*, 79, 737-755

[13] Saetta, A., Scotta, R., Vitaliani, R. (1999). Coupled environmental-mechanical damage model of RC structures, *J. Eng. Mech.*, 125, 930-940

[14] Bazant, Z.P., Oh, B.H. (1983). Crack band theory for fracture of concrete, *Mat. And Struct.*, 16, 155-177

[15] Comi, C., Perego, U. (2001). Fracture energy based bi-dissipative damage model for concrete, *Int. J. Solids Structures*, 38, 6427-6454

[16] Feenstra, P.H., De Borst, R. (1996). A composite plasticity model for concrete, *Int. J. Solids Structures*, 33, 707-730

[17] Feenstra, P.H. (1993). Computational aspects of biaxial stress in plain and reinforced concrete, *PhD Thesis*, Delft University of Technology, The Netherlands

[18] Van Mier, J.G.M. (1986a). Multiaxial strain-softening of concrete, part I: fracture, part II: load-histories, *Materials and Structures*, RILEM, 19, 179-200

[19] Van Mier, J.G.M. (1986b). Fracture of Concrete under Complex Stress, *Heron*, 31

[20] Vonk, R.A. (1992). Softening of Concrete Loaded in Compression, *PhD Thesis*, University of Technology Eindhoven, The Netherlands

[21] CEB-FIP (1990). *Model Code 1990*, Lausanne, (1991)

[22] Simo, J.C., Hughes, T.J.R. (1998). Computational inelasticity, *Springer Verlag*

[23] Scotta, R., Tesser, L., Vitaliani, R., Saetta, A. (2009). Global damage indexes for the seismic performance assessment of RC structures, *Earthquake engineering and structural dynamics*, 38, 1027-1049

[24] Karsan, I.D., Jirsa, J.O. (1969). Behavior of concrete under compressive loadings, *J. Structural Division*, 95, 2543-2563

[25] Gopalaratnam, V.S., Shah, S.P., (1985), Softening response of plain concrete in direct tension, J. of the ACI, 82, 310-323

[26] Kupfer, H., Hilsdorf, H.K., Rusch, H. (1969). Behavior of concrete under biaxial stresses, *ACI J., 656-666*

[27] Arrea, M., Ingraffea, A:R., (1982)Mixed-mode crack propagation in mortar and concrete. *Cornell University Ithaca,, report 81-13*

[28] Rots, J.G., Bauta, P., Kustera, G.M.A., Blaauwendraad, J. (1985). Smeared crack approach and fracture localization in concrete, *Heron*, 30, 1-48

[29] Galvez, J.C., Cendon, D.A., Planas, J. (2002). Influence of shear parameters on mixed mode fracture of concrete, *Int. J. of fracture, 118, 163-189*

[30] Ozbolt, L., Reinhardt, H.W. (2002). Numerical study of mixed-mode fracture in concrete, *Int. J. of fracture, 118, 145-161*

CHAPTER 4:
F.E. MODELLING OF REINFORCED CONCRETE ELEMENTS

In this chapter the modeling of reinforced concrete elements is presented. In particular attention is focused on the proposal and validation on a reinforced concrete model for membranes and a reinforced concrete model for plates.

After a brief introduction in which the chosen framework for the present work, OpenSEES is described in its main characteristics and a quick overview of the programming technique within this framework, the proposed models are presented.

A membrane model for the analysis of reinforced concrete membranes suitable for the analysis of reinforced concrete structures with the most common reinforcing details is presented and validated. In particular a uniaxial tensile test, a set of uniform shear-stress loaded specimens are presented. Afterwards some validation examples for complex stress states are shown: a series of simply supported beams without shear reinforcement and three shear walls under monotonic and cyclic load conditions are selected to show the suitability and accuracy of the proposed model.

The last part of the chapter presents the reinforced concrete plate model that is validated with three different reinforced concrete structures. A slab subjected to in-plane and later load is first presented, then a box-shaped shear wall is simulated and finally a U-shaped shear wall is analyzed. The analyses presented show the suitability of the model to be adopted for the simulation of reinforced concrete structures even under large shear forces, like shear walls.

4.1 OpenSEES

OpenSEES stands for Open System for Earthquake Engineering Simulation [1] and it was developed at the Pacific Earthquake Engineering Center (PEER), University of California, Berkeley. It is a software framework for developing finite element applications. In particular it permits the development of sequential, parallel and grid-enabled applications and it is widely used for earthquake engineering analysis.

It is written primarily in C++ according to object-oriented programming paradigm and one of its key features is the ability to integrate the existing libraries and new components into the framework without the need to change the existing code. This makes it a suitable environment to implement new classes of elements, materials and other components.

Many advanced finite elements techniques useful for non-linear FE analyses have already been implemented in OpenSEES. However, as it stands OpenSEES is not applicable to reinforced concrete 2D (plane stress, plane strain, …) structures as well as to reinforced concrete 3D structures because no suitable constitutive models for such structures are included.

For these reasons it was chosen as the basic framework in which implement the models described and proposed in this work. In the following some basic concepts about object-oriented programming and the structure of OpenSEES will be discussed.

4.1.1 Objected oriented programming

In classic procedural programming paradigm the structures contained data (e.g. arrays, structures, …) while specific functions needed to be written in order to process data (Figure 4.1a). On the contrary the basic concept represented by object-oriented programming paradigm (OOP) is to have an entity called *object* that represent both data (also known as attributes) and methods [2] (Figure 4.1b).

Objects are usually instances of classes which are defined as particular constructs that define a new type. In fact the basic types (e.g. *int*, *double*, etc…) define how the particular variable of that type (i.e. its instance) will behave. In the same way classes define how an object of that type (i.e. its instance) will behave. This is very important concept in OOP.

The main idea of OOP is to divide a problem into tasks, to individuate and design self-contained entities that are good candidates to become an object in OOP representation, and to design algorithms that use objects and interact with the,. For

instance, in a finite element program, obvious candidates for objects are Node, Element, Material, Matrix while the algorithms should provide interaction between them and solution of the problem.

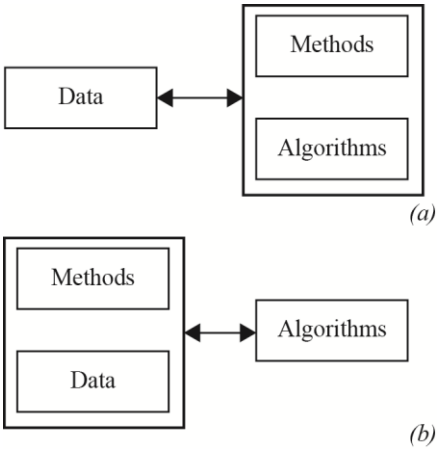

Figure 4.1 - (a) Procedural Program (b) Object-oriented program

Some of the most important features of OOP are represented by three keywords: *encapsulation*, *inheritance*, *polymorphism*. Encapsulation means that data is hidden inside the object and is not reachable from extern providing the necessary security. According to this feature, the attributes of an object should be modified only by one of its own methods. In such way, the method may be called by extern word but can prevent any undesired behavior and can contain an error-checking code. Inheritance means that one object can inherit its characteristics from another class (called superclass), in this way the subclass can be as a particular form of the more general parent class which contains the common characteristics. For instance the class Truss can be designed as a subclass of the more general Element. Polymorphism means that a method can have different implementations. In particular often a procedure is called for objects whose exact type is not known until runtime. This requires special programming techniques. For instance the procedure that forms the global stiffness matrix may call the method Element::GetStiffness() for each element. This method should behave differently for a *Truss* or for a *Quad4*.

4.1.2 OpenSEES Framework

OpenSEES is a framework, i.e. a collection of classes capable of receiving messages, processing data, and sending messages to other objects.

The main abstractions of OpenSEES are ModelBuilder, Domain, Analysis and Recorder. Their relations are shown in Figure 4.2. Domain is the entity that holds the state of the model at time t and $(t+dt)$. ModelBuilder create the objects of the

framework and adds them to the Domain. Analysis is the entity that moves the model from state at time *t* to state at time *t + dt*. Finally Recorder represents an entity that is used by user to monitor a particular parameter in the model during analysis.

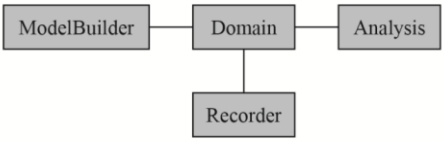

Figure 4.2 - Main abstractions of framework OpenSEES [1]

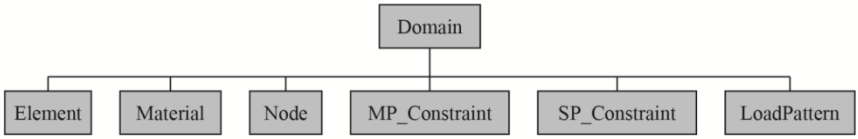

Figure 4.3 - Main abstractions of Domain

In Figure 4.3 is reported a schematic representation of the Domain component. Element is a base class that represent the abstract structure of a finite element. It is derived with an high number of elements (e.g. Truss, ZeroLenght, Brick, …) which are subclasses that represent particular Elements. The Element objects are connected to a Material Entity, which structure is reported in Figure 4.4. There are three main abstractions of Material: the first is UniaxialMaterial which provides the interface for all one-dimensional models, either stress-strain or force-deformation. The second is nDMaterial which is the multi-dimensional generalization of uniaxial materials and provides the stress-strain response at a point in a solid element. Finally SectionForceDeformation defines the interface for stress resultant models.

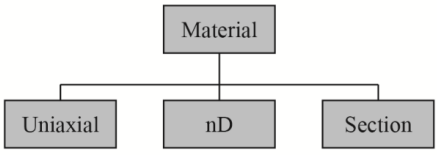

Figure 4.4 - Structure of Material Entity

4.2 Reinforcement Constitutive Laws

In the present work, generally two alternative constitutive laws are adopted for reinforcing steel.

The first one is uniaxial bilinear material as shown in Figure 4.5a. It shows an initial elastic phase followed by a strain-hardening part after yielding. The unloading and reloading paths follow a bilinear path which slopes are the same as the elastic modulus (before yielding) and hardening modulus (after yielding).

The material parameters necessary to completely define the constitutive model are the elastic Young's modulus of steel, the yield stress and the hardening modulus (Figure 4.5a). In Figure 4.5b is shown the hysteretic behavior of the model.

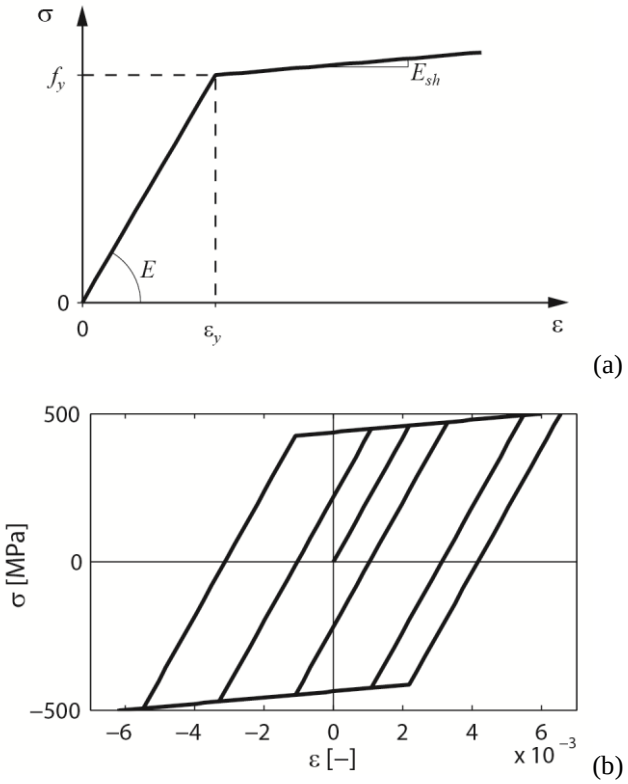

Figure 4.5 - Elastic-plastic law with kinematic hardening: (a) model parameters (b) hysteretic behavior

Furthermore the Menegotto-Pinto law with the isotropic hardening rule as presented in Filippou et al. [3] is selected due to its ability in representing the hysteretic behavior of reinforcing bars.

In Figure 4.6a is reported the shape of the constitutive law, while in Figure 4.6b an hysteretic curve is depicted. The initial elastic path represented by a straight line, moves with a gradual transition towards another straight line representing the yield asymptote. Moreover the model is able to take into account isotropic strain hardening maintaining simplicity and numerical efficiency.

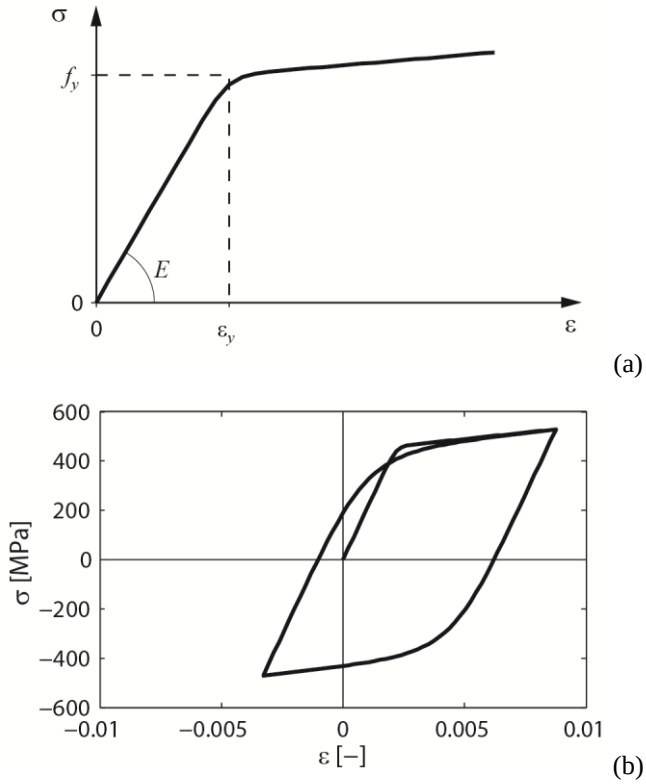

Figure 4.6 - Giuffré-Menegotto-Pinto Law Hysteretic behavior [3]

4.3 Fiber Beam-Column Elements

A widely used technique for analysis of reinforced concrete members subjected to cyclic loading is represented by one dimensional beam-columns. In one of the most common versions, the element's section is considered as the composition of steel and concrete fibers with uniaxial response; the section force-deformation is obtained via integration of the stress-strain laws at fibers, and the formulation of the element is based on the mixed method [4], [5]. According to this, interpolating shape functions are selected to describe the force distribution within the element so that the equilibrium is satisfied and independent interpolation functions are selected for the approximation of the deformation field within the element.

This class of elements has been successfully used in the last decades. One problem with the basic formulation is that the interaction between bending and shear is neglected. Thus it has been shown that these elements are profitably applicable in case of moderate shear solicitations. Some authors proposed different formulations to take into account shear and torsion coupling.

Generally these elements are based on the assumption of perfect bond, although in some works the extension of the formulation to consider bond-slip between reinforcement and concrete has been proposed.

In OpenSEES a fiber beam-column element is already available. The mechanical damage model presented in the previous chapter has been constrained to uniaxial stress state and has been implemented as a new class of type uniaxialMaterial. Thus it is possible to use a fiber beam-column element with the proposed constitutive law for concrete.

4.4 Membrane model for R/C Panels

In the FE framework OpenSEES it was developed a membrane model for the analysis of reinforced concrete structures in plane stress conditions. Taking advantage of the huge library of material models and elements present in OpenSEES, two alternatives of modeling reinforced concrete structures are made available: the first one is a discrete approach in which uniaxial elements (trusses or beams) are used to represent reinforcement and are connected with concrete elements with rigid connections or with interface elements. With the latter approach it is possible to explicitly simulate bond-slip between concrete and reinforcement (e.g. [6], [7]). The second one is a distributed representation of reinforcement in which steel bars are represented with a layer of parallel bars distributed over the concrete element with a certain orientation angle. A state of plane stress is assumed in each layer. The drawback of the first method is that generally it's an expensive approach and requires special meshing to ensure that reinforcement nodes agree with concrete nodes. The second approach is suitable for its efficiency and economy under the assumption of perfect bond between reinforcing steel and concrete, thus at the present state of the research, it neglects the existence of bond-slip between reinforcement and concrete.

For a steel layer that represents one set of parallel reinforcing bars the state determination starts with the projection of the generic total strain tensor $\boldsymbol{\varepsilon}$ in the direction of the bars. With the direction cosines $\mathbf{m}$ of the bar orientation the total strain of the steel bar is:

$$\varepsilon_{\varphi} = \boldsymbol{\varepsilon}\,\mathbf{m}\cdot\mathbf{m} \tag{4.1}$$

The strain ε_{φ} is used for the determination of the uniaxial steel stress in accordance with the constitutive relation for the reinforcing steel.

It is worth noting that the reinforcement layer material was implemented in OpenSEES as an nDMaterial (suitable for plane-stress analyses) that connects a uniaxialMaterial by means of a private pointer *uniaxialMaterial. In this way any

uniaxial material model present in OpenSEES and that may be eventually add in future can be selected as a constitutive law for the reinforcing steel.

The material state in terms of steel stress and tangent modulus is transformed back to the original element reference frame with the following operations:

$$\boldsymbol{\sigma}_s = \sigma_\varphi \, (\mathbf{m} \otimes \mathbf{m}) \tag{4.2}$$

$$\mathbf{C}_s = C_\varphi \, (\mathbf{m} \otimes \mathbf{m} \otimes \mathbf{m} \otimes \mathbf{m}) \tag{4.3}$$

The steel layer responses are summed up and then added to the response of the concrete layer. The proposed material model can be used with any plane stress finite element present in the FE library.

4.5 Validation studies of R/C Membrane Model

4.5.1 Uniaxial tension test by Bhide and Collins (Panel PB2)

The first example presented is a uniaxial tension test by Bhide and Collins [8] on a square R/C panel with side dimensions of 890 mm and thickness of 70 mm identified by the code PB2. The reinforcing ratio was 2% in the two orthogonal directions, one of which was parallel to the monotonic uniaxial load. The concrete compressive cylinder strength was 23 MPa and the reinforcing steel has tensile yield strength of 240 MPa.

The panel is represented with four membrane elements in the model (Figure 4.7). The concrete model parameters are summarized in Table 4.1.

Description	Symbol	Value
Young Modulus	E	28380 MPa
Poisson ration	ν	0.15
Compressive strength	f_c	-23.0 MPa
Elastic limit in compression	f_{01d}	$0.55f_c$
Plasticity factor	β	0.3
Fracture Energy	G_f	68 N/m

Table 4.1- Material characteristics for specimen PB2

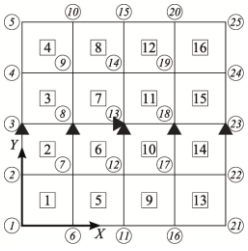

Figure 4.7 - Finite element mesh adopted for simulation of specimen PB2

The average stress versus average strain in the loading direction is shown in Figure 4.8. The membrane model captures quite well the three phases of specimen response starting with the initial elastic response followed by concrete cracking, the yielding of the longitudinal reinforcement and finally its hardening response range. When concrete starts to crack the load is transferred to reinforcement. It is worth noting that the model doesn't account explicitly for tension stiffening effect. Changing the parameter A^+ to a value of 0.2 (corresponding to a fracture energy of 220 N/m according to equation (3.92)) the load transfer from steel to concrete is better captured as it can be seen in Figure 4.8.

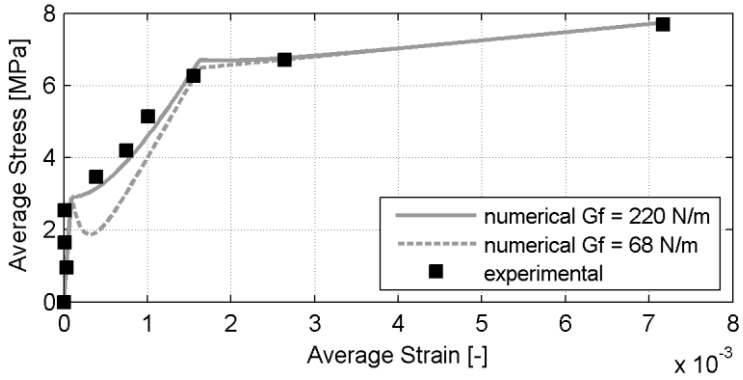

Figure 4.8 - Stress-Strain response for specimen PB2

4.5.2 Cyclic shear tests by Mansour and Hsu

The cyclic R/C panel tests by Mansour and Hsu [9] furnish an excellent opportunity to validate the proposed model, because of the significant detail of measured data that is available from the investigators upon request. The researchers carried out these tests to study the influence of two main variables: the orientation of reinforcement bars and the percentage of reinforcing steel. The results showed that orienting bars in the direction of applied principal stresses eliminates the pinching effect in the hysteretic loops permitting more energy dissipation, enhancing ductility and increasing preyield stiffness of panels [9].

The authors tested twelve full-size panels that were designed to study the effect of the two variables cited. In particular they divided in five groups the specimens, from CA to CE which correspond to different angles between steel bars and vertical principal direction (Figure 4.9). Each group was studied with different reinforcement percentages: the numbers (2, 3 or 4) are related to steel percentage ranging from lower to larger steel percentage in the range 0.54% to 2.7%. CB series has the same rebars orientation of CA series, but has different percentages of reinforcement in longitudinal and transversal directions. In this way, comparing the hysteretic loops

of panels among the series CA, CD, CF and CE it is possible to evaluate the influence of steel orientation. On the other hand, comparing the results of panels in each series (e.g. CA2, CA3 and CA4), it is possible to study the influence of the steel ratio on the hysteretic loops.

The panels are 1397 x 1397 mm^2 squares with a thickness of 178 mm, except four panels (CA4, CB4, CD4 and CE4) which are 203 mm thick, because those panels were reinforced with No. 8 bars and concrete cover was consequently increased by researchers.

Two coordinate systems are defined for all the tests: *(V, H)* coordinate system represent the vertical and horizontal principal stresses applied; *(l, t)* coordinate system represents longitudinal and transversal directions of reinforcing bars. The steel bar angle α_2 is defined as the angle between *(l, t)* and *(V,H)* coordinate systems. The values of α_2 for all series are shown in Figure 4.9 and reported in Table 4.2 which summarizes the main characteristics of all specimens with the following meaning of symbols: f_c is the compressive strength of concrete; ε_c is the corresponding peak strain; ρ_l represents the reinforcement ratio in longitudinal direction while ρ_t is the reinforcement ratio in *t* direction; f_{yl} is the tensile yield strength for reinforcement in longitudinal direction and f_{yt} is the tensile yield stress for transverse reinforcement; α_2 is the angle between vertical principal axis of specimen *(V)* and longitudinal direction of reinforcement *(l)*.

The R/C panels were submitted to cyclic load reversals of increasing amplitude under pure shear in the panel mid-plane using the Universal Panel Tester (Hsu et al. 1995a). One of the key features of this testing facility is that is equipped with a servocontrol system which permits to switch from load-control mode to strain-control mode reaching yielding conditions: in Figure 4.10 it is reported a typical loading history in which it can be seen the concept expressed.

In the load-control phase they were applied vertical and horizontal principal stresses equal in magnitude and opposite in direction, producing a state of pure shear at 45° to the horizontal (Figure 4.11). During the strain-control phase, the shear strain was used to control the principal stresses.

During the test the specimen strains were measured over a length passing through several cracks.

The model for the panel specimens consists of a single membrane element. Table 4.3 lists the concrete material parameters of the simulations. It is worth noting that not all characteristics were measured by researchers. Some of them were estimated in this work with literature relations. The steel constitutive law adopted is the Giufré-Menegotto-Pinto model with elastic modulus Es = 200 GPa and yielding stress from experimental work (Table 4.2).

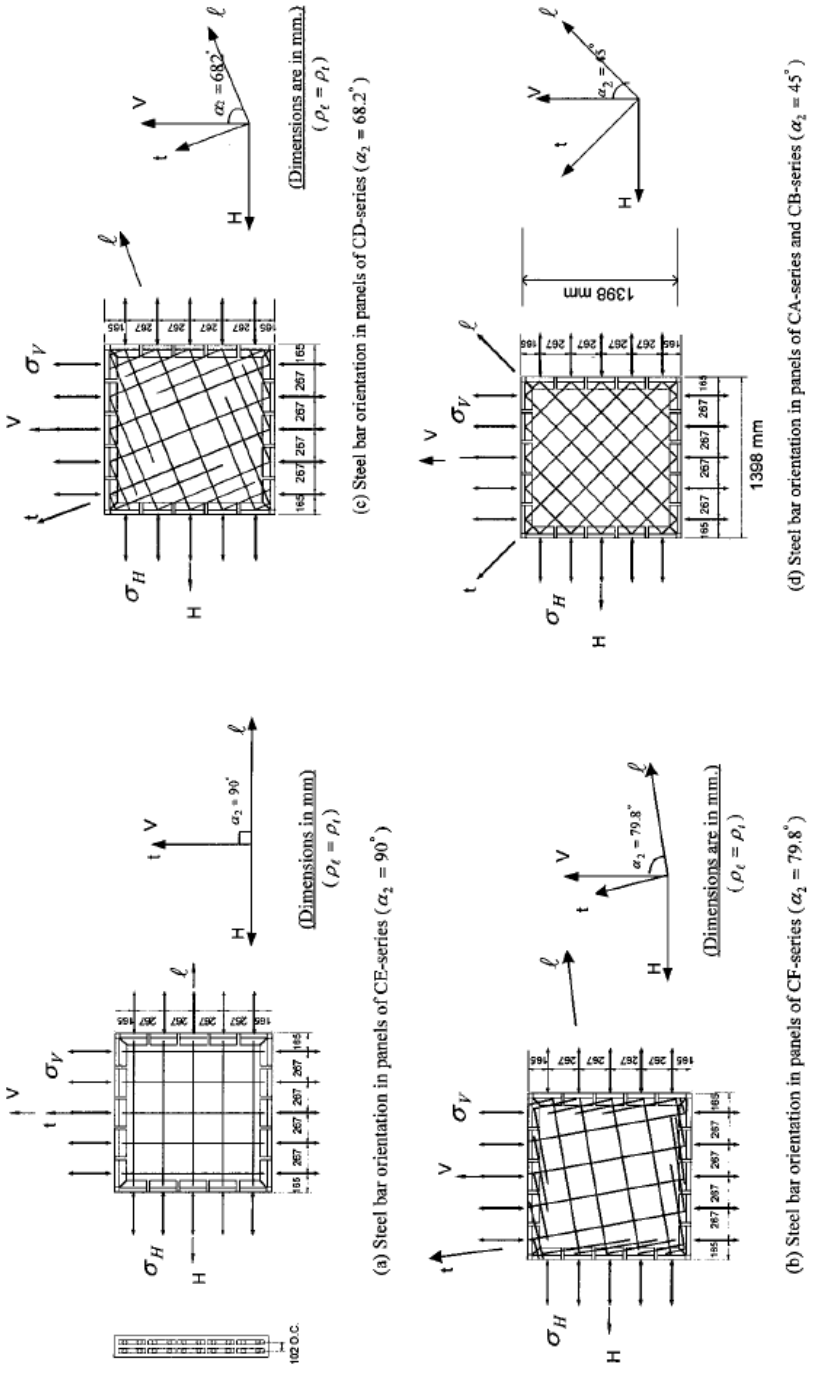

(a) Steel bar orientation in panels of CE-series ($\alpha_2 = 90^\circ$)
(b) Steel bar orientation in panels of CF-series ($\alpha_2 = 79.8^\circ$)
(c) Steel bar orientation in panels of CD-series ($\alpha_2 = 68.2^\circ$)
(d) Steel bar orientation in panels of CA-series and CB-series ($\alpha_2 = 45^\circ$)

Figure 4.9 - Reinforcement orientation in tested panels: (a) CE series (a2=90°); (b) CF series (as=79.8°); (c) CD series (a2=68.2°); (d) CA and CB series (a2=45°) [9]

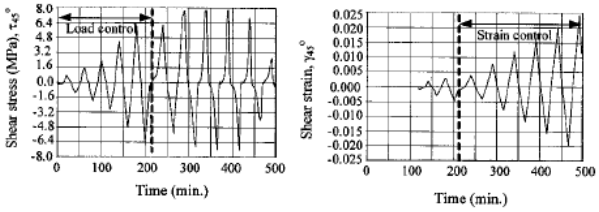

Figure 4.10 - Loading history for specimen CA3 [9]

Series	Panel	thickness	Concrete		Longitudinal reinforcement - *(l)* direction					Transverse reinforcement - *(t)* direction					α_2
			f_c	ε_c											
		[mm]	[MPa]	[‰]	No.	A [mm2]	s [mm]	ρ_l [%]	f_y	No.	A [mm2]	s [mm]	ρ_t [%]	f_y	[°]
CA	CA2	178	-45	-2.5	4	129	188	0.77	424.1	4	129	188	0.77	424.1	45
	CA3	178	-44.5	-2.4	6	284	188	1.70	425.4	6	284	188	1.70	425.4	45
	CA4	203	-45	-2.8	8	510	188	2.70	453.4	8	510	188	2.70	453.4	45
CB	CB3	178	-48	-2.6	6	284	188	1.70	425.4	4	129	188	0.77	424.1	45
	CB4	203	-47	-2.4	8	510	188	2.70	453.4	4	129	188	0.67	424.1	45
CD	CD2	178	-44.5	-2.5	4	129	248	0.59	424.1	4	129	248	0.59	424.1	68.2
	CD3	178	-47	-2.6	6	284	248	1.30	425.4	6	284	248	1.30	425.4	68.2
	CD4	203	-43	-2.4	8	510	248	2.00	453.4	8	510	248	2.00	453.4	68.2
CE	CE2	178	-49	-2.3	4	129	267	0.54	424.1	4	129	267	0.54	424.1	90
	CE3	178	-50	-2.4	6	284	267	1.20	425.4	6	284	267	1.20	425.4	90
	CE4	203	-47	-2.2	8	510	267	1.90	453.4	8	510	267	1.90	453.4	90
CF	CF2	178	-44	-2.5	4	129	262	0.56	424.1	4	129	262	0.56	424.1	79.8

Table 4.2- Characteristics of test specimens: thickness, material properties, orientation of steel bars, percentage of steel bars

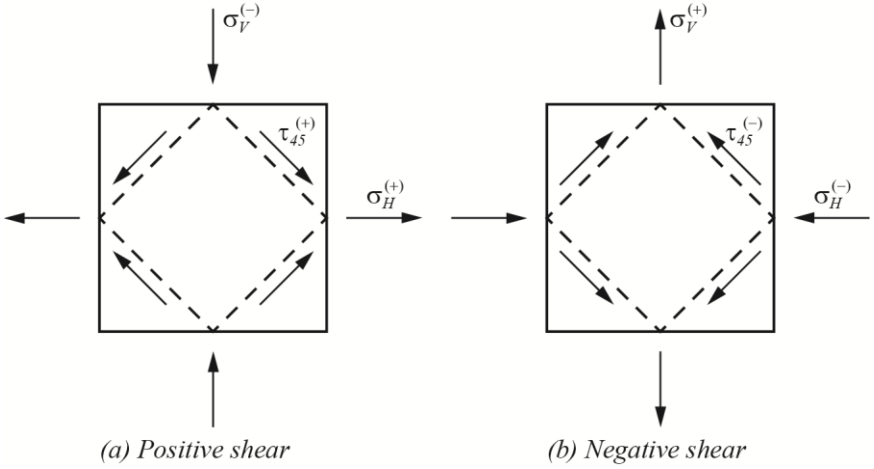

Figure 4.11 - Elements under pure shear

The specimens were loaded with nodal forces in the two principal directions *(H)* and *(V)* equal in magnitude and opposite in direction. The solution was carried on with the displacement control procedure enforcing the shear deformation to follow the experimental load-history. It is worth noting that during the experimental tests in some cases it was not possible to maintain constant and equal to -1 the ratio between the two principal stresses. In those cases an additional constant uniform load was applied to the numerical models to obtain the experimentally recorded ratio between the two principal stresses at maximum point. This could be seen for instance for specimen CA2: in Figure 4.12 it is plotted the experimental curve σ_H - σ_V in which it can be seen that the maximum positive and negative principal stresses are not equal, it is also superimposed the numerical curve in which it can be seen the effect of the constant biaxial compressive load superimposed. This is a necessary step in those cases in which the problem appears because it permits the comparison between numerical and experimental results.

		thickness	Cocrete						
Series	Panel	[mm]	f_c [MPa]	f'_c [MPa]	ε_c [‰]	E [MPa]	$f_{0.1d}$ [MPa]	$f_{0.2d}/f_{0.1d}$	ft [MPa]
CA	CA2	178	-45	-38.25	-2.5	41970	-22.95	1.2	-1.91
	CA3	178	-44.5	-37.825	-2.4	41736	-22.695	1.2	-1.89
	CA4	203	-45	-38.25	-2.8	41970	-22.95	1.2	-1.91
CB	CB3	178	-48	-40.8	-2.6	43347	-24.48	1.2	-2.04
	CB4	203	-47	-39.95	-2.4	42893	-23.97	1.2	-2.00
CD	CD2	178	-44.5	-37.825	-2.5	41736	-22.695	1.2	-1.89
	CD3	178	-47	-39.95	-2.6	42893	-23.97	1.2	-2.00
	CD4	203	-43	-36.55	-2.4	41027	-21.93	1.2	-1.83
CE	CE2	178	-49	-41.65	-2.3	43796	-24.99	1.2	-2.08
	CE3	178	-50	-42.5	-2.4	44241	-25.5	1.2	-2.13
	CE4	203	-47	-39.95	-2.2	42893	-23.97	1.2	-2.00
CF	CF2	178	-44	-37.4	-2.5	41501	-22.44	1.2	-1.87

Table 4.3 - Concrete model parameters adopted in simulation

Specimen CA2 is characterized by the 45° inclination of steel bars and a percentage of reinforcement equal to 0.77% in both directions (Table 4.2). The complete collapse of specimen CA2 could not be reached because of equipment limitation [9].

The resulting shear stress-shear strain relation is compared with the experimental response in Figure 4.13. The simulation shows that the proposed model can describe quite well several features of the measured panel behavior such as the yielding and subsequent hardening behavior, the residual deformation after each load reversal, and the shape of the hysteretic loop with a well defined pinching effect.

It is worth noting that the softening exhibited in experimental test during last loops is not due to failure of the specimen rather than to the limitation of the equipment as evidenced by researchers in [9].

The pinching effect characterizes all specimens of series CA, CB and CD. This was individuated by researchers to be caused by the inclination of steel bars. In fact

series CE is characterized by the absence of the pinched shape with rounded hysteretic loops.

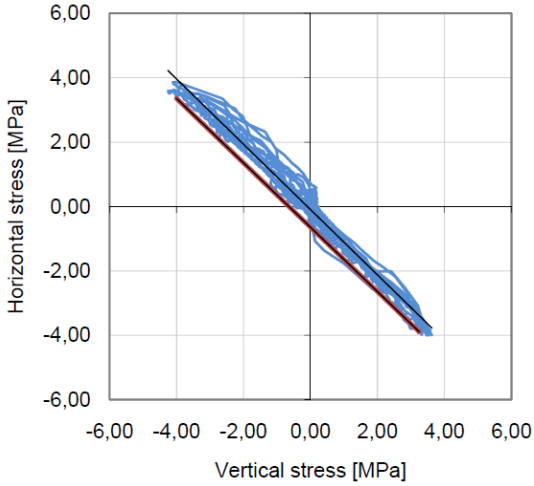

Figure 4.12 - Horizontal stress vs. Vertical stress for panel CA2

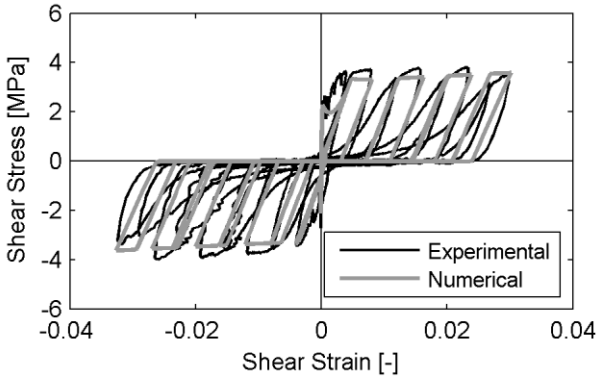

Figure 4.13 - Comparison numerical-experimental of shear stress-shear strain responses of panel CA2

The presence of pinching mechanism in series CA (α_2 = 45°) can be explained examining the equilibrium of a cracked element (Figure 4.14). Both the vertical and horizontal cracks are open when the reverse loading stage under negative shear starts. The applied compressive stress σ_H and tensile stress σ_V thus must be resisted by steel. Stress σ_H induces a compressive stress in the two 45° steel bars, while σ_V induces a tensile stress of equal magnitude in the same bars. Thus the stresses in steel bars are zero, and the R/C element offers nearly no shear resistance to the applied load while the shear strain increases rapidly due to the closing of the vertical cracks and the opening of horizontal ones. For this reason the shear stiffness

becomes nearly zero. This mechanism continues until the horizontal cracks close permitting the formation of horizontal concrete struts that resist to the horizontal compressive stress σ_H while the steel bars offer resistance to vertical tensile stress σ_V leading to a stiffness recovery.

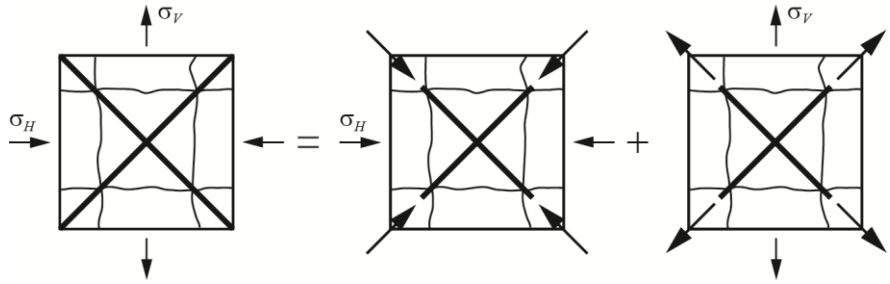

Figure 4.14 - Cracked R/C element with α_2 = 45° (CA series)

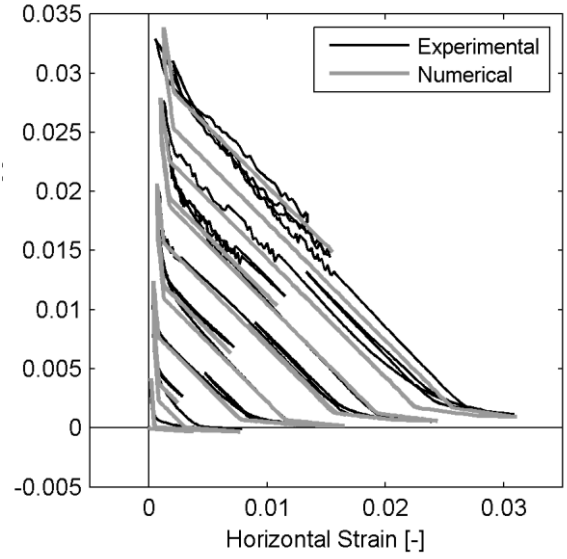

Figure 4.15 - Vertical strain vs. horizontal strain. Comparison numerical-experimental for panel CA2

This mechanism can be also seen in Figure 4.15 in which is plotted the numerical vertical strain vs. horizontal strain compared to the experimental one. It is evident that under positive shear stress (Figure 4.11a) the vertical strain ε_V reaches the compression region in every cycles, indicating therefore that horizontal cracks are fully closed and vertical concrete struts are formed to resist the vertical compression. In the same way, under negative shear stress (Figure 4.11b), the horizontal strain ε_H reaches the compression region in every cycle, indicating that vertical cracks are

fully closed and horizontal struts are formed to resist the horizontal compression. It can be seen that the proposed model is able to capture this mechanism quite well.

The unloading stiffness after yielding conditions and the progressive stiffness recovery at load reversals is not represented very well. This evidence could be ascribed to the inability of the model to account for bar dowel action and bond-slip effects, and interlocking effects.

Specimen CA3 is characterized by the 45° inclination of steel bars and a percentage of reinforcement equal to 1.70% in both directions (Table 4.2).

In Figure 4.16 is reported the result of the simulation compared to the experimental response in terms of shear stress-shear strain curves. The model is able to describe quite accurately the crack load, the yielding and subsequent hardening behavior, the unloading stiffness after yielding, the failure mode (concrete crushing) with a softening stage, and the shape of the hysteretic loop with a well defined pinching effect.

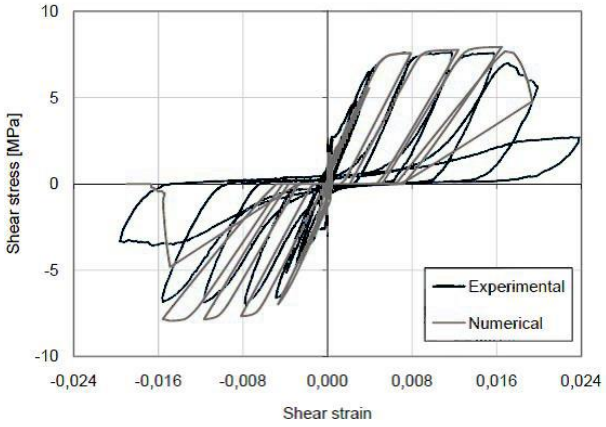

Figure 4.16 - Comparison numerical-experimental of shear stress-shear strain responses of panel CA3

The unloading-reloading stiffness during the last steps is not well captured by the numerical model and an appreciable difference exhibits between experimental and numerical data. This can be due the inability of the model in taking into account bond-slip between concrete and still that could be an important factor since the progressive crushing of concrete can extremely affect the adherence between steel bars and concrete.

As a direct consequence the numerical dissipated energy is lower than the experimental one. But a light underestimation of the dissipated energy is pro-safety in executing seismic analyses

Specimen CA4 is also characterized by the 45° inclination of steel bars and a percentage of reinforcement equal to 2.70% in both directions (Table 4.2). This panel was thicker than the previous ones to accommodate the larger steel bars used (No. 8 bars) increasing the cover.

In Figure 4.17 is reported the result of the simulation compared to the experimental response in terms of shear stress-shear strain curves. The model is quite able to describe the crack load, the failure load corresponding to concrete crushing and the subsequent softening stage, and the shape of the hysteretic loop with a well defined pinching effect. Also for this specimen the dissipated energy is underestimated by the numerical model and the unloading-reloading stiffness of the last loops is relatively underestimated. Again, the source of this error should be explained considering the simplifications of the model: inability in representing the bond-slip behavior between bars and concrete, impossibility to take into account dowel effect and aggregate interlock. Indeed during numerical simulation it was not reached the yielding of the bars leading to a consequent lower accumulation of positive plastic strains. During experimental test the researchers reported the yield of steel bars. This could be explained considering that the model doesn't take into account dowel effect: in reality the bars may be subjected to a more complicated stress-state than the uniaxial one considered by the numerical model due to dowel effect and may have experienced yielding.

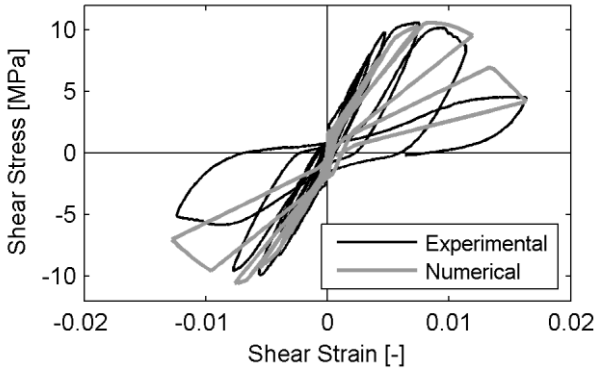

Figure 4.17 - Comparison numerical-experimental of shear stress-shear strain responses of panel CA4

Regardless these inaccuracies the model is able to represent reasonably well the overall response of the specimen and correctly assessed the reduction of ductility of this panel, its inability in dissipating energy (panel CA4 was the one with the lowest energy dissipation [9]) and its brittle failure mode due to concrete crushing.

Specimen CB3 is characterized by the 45° inclination of steel bars as CA series, but it has different percentages of reinforcement equal to 0.77% and 1.70% in longitudinal and transvers direction respectively (Table 4.2).

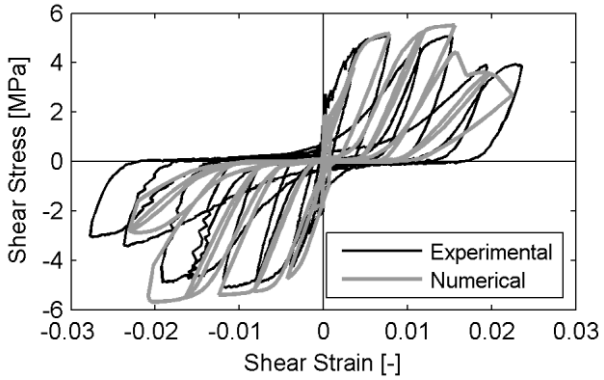

Figure 4.18 - Comparison numerical-experimental of shear stress-shear strain responses of panel CB3

In Figure 4.18 is reported the result of the simulation compared to the experimental response in terms of shear stress-shear strain curves. The model is quite able to describe the crack load, the yielding load, the failure load corresponding to concrete crushing and the softening behavior after this point, and the shape of the hysteretic loop with a well defined pinching effect. Like previous panels, the model is not evaluating correctly the unloading-reloading stiffness after maximum shear stress.

Similar considerations can be given for specimen CB4 which is characterized by the 45° inclination of steel bars and percentages of reinforcement equal to 0.67% and 2.70% in longitudinal and transvers direction respectively (Table 4.2).

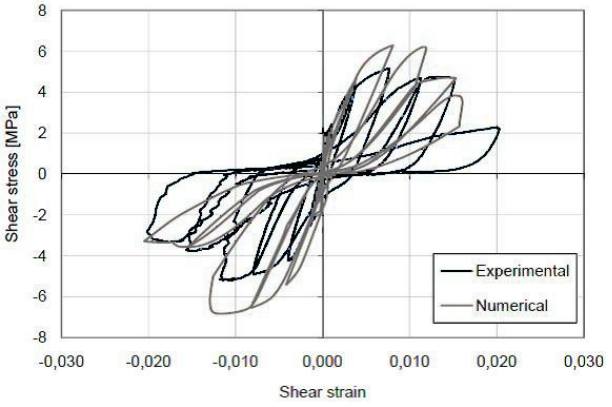

Figure 4.19 - Comparison numerical-experimental of shear stress-shear strain responses of panel CB4

In Figure 4.19 is reported the comparison between experimental and numerical curves in terms of shear stress vs. shear strain. It can be noted that the model represent the overall behavior of the specimen with a good estimation of crack loading, initial stiffness, post-crack stiffness, and shape of the hysteretic loop characterized by an evident pinching effect. On the other hand, the strength of the panel is overestimated. The reason of this issue may be looked into the different ratio of steel in the two directions.

Specimen CD2 is characterized by the 68.2° inclination of steel bars and a percentage of reinforcement equal to 0.59% in both directions (Table 4.2). The experimental procedure had to be stopped because the limit of LVDTs was reached [9].

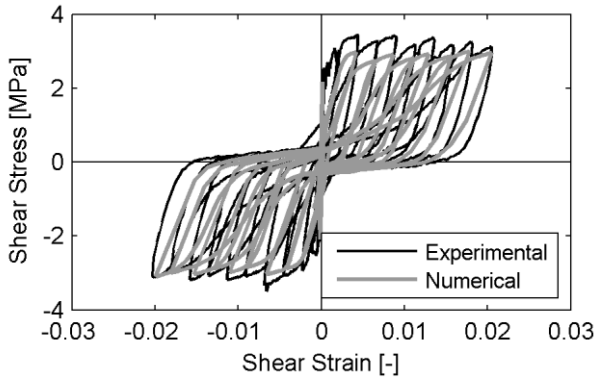

Figure 4.20 - Comparison numerical-experimental of shear stress-shear strain responses of panel CD2

In Figure 4.20 is reported the result of the simulation compared to the experimental response in terms of shear stress-shear strain curves. The model is quite able to describe the crack load, the stiffness, the residual deformations, and the shape of the hysteretic loop with a well defined pinching effect. The strength of the panel is estimated with a reasonably error lightly lower than 20%.

Specimen CD3 is characterized by the 68.2° inclination of steel bars and a percentage of reinforcement equal to 1.3% in both directions (Table 4.2).

In Figure 4.21 is reported the stress-strain curve for experimental and numerical results. The experimental data show a discrepancy of symmetry in the load-displacement response of the panel. Regardless of this fact, the simulation shows that the proposed model can describe accurately several features of the measured panel behavior such as the cracking load, unloading-reloading stiffness, residual deformations, and the energy dissipation capacity. Moreover the model correctly assess the failure of the specimen due to concrete horizontal struts that fail under excessive compressive stress as it can be seen in the last negative shear load. The

panel strength is estimated by the numerical model with a reasonable error of almost 15%.

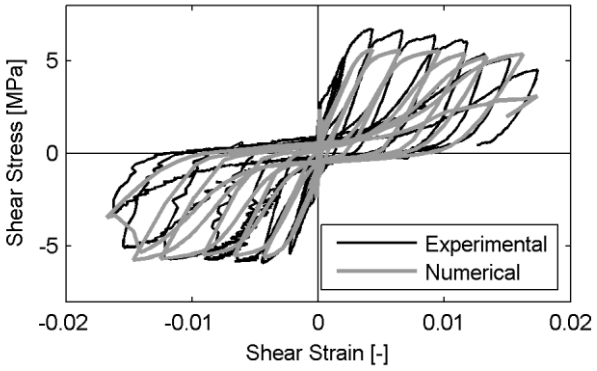

Figure 4.21 - Comparison numerical-experimental of shear stress-shear strain responses of panel CD3

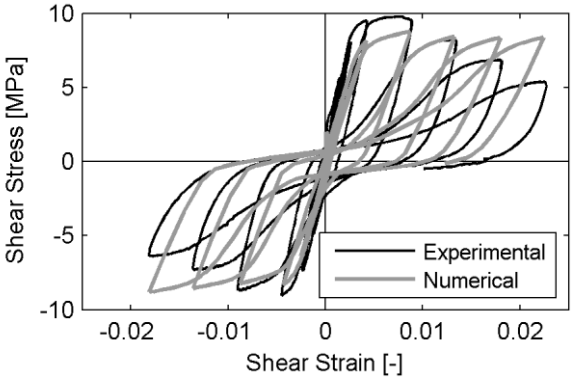

Figure 4.22 - Comparison numerical-experimental of shear stress-shear strain responses of panel CD4

Similar conclusions can be drawn for specimen CD4 which is characterized by a steel percentage of 2.0% in both directions (Table 4.2). The result of numerical simulation for this specimen is shown in Figure 4.22 superimposed to the result of experimental test. Also in this case the experimental curve exhibits a relevant discrepancy of symmetry in the curve reported. Again, the overall characteristics of the behavior are reasonably well represented by numerical model with a shear strength almost 15% lower than experimental strength.

Specimens of CE series are characterized by the 90° inclination of steel bars and a percentage of reinforcement equal to 0.54%, 1.2% and 1.9% in both directions respectively for CE2, CE3 and CE4 (Table 4.2). The complete collapse of specimen these specimens could not be reached because of equipment limitation [9].

The resulting shear stress-shear strain relation are compared with the experimental responses in Figure 4.23-Figure 4.24-Figure 4.25. The model captures correctly several features of the measured panel behavior such as the cracking load, initial stiffness, yielding load and subsequent hardening behavior, the residual deformation after each load reversal thus the unloading-reloading stiffness, and the shape of the hysteretic loop with the absence of pinching effect showing rounded hysteretic loops.

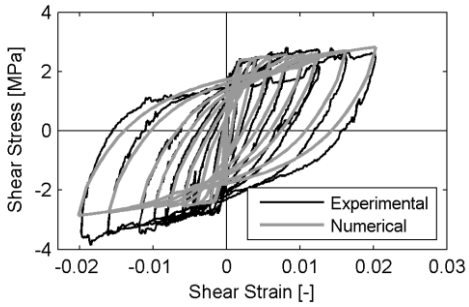

Figure 4.23 - Comparison numerical-experimental of shear stress-shear strain responses of panel CE2

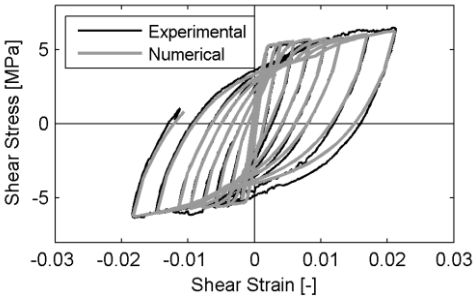

Figure 4.24 - Comparison numerical-experimental of shear stress-shear strain responses of panel CE3

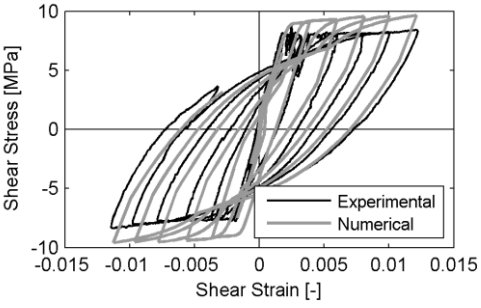

Figure 4.25 - Comparison numerical-experimental of shear stress-shear strain responses of panel CE4

The absence of pinching mechanism in series CE (α_2 = 90°) can be explained examining the equilibrium of a cracked element (Figure 4.26). Both the vertical and horizontal cracks are open when the reverse loading stage under negative shear starts. The applied compressive stress σ_H and tensile stress σ_V thus must be resisted by steel. Stress σ_H induces a compressive stress in the horizontal steel bars, while σ_V induces a tensile stress of equal magnitude in vertical stress bars. Thus the stresses in steel contribute to offer nearly the shear resistance to the applied load until yielding of the bars. After yielding the stiffness is low compared to the stiffness of the preceding stage and thus a fully rounded hysteretic loop takes place.

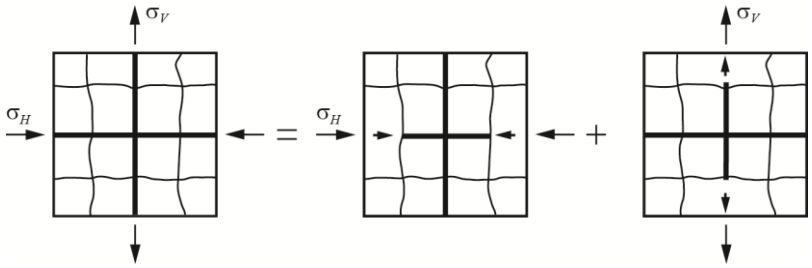

Figure 4.26 - Cracked R/C element with α_2 = 90° (CE series)

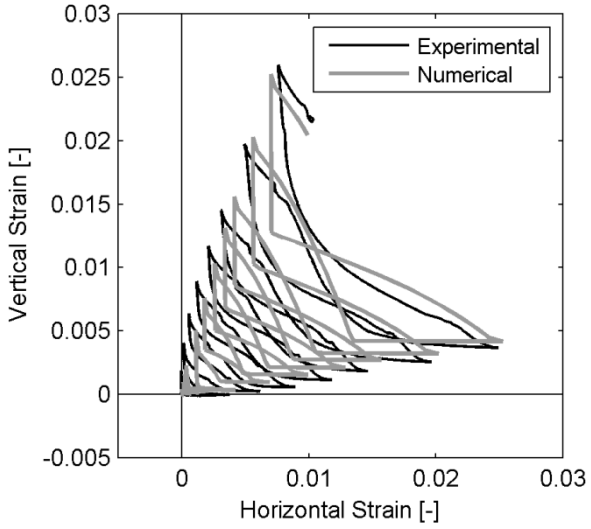

Figure 4.27 - Vertical strain vs. horizontal strain. Comparison numerical-experimental for panel CE3

This mechanism can be also seen in Figure 4.27 in which is plotted the numerical vertical strain vs. horizontal strain compared to the experimental one. It is evident

that under positive shear stress (Figure 4.11a) the vertical strain ε_V doesn't reach the compression region in every cycle, indicating therefore that horizontal cracks remain open, and widen with every cycle. The vertical compressive load is then resisted by reinforcing bars, rather than concrete. In the same way, under negative shear stress (Figure 4.11b), the horizontal strain ε_H doesn't reach the compression region in every cycle, indicating that vertical cracks remain open and widen with every cycle. Thus, the horizontal compressive load is resisted by steel bars. It can be noted that this mechanism is well captured by the model with which the axial strains are evaluated with high accuracy. The progressive expansion of the panel due to the accumulation of plastic strain is correctly captured by the proposed model. The gap between the two curves visible in the central part between following tips is explained by the sudden closure of the cracks in the numerical model, whereas the specimen exhibits a progressive stiffness recovery when rough cracks close. This fact is evident also comparing the vertical stress-strain response depicted in Figure 4.28.

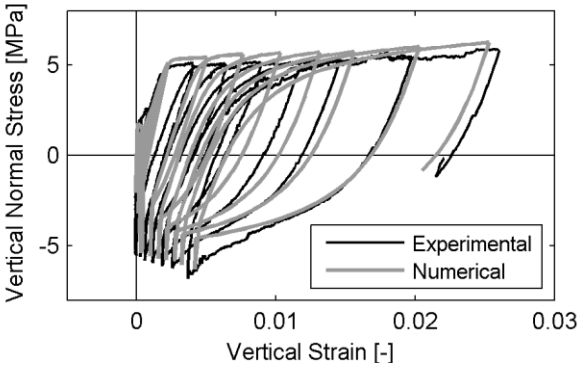

Figure 4.28 - Vertical stress vs. vertical strain. Comparison numerical-experimental for panel CE3

Finally specimen CF2 is characterized by the 79.8° inclination of steel bars and a percentage of reinforcement equal to 0.56% in both directions (Table 4.2). The complete collapse of specimen these specimens could not be reached because of equipment limitation [9].

In Figure 4.29 is reported the stress-strain curve for experimental and numerical results. Also in this case the simulation shows that the proposed model can describe accurately several features of the measured panel behavior such as the cracking load, yielding load, unloading-reloading stiffness, residual deformations, and the energy dissipation capacity.

It can be concluded that the model is able to take into account the main aspects evidenced by the authors assessing correctly the overall behavior with different

reinforcement alignments and different steel percentages confirming that aligning the steel bars with the principal directions lead to a more ductile shear structure with larger energy dissipation capacity.

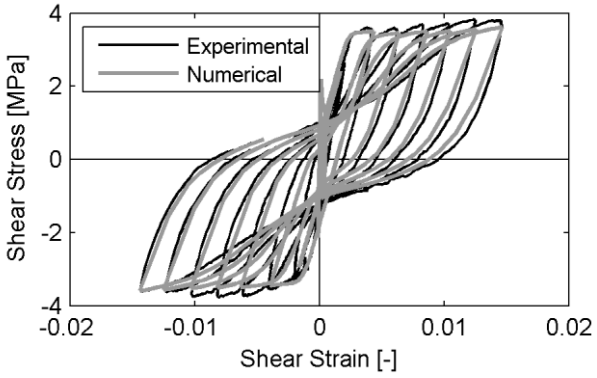

Figure 4.29 - Comparison numerical-experimental of shear stress-shear strain responses of panel CF2

4.5.3 Shear test by Vecchio and Collins (specimen PV20)

Among the extensive set of panel tests by Vecchio and Collins [10] specimen PV20 is selected for the extensive amount of reported measurements. The R/C panel was submitted to monotonically increasing in-plane shear.

The panel specimen is 890 mm square with a thickness of 70 mm. It is reinforced with two layers of welded wires parallel to its edges with 1.79% and 0.89% reinforcement ratios. The compressive concrete strength reported by the investigators is 19.6 MPa and the corresponding strain is 0.0018. The steel wires have different tensile yielding strength of 460 MPa for longitudinal steel and 297 MPa for transverse steel. The panel edges are loaded by shear forces producing a homogeneous pure shear solicitation. In the test, known values of stress are applied to the R/C while the resulting specimen strains are measured. The investigators characterized the panel failure as concrete shear failure.

The specimen is represented with only one membrane element and the resulting shear stress-strain relation is compared with the experimental one in Figure 4.30. The evolution of the concrete compressive damage parameter is superimposed in the same figure.

The overall behavior of the panel is represented well in terms of cracking load, post-cracking response, shear strength and ductility. The compressive damage parameter approaches the value 1 for a shear strain of about 0.012. This result agrees quite well

with the measured failure strain. Moreover, the limit value of the compressive damage parameter indicates concrete shear failure, as reported in the test.

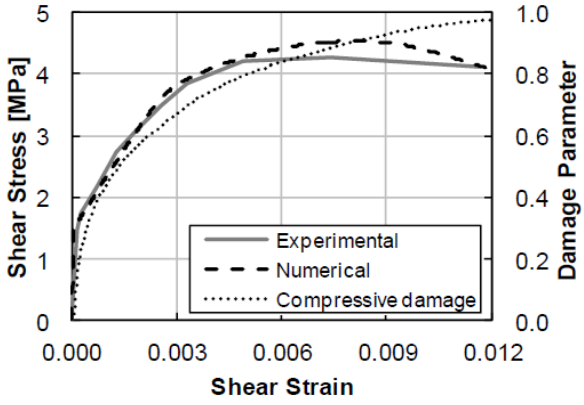

Figure 4.30 - Shear stress-shear strain curve for specimen PV20

4.5.4 Simply supported beams without shear reinforcement testes by Leonhardt

The well known R/C beams tested by Leonhardt and Walther [11] are selected as first examples to show the practical relevance of the proposed model. In fact the beams are suitable to show the capability of the R/C membrane element to predict the transition from flexural to shear failure modes.

Table 4.4 summarizes their geometrical properties and their reinforcing steel amount. The beams are characterized by the absence of shear reinforcement and a constant longitudinal reinforcement ratio of μ = 2,0%. They are simply supported beams with two concentrated vertical loads symmetric respect to the beam mid-span.

In Figure 4.31 is reported a scheme of a typical beam indicating the main variables reported in Table 4.4. In Figure 4.32 is reported a picture taken from the investigators [11] in which all beams, in their failure condition, are shown.

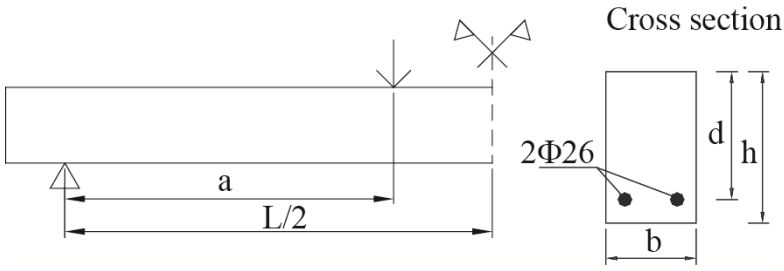

Figure 4.31 – Geometry of the simply supported beams without shear reinforcement tested by Leonhardt [11]

Beam	L [m]	a [m]	h [cm]	b [cm]	a/d	μ [%]
T4	1.70	0.675	32	19	2.5	2
T5	1.95	0.81	32	19	3	2
T6	2.35	1.08	32	19	4	2
T7	3.10	1.35	32	19	5	2
T8	3.60	1.62	32	19	6	2
T9	5.80	1.89	32	19	7	2
T10	4.70	2.16	32	19	8	2

Table 4.4 - Geometric characteristics of analyzed beams

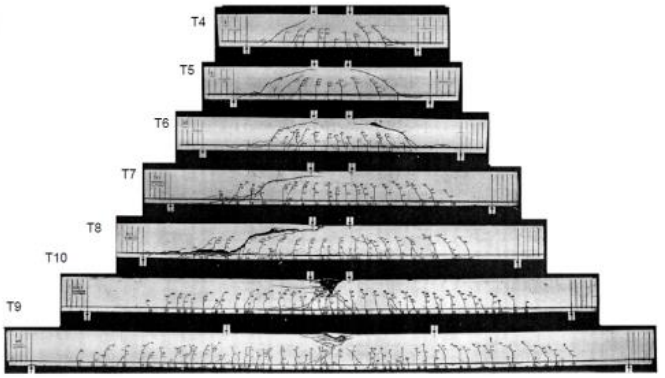

Figure 4.32 – Pictures of crack pattern at failure condition as reported by Leonhardt [11]

The shear span-to-depth ratio *a/d* conditioned the experimental failure mode: flexural failure took place for high ratios while shear failure occurred for low ratios. In particular the transition from flexural to shear failure can be distinguished for *a/d* = 6.

The experimental setup has been numerically simulated with the maximum mesh size assumed as half of the beam depth. The constitutive laws of concrete and steel are characterized by the parameters of Table 4.5, calculated from the mechanical properties of the specimens [11].

Figure 4.33 depicts the comparison between the experimental failure loads of all the beams and the numerical ones. Moreover the theoretical flexural strengths are reported. The good agreement between the experimental and the numerical values is also confirmed by the average error and its standard deviation calculated in Table 4.6.

In Figure 4.34 the load vs. displacement curves obtained by the numerical models are reported. The corresponding experimental curves were not reported by the test authors. As it is evident from this figure, beams T9 and T10 exhibit high plastic

deformations after the longitudinal bar yielding, which is characteristic of a flexural failure mode. On the other hand, the remaining beams with lower span-to-depth ratios suffered shear failure as the abrupt termination of their curves demonstrates.

Description	Symbol	Value
Young Modulus of concrete	E	36000 MPa
Poisson's ratio	ν	0.15
Compressive strength	f_{c1d}	-28.0 MPa
Biaxial strength factor	R_0	1.2
Elastic limit in compression	f_{01d}	$0.65f_{c1d}$
Tensile strength	f_t	2.0 MPa
Plasticity factor	β	0.3
Reinforcement young modulus	E_s	190 GPa
Yield strength	f_{ys}	360 MPa
Hardening Modulus	E_h	3 GPa

Table 4.5 - Material characteristics adopted for simulation of Leonhardt beams

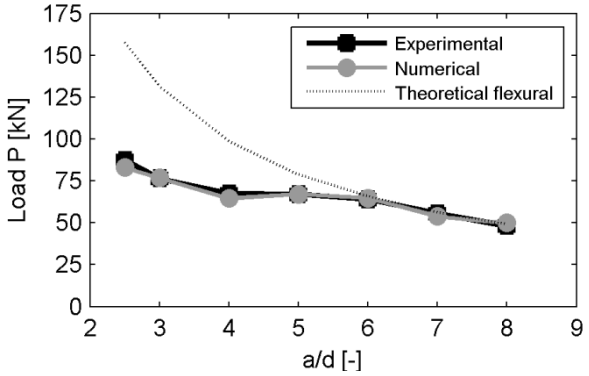

Figure 4.33 - Comparison of numerical and experimental results in terms of failure load vs. shear span to depth ratio

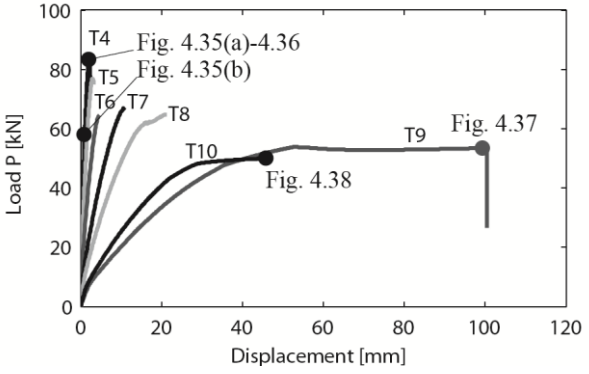

Figure 4.34 - Load-displacement curves for all beams

ID	*total span* (mm)	*shear span* (mm)	*depth* (mm)	*width* (mm)	*a/d*	ρ (%)	mesh of half beam	$P_{u,exp}$ (kN)	$P_{u,num}$ (kN)	error
T4	1700	670	320	190	2.5	2.0	8x23	87.5	82.9	-5%
T5	1950	810	320	190	3.0	2.0	8x26	76.5	76.7	0%
T6	2350	1080	320	190	4.0	2.0	8x32	67.5	64.2	-5%
T7	3100	1350	320	190	5.0	2.0	8x42	67.0	68.7	3%
T8	3600	1620	320	190	6.0	2.0	8x49	64.0	65.0	0%
T9	5800	1890	320	190	7.0	2.0	8x75	55.5	53.8	-3%
T10	4700	2160	320	190	8.0	2.0	8x64	48.0	49.9	4%
								average		-1%
								std deviation		4%

Table 4.6 - Results of simulation of Leonhardt beams

The specimen T4, with the lowest *a/d* = 2.5, showed a so-called "shear compression failure" that is the crushing of upper compressed concrete area due to the progressive development of the diagonal cracks induced by shear stresses under the point of load application. The experimental failure occurred at the load of 87.5 kN, while the numerical simulation provides a corresponding value of 82.9 kN. This beam characterizes the deepest point for the "shear valley" of the specimens with a reduction of the failure moment equal to the 53% of the theoretical flexural value.

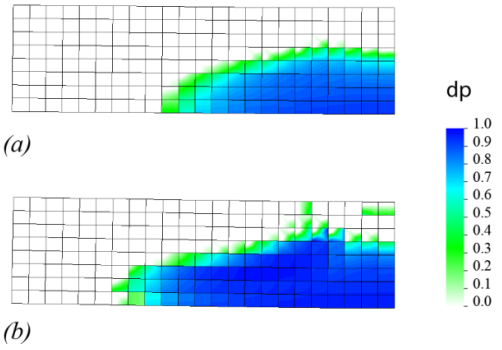

Figure 4.35 - Tensile damage contour for beam T4 at: (a) 1 mm displacement; (b) 2.2 mm displacement

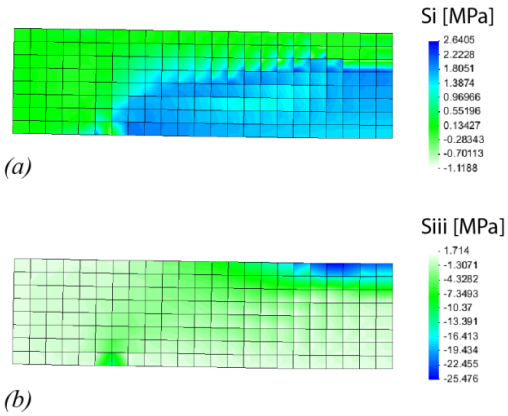

Figure 4.36 - Results for beam T4 at failure load (a) Maximum principal stress; (b) Minimum principal stress

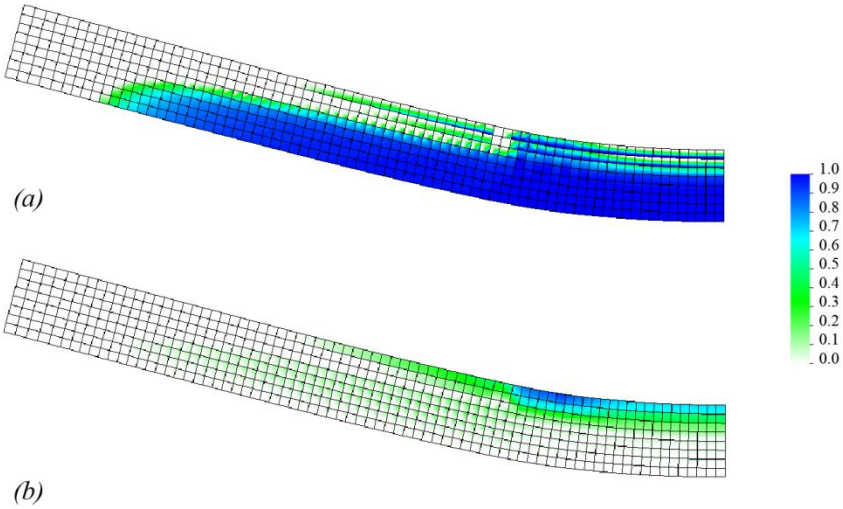

Figure 4.37 - Results for beam T9 at incipient failure (displacement near 100 mm). (a) positive damage contour; (b) negative damage contour

In Figure 4.35a and Figure 4.35b are reported the tensile damage contours at displacement of 1 mm and 2.2 mm respectively. The latter corresponds to the failure load. Figure 4.36 depicts the tensile and compressive stress contours at the failure load. In these figures is possible to see the formation of a compression damaged zone in the upper concrete layer that causes the failure mechanism. No plasticization

of the longitudinal reinforcements is recorded in the analysis. Similar contours were found in the numerical simulation of beams T5 and T6.

On the other hand, the beams T9 and T10, respectively with *a/d* equal to 7 and 8, show a typical flexural failure. In Figure 4.37(a) and (b) are reported the tensile damage contour and the compressive damage contour for beam T9 at incipient failure with a corresponding displacement near 100 mm. Moreover Figure 4.38(a) and (b) represent the positive and negative damage contours respectively for beam T10 at incipient failure. In both situations, the spread of the tensile damage in the lower central zone of the beams shows the effect of cracking due to flexural and shear forces. The large plasticization of the longitudinal reinforcement explains the ductile failure evidenced in Figure 4.34.

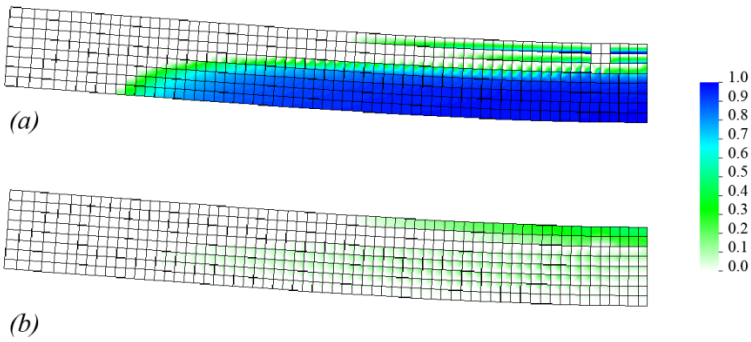

Figure 4.38 - Results for beam T10 at incipient failure (displacement near 100 mm). (a) positive damage contour; (b) negative damage contour

4.5.5 Shear walls tested by Maier – Thürlimann

In the following, the model proposed for reinforced concrete membranes is adopted to simulate the response of squat R/C shear walls tested by Maier and Thürlimann [12], that are selected as good example of the possible application of the proposed model. In particular, three shear walls, with a rectangular cross section (specimen S4) and two I sections (specimens S2 and S5), are reproduced by the developed membrane model. The walls underwent monotonic and cyclic horizontal quasi-static loadings. The experimental setup is shown in Figure 4.39. The panels are supported on a base block and loaded through a thick top slab.

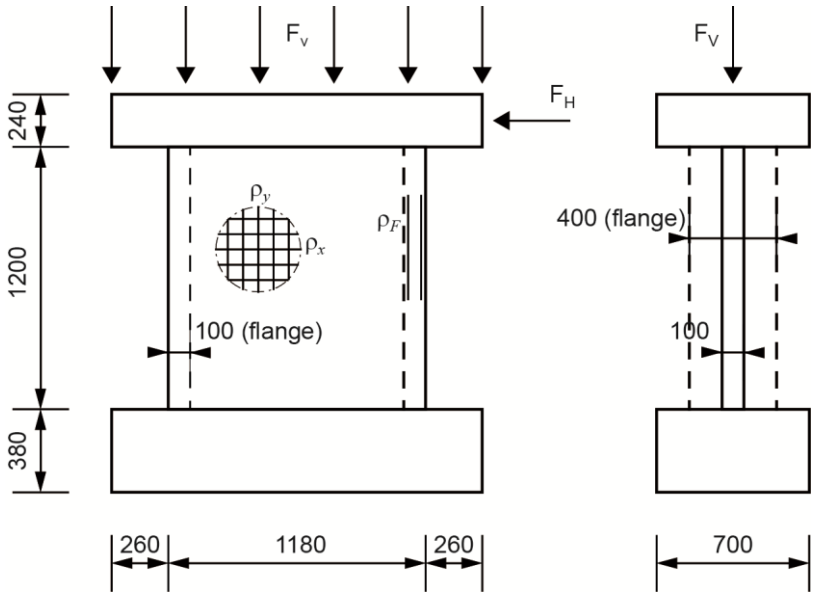

Figure 4.39 - Experimental setup of shear walls testes by Maier and Thürlimann [12]

4.5.5.1 Rectangular cross section under monotonic loading (Specimen S4)

The first specimen has a rectangular cross section and lies in a plane. The height of the wall is 1200 mm, the width is 1180 mm and the depth is 100 m (see Figure 4.39). The vertical reinforcement ratio is 1.05% and the horizontal one is 1.03%. The cylinder compressive concrete strength is 41.7 MPa and the splitting tensile strength is 2.70 MPa. The steel bars have tensile yielding strength of 574 MPa. The constant axial load is about 262 kN, while the horizontal load is increased monotonically up to failure.

The wall is modeled by a 6x6 mesh with 4 node quadrilateral elements. In Figure 4.40 is reported the comparison between the numerical and the experimental results in terms of load displacement curves.

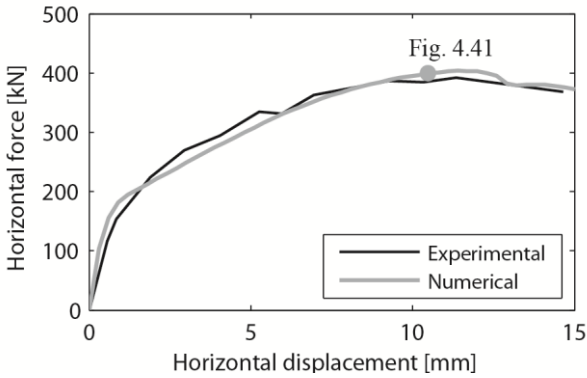

Figure 4.40 - Load-displacement curve for specimen S4 and comparison with experimental data

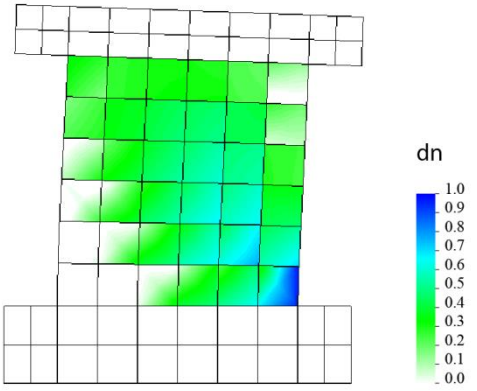

Figure 4.41 - Compressive damage contour at the horizontal displacement of 11 mm for panel S4

The model shows an initial linear response followed by the concrete cracking under the load of about 150 kN and the yielding of the vertical reinforcing bars in tension at the load of 300 kN and at the displacement of 5 mm. After the development of a moderate ductility the panel showed a shear failure due to the compressed concrete crushing. The deformed shape and the contour map of the negative damage parameter at the peak strength are presented in Figure 4.41. In this figure, the severe inelastic shear deformations and the progressive damaging of the diagonal concrete strut can be observed. The predicted failure mode is confirmed by the pictures attached to the experimental report [12] (see Figure 4.42).

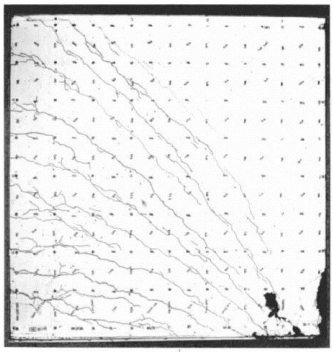

Figure 4.42 - Picture of specimen S4 at failure [12]

4.5.5.2 I cross section under monotonic loading (Specimen S2)

The second specimen tested has an I cross section. The height of the wall is 1200 mm, the web width is 980 mm while the flange width is 400 mm and the depth of both web and flanges is 100 mm (see Figure 4.39). The vertical reinforcement ratio is 1.16% and the horizontal one is 1.03%. The cylinder compressive concrete strength is 41.6 MPa and the splitting tensile strength is 2.29 MPa. The steel reinforcing bar mechanical properties are the same of the specimen S4. The constant axial load is about 1653 kN and the horizontal load was increased monotonically up to failure.

All the shear wall is modeled with the reinforced concrete membrane elements with thicker elements for the flanges. The wall web is modeled by a 6x6 mesh, while each flange has 1x6 mesh. The comparison between the numerical and the experimental results in terms of load displacement curves is pictured in Figure 4.43. The deformed shape and the positive damage parameter, depicted at the cracking load of about 500 kN in Figure 4.44, show that the first cracking pattern appear on the web in agreement with the experimental evidence. The tensile yielding of the vertical bars is reached at the load of about 800 kN and at the top displacement of about 5.8 mm.

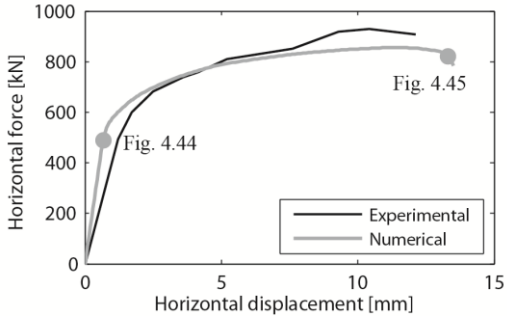

Figure 4.43 - Load-displacement curve for specimen S2 and comparison with experimental data

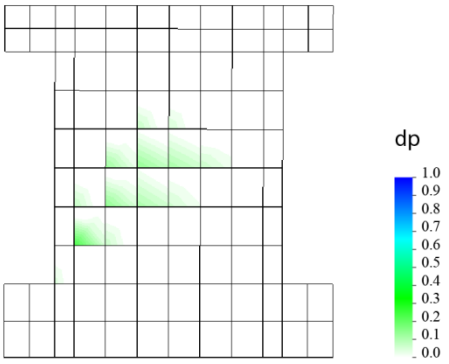

Figure 4.44 - Positive damage parameter at displacement of 0.7 mm for specimen S2

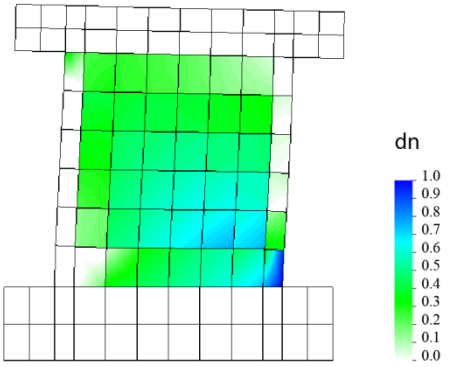

Figure 4.45 - Negative damage parameter at incipient failure for specimen S2

Figure 4.45 shows the deformed shape and the contour map of the compressive damage parameter at the horizontal displacement of about 13 mm. It can be immediately seen that the failure of the model is due to the compressed concrete crushing along the diagonal strut starting form one flange and progressing on the web. The damage pattern matches quite well the damage state of the specimen pictured in the experimental report [12].

4.5.5.3 I cross section under cyclic loading (Specimen S5)

The third specimen geometry and reinforcement configuration are similar to those of specimen S2 (see Figure 4.39). The cylinder compressive concrete strength is 43.2 MPa and the splitting tensile strength is 2.21 MPa. The steel reinforcing bar mechanical properties are the same of the specimen S4 and S2. The wall was

submitted to a constant axial load of 416 kN and to horizontal load reversals with cycles of increasing ductility.

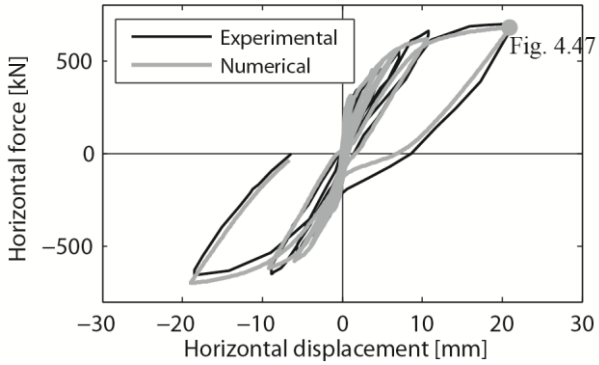

Figure 4.46 - Load-displacement curve for specimen S5 and comparison with experimental data

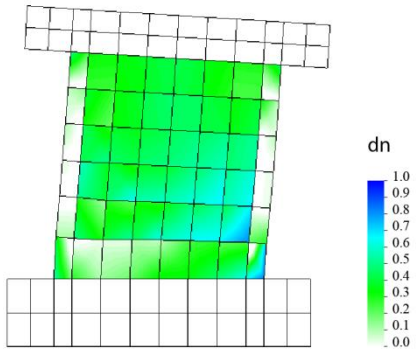

Figure 4.47 - Negative damage parameter at displacement of 20 mm for specimen S2

The comparison between the numerical and the experimental results in terms of load displacement curves is pictured in Figure 4.46. The numerical model reaches the cracking load at about 240 kN for a displacement of 0.4 mm. The yielding of the longitudinal displacement occurs at about 500 kN for a displacement of 5.1 mm.

The deformed shape and the distribution of the compressive damage parameter are shown in Figure 4.47 for the positive maximum displacement of 20 mm. The compressive damage parameter approaches the unit in the compressed flange and high values in the web element close by. The comparisons between the damage contour and the specimen damage state [12] (see Figure 4.48) confirms the accuracy and the potentiality of the developed membrane model.

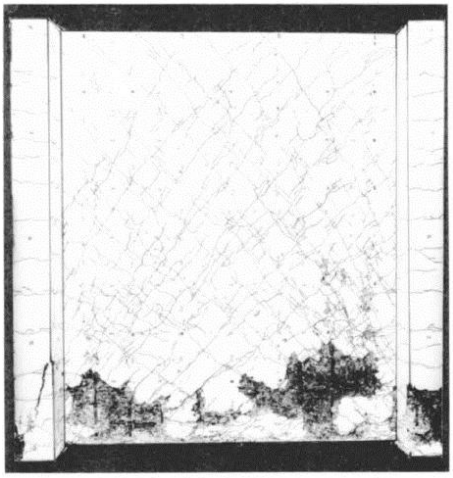

Figure 4.48 - Picture of specimen S5 at failure [12]

4.6 Plate Model for R/C panels

The present paragraph introduces the definition of the inelastic RC shell model accounting for the interaction of in-plane membrane, out-of-plane bending and shear actions.

The 4-node MITC element by Bathe and Dvorkin [13] based on Mindlin/Reissner plate theory is employed. Such element is exempt from shear locking and has provided excellent results in linear analysis, geometrically nonlinear analysis (Bathe and Dvorkin [14]) as well as in inelastic analysis (Dvorkin [15]) of plates and shells. A 2x2 Gauss numerical integration evaluates the element stiffness matrix and force vectors in the mid-surface of the element. The response of each integration point accounts for the presence of concrete and reinforcing bars in the section as it will specified herein.

The concrete section is modeled by the continuum plastic-damage constitutive law presented in CHAPTER 3: condensing the normal stress perpendicular to the element plane. The algorithm of de Borst [16] is implemented to obtain an efficient static condensation. The integration over the thickness of the section adopted to compute the stress resultants is performed with a mid-point integration rule. In fact Gauss-type numerical integration schemes across the thickness show higher sensitiveness because the stress fields have discontinuous derivatives (Kostic and Filippou [17]). In the following examples, 11 mid-points are used through the thickness for the concrete material.

Similarly to the membrane model, the reinforcing bars are simulated with a smeared embedded approach by placing appropriate layers in different positions across the element thickness. Each reinforcement layer satisfies the kinematic of the shell element and has uniaxial response along the direction of the bars. According to these hypotheses the present model doesn't consider steel-concrete bond slip and bar dowel action. The number and the position of steel layers within the section as well as the rebar orientations are all model input parameters to represent most common reinforced concrete configurations.

For a steel layer the material state determination starts with the projection of the generic total strain tensor ε in the direction of the bars. With the direction cosines **m** of the bar orientation φ the total strain of the steel bar is:

$$\varepsilon_{\varphi} = \boldsymbol{\varepsilon}\,\mathbf{m}\cdot\mathbf{m} \tag{4.4}$$

The strain ε_{φ} is used for the determination of the uniaxial steel stress in accordance with the constitutive relation for the reinforcing steel. The material state in terms of steel stress and tangent modulus is rotated back to the original element reference frame with the following operations:

$$\boldsymbol{\sigma}_s = \sigma_{\varphi}\,(\mathbf{m}\otimes\mathbf{m}) \tag{4.5}$$

$$\mathbf{C}_s = C_{\varphi}\,(\mathbf{m}\otimes\mathbf{m}\otimes\mathbf{m}\otimes\mathbf{m}) \tag{4.6}$$

A schematic representation of the presented model is depicted in Figure 4.49, where the integration points of concrete are shown in Figure 4.49a, and the additional integration points of reinforcing steel are illustrated in Figure 4.49b.

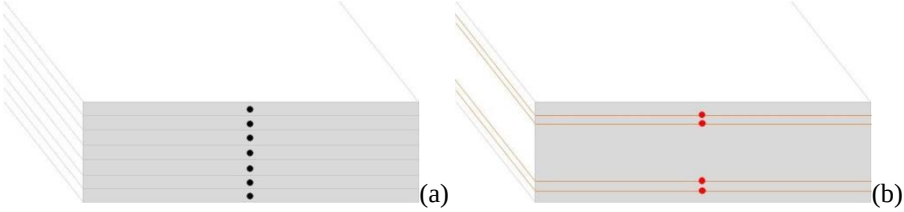

Figure 4.49 - Schematic representation of the R/C plate model

4.7 Validation studies for R/C plate model

In the present section some experimental tests are simulated in order to show the suitability of the proposed model for the simulation of reinforced concrete plates

In particular, a slab subjected to combined in-plane and out-of-plane forces is first presented. The results are shown to be quite good in representing the experimental behavior. The second application is a box shear wall tested by the Japan Nuclear Energy Safety Organization. The results are quite good in representing the overall

experimental behavior. The third application is a U-shaped shear wall testes in Ispra under cyclic forces in the principal directions of the wall. The results are shown to be acceptable.

4.7.1 Reinforced concrete slab

A set of reinforced concrete slabs under combined compressive in-plane and lateral loads was tested by Ghoneim and MacGregor [18]. The specimen C2 is selected for simulation because of the availability of extensive measurements of reinforcing bar strains. The specimen is a square slab with side dimension of 1829 mm and thickness of 67.6 mm. It is reinforced with upper and lower grids of hot rolled steel bars parallel to the specimen edges. The total reinforcement ratio is 0.77% in both directions.

The concrete compressive cylinder strength is 25.27 MPa and the splitting tensile strength is 2.32 MPa. The reinforcing steel has an ultimate strength of 620 MPa and the 0.2% offset yield strength was 450 MPa.

The specimen is simply supported along the four edges with unilateral constrain and it is subjected to a constant uniaxial in-plane compressive load of about 1196 kN (referred as longitudinal direction that is orthogonal to the so-called in-plane transverse direction) and to an increasing out-of-plane load equally distributed in 9 loading points to simulate an out-of-plane uniform pressure.

Taking advantage of the symmetry of the specimen only a quarter of slab is modeled with a 6x6 mesh of four-node shell elements. The section solicitation and stiffness are integrated over the thickness with eleven integration points for the concrete material and four additional integration points for the reinforcement meshes.

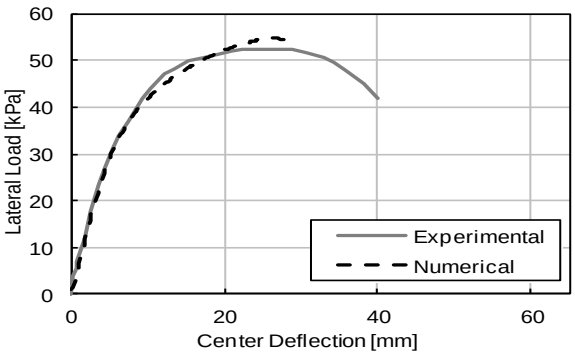

Figure 4.50 – Load-center deflection curves for numerical and experimental results

In Figure 4.50 are depicted the lateral load vs. center deflection curves where the vertical axis represents the equivalent average transverse pressure applied to the

slab. It can be seen that the model represents the global behavior of the experiment quite good in terms of stiffness, failure load and the corresponding displacement.

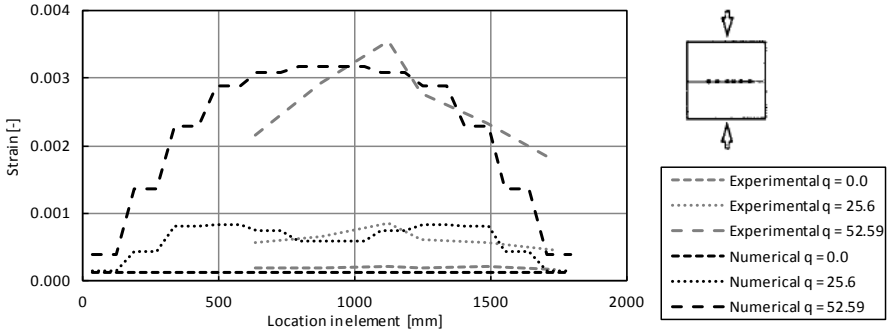

Figure 4.51 - Strains along bottom transverse bar at center of specimen and comparison with experimental data

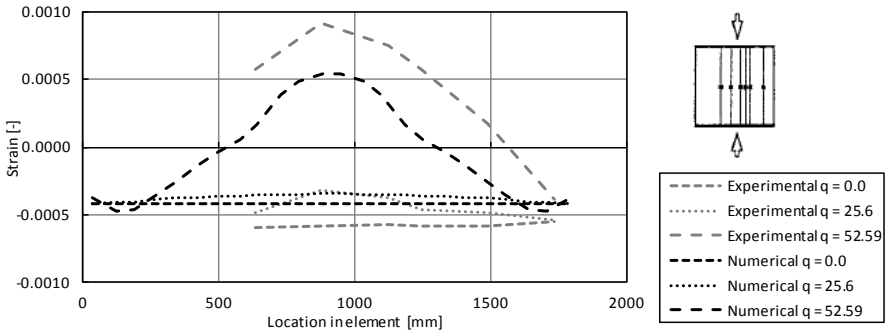

Figure 4.52 - Strains at center of specimen in bottom bars running in the direction of in-plane load and comparison with experimental data

Figure 4.51 shows the axial strains of a bottom bar, aligned in the transverse direction passing by the center of the specimen, while Figure 4.52 displays the axial strains of different bottom bars aligned in the longitudinal direction also passing by the center of the specimen.

In Figure 4.53 the distribution of the positive damage parameter in the bottom (11^{th}) layer is depicted at incipient failure. In this figure the vertical axis coincides with the longitudinal direction while the horizontal axis corresponds to the transverse direction. Moreover the picture of a similar specimen (specimen CE3) is reported as a comparison with the tensile damage contour.

The cracking onset happens at about 6 kPa of lateral load in the middle of the bottom layer. The compression stresses approaches the peak strength at about 45 kPa. The upper compressive steel layer in the longitudinal direction yields in the middle of the slab at about 52 kPa and at a mid-deflection of about 25 mm while the

lower tensile steel layer in the transverse direction yields in the middle of the slab when the slab strength is reached at about 54 kPa and at a mid-deflection of about 27 mm. Comparing the numerical results with the experimental data it is possible to see that the numerical model seems to be able to capture the initial stiffness as its progressive degradation as well as the following hardening behavior until the flexural strength is reached for crushing of the upper concrete at the top-center of the slab in the direction of the applied constant in-plane load. The stresses along the bottom steel bars in both directions, at different loading steps, confirm that the model is quite satisfactory able to represent the actual local response. Finally the contour map of the positive damage parameter at the bottom layer represents the location of the concrete cracking. Such image confirmed an excellent qualitative tool if compared with the pictures of the failed specimen [18].

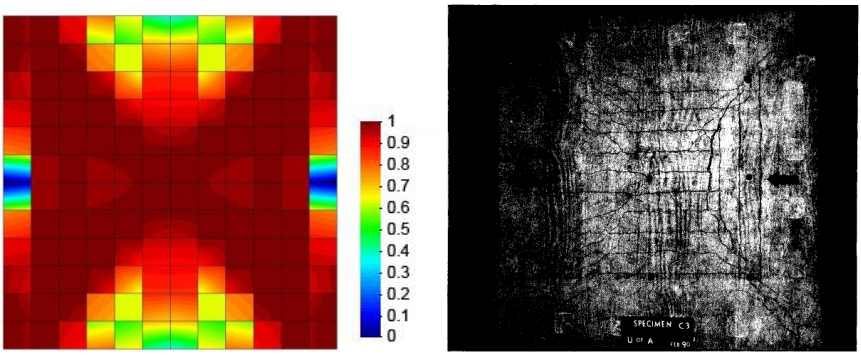

Figure 4.53 - Distribution of positive damage in the bottom layer of the specimen and comparison with the picture of a similar panel

4.7.2 Box-shaped shear wall

Pseudo-static cyclic and dynamic shaking table tests on RC box-type shear walls were conducted by the Japan Nuclear Energy Safety Organization (Habasaki, A., et al., [19]). The U.S. Nuclear Regulatory Commission staff considers the JNES test data benchmarks for validations or confirmations of the adequacy of analytical methods or computer programs for the seismic response analysis of Nuclear Power Plant shear wall structures.

The specimen SD-08 is a box 1.0 m high with 1.5 m square section and it is capped with the reinforced concrete top loading slab and a base slab. The slabs have a plan dimension of 2.7 m x 2.7 m. The base slab has a thickness of 0.5 m, while the top loading slab is 0.4 m thick. The thickness of the wall is about 0.075 m and is constant on each side. The reinforcement ratio in both vertical and horizontal direction is about 1.2% and it is made by double-fold in 0.070 m pitch. The vertical reinforcing bars of the specimen are sufficiently extended into the loading slabs to

ensure adequate load transfer to the shear walls. The concrete has a compressive strength of 34.9 MPa and the reinforcing bars have yield strength equal to 375 MPa. A vertical gravity load of 670 kN is applied and kept constant during all the test period. Multiple loading cycles were applied to the specimen to reach specific horizontal target deformations in terms of the shear strain: 0.5, 1.0, 2.0, 4.0, 6.0 and $8.0x10^{-3}$ rad each repeating twice in both positive and negative directions within one cycle. The cyclic load is applied parallel to a couple of shear walls.

The numerical results are showed by the shear load-displacement curve in Figure 4.54. The tensile damage contour map after the completion of the first loading cycle depicted in Figure 4.55 displays the diagonal cracking of the walls parallel to the load due to the shear stresses. The compressive damage parameter contour map during the last cycle (at a shear strain of about $-8.0x10^{-3}$) pictured in Figure 4.56 shows the model failure for concrete crushing due to the combined flexure and shear actions in the plane of the walls parallel to the horizontal load. The deformed shape evidenced a concentrated high shear deformation in the bottom part of the wall.

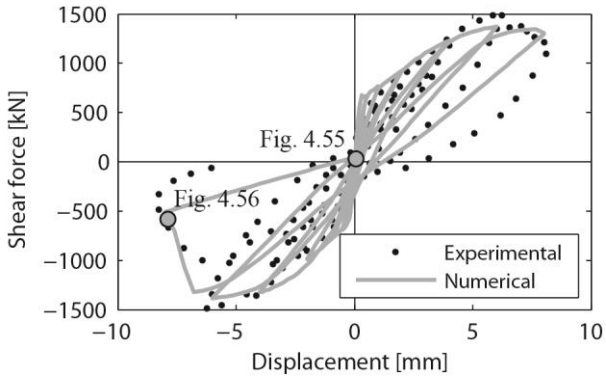

Figure 4.54 - Load-displacement curve for box-shaped shear wall and comparison with experimental data

The initial stiffness of the model appears to be 20% higher respect to the experimental one; the difference probably depends on the initial micro-cracks induced by shrinkage. The onset of cracking in the numerical model appears at the bottom corner of the tensile part for an horizontal load of about 400 kN and it is rapidly followed by a shear diagonal cracking of the walls parallel to the load (at about 500 kN). The yielding of the horizontal bar happens when the applied load reaches the value of about 1220 kN and the displacement is about 4.0 mm. The maximum strength of the model is about 1400 kN at the displacement of about 6.0 mm. The model exhibits a shear failure followed by an evident sliding of the wall in a section a little higher respect to the basement.

Although some discrepancy between numerical and experimental results is evident, the model was quite capable to represent the inelastic behavior under cyclic loading with good accuracy in the evaluation of the post cracking behavior and the strength. An important result for practical engineering considerations is the correct evaluation of the shear failure for concrete crushing followed by a significant sliding that represented well the experimental evidence. The damage parameter contour maps help the analyst in interpretation of the failure mechanisms as they clearly evidence the accumulation of damage during the analysis. Furthermore they also match very well the pictures of the tested specimen from the quality stand point.

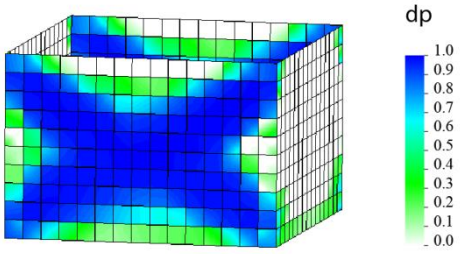

Figure 4.55 - Positive damage distribution after the first cycle is complete

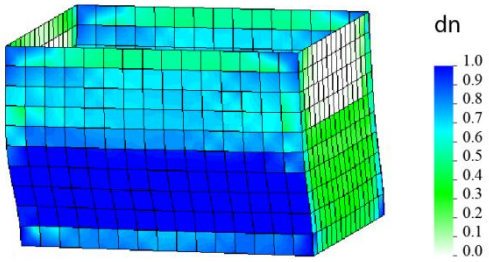

Figure 4.56 - Negative damage distribution during at incipient failure during the last loading cycle

4.7.3 U-shaped shear wall

Quasi-static cyclic tests on RC U-shaped shear walls were conducted at the reaction wall facility of the ELSA Laboratory (Pégon et al. [20]). The experimental program consisted in a cyclic quasi-static test in Y direction (parallel to flanges), a cyclic test in X direction (parallel to the web), and a bi-axial test in X and Y directions. The simulation of the cyclic bi-axial experiment is considered here because it is the most severe test for the developed model.

The height of the wall is 3600 mm while the section is a U-shape with size of 1500 mm x 1250 mm and thickness of 250 mm. The top section ends in a transversal concrete plate with a thickness of 600 mm.

The concrete has a compressive strength of about 20.8 MPa. Various reinforcing steel bar diameters have been used with an average yield strength of about 520 MPa. In Figure 4.57 is illustrated the cross section geometry with the reinforcement arrangement. For a detailed description of the specimen and the reinforcement cage the reader is referred to the test report [20].

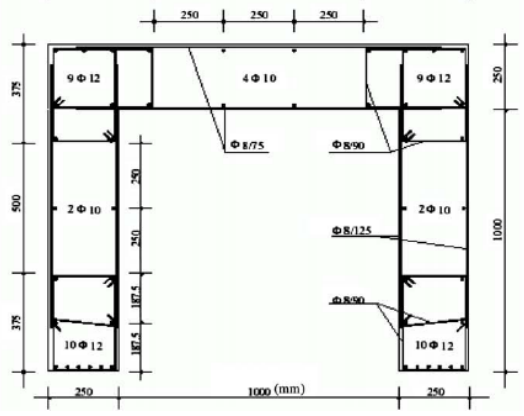

Figure 4.57 - Section scheme with reinforcement detail [20]

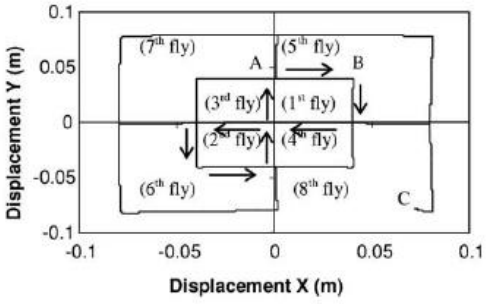

Figure 4.58 - Load history applied to the U-shaped wall

The specimen is subjected to the quasi-static horizontal loads imposing top cyclic displacements in the two principal directions of the U-shaped section according to a butterfly path of 16 rectilinear segments. In particular, two butterfly cycles with increasing amplitudes of 40 mm for the first path and 80 mm for the second path are imposed to the shear wall (see Figure 4.58). The torsion is constrained through the top transversal plate and the load in X direction is orthogonal to the symmetry plane. Hence a complex non-linear warping was reported by the investigators. The specimen failed before the end of the second butterfly cycle during the last fly.

The experimental results are compared in Figure 4.59 in terms of force-displacement curves for the direction parallel to web (i.e. x direction) and in Figure 4.60 for the direction parallel to flanges (i.e. y direction).

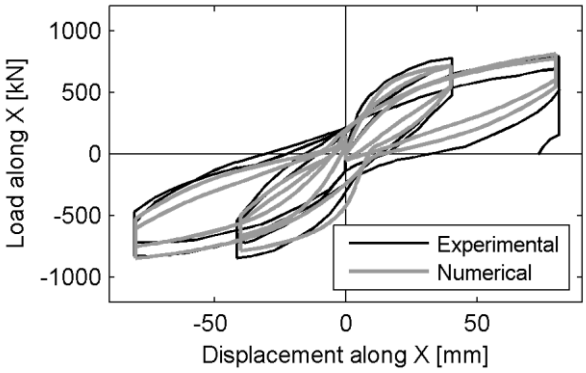

Figure 4.59 - Load-displacement curve of U-shaped wall and comparison with experimental data along x direction (parallel to web)

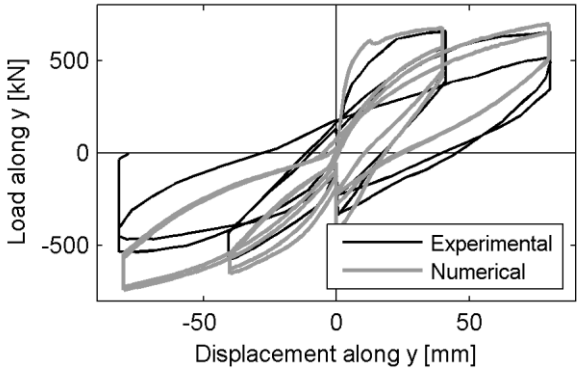

Figure 4.60 - Load-displacement curve of U-shaped wall and comparison with experimental data along y direction (parallel to flanges)

As it can be seen the model represents well the global behavior of the specimen in X direction and in +Y direction, while the strength of the panel is overestimated in –Y direction. The investigators reported the buckling of reinforcing steel bars near the edge of the flanges when loading the wall in –Y direction for a displacement of 80 mm correspondent to the amplitude of the second butterfly cycle. The present model doesn't take into account this phenomenon. The use of a steel model including the reduction of resistance in compression due to buckling would surely improve the accuracy of the results.

In Figure 4.61 is reported the comparison between experimental and numerical results in terms of local deformations measured at the base edge of the two flanges.

The model seems to overestimate the local deformations of the shear wall. It is worth noting that strain localization is expected with all model having local softening behavior. The adopted regularization technique and described in previous chapter, assurers the mesh-independency only in terms of global response. The use of a non-local regularization method could improve the accuracy of the representation of the local behavior at the cost of a considerably higher computational effort.

Finally in Figure 4.62 are reported the deformed shape and the contour of the compression damage parameter at a top displacement of -40 mm in both directions. The picture helps the detection of the damaging process of the model. In particular the onset failure mechanism takes place in the bottom section of the web because of the combined flexural and shear actions. This is in agreement with the experimental evidence [20].

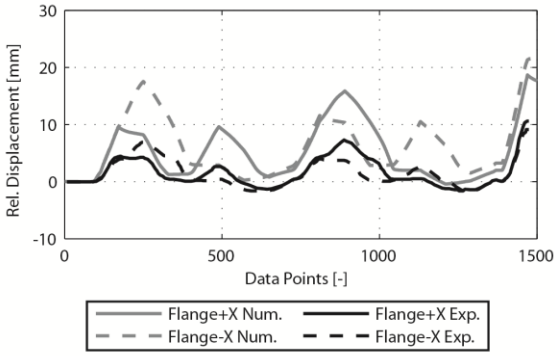

Figure 4.61 - Experimental and numerical deformations at the base edge of the flanges for U-shaped wall

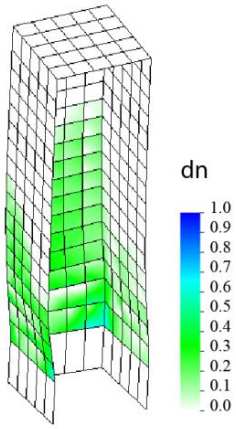

Figure 4.62 - Negative damage distribution at displacement of -40 mm in both directions

Concluding, it is possible to see that the model is able to represent quite acceptably the observed experimental behavior, demonstrating its suitability for application on real structures.

4.8 References

[1] McKenna, F., Fenves, G.L., Scott, M.H., Jeremic, B. (2000). Open System for Earthquake Engineering Simulation (OpenSEES). *Pacific Earthquake Engineering Research Center*, University of California, Berkeley

[2] Prata, S. (2004). C++ Primer Plus, *5th edition*, Sams Publishing

[3] Filippou, F.C., Popov, E.P., Bertero, V.V. (1983). Effects of Bond Deterioration on Hysteretic Behavior of Reinforced Concrete Joints, *Report EERC 83-19*, Earthquake Engineering Research Center, University of California, Berkeley

[4] Taucer, F.F., Spacone, E., Filippou, F.C. (1991). A fiber beam-column element for seismic response analysis of reinforced concrete structures, *Report UBC/EERC 91-17*, Earthquake Engineering Research Center, University of California, Berkeley

[5] Spacone, E., Filippou, F.C., Taucer, F.F. (1996). Fibre beam-column model for non-linear analysis of R/C frames. Part I: formulation, *Earth. Eng. Struct. Dyn.*, 25, 711-725

[6] Feenstra, P.H. (1993). Computational aspects of biaxial stress in plain and reinforced concrete. *PhD Thesis*, Technische Universiteit Delft, The Netherlands

[7] Simioni, P. (2009). Seismic response of reinforced concrete structures affected by reinforcement corrosion. *PhD Thesis*, University of Florence-University of Braunschweig, Italy-Germany

[8] Bhide, S.B., Collins, M.P. (1987). Reinforced concrete elements in shear and tension, *Publication No. 87-02*, Department of Civil Engineering, University of Toronto

[9] Mansour, M., Hsu, T.T.C. (2005). Behavior of reinforced concrete elements under cyclic shear. I: experiments, *J. Struct. Eng. ASCE*, 131, 44-53

[10] Vecchio, F.J., Collins, M.P. (1986). The modified compression-field theory for reinforced-concrete elements subjected to shear, *ACI Journal*, 83, 219-231

[11] Leonhardt, F., Walter, R. (1962). Beiträge zur Behandlung der Schubprobleme im Stahlbetonbau, *Beton und Stahlbeton*, 2

[12] Maier, J., Thürlimann, B. (1985). Bruchversuche an Stahlbetonscheiben, *Birkhäuser Verlag Basel*, Switzerland

[13] Bathe, K.J., Dvorkin, E.N. (1985). A Four-Node plate bending element based on Mindlin/Reissner plate theory and a mixed interpolation, *Int. J. Num. Meth. Eng.*, 21, 367-383

[14] Bathe, K.J., Dvorkin, E.N. (1986). A formulation of general shell elements – the use of Mixed Interpolation of Tensorial Components, *Int. J. Num. Meth. Eng.*, 22, 697-722

[15] Dvorkin, E.N. (1995). Nonlinear analysis of shells using the MITC formulation, *Arch. Comput. Meth. Eng.*, 2, 1-50

[16] De Borst, R. (1991). The zero-normal-stress condition in plane-stress and shell elastoplasticity, *Commun. Appl. Numer. M.*, 7, 29-33

[17] Kostic, S.M., Filippou, F.C. (2012). Section discretization of fiber beam-column elements for cyclic inelastic response, *J. Struct. Eng., ASCE*, 138, 592-601

[18] Ghoneim, M.G., MacGregor, J.G. (1994). Tests f reinforced concrete plates under combined in-plane and lateral loads, *ACI Struct. J.*, 91, 19-41

[19] Habasaki, A., Kitada, Y., Nishikawa, T., Takicuchi, K., Torita, H. (2000). Multi-Directional Loading Test for RC seismic shear walls, *12th World Conf. Earth. Eng. (WCEE)*, Auckland, New Zeland

[20] Pégon, P., Plumier, C., Pinto, A., Molina, J., Gonzales, P., Tognoli, P. Hubert, O. (2000). U-shaped-wall: description of the experimental set-up, *Report*, Joint Research Center (J.R.C), Ispra, Italy

CHAPTER 5:
COUPLED ENVIRONMENTAL-MECHANICAL DAMAGE MODEL

The problem of durability has become a crucial problem during the last decades. It is widely acknowledged that a durable design is a critical aspect especially for reinforced concrete structures. Moreover the importance of maintenance, inspection and, if necessary, rehabilitation interventions has been recognized.

Especially for existing structures, the need of theoretical and numerical procedures that take into account both the mechanical-structural performance and the durability aspects during the whole service life of the structure are strongly required.

To this aim in previous works by Saetta et al. [10], [11], [5], [6], Saetta [7] a coupled environmental-mechanical damage model has been proposed to take into account the effects of some of the most typical degradation processes that affect reinforced concrete structures, e.g. carbonation-induced and chloride-induced corrosion, sulfate attack.

In the first part of the chapter, the most common degradation processes that affect reinforced concrete are briefly recalled. Then the coupled mechanical-environmental damage model is presented and extended in order to take into account the effect of physical deterioration of concrete due to freeze-thaw cycles. Indeed, freezing and thawing cycles have highly damaging effects on concrete structures especially in cold climate regions [1], [2], [3]. It is widely acknowledged

that two different types of frost damage can be distinguished (e.g. [1], [4]): internal damage, which causes microscopic cracks in the cement paste affecting the mechanical properties of the material, and external damage, also known as surface scaling, which affects the superficial zone of concrete and mainly occurs in presence of saline solution of weak concentration. In this chapter, an original formulation for dealing with the first type of damage, which may lead to severe consequences on the structural performance, is proposed.

5.1 Degradation processes on RC structures

Reinforced concrete structures may suffer during their service life of degradation mechanisms which may alter the material characteristics leading to a modification of their serviceability and their safety factor with respect to ultimate conditions.

Several reinforced concrete constructions are actually affected by visible signs of deterioration; in most cases this happens in aggressive environments (e.g. industrial scenario) or when poor quality materials are adopted during construction.

Two main types of degradation may involve reinforced concrete structures:

- corrosion of reinforcement;
- degradation of concrete.

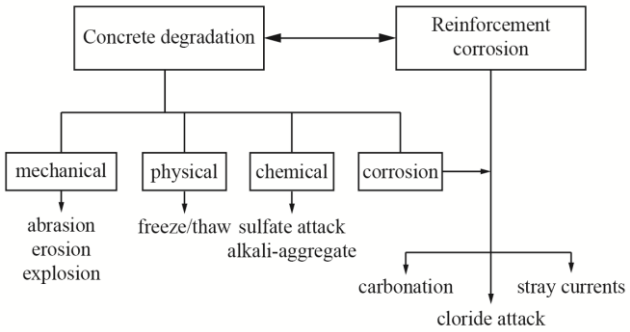

Figure 5.1 - Schematic classification of degradation processes on reinforced concrete structures

The distinction in those categories is arbitral and actually the two categories are intrinsically related each other [8]. A schematic representation is given in Figure 5.1.

5.1.1 Corrosion of reinforcement

Corrosion of reinforcement is generally caused by chloride ions penetration, by carbonation of concrete, or by the presence of stray currents [8], [9]. Carbonation is caused by the penetration of carbon dioxide into the concrete pore system and the consequent chemical reaction with calcium hydroxide of hydrated cement with the formation of calcium carbonate. Moreover the reaction needs the presence of oxygen and water to be activated [9]. It is worth noting that this reaction is generally not harmful for concrete, but the main consequence of it is the reduction of pH-value of the pore solution under a value near 9 leading to the depassivation of reinforcement, i.e. the destruction of the passive film which protects the bars against corrosion.

Chloride ions penetration on the other hand is a complex phenomenon involving many factors. Previous researches evidenced that the main parameters that should be considered when studying chloride-induced corrosion are the diffusion characteristics of concrete, its chloride-binding capacity [10], [11], the corrosion rate, and the diffusion of corrosion products [12].

The local effects of corrosion are the steel section reduction, the increasing of its brittleness with a significant reduction of its ultimate strain [13]-[16], degradation of bond, and the degradation of concrete cover caused by radial pressure generated by corrosion products. Moreover the global effects of corrosion on the structural behavior of the reinforced concrete elements include the reduction of load-carrying capacity, the reduction of ductility that may even modify the failure mechanism from ductile to brittle [17].

These aspects have been studied by many researchers both from the experimental and the numerical point of view during last decades. In particular, recent studies (e.g. [12], [18]) seem to demonstrate that the degradation of concrete cover caused by corrosion products may be correlated with the rate of artificially induced corrosion leading to a more severe damage with highly accelerated tests. The reason could be that rust is able to migrate in concrete pore system and cracks, if the corrosion rate is sufficiently low. Thus, during modeling of this phenomenon, it should take into account the migration of corrosion products. For instance in [12] the researchers showed that including the equation of rust migration, the degradation of concrete around the bar due to expansive products is less pronounced and the numerical response of the pull-out test is more adherent to experimental observations [18].

5.1.2 Degradation of concrete

The degradation of concrete may be divided in two main categories: physical and chemical degradation [19]. The fundamental difference between the two categories is that physical attacks do not involve any chemical reaction, while chemical attacks consist on a harmful chemical reaction that leads to mechanical consequences on the material.

The alkali-aggregate deterioration is a chemical degradation process since it involves the chemical reaction between the alkali in the cement paste and the silica and carbonate of the aggregates leading to alkali-silica reaction and alkali-carbonate reaction respectively. These reactions result in a volumetric expansion which may cause micro-cracks around aggregate. Moreover for alkali-silica reactions a gel layer around the aggregate is created and it attracts water inducing cracks due to osmotic

pressure [20]. Thus the alkali-aggregate reaction leads to a mechanical effect on concrete (i.e. cracks and expulsion of material).

Also the sulfate attack is a chemical degradation and involves the chemical reaction between the cement paste and sulfates. In fact concrete may be exposed to sulfates which can be often found in soil and groundwater. The reaction is actually divided in two steps: during a first step sulfates react with calcium ions to form gypsum, while during second step gypsum reacts with calcium aluminates and forms calcium sulfoaluminates. Both these reactions produce a volumetric expansion which may lead to micro-cracking of concrete which generally involves the zone near the surface [20].

The physical degradation processes don't involve any chemical reaction. They include for instance abrasion, erosion and freeze/thaw cycles. Some authors include abrasion and erosion into a mechanical category (Figure 5.1). But this distinction is beyond the scope of this work.

Abrasion and erosion have similar effects on concrete but have different causes: while the former is generally the result of dry friction on the concrete surface, for instance as result of traffic vehicle or pedestrians, the latter is commonly associated to the friction on concrete surface caused by the contact with fluids which may contain small solid particles. For instance erosion may be expected to happen in concrete elements exposed to strong wind actions or to running water.

Frost damage is an extremely dangerous degradation process which can affect concrete. The damage induced by this mechanism is generally of a character that makes concrete almost impossible to repair. It is widely acknowledged that two different types of frost damage can be distinguished (e.g. [21], [22]): internal damage, and surface scaling. While the first is caused by the freezing of water contained in the pore system of concrete, the second is mainly caused by freezing of the concrete surface when it stays in contact with weak concentration saline solutions. It was observed that freezing of concrete in pure water often leads to internal damage but can seldom lead to surface scaling too. On the other hand freezing of concrete in contact with salt solution in surface leads generally to surface scaling, but it seldom leads to internal damage. This is illustrated schematically in Figure 5.2 taken from [21].

The effects of surface scaling are mainly the reduction of concrete cover which may lead in serious cases to a big effect on the anchorage capacity of steel bars. Moreover it generally affects the service life of the structure with regard to reinforcement corrosion due to the concrete cover reduction [22].

The mechanisms of internal frost action have been studied since the middle of last century and different theories were proposed to describe the frost damaging process.

Among these theories that describe the mechanisms of frost action, some of them have gained quite a wide acceptance. In particular the first mechanism proposed is the hydraulic pressure theory by Powers ([4], [23]). According to this theory, when concrete is critically saturated, which is when approximately 91% of its pores are filled with water, and is subjected to freezing, the volume expansion of freezing water (that is +9% of volume) is restrained by the lack of space in the pore system of concrete; the excess water is driven off by the hydraulic pressure which depends on the length of the flow path, the rate of freezing, the permeability of concrete. Powers proposed the following relation to evaluate the hydraulic pressure [21]:

$$P_h = 0.09 \cdot \left(\frac{dW_f}{dt} \right) \cdot \left(\frac{1}{K} \right) \cdot f(x) \qquad (5.1)$$

where P_h is the internal hydraulic pressure, dW_f/dt is the rate of ice formation, K is the permeability of concrete and $f(x)$ is a measure of the maximum distance of flow of expelled water.

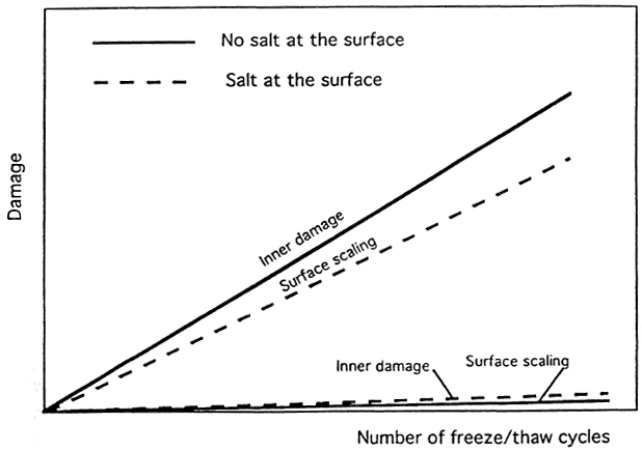

Figure 5.2 - Schematic representation of two main types of frost damage (From [21])

Another important theory well established in literature is the microscopic ice crystal growth mechanism applied to concrete by Powers and Helmuth [24]. When water in capillary pores freezes a free energy differential between ice and unfrozen water exhibits. Indeed at a temperature lower than 0°C, the unfrozen water has a higher free energy than ice. This free energy differential leads to the flow of unfrozen water from finer pores to the capillary pores in which the ice crystals are forming. When water reaches the crystals, it freezes itself. Thus, the ice crystals growth and may press the pore wall. The process can stop when the energy of ice is equal to the energy of unfrozen water. This mechanism considers the fact that when a low

temperature is kept constant expansion of concrete can occur, which cannot be considered by the hydraulic pressure mechanism.

Another accepted theory for describing the frost damaging process is the so called osmotic pressure. According to this mechanism, the solution surrounding ice in a pore has a high concentration of alkalis. Thus a flow starts from nearby water to the solution due to the difference in solute concentration [25].

In reality there is probably a combined effect of all these mechanisms, but understanding which one is dominant can be difficult [21].

The effects of the internal damage mechanism mainly affect elastic modulus, compressive and tensile strength, fracture energy and bond between concrete and bars, e.g. [1], [4] ÷ [28], and may cause a relevant reduction of load carrying capacity and stiffness of the structure, and even a change in its failure mode. Such effects are still under investigation, and to the writer's knowledge only few studies and models have been developed to capture the performance of concrete structure subjected to frost degradation, e.g. [26] ÷ [28].

5.2 Coupled environmental mechanical damage model

In order to take into account the mechanical effect of a chemical attack in concrete structures, a coupled chemical-mechanical damage model has been developed by Saetta et al. [5], [6], by introducing an additional internal variable, called *environmental damage* in the stress-strain relationship. This model is schematically represented in Figure 5.3.

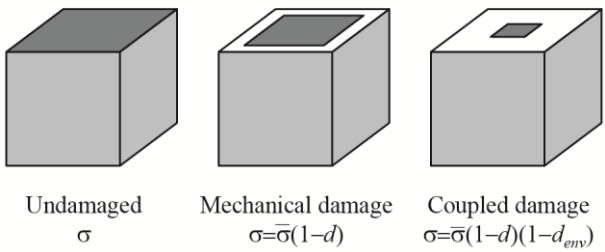

Figure 5.3 - Resisting Surface of (a) undamaged specimen (b) mechanically damaged specimen (c) specimen subjected to couple chemical-mechanical damage

In the original formulation the environmental damage parameter was a function of the degree of development of the chemical reaction $\Re$ and the relative residual strength φ of the material (due only to the chemical phenomena) according to the following [5]:

$$d_{chem} = (1-\varphi) - \frac{1-\varphi}{1+(2\Re)^4} \tag{5.2}$$

Equation (5.2) is depicted in Figure 5.4 for different values of the parameter φ.

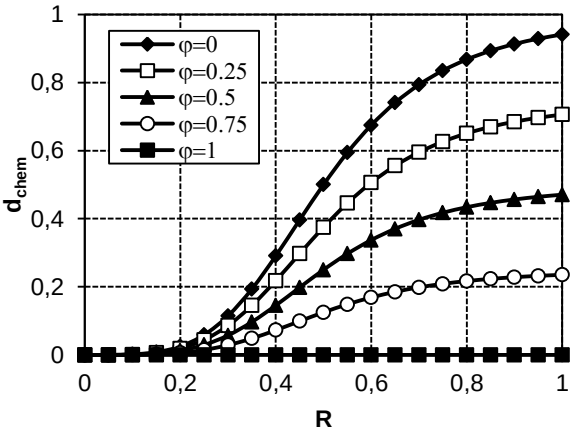

Figure 5.4 - Evolution of damage variable d_{chem} with different values of φ

It is clear that when $\varphi = 1$ the residual strength of the material is equal to the initial strength of the sound material and therefore the related environmental damage parameter is equal to zero.

Since the damage parameter was related only to the chemical deterioration, it was named as d_{chem}. In this work the formulation of the environmental damage was enhanced to include also the effect of physical damage phenomena, such as internal frost degradation. Therefore the damage parameter $d_{chem,}$ was renamed with the more appropriate symbol d_{env} in order to extend its meaning.

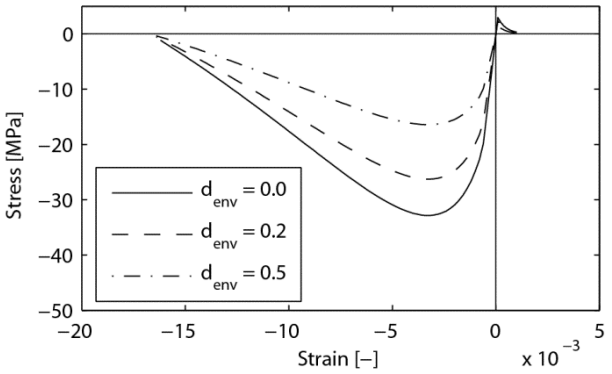

Figure 5.5 - Effect of d_{env} on stress-strain constitutive law

With this assumption the relationship (3.31) becomes:

$$\boldsymbol{\sigma} = (1-d_{env})\left[(1-d^{+})\bar{\boldsymbol{\sigma}}^{+} + (1-d^{-})\bar{\boldsymbol{\sigma}}^{-}\right] = (1-d^{*+})\bar{\boldsymbol{\sigma}}^{+} + (1-d^{*-})\bar{\boldsymbol{\sigma}}^{-} \tag{5.3}$$

where d^{*+} and d^{*-} are the coupled damage parameters. Independent from its specific definition, the environmental damage parameter is represented by an increasing function with time, which means $\dot{d}_{env} \geq 0$, and to act in the same way in tension and in compression. In Figure 5.5 is depicted the stress strain curve for concrete at different levels of deterioration, i.e. for different values of d_{env}.

The environmental damage induced by frost degradation is evaluated as a function of the number N of the freeze-thaw cycles (FTC).

5.3 Modeling of some common degradation processes

A brief description of the main characteristics, the basic concepts and the abilities of the original coupled environmental-mechanical are reported in this section. In particular after a recall of the diffusion model adopted, the application to degradation processes that can be studied is briefly presented. The model can be effectively adopted to simulate diffusive processes that lead to the damage of concrete producing expansive phenomena, like sulfates and calcium chloride. Similarly, the simulation of diffusion processes that lead to reinforcement corrosion, like carbonation phenomena and chlorides, has been profitably performed with the model.

The environmental damage parameter originally presented by Saetta et al. [5], [6], [7] is assumed to be strongly related to the diffusion process and to the chemical reaction between pollutant and cementitious components. Indeed, the diffusion model based on the works of Bazant and Najjar [29], Saetta et al. [10], [11] takes into account the coupling of moisture, heat and pollutant (e.g. CO_2, Cl^-, $SO_4^{=}$) flows through concrete, including the possible chemical reactions between cementitious constituents and the aggressive species.

The governing equations of moisture, heat and pollutant flows through concrete within the framework of a distributed parameter model can be expressed as follows:

$$\frac{\partial h}{\partial t} = div(C \cdot \nabla h) + \frac{\partial h_s}{\partial t} + K \cdot \frac{\partial T}{\partial t} + \frac{\partial h_{\Re}}{\partial t} \qquad \textit{moisture flow} \tag{5.4}$$

$$\rho \cdot C_q \cdot \frac{\partial T}{\partial t} = div(b \cdot \nabla T) + \frac{\partial Q_h}{\partial t} + \frac{\partial Q_{\Re}}{\partial t} \qquad \textit{heat flow} \tag{5.5}$$

$$\frac{\partial c}{\partial t} = div(D_c \cdot \nabla c) + \frac{c}{\alpha} \cdot \frac{\partial w}{\partial t} + \frac{\partial c_{\Re}}{\partial t} \qquad \textit{pollutant flow} \tag{5.6}$$

$$\frac{\partial \Re}{\partial t} = \alpha_4 \times f_1(h) \times f_2(c) \times f_3(\Re) \times f_4(T) \qquad \textit{chemical reaction's rate} \tag{5.7}$$

where diffusivities of relative humidity C and of aggressive species D_C are assumed to be strongly dependent on pore humidity h, temperature T, degree of hydration of cement (that is, on the equivalent curing time t_e), the degree of reaction $\Re$, and the coupled damage parameters d^{*+} and d^{*-}. In the cited works, the following relations multi-factor law, inspired to the work of [29], is proposed:

$$C = C_{rif} \cdot F_1^*(h) \cdot F_2(T) \cdot F_3(t_e) \cdot F_4(\Re) \cdot F_5(d^*) \tag{5.8}$$

$$D_c = D_{c,rif} \cdot F_1(h) \cdot F_2(T) \cdot F_3(t_e) \cdot F_4(\Re) \cdot F_5(d^*) \tag{5.9}$$

where C_{rif} and $D_{c,rif}$ are the diffusivities in standard conditions after 28 days. For the definition of the functions $F_1^*(h)$, $F_1(h)$, $F_2(T)$, $F_3(t_e)$, $F_4(\Re)$ and $F_5(d^*)$ the reader is referred to Saetta et al. [10], [11], [5]. It is worth noting that the function $F_4(\Re)$ permits to take into account the fact that the diffusion process is slowed down when the chemical reaction considered produces a precipitate, like the case of calcium carbonate in the carbonation process. Another important characteristic of the model is represented by the function $F_5(d^*)$ that describes the effect of the coupled damage variables on the diffusivities C and D_c; even if the diffusion mechanisms of pore moisture and chemical species in concrete are quite different, it is proved that both the diffusivities C and D_c grow with the coupled damage parameter d^*, being the damage a measure of fracture growth and void nucleation [5].

The equation (5.7) describes the rate of the chemical reaction: the functions $f_1(h)$, $f_2(c)$, $f_3(\Re)$, $f_4(T)$ represent the influence of the presence of water, of the aggressive species concentration, of the chemical reaction degree and of the temperature on the evolution of the chemical process respectively. These functions need to be defined in dependence of the considered degradation phenomenon (e.g. sulfate attack, chloride attack, carbonation process, etc.). Finally α_4 is a parameter that takes into account the kinetic of the chemical reaction [5].

The partial derivatives $\partial(\cdot)_{\Re}/\partial t$ in (5.4)-(5.6) represent the change of the quantity in brackets due to the chemical reaction per time unit:

$$\frac{\partial h_{\Re}}{\partial t} = \alpha_1 \frac{\partial \Re}{\partial t}; \frac{\partial Q_{\Re}}{\partial t} = \alpha_2 \frac{\partial \Re}{\partial t}; \frac{\partial c_{\Re}}{\partial t} = \alpha_3 \frac{\partial \Re}{\partial t} \tag{5.10}$$

where α_1, α_2 and α_3 are parameters that vary accordingly to the characteristics and reagents. For a detailed description of these symbols the reader is referred to Saetta and Vitaliani [30].

The model described has been successfully adopted to analyze the phenomenon of sulfate attack [5]. This class of degradation process, classified as a chemical degradation process according to 5.1.2, is common in structures exposed to marine environments or industrial areas. For instance it was observed in last decades in piers of bridges which are in the splash zone. In [5], an example of a pier of a bridge

in the south of Italy is presented. A proper evaluation of the main parameters needed in equations (5.4)- (5.7) and (5.2) is carried out with considerations derived from experimental evidences. After that the set of equations (5.4)- (5.7) can be solved numerically with discretization in space (e.g. within the finite element approach) and a time discretization (e.g. Wilson algorithm). After the assignment of boundary and initial conditions, it is possible to determine the pollutant concentration in concrete at a selected time step of interest. By using (5.2) the chemical damage parameter is evaluated at that time step and a structural analysis is performed to evaluate the safety factor of the pier at the time step of interest. Repeating the procedure for different time steps it is possible to evaluate the safety factor of the structure over time. The safety factor may strongly reduce; moreover it can assume values below one at a particular time, indicating that after that time the structure is no longer safe. It is evident that this procedure is able to verify the vulnerability of the structure for its whole service life.

It is worth noting that, as mentioned in 5.1.2, sulfate attacks lead to concrete deterioration (micro-cracking) because of the expansive products of the chemical reaction involved. Thus structural effects of concrete's degradation are interpreted with the environmental damage parameter d_{env}.

The presented model has been also used to model the carbonation process in reinforced concrete structures [30]. In this case the pollutant is a gas and therefore the proper evaluation of the functions and parameters presented in (5.4)- (5.7) are carried out with considerations on the nature of this specific phenomenon. The carbonation is generally not harmful for concrete, but the main consequence is the corrosion of reinforcing bars. The model is then mainly used to identify the corrosion initiation time.

Also chloride attacks lead to corrosion of reinforcement, although it was observed that chlorides (especially calcium chloride) may react with cementitious components forming expansive products and thus leading to micro-cracking of concrete; the main difference between carbonation-induced and chlorides-induced corrosion is that the former is generally uniformly distributed, while the latter is localized (pitting corrosion). The proposed model is used also in this case for the evaluation of the initiation time. The proper definition of the parameters and the functions of (5.4)- (5.7) is of course needed since in this case the pollutant is a ion and therefore the nature of the phenomenon is different. For instance the function $F_1(h)$ assumes different formulations in case of gas diffusion or ion diffusion phenomenon [7].

As already mentioned the effects on structure of corrosion include: steel cross area reduction, change in ductility of steel bars, bond deterioration and its dependence on the corrosion level of the reinforcing bars, micro-cracking of concrete induced by expansion products, cover cracking and spalling. In the work of Berto et al. [31] the

authors discussed these topics and proposed a practical approach for their modeling. Moreover they enhanced the presented model that was not able to take into account the effects of corrosion on bond degradation. In particular they proposed an original formulation for a damage-type bond law. This law was implemented as τ-γ relation in 2D interface elements. In the present work this law, briefly reported in the following, is adopted, but it is implemented in terms of τ-slip law. Thus it is suitable for use in zero-length interface elements.

The reduction of steel cross-section area can be expressed by the following expression, according to the model for steel bars degradation proposed in [32]:

$$A_s(t) = \frac{N_s \pi [D_0 - nx(t)]^2}{4} \tag{5.11}$$

where D_0 and N_s are the initial diameter and the number of reinforcement bars, n takes into account the possibility of a one-side or two-side corrosion attack and $x(t)$ is the corrosion depth in the reinforcement. The corrosion rate dx/dt depends on the environmental conditions (e.g. relative humidity, temperature, etc.), the type of chemical attack (*e.g.* carbonation, chlorides, etc.), concrete and steel characteristics and crack profile geometry. Some typical values of the rate of corrosion are reported in [32].

It was observed experimentally that a reduction of the ductility of the steel bar is generally associated with the tendency for notch formation with increasing levels of corrosion, typical condition of pitting corrosion [33]. On the other hand, other results evidenced a strong loss of ductility in case of uniform corrosion (typical of carbonation-induced corrosion), while only a significant decrease of fatigue performance seems to be produced from localized corrosion [34]. Such considerations highlight that further research is needed to completely understand the phenomenon.

The effect of localized corrosion on steel bars may be taken into account adopting the approach proposed in [35], according to which the steel ultimate strain ε'_{su} may be considered as linearly-dependent on the steel cross-sectional area reduction. The relative reduction of the bar cross-section is defined as:

$$\alpha_{pit} = \frac{\Delta A_{pit}}{A_0} \tag{5.12}$$

where ΔA_{pit} is the area reduction due to pitting corrosion and A_0 is the initial nominal bar cross-sectional area. The following law for ultimate strain of pitting corroded steel may be assumed:

$$\varepsilon_{su}^{'} = \varepsilon_{sy} + \left(\varepsilon_{su} - \varepsilon_{sy}\right)\left(1 - \frac{\alpha_{pit}}{\alpha_{pit}^{MAX}}\right) \qquad \text{for } \alpha_{\text{pit}} \le \alpha_{pit}^{MAX} \tag{5.13}$$

where for the virgin material ($\alpha_{\text{pit}} = 0$) the ultimate strain is ε_{su} , while the complete loss of ductility is achieved for $\alpha_{\text{pit}} = \alpha_{pit}^{MAX}$. Typical values of α_{pit}^{MAX} range from 0.5 and 1.

The expansion of corrosion products may cause micro-cracking of the surrounding concrete, spalling or delamination of the outer layers of concrete. It is worth noting that the degree of the volumetric expansion is different in case of uniform or local corrosion, in particular the tendency of the corroded bar to cause the break for splitting of the concrete cover is less with local corrosion than with uniform attack. The effect of the degradation of concrete may be described by reducing the thickness of concrete elements and changing the material properties of concrete, reducing the compressive strength and using a more brittle post-peak path in the constitutive law (e.g. [35]). Within such an approach the damage environmental variable described by (5.2) may be increased to consider the effect of corrosion products on degradation of concrete. Moreover, also the different effects produced by uniform or localized corrosion may be taken into account.

The damage-type bond law originally proposed in [31] is adopted as function of slip:

$$\begin{cases} \tau = (1 - d_{bond})(1 - d)\bar{\tau} = (1 - d_{bond})(1 - d)\overline{G}s & \text{for } s \le s_{res} \\ \tau = \tau_{res} & \text{for } s > s_{res} \end{cases} \tag{5.14}$$

where $\overline{G}$ is a parameter that represents the elastic bond stiffness equal to τ_1/s_1 (see Figure 5.6) and τ_{res} and s_{res} may be evaluated according to CEB FIB Model Code 90 (typical values for τ_{res} are 0.15 τ_{max} and 0.4 τ_{max} for unconfined and confined concrete respectively). This law shows an initial linear elastic behavior up to the value, an ascending branch up to τ_{max}, followed by a descending curve and the residual bond strength τ_{res}. In the law depicted in (5.14) the coupling of a mechanical damage parameter with a bond damage parameter is similar to the couple environmental-mechanical damage model for concrete. With such an approach, it is possible to describe both the reduction of bond stiffness and the reduction of peak stress with the increasing of corrosion levels. Moreover an internal parameter β is adopted in this model with the meaning of equivalent inelastic parameter for corrosion effect in analogy with the concrete mechanical damage model where it represented the plasticity factor. Thus, the model may consider the effects of corrosion on bond between steel and concrete by using the two parameters d_{bond} and β. A schematic representation of the effects of the two parameters is depicted in Figure 5.7.

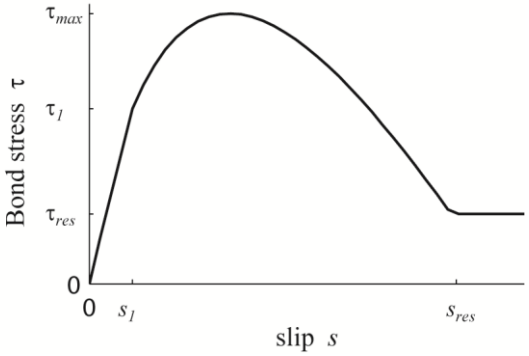

Figure 5.6 - Damage-type bond law [31]

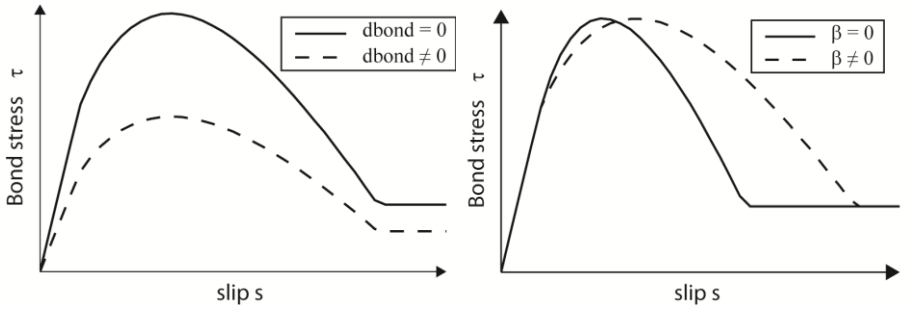

(a) *(b)*

Figure 5.7 - Effect of d_{bond} and β on the bond law [31]

5.4 Enhancement for freeze-and-thaw cycles

The original coupled environmental-mechanical damage model is enhanced to capture the mechanical behavior of concrete elements subjected to frost damage. As introduced previously, frost damage may lead to loss in compressive and tensile strength, in elastic modulus and in bond strength. At this stage of research only the reduction of bond strength is not taken into account.

Indeed experimental observations demonstrate that the compressive strength of concrete and its elastic modulus are reduced for increasing levels of frost damage, while deformation at peak strength (i.e. peak deformation) is higher for increasing levels of frost damage (see Figure 5.8, [28]) Concerning the behavior of concrete affected by FTC under uniaxial tensile load conditions, it was observed experimentally a reduction of tensile strength and an increasing of fracture energy. In Figure 5.9 are reported load-displacement curves of concrete specimens subjected to a splitting test, for different levels of frost degradation.

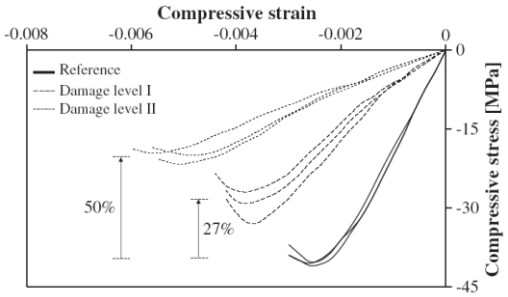

Figure 5.8 – Effect of FTC on compressive behavior of concrete [28]

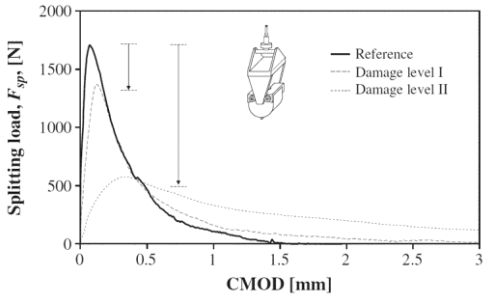

Figure 5.9 – Effect of FTC on tensile behavior of concrete [28]

To capture these aspects, appropriate relationships which relate the model parameters d_{env}, β and R_0 to the number N of freezing-thawing cycles (FTC) are proposed. As shown previously in 5.2, the parameter d_{env} controls the loss of strength (see Figure 5.5). On the other hand, the parameter β controls the peak strain and the ductility, while the parameter R_0 controls the compressive strength under biaxial compression as shown in Chapter 3. The proposed relations are:

$$d_{env} = a_d N_{eq} \tag{5.15}$$

$$\frac{\beta}{\beta_{sound}} = a_\beta N_{eq} + 1 \tag{5.16}$$

$$\frac{R_0}{R_{0,sound}} = a_R N_{eq} + 1 \tag{5.17}$$

where the parameters a_d , a_β, a_R are model parameters that are assumed to depend on concrete characteristics (e.g. porosity), β_{sound} and $R_{0,sound}$ are respectively the values of parameters β and R_0 for sound concrete. N_{eq} is equal to the actual number N of the FTC if the concrete is subjected to frost deterioration conditions according to "Procedure A" described in ASTM C 666 [38]; according to this procedure, the specimens are both frozen and thawed in water in order to provide a very severe freeze-thaw condition being the specimen saturated. In the case that different frost deterioration conditions (e.g. freezing and thawing velocity, moisture content, etc.)

are applied, N_{eq} represents the equivalent number of FTC according to ASTM C 666 "Procedure A" which leads to the same strength reduction. Further investigation is necessary to better understand the relation between N and N_{eq} under different experimental conditions. To this aim more experimental campaigns could be considered if available.

The effect of different values for parameters a_d , a_β, a_R is depicted in Figure 5.10. These parameters are assumed to depend on concrete characteristics, reflecting the experimental evidence of increasing of frost-resistance with increasing quality of concrete (e.g. [21], [22]).

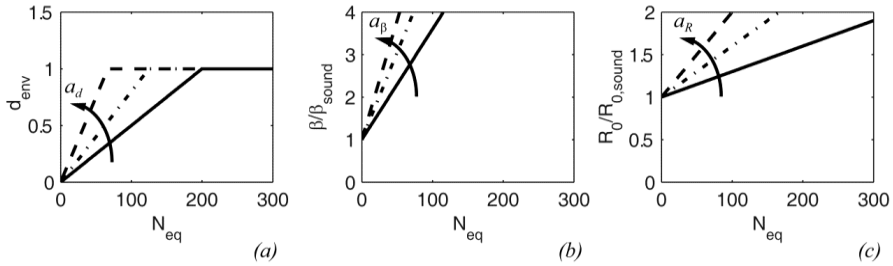

Figure 5.10 – Effect of different concrete characteristics on frost damage model

In this stage of the research limited experimental data were available. Thus the parameters of equations (5.15)-(5.17) were calibrated considering the experimental results of both uniaxial and biaxial compression tests carried out by Shang and Song [36] on plain concrete cubes subjected to freezing-and-thawing cycles.

In [36], the authors submerged the specimens in water before the test and therefore they were both frozen and thawed in water according to GBJ82-85 Standard [37]. This procedure is similar to "Procedure A" described in ASTM C 666 [38]. For this reason it was assumed $N_{eq} = N$.

5.4.1 Uniaxial compressive load

The attention is focused first on the experimental tests performed by Shang and Song [36] on plain concrete cubes under uniaxial compression load. The experimental evidences have shown that with increasing number N of freeze-thaw cycles the strength decreased, while ductility increased.

Within the framework of the coupled damage approach briefly introduced previously, such characteristics are taken into account with the equations (5.15)-(5.16) between the damage model parameters, d_{env} and β, and N_{eq}. The parameters a_d and a_β, are calibrated considering the results of three tests (with N = 0, 25 and 75 respectively). An optimization procedure with an Ordinary Least Squares

approach is used. In particular the best parameters that fit the experimental results are computed minimizing the following cost-function:

$$C = \sqrt{\sum_{i=1}^{n} (\sigma_i(\varepsilon_i) - \sigma_i^{num}(\varepsilon_i))^2} \tag{5.18}$$

where ε_i and σ_i are strains and stresses of the *n* experimental data, while σ_i^{num} is evaluated according to (5.3). The resulting stress-strain curves are depicted in Figure 5.11; the corresponding material parameters, which are kept constant for all the tests regardless the number *N* of FTC, are summarized in Table 5.1.

$\boldsymbol{E}$	30000 MPa
$\boldsymbol{\nu}$	0.18
$\boldsymbol{f_{c1D,sound}}$	-34.2 MPa
$\boldsymbol{f_{01D}}$ / $\boldsymbol{f_{c1D,sound}}$	0.55
$\boldsymbol{\beta}$	0.2

Table 5.1 - Material parameters for uniaxial compression tests on frost-damaged concrete

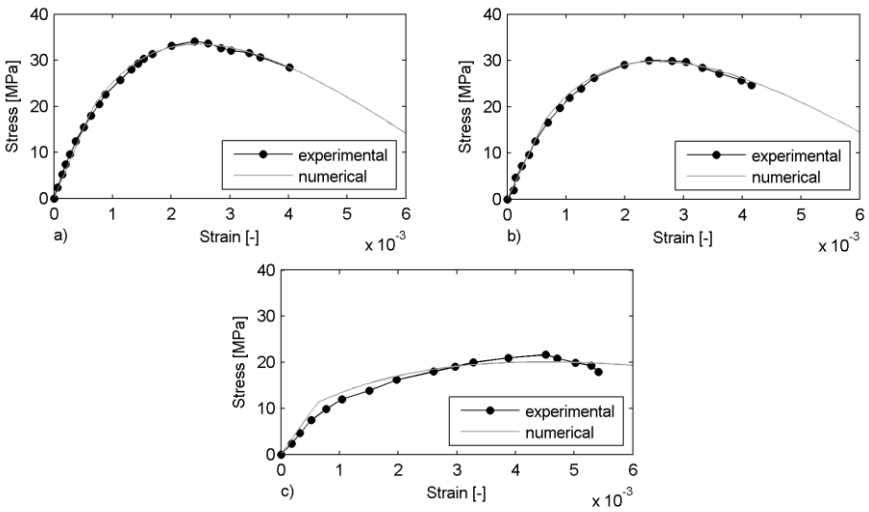

Figure 5.11 - Stress-strain curves obtained from optimization of 1D compression tests compared with experimental results for: (a) N = 0 FTC; (b) N = 25 FTC; (c) N = 75 FTC

Observing the obtained results it is possible to notice a strong linear correlation between the damage model parameters, d_{env} and β, and *N*, as it can be seen in Figure 5.12 where the linear correlation factor is also reported. The relations between *N* and the parameters d_{env} and β are obtained with a linear regression procedure considering the point corresponding to $N = 0$ as a constrain for the linear relation, since it

represents the value of the parameters in sound condition. Thus the intercept of the straight line with vertical axis is fixed and the remaining 2 points (corresponding to N= 25 and N=75) are used to determine the slope of the straight line with a Least Squares approach. According to this procedure, the relationship obtained read respectively:

$$d_{env} = 0.005\,N \tag{5.19}$$

$$\frac{\beta}{\beta_{sound}} = 0.026N + 1 \tag{5.20}$$

where β_{sound} is the value of parameter β for sound concrete, in this test equal to 0.2.

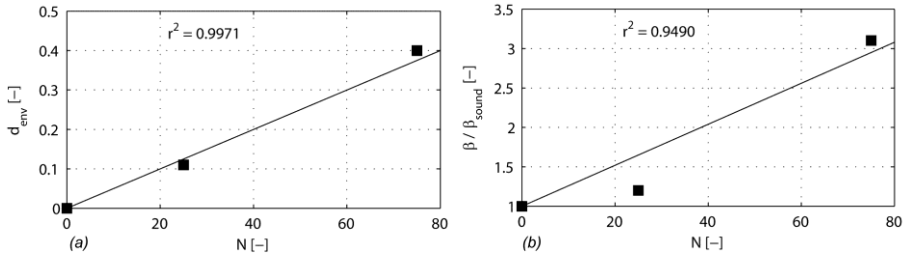

Figure 5.12 - Proposed relations between: (a) d_{env} – N_{eq}; (b) β - N_{eq}

As a first validation of the proposed model, the uniaxial compressive test for N = 50 is simulated. From relations (5.19) and (5.20), the values of d_{env} and β are predicted. The values obtained are respectively 0.25 and 0.46.

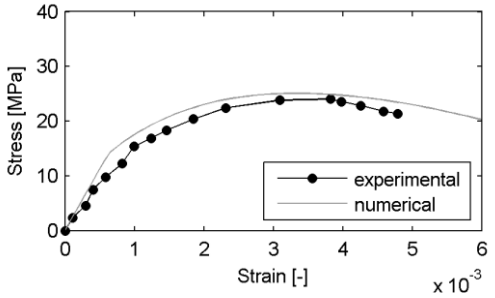

Figure 5.13 - Simulation of uniaxial compression test for N = 50 and comparison with experimental results

N=50	σ_1	σ_1/f_c	ε_1
EXP	-24,10	0,70	-0,003801
PRED	-25,10	0,7339	-0,003292
ERROR	4,1%	4,1%	-13,4%

Table 5.2 - Uniaxial compression test on frost damage concrete: experimental (EXP) and numerically predicted (PRED) solution

The results of the simulation are compared with the experimental ones in Figure 5.13 in terms of stress-strain curve and in Table 5.2 where the peak stress and peak strain for experimental (EXP) and numerically predicted (PRED) solution as well as the corresponding errors are reported. It is possible to see a good agreement, showing the ability of the proposed relationships to capture the main features of uniaxial compression behavior of frost degraded concrete.

5.4.2 Biaxial compressive load

In [36] the authors studied also the behavior of the concrete specimens subjected to biaxial compressive load conditions. In accordance with the experimental evidences reported in 2.2.3 and 3.9.3, the experimental results showed that for all stress ratios $\alpha = \sigma_2/\sigma_1$ the biaxial compressive strength $f_{0,2D}$ was greater than the uniaxial compressive strength f_{01D} for the same number of FTC. Moreover, in [36] the authors evidenced that the biaxial compressive strength decreases as FTC are repeated. Furthermore, analyzing the experimental results, it can be observed that the ratio R_0 between the biaxial compressive strength and the uniaxial compressive strength increases with N.

Such experimental evidences are taken into account, as already mentioned, with the third equation of the model (5.17) which relates R_0 with N_{eq}. The parameter a_R is calibrated considering the experimental results for three levels of frost damage (corresponding to N = 0, 25 and 75 respectively). It is possible to notice a strong linear correlation between the experimental values of R_0 and the number of freeze-thaw cycles N, as can be seen in Figure 5.14 where it is also reported the linear correlation factor.

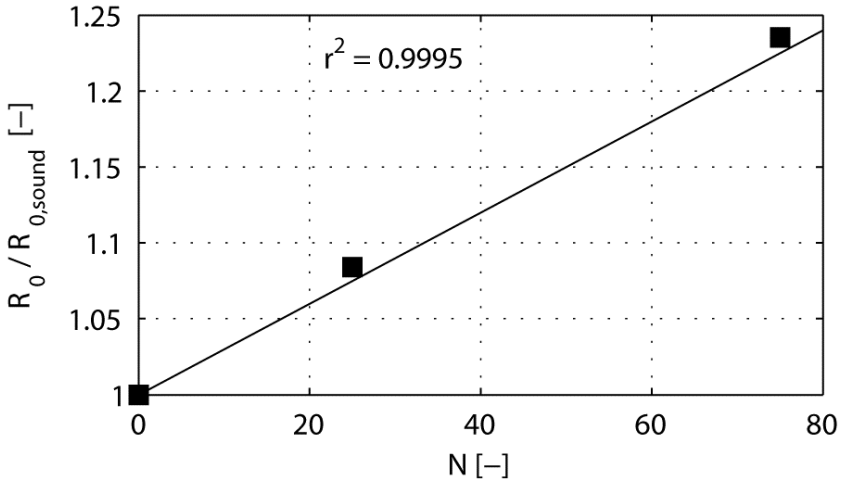

Figure 5.14 - Proposed relation between: R - N_{eq}

Following a similar procedure as the uniaxial case, the following linear relation is proposed:

$$\frac{R_0}{R_{0,sound}} = 0.003N + 1 \tag{5.21}$$

where $R_{0,sound}$ is the value of parameter R_0 for sound concrete, which in this case is equal to 1.19.

A predictive simulation for N = 50 is carried on as validation of the proposed formulation. The corresponding value of R_0 obtained is 1.37.

A simulation of all the biaxial compression tests is then performed assuming the parameters d_{env} and β in accordance to equations (5.19) and (5.20).

The results obtained are summarized in Table 5.3 where the errors on failure strength are reported. It can be seen that these errors are limited and can be considered acceptable: the mean value is about -3.5%, and the peak value is -18.8%.

The results obtained are also presented in Figure 5.15 in terms of failure points and compared with the experimental data.

Finally, it is worth noting that six of the twenty experimental tests are used to propose the relations (three for uniaxial condition and three for biaxial condition) while the other fourteen points are profitably predicted by the proposed coupled environmental-mechanical model.

		α				
		0	0,25	0,5	0,75	1
N	0	-2,1%	-8,0%	-3,8%	2,8%	-2,1%
	25	-0,7%	-10,0%	-0,9%	4,3%	-0,6%
	50	4,2%	-3,6%	-1,9%	5,8%	3,7%
	75	-7,3%	-18,8%	-14,2%	-8,8%	-7,3%

Table 5.3 - Biaxial compression test on frost damage concrete: errors between numerical and experimental results

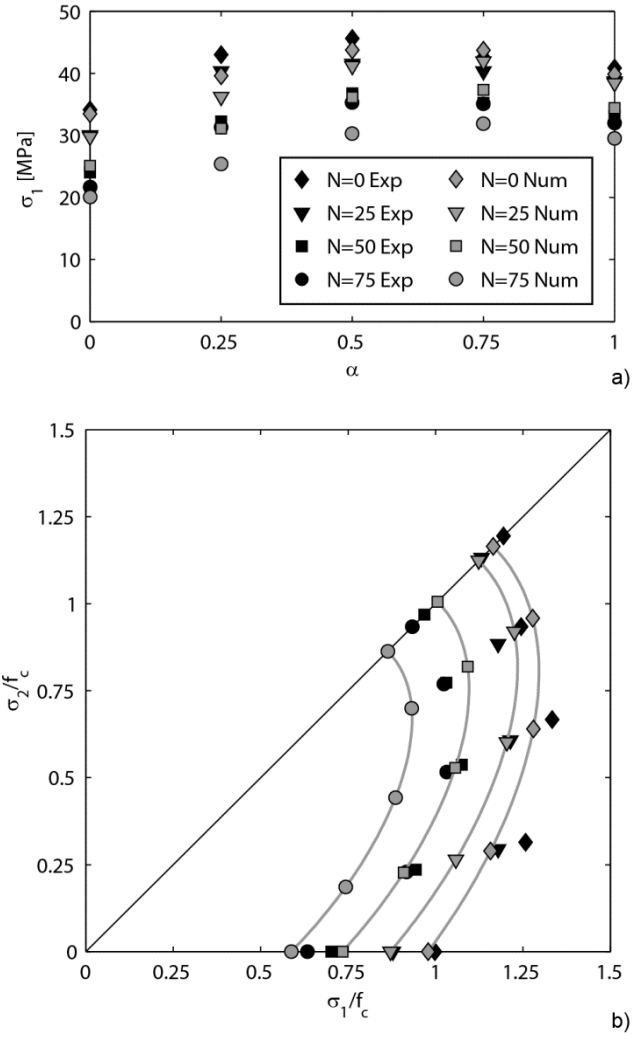

Figure 5.15 - Comparison between experimental and numerically predicted results for 2D compression test represented in: (a) stress - α plane (b) principal stress plane

5.5 Validation example

5.5.1 Frost-Damaged Beam

An application on a real structure is here presented to show the ability of the proposed couple environmental-mechanical model in capturing the main aspects of a frost-damaged structure. In particular the proposed model has been applied to evaluate the load carrying capacity of two beams tested by Hassanzadeh and Fagerlund [39]. The authors tested 12 simply supported beams: six reference and six frost-damaged beams with two different geometries and including different reinforcement ratios and stirrups. It is worth noting that in the experimental program, the damaged beams were vacuum treated, submerged in water and then subjected to two complete freeze-thaw cycles ([39], [40]).

As introduced previously, the proposed relations (5.15)-(5.17) relates the damage model parameters to the equivalent number of FTC N_{eq} which is equal to the actual number of FTC N only if the experimental procedure performed is in accordance with ASTM C666 Proc A. In the case under analysis, the authors applied a deeply different FTC procedure. For this reason, the equivalent number of FTC N_{eq} has been estimated considering the experimentally observed degradation of compressive strength due to frost damage that decreases from 37.6 MPa for sound condition to 17.5 MPa for damaged one. In particular, considering these values, the parameter d_{env} can be estimated resulting in d_{env} = 0.5 which corresponds, using the (5.19), to N_{eq} = 100 cycles.

In the present work two beams, one reference and one damaged are analyzed. In particular specimens R1 and D1 are selected as reference and damaged beams respectively. They are simply supported beams with 4.4 m span and two concentrated loads at 1.8 m from support. The cross section is (0.2 x 0.5) m^2 and reinforcement consists in 4Φ20 longitudinal bars and 28Φ8 stirrups (see Figure 5.16).

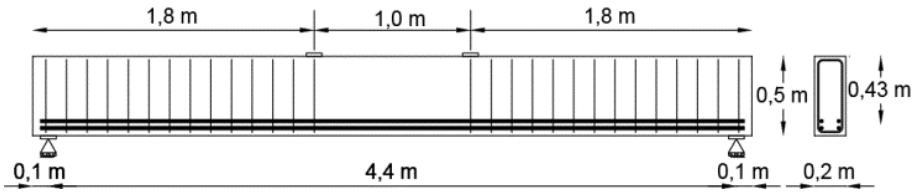

Figure 5.16 - Geometry and reinforcement of beams R1 (sound) and D1 (degraded)

E	33000 MPa
ν	0.18
f_{c1D}	-37.6 MPa
f_{01D}/f_{c1D}	0.65
f_{02D}/f_{01D}	1.2
f_0^+	3.6 MPa
β	0.3
G_f	139 N/m

Table 5.4 - Material parameters for beams R1 and D1

The beams are modeled with four-point plane stress elements for concrete. The longitudinal reinforcement and stirrups are embedded in concrete elements assuming perfect bond between the two materials. Taking advantage of the geometrical symmetry of specimen, only half specimen is simulated. The concrete parameters are reported in Table 5.4. Steel has been modeled with an elastic-plastic law with kinematic hardening; the adopted parameters are Young Modulus E= 200.000 MPa, Hardening Modulus H = 2.000 MPa, yield stress f_y= 670 MPa.

In Figure 5.17 the numerical and experimental results in terms of load-displacement curves are compared. It is possible to see that the global behavior of beam R1 is quite well captured; in fact the model is able to correctly predict yielding and failure loads. A sensible difference can be observed in the initial slope of the curves. Looking at the numerical results it is possible to see that the numerical analysis gives an initial slope that corresponds to the gross uncracked section stiffness while in the experimental result it seems equal to the cracked section stiffness, suggesting a possible initial pre-cracking state of the tested beam, as frequently occurs in experimental test due for instance to shrinkage. Similar conclusions can be drawn for the degraded beam D1, for which the failure load is quite well captured with an acceptable error of about -9 %. Furthermore also the value of failure displacement is profitably predicted. Finally comparing the force displacement curves of the reference (R1) and the damaged beams (D1), it can be noted that the proposed model is able to capture the change in the failure mode from a ductile one to a brittle one, due to frost degradation, in accordance with experimental observations for this test. This can be seen also from the positive and negative damage contour maps for beams D1 and R1 depicted in Figure 5.18 and Figure 5.19 respectively. Indeed the damage maps of the reference beam represent the typical ductile flexural failure, while the damage maps of the degradated beam indicate the failure of the specimen due to crushing of concrete in the compressive zone, in agreement with the experimental observations.

Analyzing the properties of the frost-damaged concrete it is possible to see that the effect of freeze and thaw cycles leads to a more severe reduction of tensile strength,

rather than compressive one. This evidence is not taken into account by the present model which, in this work, affects with the same environmental damage parameter, both the tension and compression parts.

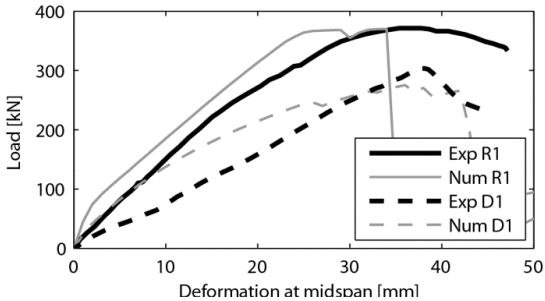

Figure 5.17 - Load displacement curves for beams R1 and D1 compared with experimental curves

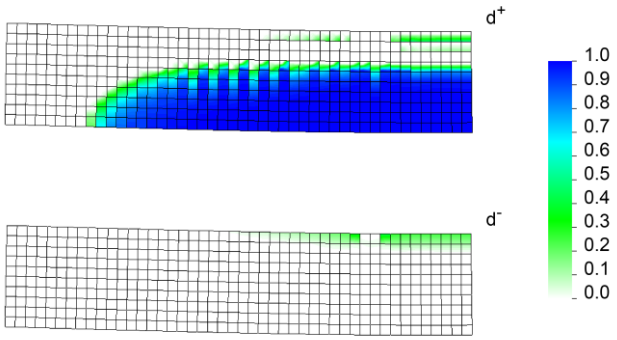

Figure 5.18 – Damage parameters distribution at incipient failure for beam R1

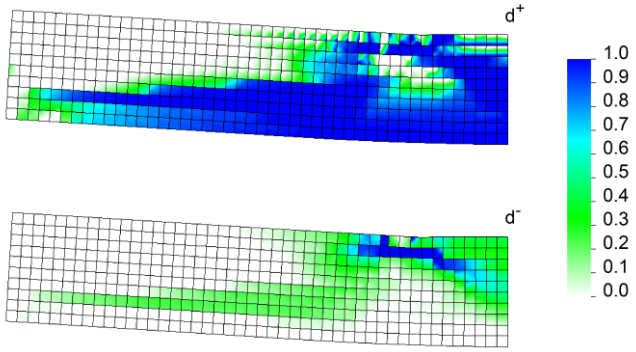

Figure 5.19 - Damage parameters distribution at incipient failure for beam D1

5.6 References

[1] Fagerlund, G. (2004). A service life model for internal frost damage in concrete. *Report TVBM-3119*, Div. Building Materials, Lund Institute of Technology

[2] Pigeon, M., Pleau, R. (1995). Durability of concrete in cold climates, *Taylor & Francis*, London

[3] Duan, A., Jin, W., Qian, J. (2011). Effect of freeze-thaw cycles on the stress-strain curves of unconfined and confined concrete, *Materials and Structures*, 44, 1309-1324

[4] Powers, T.C. (1945). A working hypothesis for further studies of frost resistance of concrete, *J. American Concrete Institute*, 16, 245-272

[5] Saetta, A., Scotta, R., Vitaliani, R. (1998). Mechanical behavior of concrete under physical-chemical attacks, *J. Eng. Mech., ASCE*, 124, 1100-1109

[6] Saetta, A., Scotta, R., Vitaliani, R. (1999). Coupled environmental-mechanical damage model of RC structures, *J. Eng. Mech., ASCE*, 125, 930-940

[7] Saetta, A. (2005). Deterioration of reinforced concrete structures due to chemical-physical phenomena: model-based simulation, *J. Materials Civil Eng., ASCE*, 17, 313-319

[8] Pedeferri, P., Bertolini, L. (2000). La durabilità del calcestruzzo armato, *McGraw-Hill*,

[9] Bertolini, L., Elsener, B., Pedeferri, P., Polder, R. (2004). Corrosion of steel in concrete – Prevention, Diagnosis, Repair, *Wiley-VCH*, Weinheim

[10] Saetta, A., Schrefler, B.A., Vitaliani, R. (1993a). The carbonation of concrete and the mechanism of moisture, heat and carbon dioxide flow through porous materials, *Cement and Concrete Research*, 23, 761-772

[11] Saetta, A., Scotta, R., Vitaliani, R. (1993b). Analysis of chloride diffusion into partially saturated concrete, *ACI Materials J.*, 90, 441-451

[12] Ozbolt, J., Orsanic, F., Kuster, M.M. (2012). Modelling bond resistance of corroded steel reinforcement, *Bond in concrete 2012*, 10^{th}-20^{th} June 2012, Brescia, Italy

[13] Castel, A., Francois, R., Arliguie, G. (2000a). Mechanical behavior of corroded reinforced concrete beams-Part 1: Experimental study of corroded beams, *Materials and Structures*, 33, 539-544

[14] Castel, A., Francois, R., Arliguie, G. (2000b). Mechanical behavior of corroded reinforced concrete beams-Part 2: Bond and notch effects, *Materials and Structures*, 33, 545-551

[15] Almusallam, A.A., (2001). Effect of degree of corrosion on the properties of reinforcing steel bars, *Constr. And Building Mat.*, 15, 361-368

[16] Apostolopous, C.A., Papadakis, V.G. (2008). Consequences of steel corrosion on the ductility properties of reinforcement bar, *Constr. And Build. Mat.*, 22, 2316-2324

[17] Almusallam, A.A., Al-Gahtani, A.S., Aziz, A.R., Dakhil, F.H., Rascheeduzzafar (1996). Effect of reinforcement corrosion on flexural behavior of concrete slabs, *J. of Materials in Civ. Eng.*, 8, 123-127

[18] Fischer, C. (2012). Beitrag zu den Auswirkungen der Bewehrungsstahlkorrosion auf den Verbund zwischen Stahl, *PhD Thesis*, Insititute of Construction Materials, University of Stuttgart

[19] MacGregor, J.G. (1997). Reinforced concrete mechanics and design, 3rd edition, *Prentice Hall*, Upper Saddle River, New Jersey

[20] Derucher, K.N., Korfiatis, G.P., Ezeldin, A.S. (1998).Materials for highway and civil engineers, 4th edition, *Prentice Hall*, Upper Saddle River, New Jersey

[21] Fagerlund, G. (1995). Freeze-thaw resistance of concrete Denstruction mechanisms. Concrete technology. Test methods. Quality control., *Report TVBM-3060*, Div. Building Materials, Lund Institute of Technology

[22] Fagerlund, G. (2001). Manual for assessing the residual service life of structures affected by frost, , *Report TVBM-7161*, Div. Building Materials, Lund Institute of Technology

[23] Powers, T.C. (1949). The air requirement of frost resistant concrete, *Proc. Highway Res. Board*, 29, 184-211

[24] Powers, T.C., Helmuth, R.A. (1953). Theory of volume changes in hardened Portland cement paste during freezing , *Proc. Highway Res. Board*, 32, 285-297

[25] Powers, T.C. (1975). Freezing Effects in Concrete, *Durability of Concrete, ACI Special*, SP-47, 1-11

[26] Petersen, L., Ludger, L., Polak, M. (2007). Influence of freezing-and-thawing damage on behavior of reinforced concrete elements, *ACI Mat. J.*, 104, 369-378

[27] Shih, T., Lee, G., Chang, K. (1988). Effects of Freezing Cycles on Bond Strength of Concrete, *J. Struct. Eng.*, 114, 717-726

[28] Hanjari, Z.K., Utgenannt, P., Lundgren, K. (2011). Experimental study of the material and bond properties of frost-damaged concrete, *Cem. Concr. Res.*, 41, 244-254

[29] Bazant, Z.P., Najjar L.J. (1972). Nonlinear water diffusion in nonsaturated concrete, *Materials and Structures, RILEM*, 5, 3-20

[30] Saetta, A., Vitaliani, R. (2004). Experimental investigation and numerical modeling of carbonation process in reinforced concrete structures. Part I: Theoretical formulation, *Cem. And Conr. Res.*, 34, 571-579

[31] Berto, L, Simioni, P., Saetta, A. (2008). Numerical modeling of bond behavior in RC structures affected by reinforcement corrosion, *Eng. Struct.*, 30, 1375-1385

[32] Rilem Report 14 (1996). In: Sarja, Vesikari, editors. Durability design of concrete structures, *E&FN* Spon, London

[33] Almusallam, A.A. (2001). Effect of degree of corrosion on the properties of reinforcing steel bars, *Constr. Build. Mat.*, 15, 361-368

[34] Al Hashemi, M., De Sanctis, M., Salvatore, W., Valentini, R. (2007). Effects of corrosion induced damages on tensile and fatigue properties of concrete reinfrocinhg bars, *XII Convegno ANIDIS – L'ingegneria Sismica in Italia*, Pisa, Italy

[35] Coronelli, P., Gambarova, P. (2004). Structural assessment of corroded reinforced concrete beams: modeling guidelines, *J. Struct. Eng.*, 130, 1214-1224

[36] Shang, H.S., Song, Y.P. (2006). Experimental study of strength and deformation of plain concrete under biaxial compression after freezing and thawing cycles, *Cem. Concr. Res.*, 36, 1857-1864

[37] GBJ82-85 (1997). National standard of the People's Republic of China, The test method of long-term durability on ordinary concrete

[38] American Standard ASTM C666 (1997). Standard test method for resistance of concrete to rapid freezing and thawing

[39] Hassanzadeh, M., Fagerlund, G. (2006). Residual strength of the frost-damaged reinforced concrete beams, *III European Conf. Comp. Mech.*

[40] Hanjari, K.Z., Kettil, P., Lundgren, K. (2013). Modeling the structural behavior of frost-damaged reinforced concrete structures, *Struc. And Infrastruc. Eng.*, 9, 416-431

CHAPTER 6:
CONCLUSIONS AND FUTURE DEVELOPMENTS

The evaluation of structural response of deteriorated concrete structures, in particular by predicting their load-carrying capacity and their remaining ductility, is still an evolving research topic in the assessment of existing structures. Actually the modification of both the strength and ductility behavior of RC structures due to environmental attacks which cause the volume expansion, e.g. reinforcement corrosion and frost damage, mainly affects the seismic response of existing reinforced concrete structures subjected by different levels of deterioration, which is become a very hot issue in these recent years.

In the present work, a set of theoretical and numerical tools has been developed and presented as a suitable instrument for the safety analysis of both new and existing structures. In particular a mechanical damage model, enhanced to better represent the behavior of concrete under mixed tension-compression stress states, is presented and validated. Efficient models for reinforced concrete membranes and plates are developed in this work. The models consider the superposition of different material layers with perfect bond assumption. A wide set of validation tests taken from literature are presented to demonstrate the reliability of the model in representing the behavior of reinforced concrete structures under different stress states.

The mechanical damage model is then coupled with an environmental damage variable, following the formulation of the coupled environmental-mechanical damage model developed in previous works. The environmental-mechanical damage model is enhanced to consider the degradation of concrete due to freeze-and-thaw

action. In particular the formulation proposed is able to take into account some of the main effects of freeze-and-thaw cycles degradation: the strength decreasing and ductility increasing as the number N of freeze-thaw cycles increases in uniaxial compressive test; the biaxial compressive strength decreasing as N increases, as well as the increasing of the ratio R_0 between the biaxial compressive strength and the uniaxial compressive strength with N.

To develop and asses the performance of the proposed coupled environmental-mechanical model, some experimental tests carried out on concrete specimens subjected to uniaxial and biaxial load conditions were reproduced. The comparison with the experimental results evidences the reliability of the model in effectively capturing the behavior of frost damage elements, also proving the efficiency of the proposed relations between the parameters d_{env}, β and R_0 with the number N of freeze-thaw cycles. Therefore the model demonstrates to be an effective tool for describing the effects of frost degradation.

Moreover some preliminary results of the application of the coupled damage model on two beam tests were presented. Also in this case the numerical and the experimental results compare well, showing the potentiality of the model in reproducing the structural behavior of real reinforced concrete structures.

The proposed models can be profitably used to design new structures and to evaluate the variation of the safety factory for its whole service time, thus it can constitute a suitable tool for the designer. Moreover it could be used to predict the service time and safety factor of existing reinforced concrete structures. Since the model is numerically efficient it is particularly effective for large structure's analysis.

Further research is needed both in the mechanical and environmental aspects. From the mechanical point of view, the negative damage evolution law could be deeply investigated and possibly modified in a way that the pre-peak response could be described independently from the post-peak response. This is particularly important in case of the mesh-adjusted softening modulus for compression presented, since the actual procedure leads to the inevitable shift of the peak strain making the regularization technique less effective. Another aspect that needs more investigation is the shear retention factor. In the present work, the formulation originally proposed in previous works for a one-parameter scalar damage model, has been adopted and extended to the two-parameters scalar damage model. Even if a variable shear retention factor is adopted, the reference strain is a parameter that needs to be carefully evaluated; moreover it was observed a certain sensibility of this parameter on the results in some cases. Furthermore the direction of principal stresses deviates due to the residual shear strain and the corresponding principal positive stress can be sensibly greater than the tensile strength of concrete. These aspects deserve further investigation and the possibility of correlating the shear retention factor with some

characteristics of the material (e.g. maximum aggregate diameter, number and diameter of steel bars, etc.) should be evaluated.

From the environmental point of view, further research could deal with the definition of a relationship between the frost-related parameters (e.g. d_{env}, β and R_0) and some other key characteristics of the materials and test conditions (i.e. porosity, freezing-and-thawing velocity, moisture content), on the basis of available experimental and numerical data. Furthermore a refinement of the formulation of d_{env} could be included in the model, by introducing the dependence on the stress state (i.e. tension or compression). In this way the degradation of the concrete due to frost attack will also account for the different behavior in tension and in compression. Moreover, the effect of frost on bond between concrete and steel should be taken into account. Finally, further research could include the investigation of coupled degradation process, like chloride-induced corrosion and frost-attack, which can typically affect reinforced concrete structures and infrastructures in cold-climate regions.

APPENDIX A:
MESH REGULARIZATION IN COMPRESSION

In Chapter 3, the mesh-adjusted softening modulus in compression is presented.

The set of equations is reported here for clarity:

$$\begin{cases} f_{c1d} = \sigma\left(\varepsilon_{c1d}\right) & \text{peak evaluation} \\ \left.\dfrac{\partial\sigma}{\partial\varepsilon}\right|_{\varepsilon=\varepsilon_{c1d}} = 0 & \text{peak evaluation} \\ \sigma\left(\varepsilon_u\right) = 0 & \text{evaluation of } \varepsilon_{\mathrm{u}} \\ \displaystyle\int_{\varepsilon_{c1d}}^{\varepsilon_u} \sigma(\varepsilon)d\varepsilon + \frac{1}{2} f_{c1d}\varepsilon_{c1d}^{e} = g_c & \text{crusching energy} \end{cases} \tag{6.1}$$

The set of equations (6.1) is derived in the present section. The system is solved with a Newton-Raphson technique in the present work.

During a uniaxial compressive test, the constitutive equation $\sigma(\varepsilon)$ can be written by the following:

$$\sigma = \left(1-d^{-}\right)\bar{\sigma} = \left(1-d^{-}\right)E\varepsilon^{e} = \left(1-d^{-}\right)E\left(\varepsilon-\varepsilon^{p}\right) \tag{6.2}$$

where $\bar{\sigma}$ is the effective stress, E is the Young modulus, ε^{e} is the elastic strain and ε^{p} represents the plastic strain.

In the following the proposal A is considered, but it can be easily verified the result is valid also for proposal B. The negative damage evolution law is described by equation (3.64) which is here reporter for simplicity:

$$d^{-} = 1 - \left(\frac{r_0^{-}}{\bar{\tau}^{-}}\right)^{0.5} \cdot \left(1-A^{-}\right) - A^{-} \cdot \exp\left[B^{-} \cdot \left(1-\left(\frac{\bar{\tau}^{-}}{r_0^{-}}\right)^{0.5}\right)\right] \tag{6.3}$$

For uniaxial compressive load the following are valid:

$$r_0^{-} = \frac{K-\sqrt{2}}{\sqrt{3}} f_{01d} \tag{6.4}$$

$$\tau^{-} = \frac{K-\sqrt{2}}{\sqrt{3}} \bar{\sigma} \tag{6.5}$$

During an uniaxial compressive load test, the accumulation of damage and plastic strain starts when the equivalent negative strain expressed by (6.5) overcome the threshold (6.4). This is when the strain is equal to:

$$\varepsilon_{01d} = \frac{f_{01d}}{E} \tag{6.6}$$

When the total strain ε is greater than ε_{01d}, the plastic strain, the elastic strain and the total strain can be written as:

$$\varepsilon^{p} = \beta\varepsilon - \beta\varepsilon_{01d} \tag{6.7}$$

$$\varepsilon^{e} = \varepsilon(1-\beta) + \beta\varepsilon_{01d} \tag{6.8}$$

$$\varepsilon = \frac{\varepsilon^{e} - \beta\varepsilon_{01d}}{(1-\beta)} \tag{6.9}$$

Equations (6.4) and (6.5) can then be written in the equivalent way:

$$r_0^{-} = \frac{K-\sqrt{2}}{\sqrt{3}} E\varepsilon_{01d} \tag{6.10}$$

$$\tau^{-} = \frac{K-\sqrt{2}}{\sqrt{3}} E\varepsilon^{e} \tag{6.11}$$

and equation (3.64) can be written as:

$$d^{-} = 1 - \sqrt{\frac{\varepsilon_{01d}}{\varepsilon^{e}}} \cdot (1-A^{-}) - A^{-} \cdot \exp\left[B^{-} \cdot \left(1 - \sqrt{\frac{\varepsilon^{e}}{\varepsilon_{01d}}}\right)\right] \tag{6.12}$$

Finally the constitutive law expressed by (6.2) reads:

$$\sigma = \left\{\sqrt{\frac{\varepsilon_{01d}}{\varepsilon^{e}}} \cdot (1-A^{-}) + A^{-} \cdot \exp\left[B^{-} \cdot \left(1 - \sqrt{\frac{\varepsilon^{e}}{\varepsilon_{01d}}}\right)\right]\right\} E\varepsilon^{e} \tag{6.13}$$

The method as shown in Chapter 2 and Chapter 3 relates the constitutive law to the specific crushing energy via a characteristic element length. This condition is expressed by the fourth equation in (6.1). The ultimate deformation ε_u that appears in the interval of integration on the fourth of (6.1) is unknown, thus a proper equation to define this point is needed. This is represented by the third equation which can be written also as:

$$d^{-}(\varepsilon_u) = 1 \tag{6.14}$$

Substituting equation (6.12) in (6.14) one obtains:

$$\sqrt{\frac{\varepsilon_{01d}}{\varepsilon_u^{e}}} \cdot (1-A^{-}) + A^{-} \cdot \exp\left[B^{-} \cdot \left(1 - \sqrt{\frac{\varepsilon_u^{e}}{\varepsilon_{01d}}}\right)\right] = 0 \tag{6.15}$$

where ε_u^{e} is the elastic strain corresponding to the total strain ε_u.

The solution by parts of the integral on the fourth equation in (6.1) permits to write the extended version of it:

$$g_c = \frac{1}{2} f_{c1d} \varepsilon^e_{c1d} + \frac{2E}{(1-\beta)}\left(I_1 + I_2 + I_3\right) \tag{6.16}$$

where ε^e_{c1d} is the elastic strain corresponding to the total strain ε_{c1d} and I_1, I_2 and I_3 are defined as:

$$I_1 = \frac{1}{2}\sqrt{-\varepsilon_{01d}}\left(1-A^-\right)\left(\sqrt{-\varepsilon^e_u}^{\,3} - \sqrt{-\varepsilon^e_{c1d}}^{\,3}\right) \tag{6.17}$$

$$I_2 = -A^- \exp\left[B^-\left(1-\frac{\sqrt{-\varepsilon^e_u}}{\sqrt{-\varepsilon_{01d}}}\right)\right]\times \\ \times\left(\sqrt{-\varepsilon^e_u}^{\,3}\frac{\sqrt{-\varepsilon_{01d}}}{B^-} + 3\sqrt{-\varepsilon^e_u}^{\,2}\frac{\sqrt{-\varepsilon_{01d}}^{\,2}}{B^{-2}} + 6\sqrt{-\varepsilon^e_u}\frac{\sqrt{-\varepsilon_{01d}}^{\,3}}{B^{-3}} + 6\frac{\sqrt{-\varepsilon_{01d}}^{\,4}}{B^{-4}}\right) \tag{6.18}$$

$$I_3 = A^- \exp\left[B^-\left(1-\frac{\sqrt{-\varepsilon^e_{c1d}}}{\sqrt{-\varepsilon_{01d}}}\right)\right]\times \\ \times\left(\sqrt{-\varepsilon^e_{c1d}}^{\,3}\frac{\sqrt{-\varepsilon_{01d}}}{B^-} + 3\sqrt{-\varepsilon^e_{c1d}}^{\,2}\frac{\sqrt{-\varepsilon_{01d}}^{\,2}}{B^{-2}} + 6\sqrt{-\varepsilon^e_{c1d}}\frac{\sqrt{-\varepsilon_{01d}}^{\,3}}{B^{-3}} + 6\frac{\sqrt{-\varepsilon_{01d}}^{\,4}}{B^{-4}}\right) \tag{6.19}$$

The last two conditions needed is that the derivative of the stress function should be zero for ε_{c1d} as illustrated by second equation in system (6.1), providing a maximum point of the constitutive law and that for ε_{c1d} the corresponding stress should be equal to the compressive f_{c1d} as depicted in the first equation of the system (6.1). The latter equation is straight forward considering (6.13), while the former is obtained by deriving the same (6.13) leading to the following resulting system:

$$\begin{cases} f_{c1d} = \left\{\sqrt{\dfrac{\varepsilon_{01d}}{\varepsilon^e_{c1d}}}\cdot\left(1-A^-\right) + A^-\cdot\exp\left[B^-\cdot\left(1-\sqrt{\dfrac{\varepsilon^e_{c1d}}{\varepsilon_{01d}}}\right)\right]\right\} E\varepsilon^e_{c1d} \\ \sqrt{\varepsilon_{01d}}\left(1-A^-\right) + A^-\exp\left[B^-\left(1-\dfrac{\sqrt{\varepsilon^e_{c1d}}}{\sqrt{\varepsilon_{01d}}}\right)\right]\left[2\sqrt{\varepsilon^e_{c1d}} - \dfrac{\sqrt{\varepsilon^e_{c1d}}^{\,2}}{\sqrt{\varepsilon_{01d}}}B^-\right] = 0 \\ \sqrt{\dfrac{\varepsilon_{01d}}{\varepsilon^e_u}}\cdot\left(1-A^-\right) + A^-\cdot\exp\left[B^-\cdot\left(1-\sqrt{\dfrac{\varepsilon^e_u}{\varepsilon_{01d}}}\right)\right] = 0 \\ g_c = \dfrac{1}{2} f_{c1d}\varepsilon^e_{c1d} + \dfrac{2E}{(1-\beta)}\left(I_1 + I_2 + I_3\right) \end{cases} \tag{6.20}$$

which is a non-linear system of four equations in four variables. The variables of the system are A^-, B^-, ε^e_u and ε^e_{c1d}. The input parameters are assumed to be: ε_{01d}, f_{c1d}, g_c, E and β which represent respectively the initial elastic strain (i.e. damage threshold), the uniaxial compressive strength, the specific crushing energy,

the young modulus and the plasticity parameter. The solution of the system is performed with a Newton-Raphson technique.

The aim of this work is to assess the collapse safety of both new and existing reinforced concrete structures. The latter can also be subjected to environmental degradation process. To this aim the behavior of concrete and reinforced concrete structures eventually degraded by physical-chemical attacks need to be accurately described with theoretical and numerical models that can take into account the main characteristics of this kind of structures.

In this work a coupled environmental-mechanical scalar plastic-damage model originally developed by other authors was modified, enhancing both the mechanical and the environmental aspects. In particular an innovative formulation able to account for the physical deterioration mechanism due to freeze-thaw cycles was developed within the framework of the environmental damage approach, while a more comprehensive representation of the mixed tension-compression domain and an enhancement of the plastic evolution law were proposed within the framework of the mechanical damage approach. The model was enriched with a Shear Retention Factor extended to the two-parameters scalar damage model here presented.

To validate and calibrate the mechanical damage model, it was applied to reproduce different tests taken from literature. Particular attention was dedicated in reproducing the Kupfer tests and the response of a Single-Edge-Notched beam, typical example of mixed-mode failure. In both cases experimental and numerical results compare well, demonstrating the ability of the model to predict structural response and crack patterns of such examples.

To simulate the inelastic behavior of reinforced concrete panels, an efficient membrane model was proposed assuming superposition of different membranes (i.e. concrete and an appropriate number of steel bars). On the other hand, to assess the nonlinear behavior of reinforced concrete plates, an efficient plate model was proposed following a layered approach.

Concerning the environmental aspect, the coupled environmental-mechanical damage model was calibrated by using a limited number of tests carried out on concrete specimens under mono-axial and bi-axial compressive stresses, subjected to freeze-thaw cycles with different levels of deterioration. Finally the proposed coupled model was used as a predictive tool both for simulating a different series of biaxial concrete specimens subjected to freeze-thaw cycles and to evaluate the load carrying capacity of a frost damaged beam.